SYNTHESIS, CHARACTERIZATION AND CATALYTIC ACTIVITY OF NOVEL MIXED OXIDES FOR ENERGY AND ENVIRONMENTAL RELATED REACTIONS

by

ATINDRA MOHAN BANERJEE

(Enrolment No. CHEM01200604010)

Bhabha Atomic Research Centre, Mumbai, India

A thesis submitted to the

Board of Studies in Chemical Sciences

In partial fulfillment of requirements

For the Degree of

DOCTOR OF PHILOSOPHY

of

HOMI BHABHA NATIONAL INSTITUTE

October, 2012

STATEMENT BY AUTHOR

This dissertation has been submitted in partial fulfillment of requirements for an advanced degree at Homi Bhabha National Institute (HBNI) and is deposited in the Library to be made available to borrowers under rules of the HBNI. Brief quotations from this dissertation are allowable without special permission, provided that accurate acknowledgement of source is made. Requests for permission for extended quotation from or reproduction of this manuscript in whole or in part may be granted by the Competent Authority of HBNI when in his or her judgment the proposed use of the material is in the interests of scholarship. In all other instances, however, permission must be obtained from the author.

Atindra Mohan Banerjee

DECLARATION

I, hereby declare that the investigation presented in the thesis has been carried out by me. The work is original and has not been submitted earlier as a whole or in part for a degree / diploma at this or any other Institution / University.

Atindra Mohan Banerjee

Dedicated to

Ma, Baba

&

Seemita

Acknowledgements

This thesis owes its existence to the help, support, encouragement and inspiration of many people. It is indeed a pleasure to express my deep gratitude to my guide Dr. (Mrs.) S. R. Bharadwaj, Head, Fuel Cell Materials and Catalysis Section, Chemistry Division, BARC for her invaluable guidance and constant support and encouragement during the entire course of this study.

Sincere thanks are to Dr. A. K. Tripathi and Dr. M. R. Pai who introduced me to the field of heterogeneous catalysis and taught several aspects of thermal catalysis and photocatalysis.

I sincerely acknowledge the support and encouragement rendered to my research work by Prof. T. Mukherjee, Director, Chemistry Group and Dr. D. Das, Head, Chemistry Division.

Chairman (Dr. D. Das) and members (Dr. C. G. S. Pillai, Prof. A. K. Tyagi, Dr. V. K. Jain) of the doctorial committee are gratefully acknowledged for their critical review and suggestions during progress review and pre-synopsis viva-voce.

It is my pleasant duty to thank Shri C. S. R. Prasad, Head Chemical Technology Division, BARC for enlightening me with the engineering aspects and applications of our work and Dr. P.K. Sinha, Head, ECMS, BARC for his help in the preparation of oxides of iron in large scale. I also sincerely thank Dr. R. Tewari (MSD, BARC) for recording the TEM images, Dr. Anshu Singhal (ChD, BARC) for preparation of indium titanate nanoparticles by solvothermal method, Dr. A. Arya for helping me with the theoretical results, Shri. Jagannath (TPD, BARC) for recording the XPS spectra, Shri. N. Manoj (ChD, BARC) for recording the SEM images of our samples, Shri. S. S. Meena (SSPD, BARC) for recording the Mossbauer spectra, Shri. Siddharta Kolay (ChD, BARC) for recording the EGA spectra and Mrs. Archana Gaikwad (ChD, BARC) for her help in analysis of products of reaction by titrimetry. I express big thanks to my colleagues Dr. K. Bhattacharyya, Dr. B. P. Mandal, Dr. S. Verma, Shri D. Tyagi, Shri. Asheesh Kumar for useful scientific discussions with them and maintaining a cordial environment. I also express my appreciation to Mr. Ganesh Mane for his assistance. The nice and congenial environment provided by other members of Chemistry Division is also worth mentioning.

I would express special thanks to my wife Seemita for her constant, support encouragement and useful scientific discussion.

I wish to express my sincere gratitude and indebtedness to my parents for their love and blessings on me. I am also grateful to my brother for being caring, loving and helpful to me. Finally I would like to give credit and love to my daughter Asmita, for her support and love at home.

Atindra Mohan Banerjee

Contents

Introduction

Sulfuric acid decomposition in small scale over spinel ferrite powder catalyst

Sulfuric acid decomposition in enhanced scale with iron oxide based granular catalysts

Synopsis

The main focus of this thesis is invoking the use of mixed oxide based heterogeneous catalysts to address the need for CO_2 - free cleaner future energy system. Hydrogen being a clean, sustainable and renewable energy carrier there is a global effort for large scale hydrogen generation by water splitting. Hydrogen generation from water can be achieved by thermochemical cycles, electrolysis, photocatalytic, photobiological or other means. Thermochemical water splitting cycles and high temperature steam electrolysis are the two important methods to generate hydrogen on an industrial scale. Detailed investigations have been carried out on iron oxide based catalysts for sulfuric acid decomposition reaction - the most energy intensive step of sulfur based thermochemical water splitting cycles for hydrogen production. Photocatalysis is a challenging method for hydrogen generation from water under ambient conditions using solar light. Indium titanate based photocatalysts has been investigated for photocatalytic hydrogen generation.

The thesis is divided into the following nine chapters:

Chapter 1: Introduction

In this chapter we initially analyze the recent trends in global energy production and the rising CO_2 emissions with its impact on global climate. In future, the world will be facing production decline of conventional oil even though there will be a spurt in demand and moreover there are serious environmental problems accompanying their combustion - rising CO_2 levels in the atmosphere is resulting in global warming. These facts suggest the need for a CO_2 - free clean energy future and modern society thus, has been in search for a new form of energy that is clean, renewable, cheap, and a viable alternative to fossil fuels and hydrogen seems to be a promising solution. A large research initiative over several decades has focused on developing environmentally friendly, efficient, and economic pathways for hydrogen production. Free hydrogen does not occur naturally in large quantity, and thus it must be generated from compounds containing hydrogen using some other energy source. Hydrogen is therefore an energy carrier (like electricity), not a primary energy source (like coal). Feedstocks of hydrogen like methane, coal, and biomass are carbon-based, so they will release carbon monoxide or carbon dioxide as a by-product of the conversion process. Water contains only hydrogen and oxygen, so no carbon dioxide is released in its decomposition and so hydrogen from water is the ultimate solution. Role of heterogeneous catalyst for the two hydrogen production processes – thermochemical and photocatalytic along with the current global status are then discussed. Basic aspects of heterogeneous catalysis are also provided in brief.

Thermochemical cycles consist of a series of chemical reactions to produce hydrogen from water at much lower temperatures than required for the direct thermal decomposition of water [1]. Water splitting into hydrogen and oxygen is achieved via chemical reactions using intermediate elements which are recycled. The sum of all the reactions is equivalent to the dissociation of the water molecule. Among the large number of thermochemical water-splitting cycles proposed in the literature [2], the sulfur-based group is of considerable interest owing to their higher efficiencies, large scale hydrogen production potential and other advantages including operational ease due to no solid phase involved etc. All the sulfur-based cycles, which include the sulfur–iodine cycle [3], the hybrid sulfur cycle [4], and the sulfur–bromine hybrid cycle [5], employs the sulfuric acid decomposition reaction as the most energy demanding thermal to chemical energy conversion step. The reactions involved in these sulfur based thermochemical cycles are as follows:

Sulfur-Iodine Cycle:

$$I_2\ (l) + SO_2\ (g) + 2H_2O\ (l) \rightarrow 2HI\ (l) + H_2SO_4\ (l)\ (70 - 120°C) \qquad ...\ (1.1)$$

$$2HI\ (g) \rightarrow I_2\ (g) + H_2\ (g)\ (300 - 450°C) \qquad ...\ (1.2)$$

H_2SO_4 (g) → H_2O(g) + SO_2(g) + 1/2O_2(g) (800- 900°C) ... (1.3)

Hybrid-Sulfur Cycle:

SO_2 (aq) + 2H_2O (l) → H_2SO_4 (aq) + H_2 (g) (70 - 120°C, electrolysis) ... (1.4)

H_2SO_4 (g) → H_2O(g) + SO_2(g) + 1/2O_2(g) (800- 900°C) ... (1.5)

The sulfur–iodine thermochemical cycle, comprising mainly of three chemical reactions - - Bunsen reaction (Eqn.1.1), Hydriodic acid decomposition (Eqn.1.2) and sulfuric acid decomposition (Eqn.1.3), was originally proposed by General Atomics (GA) [6]. The hybrid sulfur cycle in which the Bunsen reaction and hydriodic acid decomposition is replaced by an electrolysis step is also known as Westinghouse sulfur cycle and consist of only two main reactions – aqueous SO_2 electrolysis (Eqn.1.4) and sulfuric acid decomposition (Eqn.1.5).

Thus, it can be seen sulfuric acid thermal decomposition is the most endothermic reaction in the sulfur based thermochemical cycles [1] and is normally carried out at above 800 °C in a process reactor that can withstand high temperature heat from a nuclear reactor supplying system or a solar concentrator. The sulfuric acid decomposition is comprised of following two reactions in series:

H_2SO_4 (g) → H_2O (g) + SO_3(g) (~ 450 °C) ... (1.6)

SO_3 (g) → SO_2 (g) + 1/2O_2 (g) (800- 900 °C) ... (1.7)

Sulfuric acid can be decomposed to its anhydride SO_3 (Eqn.1.6) with or without a catalyst, while the decomposition of SO_3 (Eqn.1.7) has been known to be a catalytic reaction. Apparently only a few and partial kinetic data for the global process can be found in the literature. Thus, research on newer catalysts is vital from the view point of understanding the fundamental surface phenomenon and finally development of active and stable catalysts under the high temperature and acid environments. This will in turn bring about the viability of the thermochemical cycles in terms of equipment and plant sizing, cost cuts, uninterrupted operation and successful coupling to a nuclear reactor or solar concentrator leading to massive and economic hydrogen generation. Most of the reported catalysts for sulfuric acid decomposition are supported platinum catalysts, which undergoes deactivation under the harsh catalytic environments by metal or substrate sintering, leaching and also substrate sulfation. Moreover, the ever rising demand and increasing cost of noble metals make them less preferred for the above applications. Metal oxide catalysts are active and can be a substitute for noble metal catalysts as they fulfill the essential requirement of materials with better chemical and thermal stability and modified catalytic properties. In this thesis we have investigated iron oxide based catalysts for sulfuric acid decomposition reaction.

The photocatalytic splitting of water into hydrogen and oxygen using solar energy is a potentially clean and renewable source for hydrogen fuel. Since Honda and Fujishima first found a titanium dioxide (TiO_2)-photoassisted electrochemical splitting of water in 1972 [7] semiconductor photocatalysts have attracted much attention and extensive studies have been devoted in this field. Although much work has been conducted over the past three decades to exploit new photocatalysts responsive to UV and visible light irradiation, attention has been devoted almost exclusively to titania (TiO_2) and this has been reviewed in several articles [8-11]. This thesis investigates the mixed oxide of In and Ti, In_2TiO_5 based photocatalysts for water splitting reaction in presence of a sacrificial reagent. In addition the thermal properties of these oxides have also been investigated.

Chapter 2: Experimental and Methods

Chapter 2 deals with experimental techniques used for the synthesis, characterisation and evaluation of the thermocatalytic and photocatalytic behavior of the metal oxides. Various characterization techniques that were used include X-Ray Diffraction (XRD), N_2-adsorption BET surface area, Fourier Transformed Infra Red spectroscopy (FT-IR), Scanning Electron Microscopy (SEM), Transmission Electron Microscopy (TEM), X-ray Photoelectron

Spectroscopy (XPS), Temperature Programmed Desorption Reduction Oxidation (TPD/R/O), Mossbauer Spectroscopy, Thermogravimetry with Evolved Gas Analysis (TG-EGA) and Gas Chromatograph (GC) with Thermal Conductivity Detector (TCD). A brief account of these techniques is presented in this chapter.

The catalytic reactors designed and developed for evaluation of catalytic activity for sulfuric acid decomposition are discussed in details. Work was initiated in a continuous, flow through fixed-bed quartz reactor (30 cm long, 0.8 cm I.D) fabricated in quartz, where 2 g of catalyst was employed as shown in Fig. 1. High purity nitrogen was bubbled through boiling sulfuric acid reservoir, which was kept at a temperature of ~338°C. The flowing nitrogen gas carried the acid vapors over the catalyst bed. But, some condensation of the acid occurred during its flow to the decomposition furnace from the boiler, although the temperature of the in-between region was kept at 330°C.

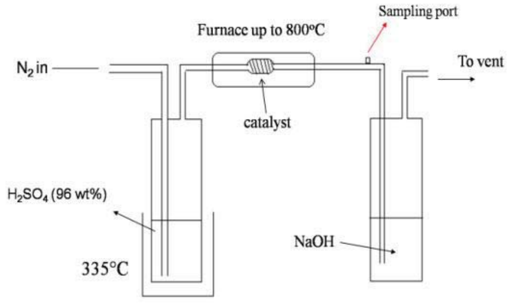

Fig.1: Block diagram of the quartz experimental set up developed initially for carrying out sulfuric acid decomposition reaction with 2 g powder catalyst

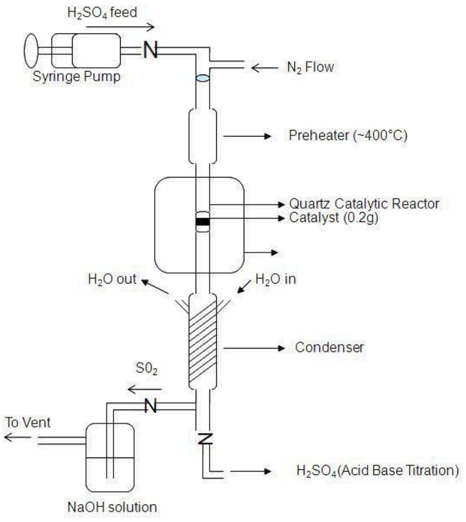

Fig. 2: Block diagram of the small scale quartz experimental set up for carrying out sulfuric acid decomposition reaction with 200 mg powder catalyst

This was rectified and another small scale experimental set up was indigenously developed for carrying out the catalytic activity measurements with 200 mg of the catalyst which also involved a flow through quartz reactor as shown schematically in Fig. 2. A syringe pump, filled with concentrated sulfuric acid (98 wt%, sp.gr = 1.84) was employed for controlled injection of sulfuric acid into the system and catalytic bed. Provision was made for N_2 to be used as a carrier. The acid pumped by the syringe at a flow rate of 0.05 ml min^{-1} were fed along with the carrier to a pre-heater kept at 400°C (heated by electrical heating tapes) to generate vapors of sulfuric acid. The acid vapors were then led to the catalytic reactor fabricated in quartz and kept inside a controlled electrically heated furnace at high temperature. A condenser was fitted downstream along with a liquid collector with tap. The gaseous products were passed through a NaOH solution (0.1 N) and finally vented out.

A catalytic reactor in an enhanced scale to evaluate activity with ~ 20 g of catalyst in absence of any diluents like N_2, was also designed and indigenously constructed of glass, quartz and Teflon tubing. The reactor as shown in Fig. 3 consists of dual quartz tubes, with sulfuric acid accumulating at the bottom of the annular region and catalyst being loaded at the top of the annular region and held on its position by a perforated quartz disc. This new design based on dual quartz tube can function as an integrated acid boiler, preheater and decomposer and the absence of high temperature connections renders it free from acid corrosion and leakage. In both the cases, product analysis was done by chemical titrimetric method, the unreacted sulfuric acid being titrated after condensation and one of the products SO_2 was measured by trapping in NaOH or I_2 solution.

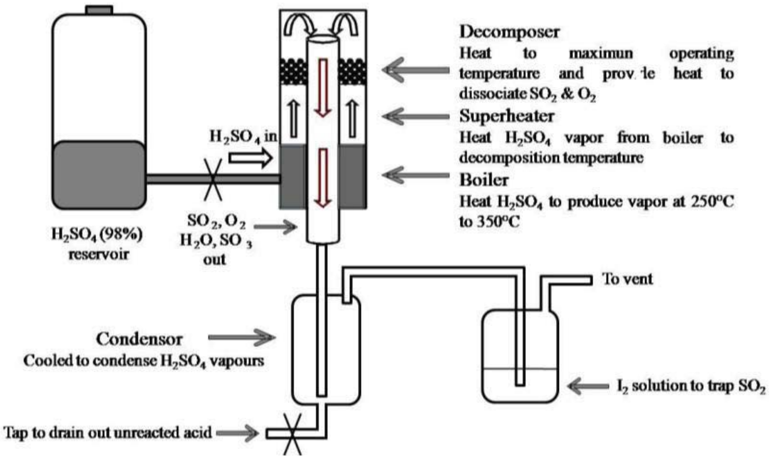

Fig. 3: Block diagram of the enhanced scale quartz experimental set up for carrying out sulfuric acid decomposition reaction with 20 g granular catalyst.

Photocatalytic activity for hydrogen generation of indium titanate based oxides were evaluated in a rectangular quartz reactor of dimensions (10 x 2.1 x 2.1 cm^3), equipped with a sampling port provided with a septum through which gas mixture could be removed for analysis. 0.1 g of catalyst was kept in contact with water + methanol mixtures (total volume of 15 ml, 2:1 v/v %) for conducting the photocatalysis experiment. The reactor was then irradiated under water-cooled medium pressure mercury vapour lamp (Hg, Ace Glass Inc., 450W) placed horizontally in a chamber close to the lamp.

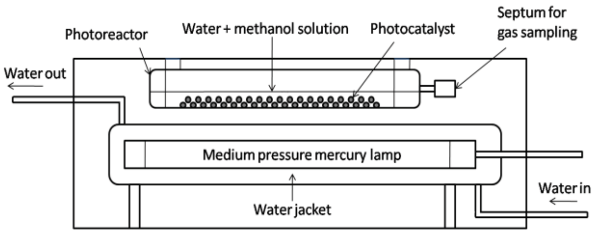

Fig. 4. Typical outer irradiation reaction assembly for evaluation of photoactivity of the samples for H_2 generation under UV-vis irradiation with medium pressure mercury lamp

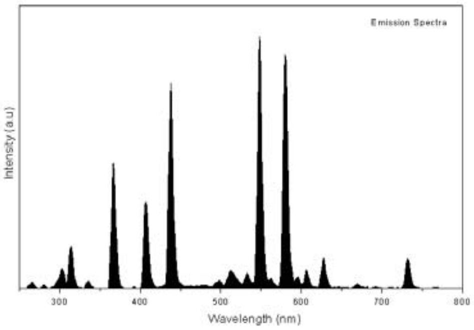

Fig. 5. Emission Spectra of the Medium Pressure mercury lamp used in the Photo-irradiator

Fig. 4 displays the typical outer irradiation quartz assembly consisting of photoreactor and the light source along with water circulation jacket to absorb IR irradiation. The emission spectra of the medium pressure mercury lamp i.e. the light source is shown in Fig. 5. The lamp exhibits broad range emission spectra with maxima at both UV and the visible range (16% UV, rest is visible light). The reaction products were analysed after every 2 h for a period of ~ 6-8 h using a gas chromatograph Netel (Michro-1100), India) equipped with a thermal conductivity detector (TCD), molecular sieve column (4m length) with argon as carrier and employed in the isothermal temperature mode at 50°C oven temperature.

Chapter 3: Sulfuric acid decomposition in small scale over iron oxide and chromium doped iron oxide powder catalyst

Chapter 3 presents the preparation, characterization and catalytic activity of chromium doped iron oxide catalysts $Fe_{2-x}Cr_xO_3$ ($0 \leq x \leq 0.4$) for sulfuric acid decomposition carried out in the small scale catalytic reactor shown in Fig. 1. The various iron oxide based samples were synthesized by ceramic route and characterized by XRD, N_2-BET surface area and FTIR. Doping Cr^{3+} in Fe_2O_3 lattice resulted in formation of solid solutions upto a maximum of 10 % substitution i.e. $x = 0.2$ in $Fe_{2-x}Cr_xO_3$ beyond which a secondary phase of Cr_2O_3 segregated in 20 % doped sample i.e. $x = 0.4$. The stability of catalysts towards repeated reduction-oxidation cycle was monitored by recording multiple temperature programmed reduction/oxidation (TPR/O) profiles. Fig. 6 presents the 3-4 successive TPR/TPO profiles recorded for both unsubstituted and substituted viz; Fe_2O_3 and $Fe_{1.8}Cr_{0.2}O_3$ samples.

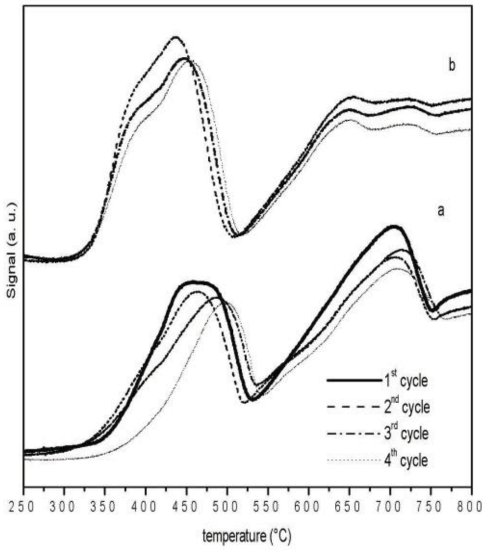

Fig. 6: Successive 4–5 TPR cycles of (a) Fe_2O_3 and (b) $Fe_{1.8}Cr_{0.2}O_3$. Each TPR cycle is followed by a TPO run.

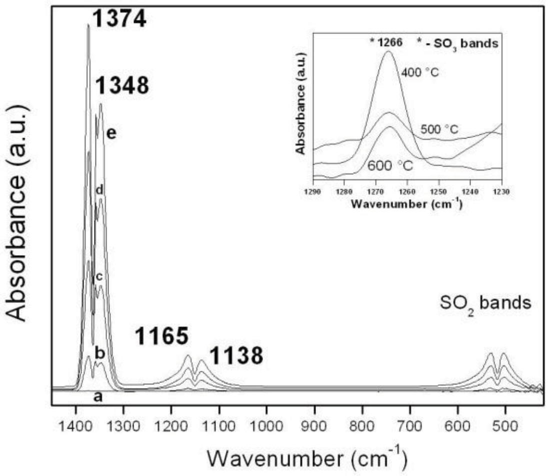

Fig. 7: FTIR spectra of effluent gases at different reaction temperatures resulting from sulfuric acid decomposition reaction using Fe_2O_3 catalyst (a) 500°C, (b) 600°C, (c) 650°C, (d) 700°C and (e) 800°C. Inset shows enlarged view of bands due to SO_3 with rise in reaction temperature.

In Fe_2O_3, as shown in Fig. 6a, the profiles of all four cycles are similar, but the TPR as a whole shifts to a higher temperature range in subsequent cycles. However 10% substitution (Fig. 6b) has resulted in reproducible behavior towards repeated TPR cycles thus minimizing the sintering effects observed in case of iron oxide, Fe_2O_3 sample. Simple oxide catalysts faces main drawback of sintering when subjected to repeated cycles of reduction and oxidation and thus for every subsequent cycle the reduction temperature of Fe_2O_3 increases. Therefore, ease with which sample undergoes reduction decreases constantly, in multi cycle application and catalyst performance detoriate after several cycles. Cr substitution helps in stabilizing active Fe_2O_3 component as evident by Fig. 6 and minimizes the sintering effects. The temperature dependent activity was evaluated using 2 g catalyst in temperature range of 500-900 °C for the sulfuric acid decomposition reaction. The catalytic reaction product SO_2 was identified by Mass and IR spectroscopy and quantitatively analyzed using gas chromatogram. Effluent stream at each reaction temperature was also analyzed by vibrational spectroscopy and typical spectra are plotted in Fig. 7. The increase in intensity for SO stretching bands in SO_2, with the increase in reaction temperature, in the IR spectrum of evolved gas using Fe_2O_3 as catalyst is shown in Fig. 7. Both doped and pristine Fe_2O_3 facilitated the thermal decomposition of sulfuric acid in temperature range of 550 - 800 °C as compared to the uncatalysed reaction. Among the three samples investigated Fe_2O_3, $Fe_{1.8}Cr_{0.2}O_3$ and $Fe_{1.6}Cr_{0.4}O_3$, highest SO_2 conversion was obtained for $Fe_{1.8}Cr_{0.2}O_3$ catalyst. 10 % Cr substitution in Fe_2O_3 lattice resulted in enhanced reproducibility towards repeated reduction oxidation cycles as shown in Fig. 6 which could be one of the possible reasons for its higher activity. The presence of XRD and IR lines due to sulfate species on the used catalyst samples along with the thermal analysis of the metal sulfates and the catalytic activity of the metal oxides confirm the formation and decomposition of metal sulfates as the intermediates in the mechanism of SO_3-SO_2 conversion on chromium doped iron oxides.

Chapter 4: Sulfuric acid decomposition in small scale over spinel ferrite powder catalyst

The promising results obtained for sulfuric acid decomposition with iron oxide catalysts as discussed in chapter 3, prompted us to investigate the above high temperature redox reaction with other oxides based on iron that offer good thermal stability, redox and catalytic properties like spinel ferrites. Spinel ferrites crystallize into different crystal structure but are ternary oxides of iron, viz; AFe_2O_4 (A = Cu^{2+}, Co^{3+} and Ni^{2+}). The ferrites prepared by gel combustion method were characterized for crystallinity, structure, morphology and redox properties. The first cycle TPR profiles of three ferrospinel catalysts AFe_2O_4 (A = Cu^{2+}, Co^{3+} and Ni^{2+}) are shown in Fig. 8 which depicts that the reduction temperature of the spinels increases in the order of $CuFe_2O_4<CoFe_2O_4<NiFe_2O_4$. The great interest of these TPR studies is to establish correlations between the reducibilities of the spinels and reactivities for redox reactions like sulfuric acid decomposition. Fig. 9 exhibits the temperature dependent catalytic activities of the ferrospinels for sulfuric acid decomposition reaction which were carried out with 200 mg of catalyst in the catalytic reactor shown in Fig. 2, in the temperature range of 650°C to 825°C at a sulfuric acid flux of 0.05 ml/min. All the three spinel ferrites were found to be active but copper ferrite was the most promising catalyst for sulfuric acid decomposition reaction among the three ferrospinels investigated. It is evident from Fig. 9 that the maximum activity is obtained for copper ferrite with a conversion of about ~ 78% at 800°C. Sulfuric acid decomposition in sulfur based thermochemical cycles is normally carried out at above 800 °C in a process reactor and so under the required process conditions copper ferrite is found to be the most active catalyst. It is pertinent to mention here that blank experiments in absence of catalysts verified that homogeneous vapor phase reactions did not occur under these conditions.

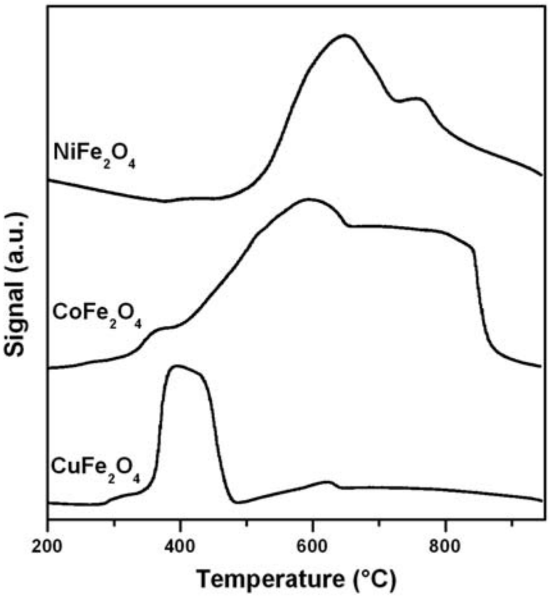

Fig. 8: Typical first cycle temperature programmed reduction profiles of the ferrospinel catalysts

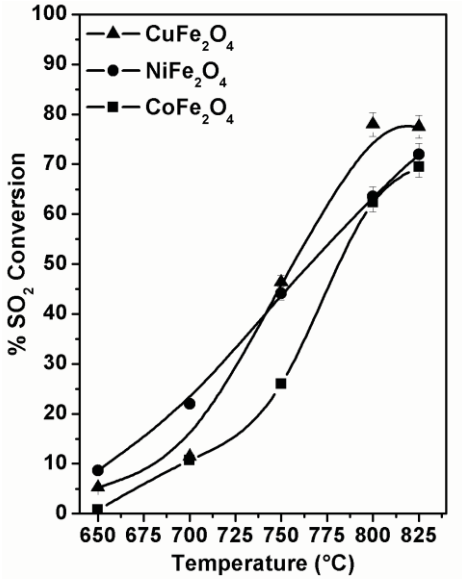

Fig. 9: Temperature dependent catalytic activity profiles of the three ferrospinel catalysts for H_2SO_4 decomposition reaction

The spent catalyst were collected and characterized by XRD, FTIR, SEM and EGA for evaluating the probable reasons in observation of the catalytic activity trend and subsequently through insights into the reaction mechanism. FTIR spectra of all the three spent catalyst samples exhibit four prominent peaks in the region 950-1200 cm^{-1}, which is indicative of C_{2v} symmetry and bidentate sulfate coordination. The presence of sulfates on the surface of the spent catalyst was also exhibited by SEM. Evolved Gas Analysis (EGA) showed evolution of SO_2 as a decomposition product from the existing sulfate of spent catalysts at high temperatures, with the temperature at which highest SO_2 is evolved following the order: $CuFe_2O_4 > NiFe_2O_4 > CoFe_2O_4$ (shown in Fig. 10) which is same as the catalytic activity trend at ~ 800 °C. The plausible mechanism proposed from an *ex situ* catalyst investigation is shown in scheme 1, which involves the metal sulfate formation and then decomposition followed with an oxygen evolution step, with the metal sulfate decomposition step playing the most crucial role in determining the reaction kinetics. The lower thermal stability of sulfate and better reducibility are responsible for the improved catalytic properties of copper ferrite among the three ferrospinels investigated for sulfuric acid decomposition.

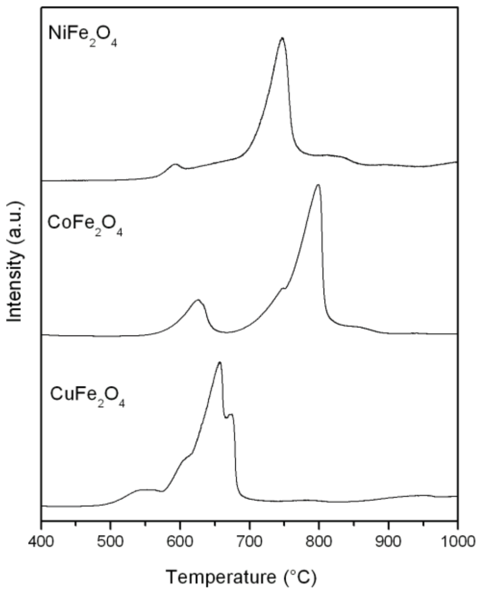

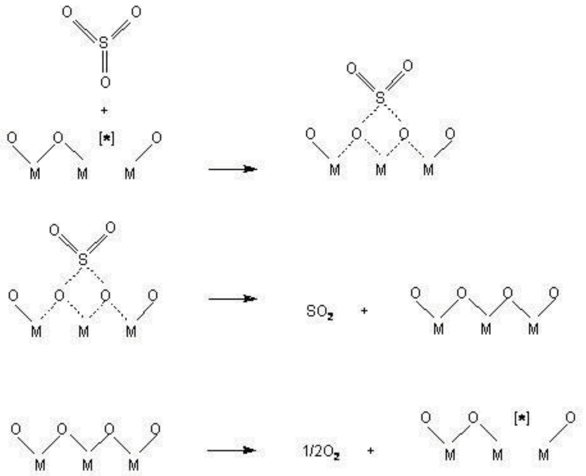

Fig. 10. Evolved gas analysis for mass no. 64 in mass spectrometer as a function of temperature of the spent spinel catalysts post sulfuric acid decomposition reaction

Scheme 1: A schematic presentation of proposed mechanism for sulfuric acid decomposition over spinel ferrites. [*] denotes surface active sites.

Chapter 5: Sulfuric acid decomposition in enhanced scale with iron oxide based granular catalysts

In chapter 5 we present the results and discuss about the sulfuric acid decomposition reaction tests that were carried out with granular iron oxide and 10 % chromium doped iron oxide (the two catalysts that showed promising results in powder form in a small scale reactor earlier discussed in chapter 3) in an enhanced scale in the quartz reactor having annular configuration which served as an integrated boiler, preheater and decomposer as shown in Fig 3. In the present study the oxide catalysts were prepared by co-precipitation method and then shaped into spherical beads of ~ 4-6 mm diameter. Catalytic activity was evaluated with 20 g of the granular catalyst as a function of temperature (700-825 °C), time (~100 h) and sulfuric acid flux (0.2-10 ml/min). Fig. 11 A-B shows the temperature and time (100 h) dependent catalytic activity which was evaluated with 20 g of spherical catalyst beads (~4-6 mm) at a sulfuric acid flux of ~ 0.63 ml/min. It is evident from fig. 11A that the Cr-doped sample showed much higher intrinsic activity at lower temperatures (< 775 °C) although at higher temperature in the range of 800 - 825 °C the catalytic activities were comparable. However, no decrease in catalytic activity for either catalyst was observed during the experiment for 100 h shown in Fig. 11B, although the doped sample exhibited slightly higher catalytic activity throughout. Both the oxide catalysts exhibited a loss in catalytic activity when subjected to very high flow of sulfuric acid of 2-10 ml/min as shown in Fig. 11 C-D.

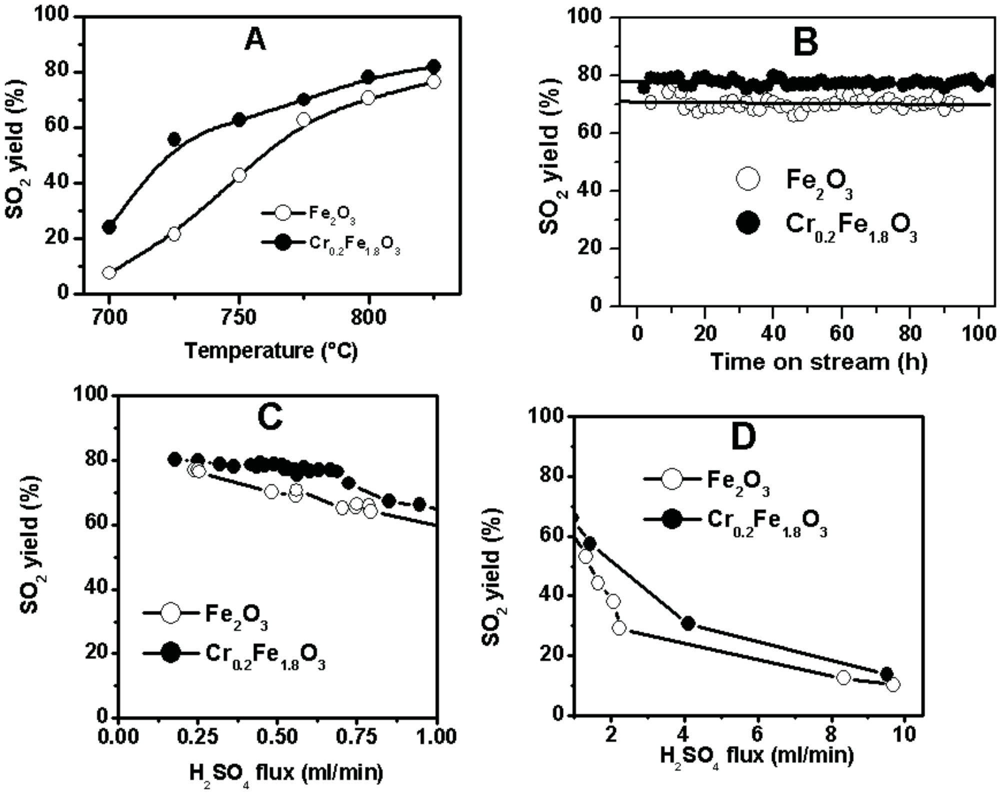

Fig. 11. The catalytic activities of Fe_2O_3 and $Fe_{1.8}Cr_{0.2}O_3$ for sulfuric acid decomposition; (A) temperature dependent catalytic activities at a H2SO4 flux of ~ 0.6 ml/min; (B) catalytic activity for 100 h time on stream at 800 °C at a H2SO4 flux of ~ 0.6 ml/min; (C and D) The effects of sulfuric acid flux on the product yield at 800

The spent as well as the fresh catalysts were analyzed ex-situ for by XRD, FTIR, SEM, XPS and EGA to monitor the structural, morphological and oxidation state changes after prolonged use for 100 h under harsh environmental conditions and also suggest the most probable mechanism. The Fe 2p XPS spectra of the fresh and spent Fe_2O_3 is shown in Fig. 12, from where we observe a shift towards higher binding energy of Fe 2p which can be attributed to iron present in a surface sulfate species. However, a more accurate assessment of the presence of sulphates was done using the sulfur 2p spectra and a prominent peak was observed at ~169 ev which is specific for sulfur present as sulfates. The spent catalyst exhibited characteristic four small peaks in the FTIR spectra between 997 and 1216 cm^{-1} which is an indicative of C_{2v} symmetry and bidentate sulfate coordination. Evolved Gas analysis from the spent catalysts showed that the evolution of SO_2 from the sulfates present on the surface of the spent catalyst was faster in the chromium doped sample. All these ex-situ spent catalyst investigation helped us to suggest the most probable mechanism which is in line with the proposed mechanism earlier (scheme-1). The morphological changes arising due to prolonged use as a catalyst for sulfuric acid decomposition at high temperatures were analyzed by SEM and are shown in Fig. 13. The enhanced catalytic activity of Cr-doped Fe_2O_3 was ascribed to the lower thermal stability of its sulfate, improved redox properties and probably more number of catalytic active sites.

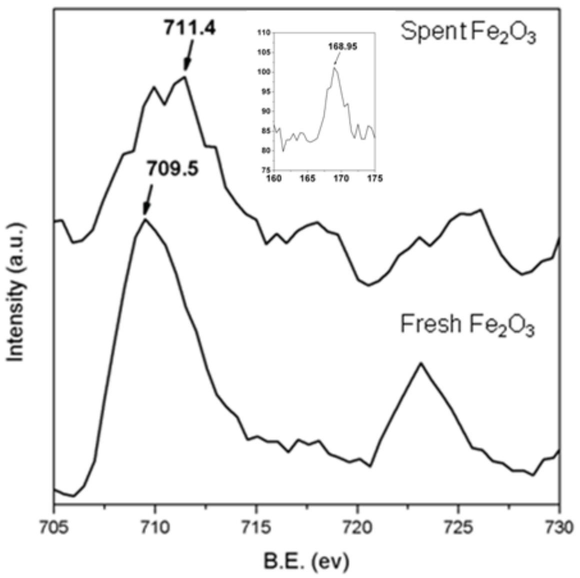

Fig. 12. Fe-2p XPS spectra of the fresh Fe_2O_3 before reaction and of spent Fe_2O_3 collected after 100 h use in high temperature sulfuric acid decomposition reaction. Inset shows the S-2p peak

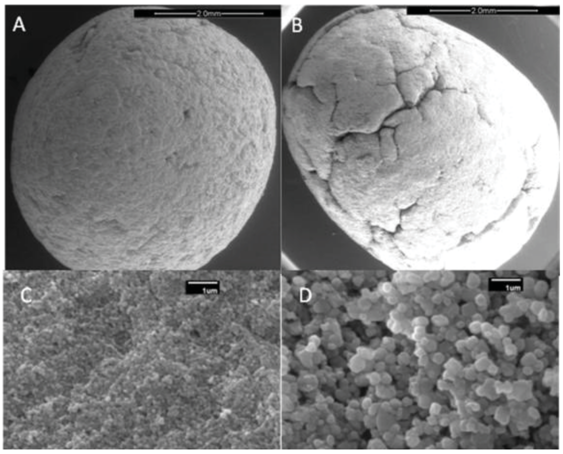

Fig. 13. Scanning Electron Micrographs of (A & C) fresh Fe_2O_3 before reaction and (B &D) of spent Fe_2O_3 collected after 100 h use in high temperature sulfuric acid decomposition reaction

Chapter 6: Performance of Pt/Al_2O_3 catalyst for sulfuric acid decomposition in comparison to iron oxide based catalysts

To compare the catalytic activity of the iron based oxide catalysts with a standard noble metal based catalyst which is a well explored catalyst for the above reaction a commercial Pt/Al_2O_3 catalyst was evaluated for sulfuric acid decomposition under similar conditions. The temperature dependent catalytic activity of Pt/Al_2O_3 catalysts was evaluated with 200 mg of powder catalyst in the catalytic reactor shown in Fig. 2, in the temperature range of 650°C to 825°C at a sulfuric acid flux ~ 0.05 ml/min. Result illustrated in Fig. 14, showed that catalytic activity increased with temperature, with Pt/Al_2O_3 catalyst showing maximum conversion of ~ 78% at 825 °C. The fresh and the spent powder catalysts were also characterized using XRD and FTIR to investigate any structural or surface modifications due to use at high temperature sulfuric acid decomposition.

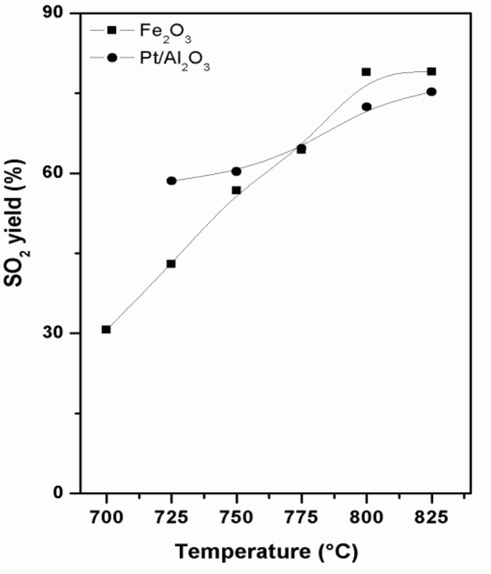

Fig. 14. The temperature dependent catalytic activities of Pt/Al_2O_3 sample compared with Fe_2O_3 and for sulfuric acid decomposition

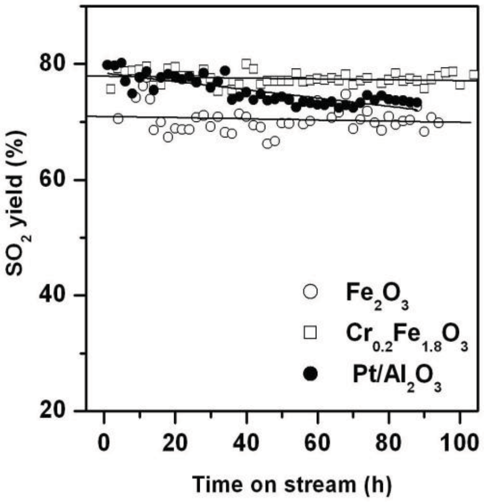

Fig. 15. The catalytic activities of Pt/Al_2O_3 sample for 100 h time on stream compared with Fe_2O_3 and $Fe_{1.8}Cr_{0.2}O_3$ for sulfuric acid decomposition

The catalytic activity of the granular Pt/Al_2O_3 (~4-6 mm) catalyst was also evaluated with 20 g catalyst in the enhanced scale in the catalytic quartz reactor shown in Fig. 3 as a function of temperature (700-825 °C), time (~100 h) and sulfuric acid flux (0.2-3.5 ml/min).

A slight decrease in activity from ~79% to ~74% SO_2 yield was observed with Pt/Al_2O_3 catalyst pellets as a function of time for 100 h under the sulfuric acid flux of ~0.63 ml/min as shown in Fig. 15. Thus it can be concluded that doped and undoped iron oxide catalyst are active and more stable than platinum based catalyst for sulfuric acid decomposition.

Chapter 7: Indium titanate as a photocatalyst for hydrogen generation

Indium titanate (In_2TiO_5) has been explored as a ternary mixed metal oxide for photocatalytic hydrogen generation. In this chapter we discuss the photocatalytic properties of bulk crystalline indium titanate prepared by ceramic route and nanocrystalline indium titanate synthesized by solvothermal and polyol methods. These oxides were well characterized for crystallinity, structure and morphology by XRD, FTIR, N_2-BET surface area, SEM and TEM. The band gap of these oxides were measured by recording the UV-vis DRUV spectra. Electronic structure and density of states for bulk In_2TiO_5 have been calculated by TB-LMTO method. The, photocatalytic activity of the indium titanate nanoparticles for water splitting reaction under UV-visible irradiation (16% UV + visible) was studied in the photoirradiator shown in Fig. 4 and compared with the bulk In_2TiO_5 as well as TiO_2 (P25) photocatalyst. A representative TEM image of In_2TiO_5 prepared by solvothermal route is shown in Fig. 16 which illustrates that the nanoparticles are quite uniform in shape and size. Although the particles are slightly agglomerated, because of lack of stabilizing surfactants, the grain boundaries are clearly distinguishable. The high crystallinity as well as the single-crystalline nature of the particles is further confirmed by SAED and HRTEM investigations. The SAED pattern can be indexed according to orthorhombic In_2TiO_5 (inset, Fig. 16). The light absorption by the photocatalyst material and the migration of the light-induced electrons and holes are the key factors controlling a photocatalytic reaction, which is relevant to the electronic structure characteristics of the material.

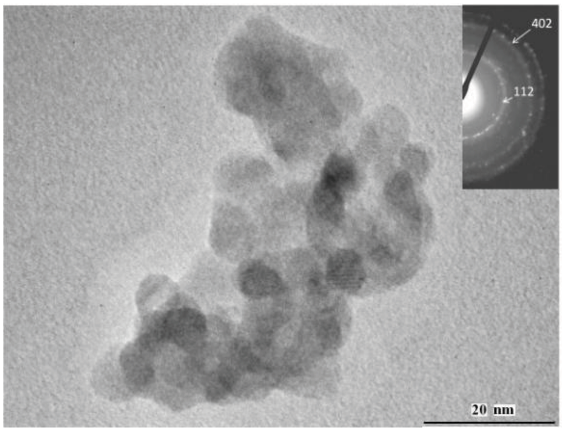

Fig. 16. TEM of In_2TiO_5 *nanoparticles synthesised by solvothermal method. SAED pattern for the nanoparticles is shown in inset*

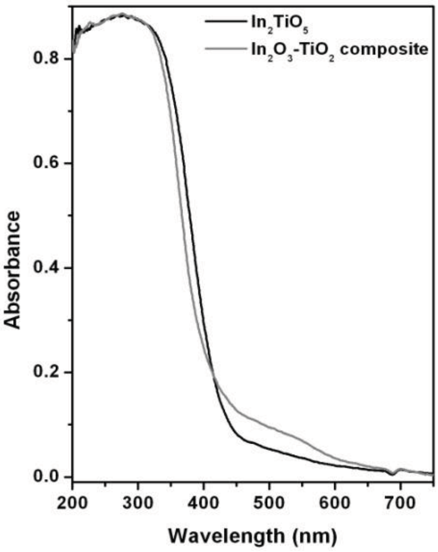

Fig. 17. DRUV pattern of In_2TiO_5 *nanoparticles prepared by solvothermal method. For comparison the spectra of the* TiO_2-In_2O_3 *nanocomposite is also shown*

The photoabsorption properties of the In_2TiO_5 nanoparticles detected by UV-visible diffuse-reflectance spectroscopy (DRS) are illustrated in Fig. 17. Based on these measurements the band gap of the nanoparticles was estimated to be 3.25 eV, which was found to be slightly larger than that of bulk In_2TiO_5 (3.02 eV). When irradiated for 6 h under UV visible irradiation H_2 evolution from water-methanol mixture (2:1) using nanoparticles prepared by solvothermal method (surface area 38 m^2g^{-1}) was ~260 μmoles, that of bulk indium titanate (surface area ~1 m^2g^{-1}) while that of standard Degussa TiO_2 (P25, surface area 50 m^2g^{-1}) was 145 μmoles. Thus, it can be concluded from these studies that indium titanate is a promising candidate photocatalyst. The band gap needs to be decreased to the visible region and the photoactivity has to be increase by adopting strategies like cationic doping which is discussed in the next chapter.

Chapter 8: Substituted indium titanates - Enhanced photocatalytic hydrogen generation and favorable redox properties

By doping suitable cations in indium titanate lattice its band gap can be decreased as cationic impurities are known to be suitably placed near the valence or conduction band of the host lattice and thereby decreasing the band gap and increasing photoactivity. Mixed oxides with nominal composition, $In_{2(1-x)}Ni_{2x}TiO_{5-\delta}$ for $0.0 \leq x \leq 0.2$, were prepared by solid state route and characterized using powder XRD and FTIR. Optical measurements by DRUV showed that Ni-doping induced a lowering in band gap of these semiconductor oxides as shown in Fig. 18.

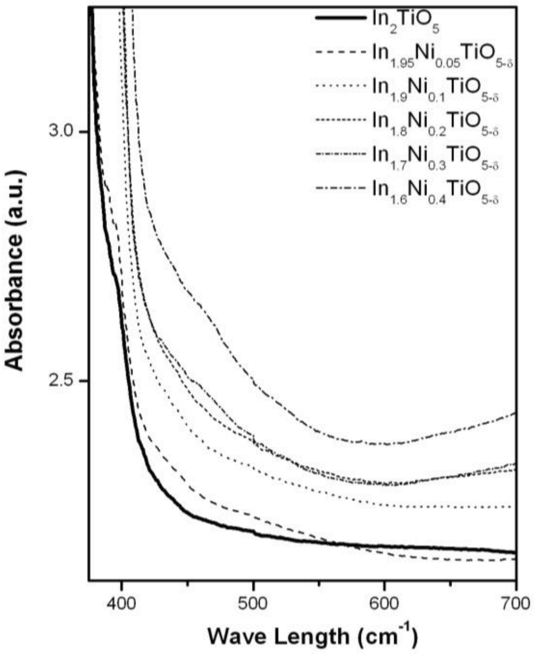

Fig. 18. DRUV spectra of the indium titanate $In_{2(1-x)}Ni_{2x}TiO_{5-\delta}$ samples which shows a progressive red shift in absorbtion with an increase in Ni content

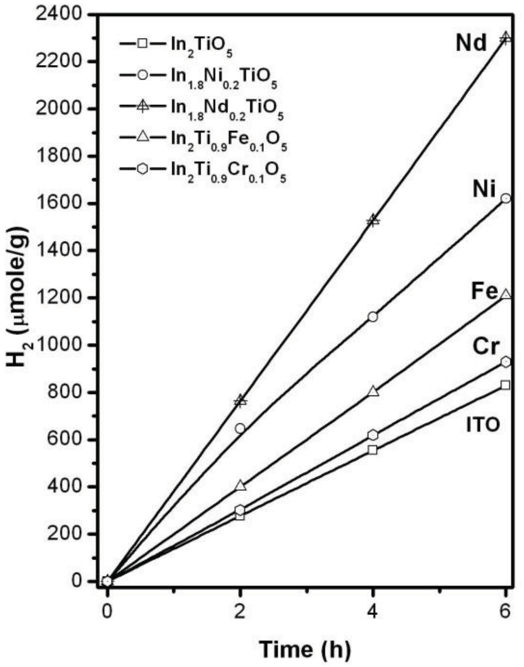

Fig. 19. Photocatalytic activity of substituted Indium titanate samples. H_2 yield is plotted as a function of time over In_2TiO_5, $In_{1.8}Nd_{0.2}TiO_5$, $In_{1.8}Ni_{0.2}TiO_{5-\delta}$ $In_2Ti_{1-x}M_xO_{5-\delta}$ ($M = Fe^{3+}$ and Cr^{3+}; $x = 0.2$), photocatalyst samples.

The photocatalytic properties of these oxides were evaluated for hydrogen generation reaction from water methanol mixture (2:1 by volume), where methanol served as a sacrificial agent, with 0.05 - 0.1 g of photocatalyst in the photoirradiator assembly shown in Fig. 4. The pristine In_2TiO_5 and all the doped samples were active for photocatalytic hydrogen generation from water + methanol mixture under UV-vis type irradiation. 10 % Ni doped sample exhibited highest activity for hydrogen generation. The higher photoactivity of the metal doped indium titanates was ascribed to the impurity levels added by the cationic dopents to the valence band of indium titanates thus increasing its photo response and consequent photoactivity. The results are compared with other A-site and B-site cationic doped samples in indium titanate In_2TiO_5 (A = Nd^{3+}; B = Fe^{3+} and Cr^{3+}; extent of doping 20 %) shown in Fig 19. Among all the catalysts, 10% Nd substituted indium titanate photoctalysts was found to be the most active under UV-vis irradiation in the photoirradiator (shown in Fig. 4 and Fig. 5) and it also showed H_2 generation photocatalytically under direct sunlight.

The thermal properties of these oxides were also investigated by recording the temperature programmed reduction (TPR/O). Ni substitution induced considerable ease in reducibility (T_{max}) of substituted samples as compared to In_2TiO_5 phase. The substitution-induced non-stoichiometry and the microstrucural defects may cause the distortion in the lattice, thus facilitating the reduction of oxides. The interesting observation was the reduction of otherwise non-reducible cation Ti^{4+}, in the 20% Ni substituted sample, $In_{1.6}Ni_{0.4}TiO_{5-\delta}$. Ni metal initially formed by the reduction of Ni^{2+} dissociate and activate the hydrogen which eased the In^{3+} reduction and even facilitated the reduction of Ti^{4+}.

Chapter 9: Conclusions and scope for future work

The final chapter addresses the summary and the outcome of this thesis, and the scope for future work in both sulfuric acid decomposition and photocatalytic hydrogen generation. In this thesis, iron based oxides like iron oxide, chromium doped iron oxide, copper ferrite were found to be suitable substitute to noble metal based catalyst for sulfuric acid decomposition. The data generated from our experiments have given suitable insights in the design and performance in the demonstration of closed loop hydrogen generation in glass by sulfur-iodine cycle at an engineering scale. The Cr-doped iron oxide catalysts qualified in our laboratory experiments are being used in the demonstration of closed loop hydrogen generation in glass by sulfur-iodine cycle. Further, these oxides can be dispersed on suitable supports like SiO_2 or Al_2O_3 and their performance evaluated as these dispersed oxides can be conveniently used under actual reactor conditions. In addition, the poisoning studies of I_2/I^- on the catalytic activities need to be studied as in Sulfur-Iodine cycle the sulfuric acid phase may contain some amount of I_2/I^- as impurity. Regarding photocatalytic water splitting it is an attractive and challenging theme in chemistry and the target for efficient water splitting into H_2 and O_2 (30% in terms of quantum yield at 600 nm) in this research field which is yet to be achieved. Hence, the development of new and superior photocatalyst materials is still a major issue. The photocatalytic studies with indium titanate materials provide insights into the band structure and the photocatalytic performance of these materials. The present work can be extended by N-doping in the anionic sublattice of indium titanate. However, efforts have to continue to find newer materials with suitable crystal and band structure which can produce hydrogen with higher efficiencies.

References:

1 C. E. Bamberger, D. M. Richardson Cryogenics 16(4) (1976) 197–208.

2 L. C. Brown, J. F. Funk, S. K. Showalter, General Atomics Report GAA23373, April 2000. Available on-line at http://web.gat.com/pubs-ext/miscpubs/A23373.pdf on March 21, 2006.

3 D. R. O'Keefe, C. Allen, G. Besenbruch, L. Brown, J. Norman, R. Sharp et al. Int J Hydrogen Energy 7(5) (1982) 831–92.

4 L. E. Brecher, S. Spewock, C. J. Warde Int J Hydrogen Energy 2(1) (1977) 7–15.

5 Beghi GE. Int J Hydrogen Energy 11(12) (1986) 761–71.

6 J. H. Norman, G. E. Besenbruch, L. C. Brown, D. R. O'Keefe, C. L. Allen General Atomic Company Report GA-A16713;1982.

7 A. Fujishima, K. Honda Nature 238 (1972) 37-38.

8 A. L. Linsebigler, G. Lu, and John T. Yates, Jr., Chem. Rev. 95 (1995) 735-758

9 T. Tachikawa, M. Fujitsuka, and T. Majima 111(14) (2007) 5259-5275.

10 M. Kitano, M. Matsuoka, M. Ueshima, M. Anpo Applied Catalysis A:General 325 (2007) 1–14

11 Ni Meng, K. H. Michael Leung, Y. C. Dennis Leung, K. Sumathy, Renewable and Sustainable Energy Reviews 11 (2007) 401–425.

List of Figures

List of Tables

Chapter 1

Introduction

1.1 Catalysts for energy and environment related reactions

The main focus of this thesis is invoking the use of mixed oxide based heterogeneous catalysts to address the need for CO_2 - free cleaner future energy system. The need for CO_2 – free clean energy arises primarily due to two reasons. Firstly, in future the world will be facing a decline in production of conventional oil even though there will be a spurt in demand and secondly the serious environmental problems accompanying their combustion. Thus, future energy systems must provide a secure, more sustainable, climate friendly and environmentally acceptable energy supply. Limited natural fuel resources and an increase in energy demand, rising CO_2 emissions and the threat of global climate change have motivated money and minds to deliver more efficient ways of extracting energy from already limited supplies, and to find more environmentally conscience energy sources.

In this chapter we initially analyze the recent trends in global energy production and the rising CO_2 emissions with its impact on global climate which suggests the need for an alternate and renewable energy carrier like hydrogen and use of renewable energy source like solar or a non CO_2 – emitting primary energy source like nuclear energy for generation of the hydrogen. Different hydrogen production processes are discussed from where it is concluded that hydrogen from water seems to be the ultimate solution to the prevailing energy and environmental problems. General overview of the water splitting processes - thermochemical and photocatalytic is presented. Role of heterogeneous catalyst for the two hydrogen production processes – thermochemical and photocatalytic along with the current global status are then discussed. Basic aspects of heterogeneous catalysis are also provided in brief.

1.2 Current global energy scenario: Supply and Demand

Energy is one of the major inputs for the economic development of any country. In the case of the developing countries like India, the energy sector assumes a critical importance in view of the ever-increasing energy needs requiring huge investments to meet them. Primary energy sources are those that are either found or stored in nature e.g. coal, oil, natural gas, biomass, nuclear, thermal energy stored in earth's interior (geothermal), and potential energy due to earth's gravity. Primary energy sources are mostly converted in industrial utilities into *secondary energy* sources; for example coal, oil or gas converted into steam and electricity.

According to the BP Statistical Review of World Energy 2010 (latest) [1], oil remains the world's largest primary energy source with ~ 34.8 % of global primary energy consumption, but it warns about the very low oil "reserves to production ratio" (R/P) of ~ 50 years. But as the demand is expected to grow on an annual basis, an energy crisis is coming, likely to be triggered by oil. The ASPO (Association for the study of peak oil & gases) in its website [2] publishes updates about the global scenario of oil and also cites peer reviewed articles related to oil production. In one such article by Nashawi et al [3] a forecasting model was developed to predict world crude oil supply with better accuracy than the existing models and estimated that the world oil production would peak in ~ 2014 as shown in Fig. 1.1 [2]. From the various predictions it can be fairly assumed that the global oil production would start declining sooner or later and as demand grows supply will then have to ration demand and oil prices will drastically increase.

Based on the projections for the various 21st century scenarios, Hoffert et al. [4] calculated the amount of primary power generation that would be necessary worldwide to meet demand—and the amount that would be required without the production of any CO_2 emissions.

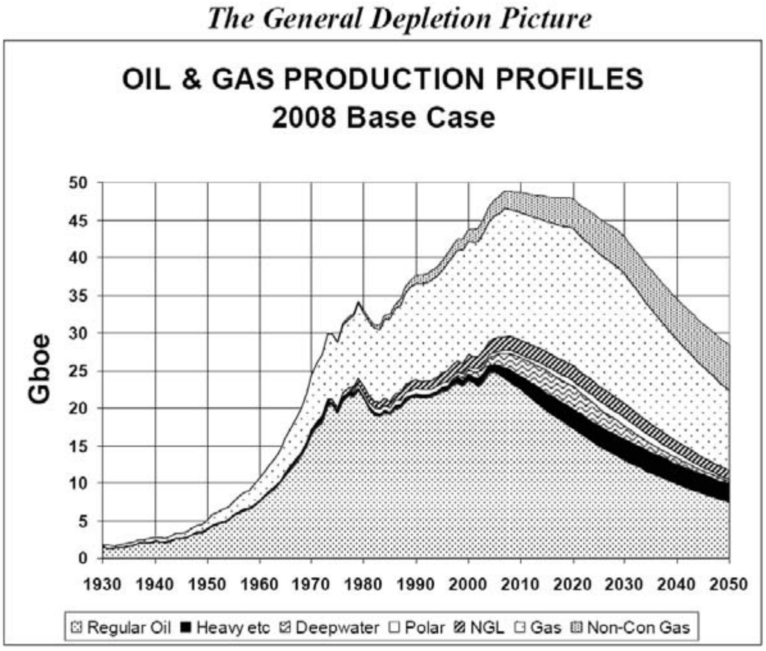

Fig. 1.1. A prediction of global oil and gas production in future from a model along with past data (adapted from ASPO Newsletter No. 100 – April 2009) [2]

By the year 2050 some 10 terawatts of primary power are required completely carbon free. To stabilize atmospheric concentrations of CO_2 at 450 ppm, this number grows to more than 20 TW by 2050. The current total rate of energy production in the world today is 14.5 TW/year; less than 1.2 TW of that is produced carbon-free (mostly by nuclear fission and hydroelectric generation). This means that within 40 years, the world's production of carbon-free energy must increase to nearly tenfold its present value, and if CO_2 levels can be expected to stabilize at twice their pre-industrial levels, this number grows to nearly twenty fold. A comprehensive picture was given by Noble Laureate R. Smalley regarding global requirement of non-CO_2 based energy [5].

Especially in a developing country like India, there will be rapid growth in the transportation sector and oil demand will increase day by day which is already evident by the rising fuel prices. In the absence of viable alternatives to fossil fuel, the developing economy like ours will be under threat. So, we the scientific community should seriously look for alternatives to fossil fuels.

1.3 Current global environmental scenario: CO_2 levels and global warming

Global CO_2 emissions increased by 0.4 Gigatonne (Gt) CO_2 between 2007 and 2008, a period which represented a growth rate of 1.5% [6]. The CO_2 emissions by fuels from 1971-2007, a continuous increasing trend in global CO_2 emission is observed by burning of the fossil fuels. The concentration of CO_2 in the atmosphere has been rising steadily for the last 100 years as shown in Fig. 1.2 (from a pre-industrial revolution level of ~300 ppm to a present-day level of over 380 ppm), [3, 4] and this growth rate has increased substantially over the last 50 years [6]. Such an increasing level of CO_2 in the atmosphere can have a tremendous impact on the climate, since CO_2 being a greenhouse gas contributes most positively to radiative forcing (radiative forcing is generally defined in climate science as the change in net irradiance between different layers of the atmosphere. A positive forcing means more incoming energy which tends to warm the system, while a negative forcing - more outgoing energy tends to cool it) [7]. An extremely thorough analysis of the likelihood that global climate change is being caused by human actions (which includes the large amounts of CO_2 released in atmosphere), and the probable outcomes of such climate change are available in the Intergovernmental Panel on Climate Change (IPCC) Fourth Assessment Report [7]. Figure 1.2 also shows the Global warming over the past century, by temperature and CO_2 level. We can see from this plot that there is a general trend of warming on a global average, along with a co-incidental increase of CO_2 levels. The slopes of these lines are increasing in recent years as compared to the past 130 years. It cannot be concluded from the IPCC reports [7, 8] that only industrialization leads to global temperature rise but it does provide an impetus to start reducing the sources of positive radiative forcing rather than risking the continued increase in global temperature and the subsequent dramatic changes in the global climate.

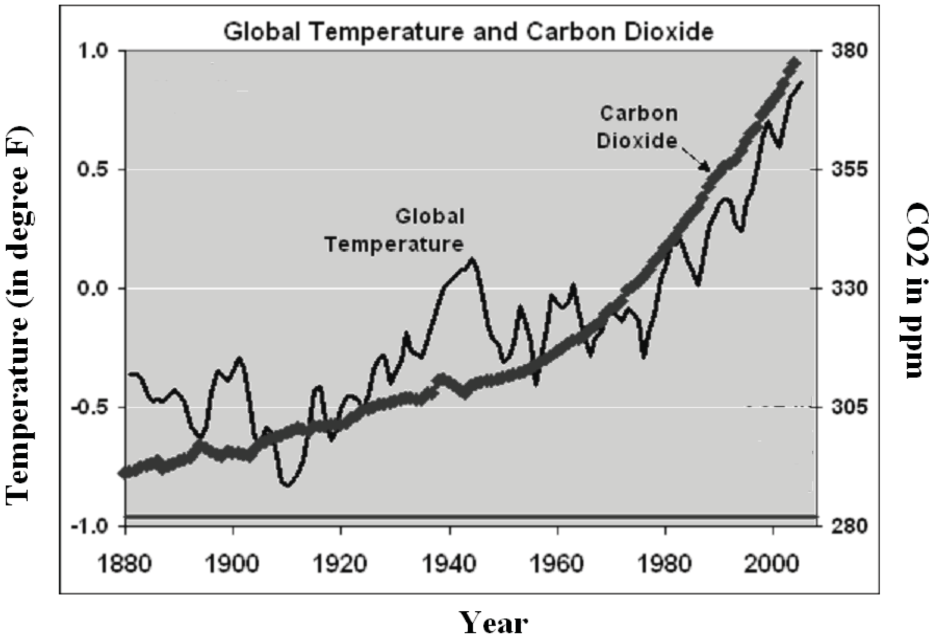

Fig. 1.2. Increase in global average temperature with increase in the CO_2 emission. Adapted from http://www.zfact.com

1.4 Hydrogen: Solution to the current energy and environmental problems

Although combustion of fossil fuels, used to generate electricity and power transportation, provide nearly 86% of the world's energy, we have now seen the drawbacks of fossil fuel utilization including the limited supply and carbon dioxide emissions. Together these argue for the replacement of fossil fuels with a combination of sustainable less-polluting primary energy source. Primary energy source like nuclear or biomass has the potential to provide suitable solution in near future. The renewable non-polluting primary energy sources like solar, wind or geothermal are the most promising in long term. But fossil fuels are firmly entrenched in the transportation sector and so an environment friendly energy carrier has to replace fossil fuels in the long run and hydrogen by virtue of its properties seems to be the attractive solution. Hydrogen has the highest energy density among all fuels

(140 MJ/kg). Hydrogen is the most abundant element on the earth, but is less common as a free element on the Earth. Hydrogen does occur on the Earth in numerous compounds, including many organic compounds and most prominently in water (the most abundant compound on Earth's surface). Thus, free hydrogen does not occur naturally in quantity, and thus it must be generated from compounds containing hydrogen using some other energy source. Hydrogen is therefore an energy carrier (like electricity), not a primary energy source (like coal). Hydrogen can be produced from a variety of sources, hence contributes to diversification and security. H_2 is a gas and is transportable and storable. H_2 does not produce any emissions at point of use. H_2 can provide full range of energy services: heat, electricity and transportation.

Presently, the commercialized hydrogen production processes are mostly fossil fuel based like steam methane reformation, partial oxidation of methane, auto-thermal reforming and coal gasification – the cheapest and largest being generated by steam methane reformation. But these processes generates CO_2 and thus not environmentally friendly. From a climate perspective, the main question facing hydrogen is where and how to get the gas and the challenge is to derive hydrogen from carbon-free renewable source using a non polluting energy source or a renewable energy source. Thus, hydrogen from water is the ultimate solution and this hydrogen has to be extracted using CO_2-free primary sources of energy such as solar energy, wind energy, tidal energy or nuclear.

The idea of 'hydrogen economy' is based on the assumption that hydrogen gas could be produced by decomposing water using inexpensive, CO_2-free and renewable primary sources of energy such as solar energy, wind energy, tidal energy. In this way, hydrogen becomes an energy carrier, which transports the power from the generation site to another location. Particularly in a developing country like India we can have decentralized power based on hydrogen energy (large areas of the country do not have access to electricity).

1.4.1 Hydrogen from water

Hydrogen generation from water can be depicted by the following equation:

$H_2O \rightarrow H_2 + 1/2\ O_2$

The reaction is highly endothermic ($\Delta H = 243\ kJmol^{-1}$ at 298 K) and for direct thermolysis very high temperatures are required (>2500 °C). The energy required to split water can be provided by a primary energy source like solar, wind, nuclear heat or by a secondary energy source like electricity or a combination of these sources using a chemical process. So, a large number of diverse processes has evolved for hydrogen generation from water some of which we list below:

Electrolysis: Electrolysis of water using electricity

High temperature steam electrolysis: Electrolyse water using a combination of electricity and heat

Thermochemical water splitting: Split water using heat or a combination of heat and electricity at much lower temperatures than direct thermolysis using a series of chemical reactions

Photoelectrochemical: Electrolyse water using a photoresponsive anode or cathode or both and solar light

Photocatalysis: Generate hydrogen from water using solar energy and a photoresponsive catalyst

Photobiological: Split water using microorganism

None of the above except electrolysis has been commercialized and although electrolysis is an established process, cost of hydrogen obtained by this method is very high. So, efforts are on to improve efficiency and to minimize the cost of these processes to make them commercially viable. Thus, R&D on various aspects like material development, catalyst development, reactor design etc. has to be carried out. In this thesis heterogeneous catalysts have been investigated for reactions involved in hydrogen generation from water using thermochemical cycles and photocatalysis. Subsequently, in this chapter, thermochemical cycles are described in brief and then photocatalytic hydrogen generation is discussed.

1.4.2 Promise of hydrogen from solar energy

Solar energy is able to meet global demand for power by several orders of magnitude: the solar flux on the surface of the Earth is about 120,000 TW. Thus, the amount of solar energy striking the earth in one year is nearly 10,000 times greater that all energy used by humans in that same year, but it is enormously underutilized (~0.5% of total energy consumption). The most efficient method of harvesting solar power is with solid-state photovoltaic (PV) devices, which have higher efficiencies but, an inherent limitation of PV devices is they can only produce electricity. As a form of energy, electricity is not the most practical for many applications because it is difficult to store efficiently. Hydrogen overcomes this problem.

The inescapable fact that any terrestrial solar energy harvesting must deal with is that the sun rises and sets each day. Therefore the energy produced during the day must be stored for usage at night. While numerous methods are available for storing electricity, all incur significant efficiency losses during the charging and discharging processes, and furthermore, many are simply not able to accommodate daily cycling or have unacceptably short operating lifetimes. While storage technology is continually improving, the additional steps required to store the electricity generated will necessarily diminish the overall efficiency of the energy production process. Instead, hydrogen can be generated by trapping the solar enegy using either thermochemical or photocatalytic processes and can be stored for future use during peak hours.

1.4.3 Hydrogen from nuclear energy

We have already seen from the perspective given by Hoffert [4] and Smalley [5] that nuclear reactors play an important role to solve the global future energy and environmental (climate) problems. Generation IV nuclear reactors like the high temperature reactors will have a very high coolant temperature and in addition to running a turbine to generate electricity it can also generate hydrogen by utilizing a thermochemical cyle or high temperature steam electrolysis. During off-peak hours when demand is low this can provide additional benefit. Some of the options of hydrogen production using future high temperature reactors are listed in Fig. 1.3.

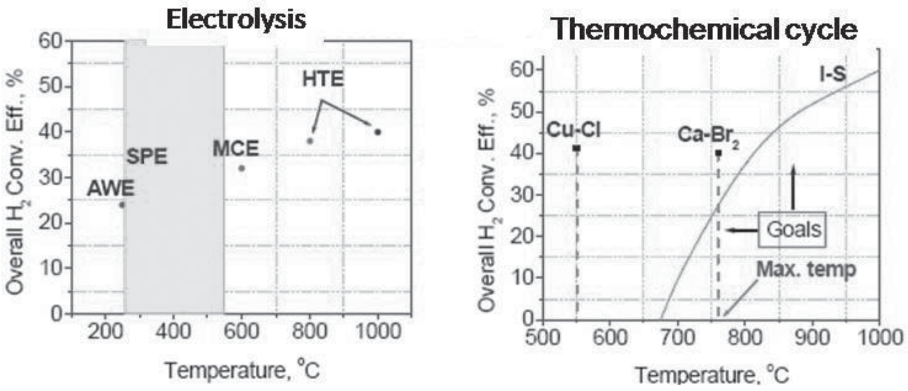

Fig. 1.3. Some options of hydrogen production using nuclear energy; AW:Alkali water, MC: Molten carbonate, SP: Solid Polymer, HT: High temperature; Cu-Cl: Copper-Chlorine, Ca-Br_2:Calcium-Bromine, I-S: Iodine-Sulfur (adapted from I. V. Dulera and R. K. Sinha [32]). Goals of the research & development in thermochemical cycles are to improve efficiency and minimize the temperature of operation

1.5 Thermochemical cycles

For direct thermolysis of water temperatures above 2500 °C is required. So water splitting is subdivided into different partial reactions, all carried out under lower temperatures. Thus, thermochemical cycles consist of a series of chemical reactions to produce hydrogen from water at much lower temperatures than required for the direct thermal decomposition of water [9]. Water splitting into hydrogen and oxygen is achieved via chemical reactions using intermediate elements and compounds which are recycled. The sum of all the reactions is equivalent to the dissociation of the water molecule. Thermochemical cycles are Carnot cycle-limiting meaning the highest temperature could improve the conversion efficiency. A schematic of the basic principle of functioning of thermochemical cycles is shown in Fig. 1.4.

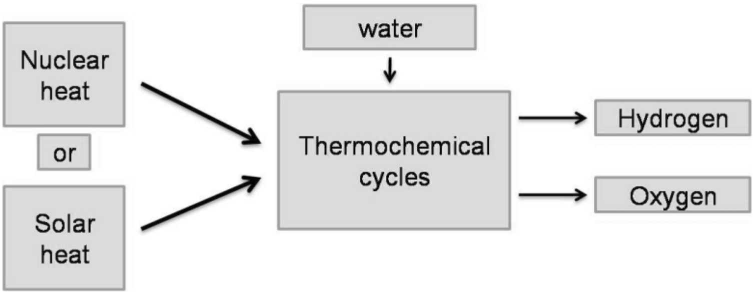

Fig. 1.4. A schematic of the concept of thermochemical cycles

The primary energy source to drive the cycle could be nuclear [9-10] or solar heat [11] and hydrogen can be produced without the need of any fossil fuels and also not releasing any green house gases considered being responsible for global warming.

1.5.1 Why Sulfur based Thermochemical cycles?

From the data of 115 thermochemical hydrogen production cycles that are available in open literature, initial screening was made by General Atomics, USA, to shortlist some potential candidates on the basis of number of reactions/separations involved, number of elements involved, cost, amount of research done etc. and then the potential cycles were compared among themselves on several issues e.g. number of reactions/separations, number of elements and their availability, efficiency and cost, requirement of solid flow, amount of research done etc. Hybrid sulfur cycle and sulfur-iodine cycle were ranked at first and fourth places respectively in the comparison [12].

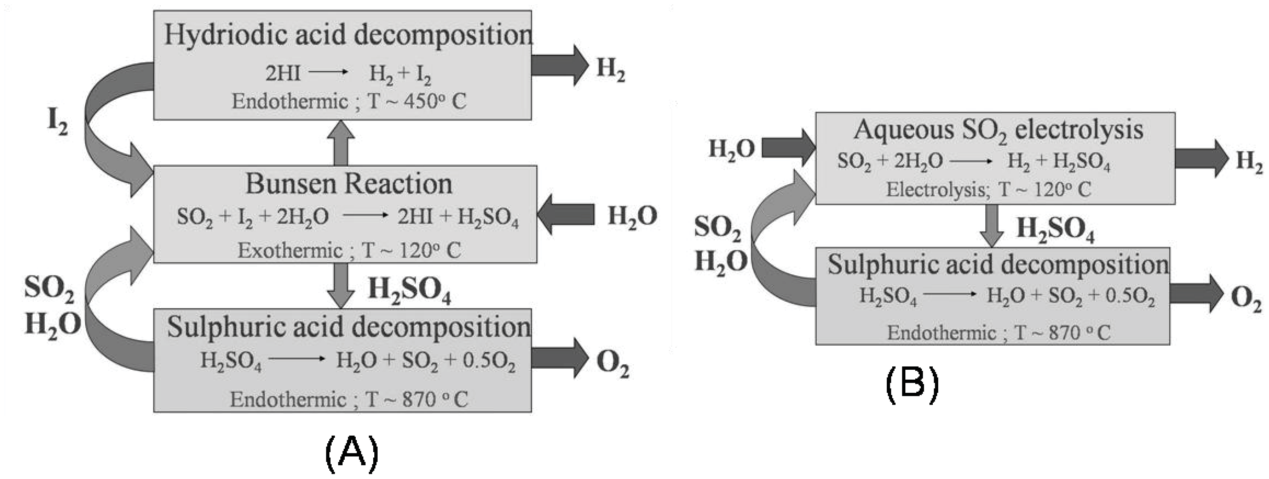

Fig.1.5. Schematic representation of the reactions involved in two sulfur based thermochemical cycle – (A) Sulfur-Iodine cycle and (B) Hybrid Sulfur Cycle

Table 1.1. Process parameters for few thermochemical processes for hydrogen production (ref 12 and 32)

	Iodine-sulfur process	Calcium bromine process	Copper-chlorine process	Hybrid sulfur process
Efficiency (%)	57	40	41	40
Operating temperature (max)	900-950 °C	700-750 °C	500 -550 °C	900-950 °C
Process streams	Liquids and gases	Solids, liquids and gases	Solids, liquids and gases	Liquids and gases
No. of chemical reactions	3	4	4	2
Corrosion	High	High	Low	high
Developmental stage	Flow-sheeted	Flow-sheeted	Flow-sheeted	Flow-sheeted

The fundamental principles of operation of these two cycles are shown in Fig. 1.5. The efficiency of these sulfur based thermochemical cycles are potentially high and thus hydrogen production costs potentially low. Table 1.1 lists some of the representative process related parameters for few thermo-chemical processes for hydrogen production.

1.6 Sulfuric acid decomposition

The catalytic decomposition of sulfuric acid to produce sulfur dioxide, oxygen and water is a topic currently gaining enormous importance as it can serve as thermal to chemical energy conversion step in all the sulfur based thermochemical cycles such as the sulfur–

iodine thermochemical cycle [13], the hybrid sulfur cycle [14], and the sulfur–bromine hybrid cycle [15], for successful massive hydrogen production by water splitting. The reactions involved in these sulfur based cycles are as follows:

Sulfur-Iodine Cycle:

I_2 (l) + SO_2 (g) + $2H_2O$ (l) → 2HI (l) + H_2SO_4 (l) (~ 120°C) ..... (1.1)

2HI (g) → I_2 (g) + H_2 (g) (300 – 450 °C) ..... (1.2)

H_2SO_4 (g) → H_2O(g) + SO_2(g) + $1/2O_2$(g) (800- 900 °C) …. (1.3)

Hybrid-Sulfur Cycle:

SO_2 (aq) + $2H_2O$ (l) → H_2SO_4 (aq) + H_2 (g) (70 - 120°C, electrolysis) ..(1.4)

H_2SO_4 (g) → H_2O(g) + SO_2(g) + $1/2O_2$(g) (800- 900°C) ...(1.5)

The sulfur–iodine thermochemical cycle, comprising mainly of three chemical reactions - Bunsen reaction (Eqn.1.1), Hydriodic acid decomposition (Eqn.1.2) and sulfuric acid decomposition (Eqn.1.3), was originally proposed by General Atomics (GA) [13] and is currently considered as one of the most promising technologies for large scale hydrogen production in future due to its high efficiency [16-17]. The thermodynamic quantities for these reactions are discussed in details by Goldstein et al. [16]. In brief, Bunsen reaction which is generally carried out at 120 °C is exothermic by -93 kJ/mole, the HI decomposition section where the HI decomposition reaction is carried out ~ 400 °C at high pressures (upto 50 bar) has a heat demand of 187 kJ/mole and the most endothermic sulfuric acid section has a total heat demand of 352.3 kJ/mole. The cost analysis shows that the hydrogen production cost by sulfur iodine cycle is lower than steam-methane reforming, and conventional and high temperature electrolysis, due to less use of electricity, no carbon related charges and no methane requirement [18-19]. Closed loop lab and bench scale testing of sulfur iodine process has been already demonstrated [10, 20-21] while designing and flow sheet proposal and evaluation is in progress for a plant scale process which can be coupled to a nuclear reactor or a solar concentrator, [22-28] as the case may be. The hybrid sulfur cycle in which the Bunsen reaction and hydriodic acid decomposition is replaced by an electrolysis step is also known as Westinghouse sulfur cycle and consist of only two main reactions – aqueous SO_2 electrolysis (Eqn.1.4) and sulfuric acid decomposition (Eqn.1.5) [14, 23]. Plant sizing and flow sheet preparation is in progress also for hydrogen generation by Hybrid sulfur cycle [29-30]. These sulfur based thermochemical cycles can be operated using solar or nuclear energy as a primary energy source.

In India, Bhabha Atomic Research Centre (BARC) has initiated efforts to develop concepts of high temperature reactors capable of supplying process heat around 1273 K. These reactors would provide energy to facilitate combined production of hydrogen, electricity and drinking water. Presently, technology development for a small power (100 kWth) Compact High Temperature Reactor (CHTR) capable of supplying high temperature process heat at 1273 K is being carried out [31]. In addition, conceptual details of a 600 MWth reactor supplying heat at 1273 K for commercial hydrogen production (IHTR-H), are also being worked out. The target hydrogen production rate from these commercial nuclear plants has been set at 80,000 Nm^3/hr [32]. So, R&D work has been initiated in BARC in most of the developmental areas, including studies on hydrogen generation by sulfur-iodine thermochemical cycle. Initially the feasibility demonstration will be carried out in a closed loop glass set up in Chemical technology division, where the target hydrogen production rate has been kept at 1 litre h^{-1}. Subsequently, bench scale and pilot scale plants are being planned.

1.6.1 The requirement of catalyst for sulfuric acid decomposition

Sulfuric acid thermal decomposition is the most endothermic reaction in the sulfur based thermochemical cycles [13] and is normally carried out at above 800 °C in a process reactor that can withstand high temperature heat from a nuclear supplying system or using solar heat concentrated by a solar concentrator. The sulfuric acid decomposition is comprised of following two reactions in series:

H_2SO_4 (g) → H_2O (g) + SO_3(g); (~ 450 °C) .... (1.6)

SO_3 (g) → SO_2 (g) + 1/2O_2 (g); (800 - 900 °C) …. (1.7)

Sulfuric acid can be decomposed to its anhydride SO_3 (Eqn.1.6) with or without a catalyst at and above 450 °C, when the reaction becomes spontaneous (ΔG^0_{298} ~ 53.8 kJ/mole; ΔG^0_{723} ~ -7 kJ/mole), while the decomposition of SO_3 (Eqn.1.7) has been known to be a catalytic reaction and is carried out at higher temperatures of 750-900 °C (ΔG^0_{298} ~ 71 kJ/mole; ΔG^0_{1073} ~ -1.8 kJ/mole). The thermodynamic quantities for the above reactions have been calculated by FACTSAGE thermodynamic software. First, we explain why we require a catalyst for carrying out sulfur trioxide decomposition (Eqn.1.7). For this purpose we refer Fig. 1.6 from Barbarossa et al [33] where we can see that although theoretical calculations predict a thermodynamic yield of ~ 80 % at 1073 K experimentally there is virtually no yield obtained. 80 % yield is obtained at a much higher temperature of ~ 1273 K.

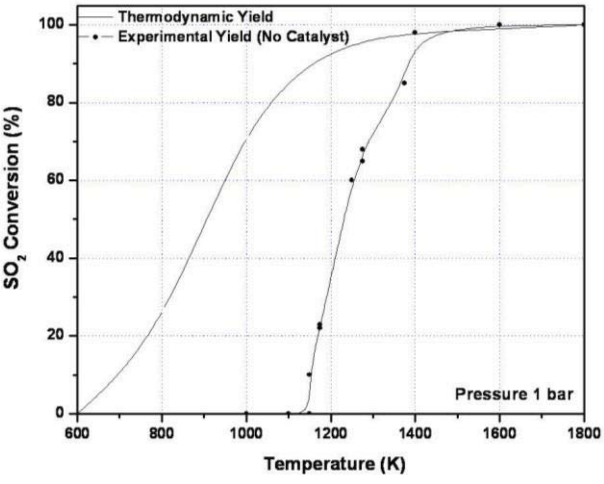

Fig. 1.6. Effect of temperature on H_2SO_4 decomposition yield (adapted from ref 33)

Thus it is evident that though thermodynamically high conversions (80 % - 90 %) are achievable at 800 °C to 900 °C (the operating reactor temperatures of high temperature nuclear reactors), due to slow kinetics very low conversions are actually achieved at these temperatures. The homogeneous vapor phase reaction proceeds at a very slow rate. To increase the kinetics of the decomposition of sulfuric acid a suitable catalyst which will increase the decomposition rate is thus required. The proper catalyst can be a heterogeneous catalyst on the surface of which the reactants will adsorb and undergo decomposition via a different mechanism than that of homogeneous gas phase reaction. The activation barrier will be decreased and the reaction rate will increase. Now, we present a brief history of catalysis followed by the status on the development of the catalyst for sulfuric acid decomposition till date.

1.7 Brief history of catalysis

It is a fascinating aspect of chemistry that certain reactions, which do not proceed to completion, even when carried for long times, gets completed within a matter of few minutes when small quantity of a certain substance is added. There are certain reactions that require drastic conditions such as high temperature and pressure, but the same reactions in presence of some substance occurs at a much lower temperature and pressure. These substances, which enhance their rate of the reactions, but itself do not get permanently involved, are called catalysts. Catalytic reactions play a foremost role in a number of natural processes including, metabolic processes of plants and animals and in the majority of industrial chemical processes. Chlorophyll, a green pigment, plays an important role in the photosynthesis of food by plants, a number of enzymes in plants and animal body regulate the life process such as, respiration, digestion etc. In chemical industries a large variety of reactions such as cracking, dehydrogenation, hydrogenation, oxidation, reduction, decomposition, molecular rearrangement, fermentation etc. require the use of a catalyst in some form or other. As an estimate, about 90% of all chemical reactions in industries rely on catalysts of one kind or another. Thus, it can be said that the catalyst technology is in fact the backbone of the chemical industry. The word “catalysis” was first used by Berzelius in a published report [34] in 1836 where an account of study and observation of various catalytic substances by Berzelius, Faraday, Thenord, Dobernier and other scientists in the early 1800 was mentioned. Berzelius used the collective title *catalyzed process* regarded by him taking place under the influence of a catalytic force. In 1894, Ostwald proposed that catalyst is a substance that alters the velocity of a chemical reaction without appearing in the end products. Catalyst-based technologies were introduced in the second half of the 19th century and by the begging of 20th century many applications of catalysts in industries were developed. A historical account regarding the development of catalysts and elated subjects may be found in literature [35-37]. In fact, The Haber-Bosch process for synthesis of ammonia which was carried out over catalyst has been earmarked as the most important invention of the 20th century [38]. The efforts of a number of researchers like Langmuir, Emmett, Taylor, Bonhoeffer, Rideal, Farkas and many others have led to present day understanding of catalysis science and a more scientific definition of catalysis is given as ***"a substance which increases the rate at which chemical reaction approaches equilibrium, without being consumed in the process and without causing any alteration in the total free energy change involved"***.

Prof. Morrison quoted[39]:

" *The development of new catalysts to accelerate specific reactions is approximately 10% theory, 50% experience and intuition and 40% empirical optimization As our knowledge of surface science grows, we can hope that these percentages will shift to the left in that tabulation, but at present heterogeneous catalysis is so complex that detailed analysis of even the simplest reactions is almost impossible*"

To understand the concept of catalyst let us consider a gaseous reaction represented by the following chemical equation

$A + B \rightarrow C + D$ ….(1.8),

The equilibrium constant of the reaction is given by,

$K_p = \frac{P_C P_D}{P_A P_B}$ and $\Delta G^0 = -RT \ln K_p$, where K_p is the equilibrium constant and P_C, P_D, P_A and P_B are the partial pressures of the different components respectively, ΔG^0 is the standard state Gibbs free energy change, R the universal gas constant and T the absolute temperature. Thus, the Gibbs free energy of the reaction will determine the value of equilibrium constant and thus the product yield. Homogeneous gas phase reaction will proceed in absence of any catalyst, the yield being determined by free energy. But if the kinetics of the reaction is slow then the equilibrium will be achieved after a long time. A catalyst does not affect the Gibbs energy of the overall reaction and thus cannot vary the equilibrium constant. The catalyst increases the rate of the reaction and since the equilibrium constant is the quotient of the rate of forward and reverse reaction, it increases the rates of both the forward and backward reaction and allows the equilibrium to be reached faster. Again, a catalyst can only accelerate a reaction which is already thermodynamically feasible but it cannot initiate a reaction which is thermodynamically impossible [40].

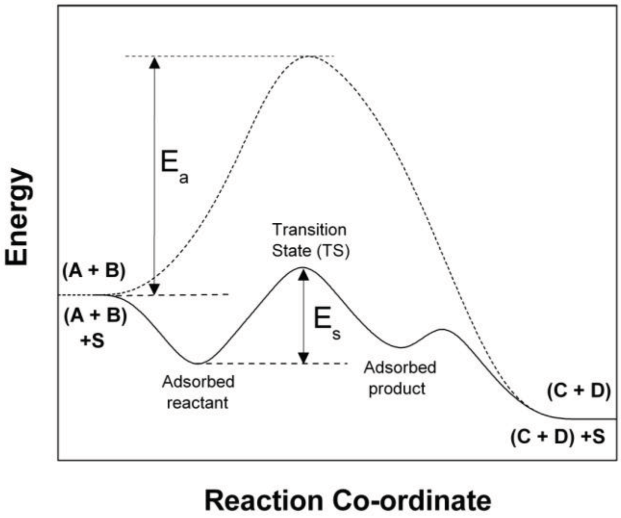

Fig. 1.7. Reaction paths of uncatalyzed (dotted line) and heterogeneously catalyzed reactions.

So, the modern definition of a catalyst is “A catalyst is a substance that allows a chemical reaction to attain equilibrium faster without itself being permanently involved”.

The barriers for the above chemical reaction with, and without a catalyst are shown in Fig. 1.7. The rate of such a reaction depends on its rate constant k, where k = A exp($-\Delta E_a/RT$), where k, A and ΔE_a refer to rate constant, frequency factor and the activation energy respectively. The reaction rate at a given temperature will therefore increase by following some alternative reaction path involving a lower value of activation energy than ΔE_a. This is possible in presence of a catalyst. In the presence of a catalyst (say heterogeneous catalyst), which might chemisorb either A or B, or both of the reactants, the system may follow a new reaction path with a lower energy of activation, ΔE_S. Here the system passes through a new chemisorbed transition state (TS). However, the value of the activation energy alone does not control the overall catalytic activity, since the role pre-exponential factor A is also important. Hence, an attempt to understand the phenomenon of catalysis must include knowledge of the structure of the surfaces of solids, the state of chemisorbed molecules and their mode of interaction.

1.7.1 Classification of Catalysts

It is convenient to categorize classify reactions into three broad categories depending on catalyst-reactant phases and their nature of applications [41].

(i) *Enzyme catalysis* means reactions catalyzed by complex organometallic compounds generally occurring in nature and known as enzymes. They help carry out a reaction at low temperatures and generally yield a single product without any side reaction. Due to requirement of stringent conditions and environmental control, they find only limited applications in chemical industry e.g. the use of enzymes to obtain products such as alcohols, carboxylic acids, carboxylic esters etc by hydrolysis of esters.

(ii) *Homogeneous catalysis* refers to processes where the catalyst is present in the same phase (mostly liquid) as the reactants. These processes are also highly product selective and find application in production of many important chemicals, including many of the vital drugs in pharmaceutical industry. A number of soluble organometallic complexes are used as catalysts for industrial processes such as hydroformylation, oxo-processes, hydrogenation, oxidation, polymerization etc. such as use of titanium complexes as homogenous catalysts in polymerization of olefins like propylene to polypropylene, a Ziegler-Natta Polymerization process.

(iii) *Heterogeneous catalysis* includes those processes in which the reactant (mostly gaseous or liquid) and catalyst (generally solid) are present in different phases. Almost 80% applications of catalysts in chemical industry belong to this class e.g. use of Fe-V_2O_5 catalyst in synthesis NH_3 from H_2 and N_2, the famous Habers process.

1.7.2 Heterogeneous catalysts

Heterogeneous catalysts have gained remarkable importance due to their easy recovery from reaction system, higher stability and applicability in both continuous or batch mode of operation. These catalysts find wide usage in several important industries viz. petroleum, petrochemicals, fine chemicals, pharmaceuticals and also in processes involved in green chemistry for environment control. On the basis of their chemical composition and physico-chemical properties, the heterogeneous catalysts can be classified as: (a) metals, (b) metal oxides, (c) supported metals, (d) solid/superacids, (e) solid bases, (f) zeolites and molecular sieves and (g) clays and heteropoly acids.

Irrespective of the class to which a heterogeneous catalyst belongs, all the catalytic reactions undergo the same basic steps [40]:

(i) Transport of reactants to the catalytic sites.

(ii) Adsorption of reactants on to the catalyst

(iii) Interaction of adsorbed reactants to form products

(iv) Desorption of the products from the catalyst

(v) Transport of products away from the catalyst

Thus, the bonding involved between the catalyst and adsorbate molecules and the transformations that they undergo during the course of a reaction are primarily responsible for the activity and the selectivity of a material as a catalyst. As a general rule, the stronger the bonding between the adsorbate and the catalyst, the less will be the catalyst activity. On the other hand, a very weak bonding will not result in a catalytic activity.

Since, heterogeneous catalysis finds usage in a widely varied range of technological applications; it cannot be explained by any single theory. Many attempts, however, have been made to generalize such processes. The electronic theory of catalysis, which became popular in the 1950s, attempted to correlate electronic energy levels of the solids (especially semiconductors) and the reactant molecules. The catalytic activity of the transition metals has been correlated to vacant atomic d-orbitals. Thus the high chemisorption activity of the transition metals is found to be due to a large number of vacant d-orbitals available for chemisorption. This has been explained in terms of a parameter defined as the *percent d-character* of a transition metal [40, 42-43]. In another approach based on localized model, the reactant molecules are said to form unstable complexes with the surface atoms of the solids, which decompose to give products. In the absence of a unique theory, attempts are made by the chemists all around the globe to relate catalytic activity to some specific properties of solids, so as to narrow down the search for a good catalyst for a given reaction. Hence, though with a very much diffused guiding light in hand, chemists are all the time searching for more efficient and stable catalyst of cheaper cost.

1.8 Decomposition of sulfuric acid on catalyst surfaces

The decomposition of sulfuric acid is not much widely investigated aspect on heterogeneous catalysis but it is a topic of great importance from both fundamental and technical point of view due to the emerging prospect of sulfur based thermochemical cycles for large scale future hydrogen generation from water using either nuclear heat or solar heat. Studies have been mostly carried out on noble metal catalysts but some work on oxide based catalysts has also been investigated in recent years. We give a comprehensive account of the catalysts studied for this reaction globally.

1.8.1 Noble metal based catalysts

The adsorption and decomposition of sulfuric acid on supported Platinum surface has been studied and the reaction mechanism has been proposed. Detailed account is given in Golodates [44], where it is suggested that reaction mechanism proceeds via adsorption and dissociation of SO_3 at the surface active sites which are the active noble metal centre via the intermediate formation of adduct [SO_2.O] on the metal centre. Some of the reported noble metal based catalysts employed for sulfuric acid decomposition include supported platinum catalysts such as (Pt/Al_2O_3, Pt/TiO_2 and Pt/ZrO_2) [45], (Pt/TiO_2 (rutile) [46], ($Pt/BaSO_4$) [47]. A theoretical study also has been carried out comparing the catalytic performance of catalysts consisting of nanoparticles several Pt-group metals (Pd, Pt, Rh, Ir, and Ru) dispersed over oxide surfaces [48]. The Nanoparticles of Platinum and Palladium were proposed to be more active than the other metal Nanoparticles for sulfuric acid decomposition reaction. In the demonstration studies on a closed-cycle hydrogen production by the thermochemical water-splitting iodine–sulfur process, JAERI mentions about the use of a “catalyst bed of platinum” [10], while GA reported the use of Pt/ZrO_2, Pt/TiO_2, $Pt/BaSO_4$ and $Pt/A1_2O_3$ for sulfuric acid decomposition reaction [13].

1.8.2 Oxide based catalyst

The ever rising demand and increasing cost of noble metals make them less preferred for the above applications as well as their applications in other reactions e.g. three way catalyst converters, PROX (preferential oxidation of Carbon monoxide) and so on. Other concerns with supported noble metal catalysts are the problems of leaching, sintering and oxidation [46] of the metal particles during catalytic operation. Substrate sulfation is also a deactivation phenomenon for supported noble metals for the acid decomposition reaction as reported by Norman et al [13]. The major phenomenon of deactivation occurs by the following:

(i) Deactivation by oxidation [46]; (ii) Pt loss by volatalisation (leaching) at high temperature harsh environment (~ 40 % Pt loss in 24 hrs experimental run) [46]; (iii) Deactivation by sintering of Pt and support [45, 46] (iv)Substrate sulfation [13]

In addition to all the problems discussed above the major disadvantage of using noble metal based catalyst is its high cost. So, we must search for more efficient and stable catalyst of cheaper cost. Metal oxide catalysts are active and can be a substitute for noble metal catalysts as they fulfill the essential requirement of materials with better chemical, thermal stability and modified catalytic properties. Long back in 1977, Dokiya et al [49] first reported the use of several metal oxide catalysts for sulfuric acid decomposition, where Fe_2O_3 was found to be the most active catalyst. However, the order of activity of metal oxides was controversial, since different results (order of activity: Pt ≈ Cr_2O_3> Fe_2O_3> CeO_2> NiO> Al_2O_3) were later reported for the same by Tagawa et al. [50] who studied sulfuric acid decomposition in the range of 600°C - 950 °C in a fixed bed reactor. In recent past, oxides samples of Fe_2O_3 and Pd-Ag alloy have been tested to evaluate their effect on dissociation efficiency by Barbarossa et al [33]. Although simple oxide catalysts are active and can be a substitute for noble metal catalysts but their limitations of thermal instability, and sintering effects on repeated use, prevent them from the actual application. So an active as well as stable viable catalyst system still eludes us.

In recent years, focus on the synthesis of multi-metal oxide systems to fulfill the essential requirement of better chemical, thermal stability and modified catalytic properties has been emphasized. This subject is reviewed in several articles [51-52]. However, attempts towards mixed metal oxide systems for the sulfuric acid decomposition reaction, are very limited and have not been fully explored.

Yannopoulos et al reported excellent catalytic activity of mixed metal oxides like $ZnFe_2O_4$ and $NiFe_2O_4$ for SO_3 decomposition [53]. Kim et al [54] in a recent study reported the use of binary metal oxide catalysts based on iron and the catalytic activity of these catalysts increased with an increase in Fe loadings, indicating that the Fe component should be active. Very recently Ginosar et al [55] reported the catalytic performance of several mixed metal oxide catalysts for sulfuric acid decomposition namely $FeTiO_3$, $MnTiO_3$, $NiFe_2O_4$, $CuFe_2O_4$, $NiCr_2O_4$, $2CuO.Cr_2O_3$, CuO and Fe_2O_3. Interestingly, in one of the closed loop demonstration of sulfur-iodine process copper chromite was used as the catalyst for sulfuric acid decomposition [21].

1.9 Aim of our work in sulfuric acid decomposition

The aim of our work in sulfuric acid decomposition is threefold. Firstly, we have to design and develop catalytic reactors for carrying out sulfuric acid decomposition, identify and prepare suitable oxide based catalyst as a substitute for noble metal based catalyst (facing serious problems of deactivation due to active metal loss, metal particle sintering, substrate sulfation) characterize their physico-chemical properties and finally evaluate their potential for the decomposition reaction. Secondly, for practical applicability of these catalysts we have to prepare these catalyst in a larger scale and evaluate their catalytic properties in an enhanced scale and compare with a known noble metal catalyst so that it is established that the catalyst is active and at the same time stable under the harsh environmental conditions (high temperatures, corrosive gases like SO_3 and SO_2, high temperature steam, O_2). Finally, we have to propose the probable mechanistic pathway for decomposition of sulfuric acid over these iron oxide based catalyst. All these aspects have been dealt in details in chapters 2, 3, 4, 5 and 6.

In chapter 2 of the thesis, the experimental methodologies have been discussed. Apart from the different instrumental techniques used for characterization, emphasis has been given to design and development of catalytic reactors also. In chapter 3, $Fe_{2(1-x)}Cr_{2x}O_3$ ($0.0 \leq x \leq 0.2$) catalysts were prepared by solid state method, well characterized and evaluated for sulfuric acid decomposition reaction in powder form. Oxide catalysts of iron, crystallized into different crystal structures like spinels ferrites viz; AFe_2O_4 (A= Cu^{2+}, Co^{3+} and Ni^{2+}), were investigated in powder form to explore their suitability under harsh reaction conditions and presented in chapter 4. For practical applicability, iron oxide and 10 % chromium doped iron oxide in granular form (~4-6 mm spherical beads) were evaluated in an enhanced scale for sulfuric acid decomposition and compared with a commercial Pt(0.5%)/Al_2O_3 catalysts and these aspects are discussed in Chapters 5 and 6. The catalytic activities were correlated with structural, morphological, redox and thermal properties of the oxide catalysts by proper characterization of the fresh and the spent catalysts. Finally, the most stable and active catalyst based on our experimental results was proposed to be used in large scale in the Sulfur-Iodine demonstration experiments.

1.10 Photocatalysis

Semiconductor photocatalysis has received much attention during last three decades as a promising solution for both energy generation and environmental problems. Since the discovering of Fujishima and Honda [56] that water can be photo-electrochemically decomposed into hydrogen and oxygen using a semiconductor (TiO_2) electrode under UV irradiation, extensive investigations have been carried out to produce hydrogen from water splitting using a variety of semiconductor photocatalysts, where the photocatalyst simultaneously functions as the photo anode and cathode. Although, the most efficient method of harvesting solar power is with solid-state photovoltaic (PV) devices, which have higher efficiencies, an inherent limitation of PV devices is they can only produce electricity. As a form of energy, electricity is not the most practical for many applications because it is difficult to store efficiently as we have discussed earlier.

Overall water splitting for the production of hydrogen using a particulate photo catalyst has also been examined since 1980 and many reviews [57-61] and several books [62] have been published. From the viewpoint of large-scale hydrogen production, particulate photo catalyst systems are considered to be advantageous over more complex multilayer or tandem structure devices and have a wider range of potential applications [63], although a method for separating the simultaneously produced H_2 and O_2 remains to be developed.

1.10.1 Basis of photo catalytic water splitting

Under irradiation at an energy equivalent to or greater than the band gap of the semiconductor photocatalyst, electrons in the valence band are excited into the conduction band, leaving holes in the valence band.

Fig. 1.8 shows a schematic illustration of the basic principle of overall water splitting on a heterogeneous photocatalyst. The photocatalyst absorbs photon energy greater than the band gap energy of the material and generates photo excited electron hole pairs. These photo generated electrons and holes cause reduction of H^+ to H_2 and oxidation of H_2O to O_2, respectively. To achieve overall water splitting, the bottom of the conduction bands must be located at a more negative potential than the reduction potential of H^+ to H_2 (0 V vs. NHE at pH 0), while the top of the valence bands must be positioned more positively than the oxidation potential of H_2O to O_2 (1.23 V vs. NHE). NHE is the normal hydrogen electrode which is a redox electrode based on the redox half cell, $2H^+(aq) + 2e^- \rightarrow H_2(g)$, the potential of a platinum electrode in 1N acid solution. Therefore, the difference between the two reduction potentials, the minimum photon energy thermodynamically required to drive the reaction, is 1.23 eV, corresponding to a wavelength of ca. 1100 nm, in the near infrared region. Accordingly, it would appear to be possible to utilize the entire spectral range of visible light.

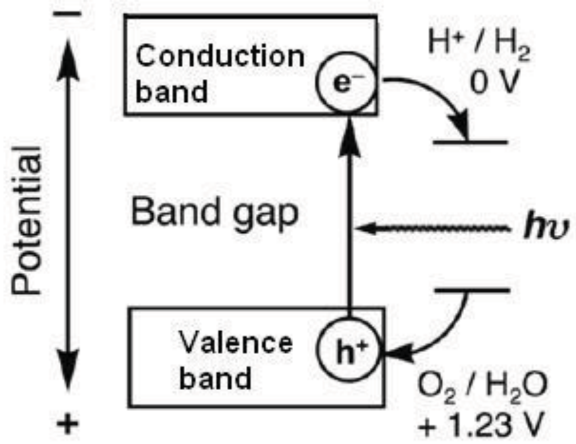

Fig. 1.8. Schematic illustration of the basic principle of overall water splitting on a heterogeneous semiconductor photo catalyst.

The relationship between Energy in ev and λ(wavelength) in nm is given by

$$\text{Energy (eV)} = 1240/\lambda \text{ (nm)}$$

But, there is an activation barrier in the charge-transfer process between photo catalysts and water molecules, necessitating photon energy greater than the band gap of the photo catalyst to drive the overall water splitting reaction at reasonable reaction rates. Moreover the backward reaction of H_2 and O_2 recombination producing water must be strictly inhibited and the photo catalysts themselves must be stable in the reaction (should not undergo photocorrosion).

1.10.2 Principle of photo catalytic water splitting

As shown in Fig. 1.9, the overall water splitting reaction on a semiconductor photo catalyst occurs in three steps,

(i) The photo catalyst absorbs photon energy greater than the band gap of the semiconductor material and generates photo excited electron hole pairs in the bulk; (ii) The photo excited electrons and holes separate and migrate to the surface with minimum recombination; (iii) Adsorbed species are reduced and oxidized by the photo generated electrons and holes to produce H_2 and O_2, respectively at different surface reaction sites.

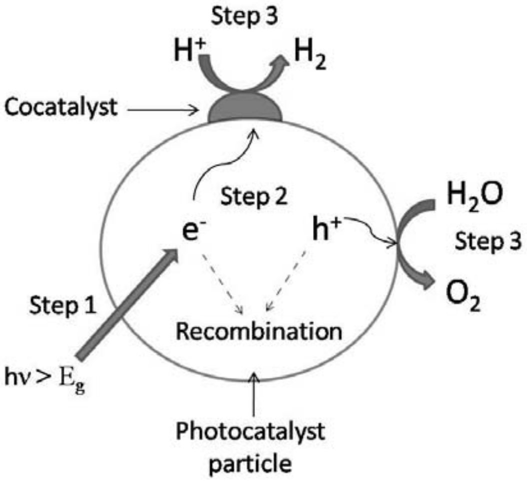

Fig. 1.9. The overall water splitting reaction on a semiconductor photo catalyst

From the above water splitting reaction steps it is clear that the structural, electronic and morphological properties of the photocatalyst are responsible for the proper functioning of the first two steps. First, the photocatalyst must be a semiconductor with a band gap greater than 1.23 ev so that it can generate electron hole pairs by absorbing light and water splitting reaction becomes feasible on its surface. Secondly, the amount of water molecules adsorbed on the photocatalyst will increase with an increase in surface area of the photocatalyst and thus increased surface area will enhance the reaction of photoexcited electron holes with the substrate. On the other hand, an increase in surface area will generate defects centres in the photocatalyst, as the surface of a catalyst can be considered as a defective site where the continuity of a crystal is terminated and these defect sites are assumed to be the electron hole recombination centres. Thus, larger the surface area faster the reaction and smaller the surface area lesser the electron hole recombination. Thus, an optimum surface area and crystallinity is required for suitable performance of the photocatalyst. The third step, on the other hand, is promoted by the presence of a solid co catalyst. The co catalyst is typically a noble metal (e.g., Pt, Rh) or metal oxide (e.g., NiO, RuO_2) and is loaded onto the photocatalyst surface as a dispersion of nanoparticles to produce active sites and reduce the activation energy for gas evolution. It is thus important to design both the bulk and surface properties of the material carefully so as to obtain high photo catalytic activity for this reaction.

1.10.3 Scheme of photocatalytic water splitting reaction

As it is already mentioned that the prospect of photocatalytic water splitting was subsequent to the pioneering work of demonstration of stoichiometric water splitting in a photoelectrochemical cell using single-crystalline TiO_2 (rutile) anode and a Pt cathode under ultraviolet (UV) irradiation and an external bias [56]. From the direction of current it was concluded that oxidation (oxygen evolution) occurred at TiO2 electrode and reduction (hydrogen evolution) at the Pt electrode. The following basic scheme could be proposed for the water splitting reaction:

$TiO_2 + 2\,h\nu = 2\,e^- + 2\,h^+$ (photoexcitation of TiO_2)

$H_2O + 2\,h^+ = \frac{1}{2}\,O_2 + 2\,H^+$ (at TiO_2 electrode)

$2\,H^+ + 2\,e^- = H_2$ (at Pt electrode)

$H_2O + 2\,h\nu = \frac{1}{2}\,O_2 + H_2$ (overall reaction)

In case of photocatalysis there will be only catalyst and water but no different electrodes. There will be generation of charge carriers i.e. electron hole pairs when light with energy greater than the band gap of the material impinges on the surface of the photocatalyst.

Subsequently, the oxidative (oxygen generation) and reductive phenomenon (hydrogen generation) takes place simultaneously on semiconductor surface, but it is only an assumption as products of both reactions will mix immediately.

1.10.4 Stoichiometry of H_2 and O_2 evolution

From the previous discussion it is evident that the ratio of hydrogen to oxygen produced should be 2:1. This is true when only photocatalyst and water is present in the system. But, often sacrificial reagents are employed to evaluate the photocatalytic activity for water splitting as shown in Fig. 1.10, because to achieve stoichiometric overall water splitting is very difficult due to rapid recombination of photogenerated electron-hole pairs. Thus, photocatalytic reaction is carried out in an aqueous solution having either electron donors or hole scavengers. Alcohol and sulfide ions are examples of hole scavengers which when present in the photocatalyst water system acts as a reducing agent and the photogenerated holes irreversibly oxidize them instead of water. It enriches electrons in a photocatalyst by consuming the holes, so electron hole recombination decreases and H_2 evolution rate is enhanced as shown in Fig. 1.10 (a). This reaction will be meaningful for realistic hydrogen production if biomass and abundant compounds in nature and industries are used as the reducing reagents [64-66]. On the contrary, photogenerated electrons in the conduction band are consumed by oxidizing reagents (electron acceptors or electron scavengers) such as Ag^+ and Fe^{3+} resulting similarly in the decrease in electron hole recombination rate and a consequent increase in O_2 evolution rate as shown in Fig. 1.10 (b). These reactions using sacrificial reagents are studied to assess whether a certain photocatalyst satisfies the thermodynamic and kinetic potentials for photocatalytic H_2 and O_2 evolution. These reactions are often regarded as half reactions of photocatalytic water splitting and are often employed as test reactions. A photocatalyst can be active for these half reactions but it does not ensure that it will be also active for the overall stoichiometric water splitting into H_2

and O_2 in the absence of sacrificial reagents. But, water splitting means to split water into H_2 and O_2 in a stoichiometric amount in the absence of sacrificial reagents.

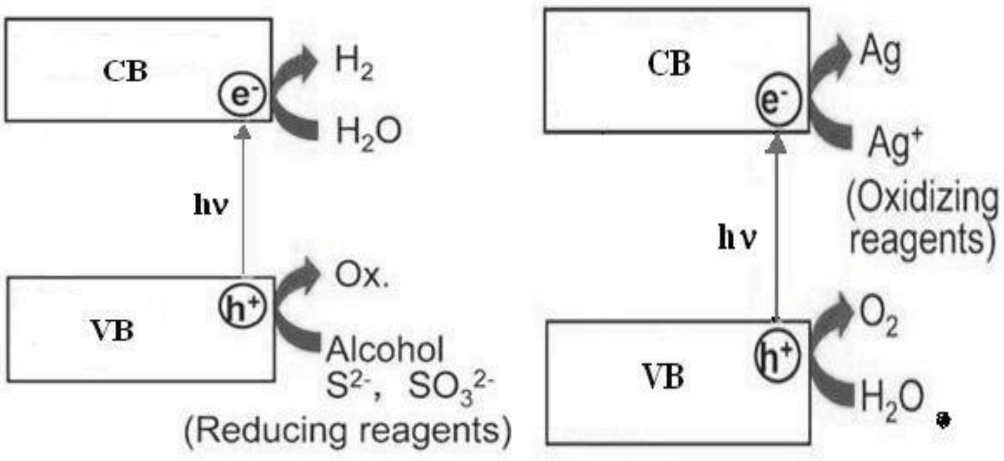

(a) **(b)**

Fig. 1.10. H_2 or O_2 evolution reaction in the presence of sacrificial reagents—Half reactions of water splitting. (a) H_2 evolution in the presence of reducing agent, (b) O_2 evolution in the presence of oxidizing agents.

1.10.5 Band bending at the interface

The minimum energetic requirement for a semiconductor photocatalyst to split water is that, the bottom of the conduction band must be located at a more negative potential than the reduction potential of H^+ to H_2 (0 V vs. NHE at pH 0), while the top of the valence bands must be situated more positively than the oxidation potential of H_2O to O_2 (1.23 V vs. NHE). But at the interface of the semiconductor and electrolyte solution the band positions of the semiconductor photocatalyst are altered. A thermodynamic equilibrium is established at the interface of the semiconductor and electrolyte, which generates a space charge layer at the surface of the semiconductor. This results in the bending of the electronic energy bands upwards or downwards respectively for n-type and p-type semiconductors as shown in Fig. 1.11 for an n-type semiconductor. The thickness of this space charge layer is of the order of 1 - 10^3 nm depending on carrier density and dielectric constant of the semiconductor. The photogenerated electron-hole pairs are produced and separated in the space charge layer. These band bending phenomenon have been discussed in detail in several electrochemistry books [67-69].

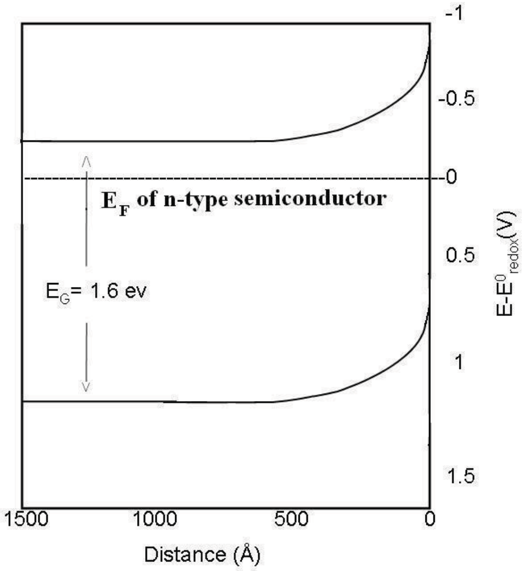

Fig. 1.11. Schematic diagram of the energy levels for an n-type semiconductor in a regenerative photoelectrochemical cell under equilibrium, dark conditions.

1.10.6 Effect of crystallinity and surface area on photocatalytic activity

The rate of photocatalytic water splitting is dependent on the surface area and crystallinity of the semiconductor photocatalyst. In general, higher the surface area of the photocatalyst higher is the photocatalytic activity. This is because when the specific surface area is high the amount of surface adsorbed water molecules is also high and so the larger amount of substrate surround and reacts with the photogenerated electron hole pair. It might also be thought that the higher surface area would also induce generation of higher number of electron hole pairs, but, in photocatalysis, a portion of the photocatalyst particles or outer bulk materials can only absorb incident photons and the remaining part does not take part in the photoabsorption process. Again, if the particle size becomes small, the distance that photo generated electrons and holes have to migrate to reaction sites on the surface becomes short resulting in a decrease in their recombination probability and thus, increase in photocatalytic activity. So, larger surface area with constant surface density of the photocatalyst leads to faster rate of photoreaction of electron hole pairs with the water molecules because of a decrease in recombination probability of the electron hole pairs and also a larger number of water molecules surrounding the electron hole pairs.

But, a decrease in particle size also increases defects and grain boundaries which in turn increases the recombination rate of electron hole pair, thus decreasing the photoactivity. The surface of a crystal can be assumed to be a defect site where the long range ordering of the crystal lattice breaks and it is assumed that charge carrier recombination occurs at crystal defects. Thus, higher surface area or lower crystallinity of the semiconductor photocatalyst leads to lower rate of photocatalytic activity because of an increase in electron hole recombination rate.

Thus, crystallinity and particle size are two important factors governing the photoactivity of a photocatalyst. The crystallinity and surface area of nanoparticles should be optimized to achieve maximum photoactivity for water-splitting reaction. When the surface reaction rate of a photocatalyst outweights the recombination rate, a photocatalyst of larger surface area is better while when the recombination rate predominates a lower surface area photocatalyst with higher cryatallinity is beneficial.

The fact that recombination occurs at crystal defects have been dealt in details in the book on recombination in semiconductors by P. T. Landsberg [70]. Several reports have been published where studies have been carried out to find the optimum crystallinity of the photocatalyst to obtain maximum photocatalytic yield of hydrogen [71-73].

1.11 Some heterogeneous photocatalyst materials used for water splitting

Numerous photocatalyst materials have been explored till date throughout the globe for water splitting reaction. The most prospective materials found were the oxides, nitrides and sulfides of metal cations having d^0 and d^{10} electronic configuration. The valence bands are generally O 2p, N 2p and S 3p for metal oxides, nitrides and sulfides respectively. The conduction bands are generally composed of d and sp orbital of the metal.

In perovskite or layered perovskite type oxides (e.g. ABO_3, $A_2B_2O_7$ etc) the alkaline, alkaline earth metal or lanthanide cations do not generally participate directly in band formation but play their role in crystal structure formation which in turn is essential for photocatalytic performance.

Some transition metal cations (Cr^{3+}, Fe^{3+}, Ni^{2+} etc) with partly filled d-orbitals play an important role in band formation when doped or substituted for the parent cation and thereby generating impurity levels and increasing photoresponse towards lower energy photons particularly visible light. However, they may also act as a trap sites for electron hole recombination and decrease photoctivity. So, an optimum doping percentage can be found out where the activity is highest by increasing the visible light photoresponse and at the same time minimum defect sites for recombination.

Some transition metal-metal oxide Ni/NiO, metal oxide RuO_2 and noble metals Pt, Pd, Rh and Au [59] are found to increase H_2 production rate when present in small amount on the surface of the photocatalyst. Here, they act as a co-catalyst which increases the H_2 production rate. The role of these co-catalysts is to suppress the backward reaction of evolved H_2 and O_2 and also act as trap sites of electrons for H_2 evolution.

Thus, we see from the above discussion that elements in the periodic table have four types of role in the allover photocatalytic water splitting reaction. The elements (a) can form the crystal structure of the photocatalyst and also participate in the energetics of band formation, (b) help in crystal structure formation but has no role in band structure, (c) form impurity levels in the band structure as dopants and (d) used as a co-catalyst.

1.11.1 Oxide photocatalyst consisting of d^0 metal cation

In this category the most promising and on which exhaustive research has been carried out is TiO_2 photocatalyst. Innumerable articles [74-79] and many reviews [80-83] have been published discussing the photocatalytic aspects of TiO_2. Two most active crystal structure of TiO_2 are the anatase and rutile phases with anatase being more active than rutile for water splitting reaction. The advantage of using TiO_2 is that it is cheap, easily available, resistant to photocorrosion and the conduction-valence band potentials satisfies the energy requirements for the reduction and oxidation of water respectively [84-85]

The major disadvantage of using TiO_2 as a photocatalyst is that it has absorption edge at 380 nm, which limits its effectiveness only to UV region of the solar spectrum. An efficient utilization of solar energy requires response of photocatalyst in visible region. There are a few more drawbacks associated with the use of bulk TiO_2, like charge carrier recombination occurring within nano seconds. Various strategies, namely, increase in the surface area, sensitization using dye molecules or doping with metals and non-metals are known to overcome these drawbacks, and in turn enhance the photocatalytic activity of TiO_2 in the visible region. The high surface area inherent to the nano particles is generally useful for photocatalysis and hence today many studies are being focused on the nano sized TiO_2 [86-88]. Dye sensitization also has been reported to be a viable tool to utilize the visible region of solar spectrum using TiO_2 [89-90]. However, the use of sensitizer molecules is limited by their instability due to self oxidation and toxicity. Therefore, doping TiO_2 with metal ions for effective modification of the band gap or separation of photon induced electron - hole pair [91-92] is one of the most efficient methods reported for enhancement of catalytic activity.

To make it visible light active, TiO_2 is doped with different cations e.g. iron [93], tin [94], europium [95], copper [96] etc. and anions e.g. nitrogen [97-98], sulfur [99] and chlorine [100], which can decrease the band gap energy resulting in enhanced absorption of light and improved photocatalytic activity. Dopants form levels within the bandgap of TiO_2 and make the bandgap narrower. Anpo et al have demonstrated metal ion-implantation, ionized cluster beam (ICB) deposition and RF-magnetron sputtering (RF-MS) deposition methods to enable the development of unique titanium oxide photocatalyst materials which are able to absorb and work not only under UV but also visible or solar light irradiation [101-102]. Several compositite catalysts with one of the component TiO_2, like CuO-TiO_2, [103] SnO_2-TiO_2 [104] have also been employed for water splitting reaction.

Besides TiO_2 other simple oxides of d^0 metal cations that were investigated for water splitting reaction are WO_3, [105] Ta_2O_5, [106] ZrO_2 [107] and more recently VO_2 [108]. All of them except WO_3 were UV-active like titania. Various other d^0 metal oxides have been explored for water splitting reaction which were mostly multi metal oxides. Some examples include perovskite e.g. $SrTiO_3$, [109] $CaTiO_3$, [110] $NaTaO_3$, [111] $KTaO_3$, [112] $AgTaO_3$; [113] layered perovskites e.g. $La_2Ti_2O_7$, [114-117] La_2TiO_5, [118] $Sr_4Ti_3O_{10}$, [119] $Ca_2Ta_2O_7$, [120] $Sr_2Ta_2O_7$, [121] $K_2SrTa_2O_7$, [122] $H_2La_{2/3}Ta_2O_7$, [123] $Ba_5Ta_4O_{15}$, [124] $Ba_5Nb_4O_{15}$, [125] $Ca_2Nb_2O_7$ [126] etc.; pyrochlore e.g. $Gd_2Ti_2O_7$, [127] $Y_2Ti_2O_7$, [128] orthorhombic $CaTa_2O_6$, [129] tunnel structure e.g. $BaTi_4O_9$, [130-132] $Na_2Ti_6O_{13}$ [133-134] etc. In most of these cases there was use of co-catalyst like Ni/NiO or Rh etc for increasing the catalytic activity. Again, in some cases authors have reported the doping or substitution of several transition metal cations (Cr^{3+}, Fe^{3+}, Ni^{2+} etc) for parent cations to decrease the band gap of these photocatalyst and increase visible light photoresponse and consequent photoactivity. In these multi metal oxides, one of the cation has an electronic configuration d^0 (Ti^{4+}, Nb^{5+}, Ta^{5+}, W^{6+}) which are the cations taking part in crystal formation and also forming the band structure with O 2p. Other cations participate in the formation of a favorable crystal structure for photocatalyst like role of La^{3+} in the formation of layered perovskite in $La_2Ti_2O_7$

or Ba^{2+} in the formation of tunnel like structure in $BaTi_4O_9$. The crystal structure of a photocatalyst plays an important role in determining the activity and stability of the photocatalyst. Valence bands of these photocatalysts, except for $AgTaO_3$, consist of O 2p orbitals of which the potential is about 3 eV vs. NHE while conduction band levels are more negative than 0 eV. It results in that these materials respond to only UV. An Ag 4d orbital forms a valence band of $AgTaO_3$ with an O 2p orbital [112].

Domen and co-workers have reported that NiO-loaded $SrTiO_3$ powder can decompose pure water into H_2 and O_2. The NiO co-catalyst for H_2 evolution is usually activated by H_2 reduction and subsequent O_2 oxidation to form a NiO/Ni double layer structure that is convenient for electron migration from a photocatalyst substrate to a co-catalyst. Hwang et al [135] showed from experimental and theoretical calculations that with Cr^{3+} and Fe^{3+} substitution at the Ti^{4+} site of $La_2Ti_2O_7$ increased the visible light photoactivity by the formation of partially filled 3d bands in the band gap of $La_2Ti_2O_7$ by the dopants and excitation of electrons from this localized interband to the conduction band of $La_2Ti_2O_7$ was responsible for visible light absorption and the H_2 evolution from water under visible light.

1.11.2 Oxide photocatalyst consisting of d^{10} metal cation

Oxides, sulfides and nitrides of several metal cations with d^{10} electronic configuration have been exploited for water splitting reaction. Ga_2O_3 [136] is a good photocatlyst but under UV irradiation. Among other simple oxides of d^{10} metal cation ZnO undergoes photocorrosion [59]. But multimetal oxides successfully tested were $NaInO_2$, $CaIn_2O_4$, $SrIn_2O_4$, [137] $NaSbO_3$, $CaSb_2O_6$, [138] Sr_2SnO_4, [139] $SrSnO_3$, [140] etc.

In fact the work done by Maeda et al [141] using GaN:ZnO solid solutions still stands as the most active photocatalyst for water splitting reaction under visible light. The quantum efficiency of overall water splitting on this catalyst was found to be about 2.5% at 420–440 nm, which is about an order of magnitude higher than the earlier reported activity of photocatalysts used in overall water splitting under visible light. Similarly $Cr_xRh_{2-x}O_3$/GaN:ZnO and Ru/$SrTiO_3$:Rh-$BiVO_4$ photocatalysts respond to about 500 nm for overall water splitting. But the quantum yield is still low when compared with the required target (30% in terms of quantum yield).

1.11.3 Non oxide photocatalyst

Extensive research has also been carried out on non oxide photocatalyst with the most promising being CdS. But, CdS suffers from photocorrosion with time. Ge_3N_4 is an UV-active photocatalyst. Instead, nitrogen, sulphur are used as anionic dopants to oxide photocatalyst as an important strategy to decrease band gap and increase photoactivity for hydrogen generation reaction [59].

1.12 Aim of our work in photocatalytic hydrogen generation

We have briefly discussed about many photocatalyst materials in this chapter that have been developed, thus ensuring that this research area is under progress. From the above discussions we definitely observe that photocatalytic hydrogen generation is extensively reported in the literature, focussing on photocatalyst candidates to solve the energy and environmental issues in the future. But, we also notice that for efficient water splitting into H_2 and O_2 (30% in terms of quantum yield at 600 nm) is yet to be achieved in this research field. Thus, photocatalytic water splitting is an attractive but challenging theme in chemistry. Moreover, powdered photocatalyst systems will be advantageous for large-scale application of solar water splitting because of their simplicity. Hence, the development of new and superior photocatalyst materials is still a major issue.

In_2TiO_5 is composed of octahedral [TiO_6] and [InO_6] motifs, containing both early transition-metal (d^0) and p-block metal (d^{10}). Up to now, very few studies have reported on In_2TiO_5 as a potential photocatalyst. Gaewdang et al. [142] studied the luminescent properties and structure details of indium titanate. Wang et al. [143] evaluated the photocatalytic activity of bulk In_2TiO_5 for methyl orange degradation. Photoactivity of vanadium-doped In_2TiO_5 semiconductors synthesized by the ceramic route was investigated by Shah et al. [144]. Our aim was to investigate the structure, UV-visible light absorption properties and photocatalytic properties of ternary oxide of indium and titanium - In_2TiO_5, for hydrogen generation reaction and establish the structure–photocatalytic activity correlation. Further, the effect of transition metal like Ni^{2+} doping on the structure, light absorption properties and the photocatalytic properties of In_2TiO_5 was also investigated.

In chapter 2 of the thesis apart from the experimental methodologies, the photocatalytic reactors used for the study has also been discussed. In chapter 7 the photocatalytic properties of Indium titanate prepared by three different methods - solid state method, solvothermal and polyol are compared to observe the effect of powder properties on photoactivity for hydrogen generation. Emphasis was also given to establish the structure-photoactivity correlation. Further Ni-doping was done at In-site with an aim to decrease band gap and increase the photoactivity and the results are discussed in chapter 8.

References:

1. BP Statistical Review of World Energy, June 2010, available online at www.bp.com/statisticalreview
2. The Association for the Study of Peak Oil and Gas “ASPO” Newsletter No. 100 – APRIL 2009, available online at http://aspoireland.files.wordpress.com/2009/12/newsletter100_200904.pdf
3. Ibrahim Sami Nashawi, Adel Malallah and Mohammed Al-Bisharah Energy Fuels, 2010, 24 (3), pp 1788–1800.
4. M. I. Hoffert, K. Caldeira, A. K.Jain, E. F. Haites, L. D. D. Harvey, S. D.Potter, M. E. Schlesinger, S. H. Schneider, R. G. Watts, T. M. L. Wigley, D. J. Wuebbles, Nature 395 (1998) 881.
5. R. E. Smalley, Future Global Energy Prosperity: The Terawatt Challenge, MRS Bulletin, 30 (2005) 412.

6. CO_2 Emissions from Fuel Combustion, Highlights (2010) International Energy Agency.
7. IPCC Fourth Assessment Report - Working Group I Report "The Physical Science Basis", 2007, available online http://www.ipcc.ch/publications_and_data/publications_ipcc_fourth_assessment_report_wg1_report_the_physical_science_basis.htm.
8. IPCC Fourth Assessment Report - Working Group III Report “Climate Change 2007: Mitigation of Climate Change”, 2007, available online http://www.ipcc.ch/publications_and_data/publications_ipcc_fourth_assessment_report_wg3_report_mitigation_of_climate_change.htm.
9. C. E. Bamberger, D. M. Richardson, Cryogenics 16(4) (1976) 197–208.
10. S. Kubo, H. Nakajima, S. Kasahara, S. Higashi, T. Masaki, H. Abe, et al. Nucl. Eng. Des. 233 (2004) 347–354.
11. S. Brutti, G. D. Maria, G. Cerri, A. Giovannelli, B. Brunetti, P. Cafarelli, E. Semprin, V. Barbarossa and Ceroli, Ind. Eng. Chem. Res. 6 (2007) 6393-6400.
12. L. C. Brown, J. F. Funk, S. K. Showalter, General Atomics Report GAA23373, April 2000. Available on-line at http://web.gat.com/pubs-ext/miscpubs/A23373.pdf on March 21, 2006.
13. J. H. Norman, G. E. Besenbruch, L. C. Brown, D. R. O’Keefe, C. L. Allen. General Atomic Company Report GA-A16713;1982.
14. L. E. Brecher, S. Spewock, C. J. Warde, Int. J. Hydrogen Energy 2(1) (1977) 7–15.
15. G. E. Beghi, Int. J. Hydrogen Energy 11(12) (1986) 761–771.
16. S. Goldstein, J. M. Borgard, X. Vitart, Int. J. Hydrogen Energy 2005;30:619-26.
17. J. Zhou, Y. Zhang, Z. Wang, W. Yang, Z. Zhou, J. Liu, et al. Int. J. Hydrogen Energy 32 (2007) 567-75.
18. Z. L. Wang, G. F. Naterer, K. S. Gabriel, R. Gravelsins, V. N. Daggupati, Int. J. Hydrogen Energy 35 (2010) 4820-30.
19. F. Mueller-Langer, E. Tzimas, M. Kaltschmitt, S. Peteves, Int. J. Hydrogen Energy 32 (2007) 3797-810.
20. J. H. Norman, K. J. Mysels, R. Sharp, D. Williamson, Int. J. Hydrogen Energy 7(7) (1982) 545-56.
21. P. Zhang, S. Z. Chen, L. J. Wang, T. Y. Yao, J. M. Xu, Int. J. Hydrogen Energy 35 (2010) 10166-72.

22. G. Cerri, C. Salvini, C. Corgnale, A. Giovannelli, D. D. L. Manzano, A. O. Martinez, et al. Int. J. Hydrogen Energy 35 (2010) 4002-14.
23. A. Le Duigou, J. M. Borgard, B. Larousse, D. Doizi, R. Allen, B. Ewan, et al. Int. J. Hydrogen Energy 32 (2007) 1516-29.
24. N. Sakaba, S. Kasahara, K. Onuki, K. Kunitomi, Int. J. Hydrogen Energy 32 (2007) 4160-4169.
25. B. J. Lee, Hc No, H. J. Yoon, H. G. Jin, Y. S. Kim, J. I. Lee, Int. J. Hydrogen Energy 34 (2009) 2133-43.
26. S. Kasahara, S. Kubo, R. Hino, K. Onuki, M. Nomura, S. Nakao, Int. J. Hydrogen Energy 32 (2007) 489-96.
27. T. Pregger, D. Graf, W. Krewitt, C. Sattler, M. Roeb, S. Mooller, Int. J. Hydrogen Energy 34 (2009) 4256-67.
28. D. Graf, N. Monnerie, M. Roeb, M. Schmitz, C. Sattler, Int. J. Hydrogen Energy 33(17) (2008) 4511-9.
29. M. B. Gorensek, W. A. Summers, Int. J. Hydrogen Energy 34(9) (2009) 4097-114.
30. J. Leybros, A. Saturnin, C. Mansilla, T. Gilardi, P. Carles, Int. J. Hydrogen Energy 35 (2010) 1019-28.
31. I. V. Dulera, R. K. Sinha, J. of Nucl. Mater. 383 (2008) 183–188
32. I. V. Dulera and R. K. Sinha Paper-IAEA-CN-152-20 International Conference on Non-Electric Applications of Nuclear Power: Seawater Desalination, Hydrogen Production and other Industrial Applications, Oarai, Japan, 16 - 19 April 2007.
33. V. Barbarossa, S. Bruttib, M. Diamantia, S. Saua, G. De Mariab, Int. J. Hydrogen Energy 31 (2006) 883-90.
34. I. Berzelius, Berz. Jahresbericht, 15 (1834/1835) 237.
35. W. R. Patterson in Catalysis and chemical processes, Eds. R. Pearce and W. R. Patterson, Leonard Hill, Scotland, (1981).
36. G. A. Somorjai in Introduction to surface chemistry and catalysis, John Wiley & Sons, Inc., New York, (1994).
37. P. Emmett, CRC Crit. Rev. Solid State Sci. 4 (1974) 127.
38. Vaclav Smil, Nature 400 (1999) 415.
39. S. Roy, Morrison, The Chemical Physics of Surfaces, Plenum, New York, (1977).
40. G. C. Bond, Principles of Catalysis, London Chemical Society, London (1972).

41. D. K. Chakrabarty in Adsorption and catalysis by solids, Wiley Eastern Limited, New Delhi, (1991).
42. S. J. Thomson and G. Webb, Heterogeneous catalysis, Oliver and Boyd, Edinburgh, (1968).
43. B. Gates, J. R. Katzer and G. C. A. Schuit, Chemistry of catalytic processes, McGraw-Hill, New York, (1979).
44. G. I. Golodates Heterogeneous catalytic reaction involving molecular oxygen, Elsevier Science Publisher
45. D. M. Ginosar, L. M. Petkovic, A. W. Glenn, K. C. Burch, Int. J. Hydrogen Energy 32(4) (2007) 482-488.
46. L. M. Petkovic, D. M. Ginosar, H. W. Rollins, K. C. Burch, P. J. Pinhero, H. H. Farrell, Appl. Catal. A: Gen. 338 (2008) 27-36.
47. B. M. Nagaraja, K. D. Jung, B. S. Ahn, H. Abimanyu, K. S. Yoo, Ind. Eng. Chem. Res. 48 (2009) 1451–1457.
48. S. N. Rashkeev, D. M. Ginosar, L. M. Petkovic, H. H. Farrell, Catal. Today 139 (2009) 291–298.
49. M. Dokiya, T. Kameyama, K. Fukuda, Y. Kotera Bull. Chem. Soc. Jpn. 50 (1977) 2657-2660.
50. H. Tagawa, T. Endo, Int. J. Hydrogen Energy 14(1) (1989) 11–17.
51. G. Busca, L. Lietti, G. Ramis, F. Berti, Appl. Catal. B: Environ. 18 (1998) 1.
52. M. Woodhouse and B. A. Parkinson, Chem. Soc. Rev. 38 (2009) 197–210.
53. L. N. Yannopoulos, J. F. Pierre, Int J Hydrogen Energy 9(5) (1984) 383 - 390.
54. T. H. Kim, G. T. Gong, B. G. Lee, K. Y. Lee, H. Y. Jeon, C. H. Shin, et al. Appl Catal A Gen 305(1) (2006) 39–45.
55. D. M. Ginosar, H. W. Rollins, L. M. Petkovic, K. C. Burch, M. J. Rush, Int. J. Hydrogen Energy 34(9) (2009) 4065-4073.
56. A. Fujishima, K.Honda, Nature 238 (1972) 37.
57. A. L. Linsebigler, G. Lu, and John T. Yates, Jr.Chem. Rev. 95, (1995) 735-758.
58. A. J. Esswein and Daniel G. Nocera, Chem. Rev. 107 (2007) 4022-4047.
59. A. Kudo and Y. Miseki, Chem. Soc. Rev. 38 (2009) 253–278.
60. K. Maeda and K. Domen, J. Phys. Chem. C 111 (2007) 7851-786.
61. S. Ekambaram J. of Alloys and Compd. 448 (2008) 238–245.

62. M. Kaneko, I. Okura Photocatalysis Science and Technology, Biological and medical physics series, Kodansha-Springer.
63. A. J. Bard, M. A. Fox, Acc. Chem. Res. 28 (1995) 141-145.
64. T. Kawai and T. Sakata, Nature (London, U. K.) 282 (1979) 283.
65. T. Kawai and T. Sakata, J. Chem. Soc., Chem. Commun. (1979) 1047.
66. T. Kawai and T. Sakata, Nature (London, U. K.) 286 (1980) 474.
67. W. Jaegermann, Modern Aspects of Electrochemistry, (R. E. White, B. E. Conway and J. O. M. Bockris, edu), Plenum Press, New York, 30, 1 (1996).
68. A. Fujishima and D. A. Tryk, Functionality in Molecular Systems, (K. Honda, ed), Springer-Verlag, Tokyo, 2, 196 (1999).
69. N. Sato, Electrochemistry at Metal and Semiconductor electrodes, Elsevier, Amsterdam, (1998).
70. P. T. Landsberg, Recombination in Semiconductor, Cambridge University press, Cambridge (1991).
71. B. Ohtani, Y. Ogawa and S. Nishimoto, J. Phys. Chem. 97 (1993) 920.
72. S. T. Martin, H. Hermann, W. Choi and M. R. Hoffman, J. Chem. Soc. Faraday Trans. 90 (1994) 3315.
73. S. T. Martin, H. Hermann and M. R. Hoffman, J. Chem. Soc. Faraday Trans. 90 (1994) 3323.
74. R. Asahi, T. Morikawa, T. Ohwaki, K. Aoki, Y. Taga, Science 293 (2001) 269–71.
75. M. Anpo, Y. Yamashita, Y. Ichihashi Optronics 186 (1997) 161–5.
76. T. Kawai, T. Sakata J. Chem. Soc., Chem. Comm. 15 (1980) 694–5.
77. G. R. Bamwenda, S. Tsubota, T. Nakamura, M. Haruta, J Photochem Photobiol A: Chem 89(2) (1995) 177–89.
78. A. Galinska, J. Walendziewski Energy Fuels 19 (2005) 1143.
79. H. Yi, T. Peng, D. Ke, D. Ke, L. Zan, C. Yan Int J. Hydrogen Energy 33 (2008) 672 – 678
80. Ni Meng, K. H. Michael Leung, Y. C. Dennis Leung, K. Sumathy, Renewable and Sustainable Energy Rev. 11 (2007) 401–425.
81. M. Kitano, M. Matsuoka, M. Ueshima, M. Anpo, Appl. Catal. A: Gen. 325 (2007) 1–14.
82. K. Shankar, J. I. Basham, N. K. Allam, O. K. Varghese, G. K. Mor, X. Feng, M. Paulose, J. A. Seabold, Kyoung-Shin Choi, and C. A. Grimes J. Phys. Chem. C 113 (2009) 6327–6359.

83. T. Tachikawa, M. Fujitsuka, and T. Majima J. Phys. Chem. C 111(14) 2007.
84. A. Kudo,. H. Kato, I. Tsuji, Chem. Lett. 33 (2004) 1534-1539.
85. K. Maeda, K. Domen, J.Phys. Chem. C 111 (2007) 7851-7861.
86. T. Sreethawong, Y. Suzuki, S.Yoshikawa, J. Solid State Chem. 178(1) (2005) 329–38.
87. P. Bouras, E. Slathatos, P. Lianos, Appl. Catal. B: Environ. 73 (2007) 51–59.
88. S. M. Prokes, J. L. Gole, X. Chen, C. Burda, W. E. Carlos, Adv. Func. Mater. 15 (2005) 161–167.
89. T. Kajiwara, K. Hasimoto, T. Kawai and T. Sakata, J. Phys. Chem. 86 (1982) 4516.
90. K. Hashimoto, T. Kawai and T. Sakata, Nouv. J. Chim. 7 (1983) 249.
91. N. Serpone, D. Lawless, J. Disdier, J. M. Herrmann, Langmuir 10 (1994) 643.
92. M. Anpo, M. Takeuchi, J. Catal. 216 (2003) 505.
93. C. Wang, C. Bottcher, D. W. Bahemann, J. K. Dohrmann, J. Mater. Chem. 13 (2003) 2322-2329.
94. R. Sasikala, V. Sudarsan, C. Sudakar, R. Naik, T. Sakuntala, S. R. Bharadwaj, Int. J. Hydrogen Energy 33 (2008) 4966-4973.
95. R. Sasikala, V. Sudarsan, C. Sudakar, R. Naik, T. Sakuntala, S. R. Bharadwaj, Int. J. Hydrogen Energy 33 (2008) 4966-4973.
96. Z. Jin, X. Zhang, Y. Li, S. Li, G. Lu, Catal. Commun. 8 (2007) 1267-1273.
97. K. Lv, H. Zuo, J. Sun, K. Deng, S. Liu, X. Li, D. Wang, J. Hazard. Mater. 161 (2009) 396-401.
98. C. Burda, Y. Lou, X. Chen, A.C.S. Samia, J. Stout, J. L. Gole, Nano Lett. 3 (2003) 1049-1051.
99. S. Yin, K. Ihara, Y.Aita, M. Komatsu, T. Sato, J. Photochem. Photobiol. A:Chem. 179 (2006) 105-114.
100. K. Lv, H. Zuo, J. Sun, K. Deng, S. Liu, X. Li, D. Wang, J. Hazard. Mater. 161 (2009) 396-401.
101. K. Iino, M. Kitano, M. Takeuchi, M. Matsuoka, M. Anpo, Current Appl. Phys. 6 (2006) 982–986.
102. M. Kitano, K. Tsujimaru, M. Anpo, Appl. Catal. A: Gen. 314 (2006) 179–183.
103. Z. Jin, X. Zhang, Y. Li, S. Li, G. Lu, Catal. Comm. 8 (2007) 1267–1273.
104. R. Sasikala, A. Shirole, V. Sudarsan, T. Sakuntala, C. Sudakar, R. Naik, S.R. Bharadwaj, Int. J. Hydrogen Energy 34 (2009) 3621-3630.
105. A. Kudo and S. Hijii, Chem. Lett. 28 (1999) 1103.

106. K. Sayama and H. Arakawa, J. Photochem. Photobiol. A, 77 (1994) 243.
107. K. Sayama and H. Arakawa, J. Phys. Chem. 97 (1993) 531.
108. Y. Wang, Z. Zhang, Yu Zhu, Z. Li, R. Vajtai, L. Ci and P. M. Ajayan, ACS Nano 2 (7) (2008) 1492–1496.
109. K. Domen, S. Naito, S. Soma, M. Onishi and K. Tamaru, J. Chem. Soc., Chem. Commun. 1980, 543.
110. H. Mizoguchi, K. Ueda, M. Orita, S. C. Moon, K. Kajihara, M. Hirano and H. Hosono, Mater. Res. Bull. 37 (2002) 2401.
111. H. Kato and A. Kudo, Chem. Phys. Lett. 295 (1998) 487.
112. K. Sayama, H. Arakawa and K. Domen, Catal. Today 28 (1996) 175.
113. H. Kato, H. Kobayashi and A. Kudo, J. Phys. Chem. B 106 (2002) 12441.
114. D. W. Hwang, J. S. Lee, W. Li and S. H. Oh, J. Phys. Chem. B 107 (2003) 4963.
115. R. Abe, M. Higashi, K. Sayama, Y. Abe and H. Sugihara, J. Phys. Chem. B 110 (2006) 2219.
116. H. Song, P. Cai, Y. Huabing and C. Yan, Catal. Lett. 113 (2007) 54.
117. S. M. Ji, H. Jun, J. S. Jang, H. C. Son, P. H. Borse and J. S. Lee, J. Photochem. Photobiol., A, 189 (2007) 141.
118. J. Kim, D. W. Hwang, H. G. Kim, S. W. Bae, J. S. Lee, W. Li and S. H. Oh, Top. Catal. 35 (2005) 295.
119. Y. G. Ko and W. Y. Lee, Catal. Lett. 83 (2002) 157.
120. S. Ikeda, M. Fubuki, Y. K. Takahara and M. Matsumura, Appl. Catal. A: Gen. 300 (2006) 186.
121. M. Yoshino, M. Kakihana, W. S. Cho, H. Kato and A. Kudo, Chem. Mater. 14 (2002) 3369.
122. K. Shimizu, Y. Tsuji, T. Hatamachi, K. Toda, T. Kodama, M. Sato and Y. Kitayama, Phys. Chem. Chem. Phys. 6 (2004) 1064.
123. K. Shimizu, S. Itoh, T. Hatamachi, T. Kodama, M. Sato and K. Toda, Chem. Mater. 17 (2005) 5161.
124. H. Otsuka, K. Kim, A. Kouzu, I. Takimoto, H. Fujimori, Y. Sakata, H. Imamura, T. Matsumoto and K. Toda, Chem. Lett. 34 (2005) 822.
125. Y. Miseki, H. Kato and A. Kudo, Chem. Lett. 35 (2006) 1052.
126. H. G. Kim, D. W. Hwang, J. Kim, Y. G. Kim and J. S. Lee, Chem. Commun. (1999) 1077.

127. R. Abe, M. Higashi, K. Sayama, Y. Abe and H. Sugihara, J. Phys. Chem. B 110 (2006) 2219.
128. M. Higashi, R. Abe, K. Sayama, H. Sugihara and Y. Abe, Chem. Lett. 34 (2005) 1122.
129. H. Kato and A. Kudo, Chem. Lett. 28 (1999) 1207.
130. S. Ogura, K. Sato and Y. Inoue, Phys. Chem. Chem. Phys. 2 (2000) 2449.
131. Y. Inoue, M. Kohno, S. Ogura and K. Sato, Chem. Phys. Lett. 267 (1997) 72.
132. T. Sato, M. Kakihana, M. Arima, K. Yoshida, Y. Yamashita, M. Yashima and M. Yoshimura, Appl. Phys. Lett. 69 (1996) 2053.
133. Y. Inoue, T. Kubokawa and K. Sato, J. Chem. Soc., Chem. Commun. (1990) 1298.
134. Y. Inoue, T. Kubokawa and K. Sato, J. Phys. Chem. 95 (1991) 4059.
135. D. W. Hwang, H. G. Kim, J. S. Lee, J. Kim, W. Li, and S. H. Oh J. Phys. Chem. B 109 (2005) 2093-2102.
136. T. Yanagida, Y. Sakata and H. Imamura, Chem. Lett. 33 (2004) 726.
137. J. Sato, H. Kobayashi, N. Saito, H. Nishiyama and Y. Inoue, J. Photochem. Photobiol., A 158 (2003) 139.
138. J. Sato, N. Saito, H. Nishiyama and Y. Inoue, J. Photochem. Photobiol., A 148 (2002) 85.
139. J. Sato, N. Saito, H. Nishiyama and Y. Inoue, J. Phys. Chem. B 105 (2001) 6061.
140. Di Chen and Jinhua Ye, Chem. Mater. 19 (18) (2007) 4585–4591.
141. K. Maeda, K. Teramura, D. Lu, T. Takata, N. Saito, Y. Inoue, K. Domen, Nature, 440 (2006).
142. T. Gaewdang, J. P. Chaminade, P. Gravereau, A. Garcia, C. Fouassier, P. Hagenmuller, R. Mahiou, Mater. Res. Bull. 28 (1993) 1051.
143. W.-D. Wang, F.-Q. Huang, C.-M. Liu, X.-P. Lin, J.-L. Shi, Mater. Sci. Eng. B. 139 (2007) 74.
144. P. Shah, D. S. Bhange, A. S. Deshpande, M. S. Kulkarni, N. M. Gupta, Mater. Chem. Phys. 117 (2009) 399.

CHAPTER-2

Instrumentation and Experimental Methods

2.1 Introduction

This chapter deals with the experimental methods adopted for synthesis of the oxides, their characterisation and evaluation of their catalytic activities for sulphuric acid decomposition or photocatalytic hydrogen generation. The oxide samples were synthesised by various techniques e.g. solid state route, co-precipitation, gel combustion or solvothermal. These samples were well characterised for structural, morphological, redox, thermal, optical properties and oxidation states by various instrumental techniques e.g. X-Ray Diffraction (XRD), Fourier Transform Infrared Spectroscopy (FTIR), Scanning Electron Microscopy (SEM), Energy Dispersive X-ray (EDX), X-ray photoelectron spectroscopy (XPS), Mössbauer Spectroscopy, Temperature Programmed Reduction/Oxidation/Desorption (TPR/O/D) and Evolved Gas Analysis (EGA). Instruments like gas chromatograph were used to quantify reaction products like SO_2 for sulphuric acid decomposition and H_2 in photocatalysis. Brief descriptions on general principles of these techniques are presented. The various experimental setups for carrying out sulfuric acid decomposition reaction or photocatalysis experiments were indigenously designed and developed and are also discussed in details.

2.2 Synthesis of catalysts

In this section we give an account of the different preparation methods used for preparation of catalysts which have been prepared and investigated in this thesis.

Fundamental basis of the catalyst preparation methods and then details of the techniques used are presented here in general. A case to case preparative procedure is however dealt in details in the respective chapters where it has been studied and reported.

2.2.1 Ceramic Route

The traditional method for the preparation of polycrystalline mixed metal oxides is the solid state reaction or ceramic route. Preparation of oxides by this method involves reacting oxides, carbonates, or other compounds of the component metals with repeated grinding and heating. The first step in this procedure is to preheat the component oxide (to remove moisture so that exact weight is taken) and then mix the stoichiometric quantities of respective oxides. The mixture of oxides is then ground thoroughly for at least half an hour in agate mortar and pestle. This grinding process is one of the most important steps in this synthesis route [1]. Long grinding times are required to achieve the phase homogeneity. The well ground powder is then pelletized in a hydraulic press at pressures up to 1.5 tonne. This process is required to maximise the total area of contact between the grains. These pellets are then heated first at lower temperatures for a time period depending upon the oxide to be prepared. Solid state reactions are diffusion controlled process, and as the reaction rate for solid state reactions is reported to increase exponentially with temperature, high temperatures are often required to obtain the appreciable level of diffusion and is appreciably fast in excess of 1000°C temperature. This process of heating is punctuated by two or more intermittent grinding so as to achieve uniformity within the sample. Final heating if required may be carried out at a higher temperature in order to improve the crystallinity of the products obtained. Highly crystalline powders are obtained by this method and if proper intermittent grinding and heating are done the product obtained are also homogeneous. One of the disadvantages of this method is that the powders obtained are in micron range as high temperature heating causes sintering and grain growth. Iron chromium binary mixed oxides

($Fe_{2(1-x)}Cr_{2x}O_3$: $0 \leq x \leq 1.0$) and $In_{2(1-x)}Ni_{2x}TiO_{5-\delta}$, samples have been prepared by this method and has been discussed in details in chapter 3 and 8 respectively.

2.2.2 Co-precipitation method

The co-precipitaion method is one of the widely used methods for the preparation of ceramic materials. It consists of preparing an aqueous solution containing the desired cations (in the form of metal nitrates, chlorides etc.) and mixing with another solution which contains the precipitating agent (alkali hydroxides, oxalic acid etc.). The precipitated product i.e. the hydroxides or oxalates is separated from the liquid by filtration and then further heated to thermally decompose to the desired compound. The hydroxides or oxalates in this procedure undergo solid-state reaction in basically the same way as in the conventional solid-state reaction [2]. The main difference here is the proximity of the reacting species. Several parameters, such as pH, mixing rates, temperature and concentration have to be controlled to produce satisfactory results. The composition control, purity and morphology of the resulting product are good. However, different rates of precipitation of each individual compound may lead to microscopic inhomogeneity. Granular catalysts Fe_2O_3 and $Fe_{1.8}Cr_{0.2}O_3$ were prepared by co-precipitation method and the method is discussed in chapter 5.

2.2.3 Gel combustion method

Gel-combustion, one of the methods of combustion synthesis, has emerged as an important technique for the synthesis and processing of advanced ceramics (structural and functional), catalysts, composites, alloys, intermetallics and nanomaterials [3-4]. This method consists of two steps – first the preparation of fuel-oxidant precursor and second the combustion of the fuel-oxidant precursor. In the first step, the nitrate salts of the metals of interest, in a required molar ratio, are mixed together in an aqueous media to produce the transparent mixed metal- nitrate solution. Since the combustion involves reaction between fuel and oxidant, nitrates fulfill the requirement of oxidant by providing the oxygen for burning of the fuel. An organic compound capable of binding the metal ions and acting as a fuel in combustion reaction is added in an appropriate amount to this mixed metal-nitrate solution. The basic characteristics of the fuel are that it should be able to maintain the compositional homogeneity among constituents and should get combusted with an oxidizer (i.e. nitrates) at low ignition temperature. The common examples of the fuels are citric acid, glycine and urea. The transparent aqueous solution containing metal nitrates and a suitable fuel is converted to a viscous liquid (hereafter termed as gel) by thermal dehydration (to remove the excess solvent) at about 80-150 °C. The nature of the fuel, its amount and pH of the starting solution are some of the important process parameters for getting the transparent viscous gel without any phase separation or precipitation. However, it is not always necessary to prepare a gel precursor through the thermal dehydration on a hot plate. The basic idea is to maintain an intimate blending between fuel and an oxidant and it can be achieved even by spray drying the aqueous solution containing metal nitrate and a suitable fuel. In the second step, the precursor is subjected to an external temperature of about 150-250 °C, which triggers the combustion reaction. At this stage, exothermic decomposition of the fuel-oxidant precursor associated with evolution of large volume of gases results in the voluminous powder. If the fuel-to-oxidant molar ratio is properly adjusted, the very high exothermicity generated during combustion reflects in the form of flame or fire and the process is termed as auto-ignition. The resultant product may either consist of powder of the required phase or a semi-decomposed precursor having a considerable amount of carbonaceous residue, depending upon the nature and amount of the fuel used in the process. Detailed methodology of preparation of ferrospinels (AFe_2O_4, A = Co, Ni, Cu) and rare earth perovskites $LaFeO_3$ and $GdFeO_3$ by gel-combustion method are given in chapter 4.

2.2.4 Solvothermal synthesis

The process involves heating reactants (often metal salts, oxides, hydroxides or metal powders) as a solution or suspension. The solvent medium containing the ions of interest is heated at elevated temperature and pressure in an autoclave. Thus, the solvent as liquid or vapour acts in two ways: (i) it acts as the pressure transmitting medium and (ii) it allows the reaction to take place as some or all of the reactants are partially soluble in the solvent under pressure. The reactions kinetics in an autoclave is altogether different compared to that in other routes. Under these conditions, reactions may occur at lower temperature compared to the absence of water. The process allows formation of crystalline, submicron oxide powders directly in a solvent at elevated temperature and pressure up to about 300 °C and 100 MPa, respectively [5]. Preparation of nanocrystalline indium titanate was done by solvothermal route the detailed procedure of which is given in chapter 7.

2.3 Characterisation techniques

2.3.1 X-Ray Diffraction

X-ray diffraction (XRD) is the most extensively used technique to identify the crystalline phase of a solid material and also to determine its crystal structures. The principle of XRD technique is based on diffraction of X-rays by a crystal consisting of well-defined array of atoms, ions and molecules. Since the lattice of a crystal consists of parallel arrays of atoms equivalent to the parallel planes of the diffraction grating, the inter-planar spacing could be successfully determined, from the separations of bright fringes of the diffraction pattern. These interplanar spacings (or distances) have nearly the same magnitude as the wavelength of X-rays (0.5 to 2 Å) and hence, crystal planes act as diffraction gratings. Interaction of X-rays reflected by a set of parallel planes satisfying Bragg's condition lead to constructive interference only at a particular angle.

The Bragg condition for the occurrence of such diffraction can be written as:

$$n\lambda = 2d \sin\theta \qquad \text{....2.1}$$

where, λ is wavelength of X-rays, θ is the glancing angle (called as Bragg's angle), d is inter-planar separations, and n is the order of diffraction.

A typical classical powder X-ray diffractometer consists of a source of X-rays and a detector for the detection of diffracted X-rays. Common diffractometer geometries are based on the Bragg-Brentano (θ-2θ) geometry (Fig. 2.1A). A block diagram of the typical powder diffractometer is shown in the Fig. 2.1B. The conventional diffractometer uses a sealed tube X-ray source in which, bombardment of high-speed electrons on a metal target produces the X-rays. A part of the electron energy is used in producing X-ray beam, which is a combination of a continuous radiation with wavelength ranging from a particular shortest value and several intense spikes, which are characteristic of the target elements (called characteristic radiation).

The monochromatic wavelength radiations are generally used for the diffraction experiments (angle dispersive). The details of the X-ray production and the typical X-ray spectra are explained in several books [6-7]. The X-rays are produced in all the direction; however, it is allowed to escape from a particular direction (usually through a Be window) in a diffractometer. The background and β-radiations are filtered using β-filters (if z is the atomic no. of the target metal then generally (Z-1) is generally the filter used). The beam of X-rays is then allowed to pass through the soller and divergence slits and then on the sample.

The powder sample is generally spread uniformly over a rectangular area of a glass slide either using binders like collodion or grease or wax. The X-rays scattered (diffracted) from the sample are collected by a film or counters. In a diffractometer, the beam diffracted from the sample is passed though the soller slits and divergence and receiving slits, monochromator and the detector. The gas filled tube or scintillation counters are commonly used as detectors for X-rays. These tubes can either be the proportional counter or Geiger-Muller counter. The tube is usually filled with a gas, which gets ionized by the impact of the radiation and by applying a potential difference between the two electrodes, the ions are collected. The typical current obtained is proportional to the number of photons reaching the detector. The detector is swept from one angle to another and thus detects the diffracted rays. The angle where the Bragg's law is satisfied for a particular plane, a constructive interference among the diffracted X-rays from that plane takes place, giving a sharp rise in the intensity which appears as a peak. Thus, the counts of the X-ray photon are measured at different angles and the output is obtained as plot of the intensity or counts of diffracted X-rays (Y-axis) *vs* angle (X-axis).

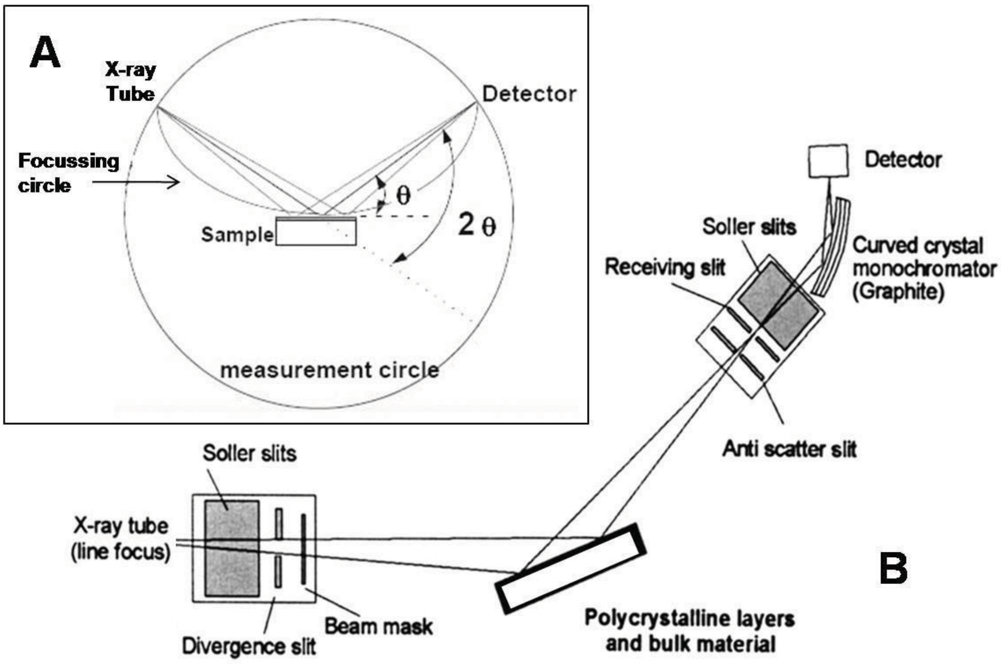

Fig. 2.1. The (A) Bragg-Brentano geometry and (B) ray diagram of a typical X-ray diffractometer

The peaks (also called as reflections) in the plot correspond to a set of parallel planes with inter-planar spacing d_{hkl}. The d-values are calculated from the position of the peaks by using the relation between angle and d-value according to equation 2.1. The peak positions are also related with the unit cell parameters of the lattice and a particular sample gives a characteristic set of d-values, which can be used for identification of the materials. The intensity distribution of the reflections is governed by the nature and kind of distribution of atoms in the unit cell. The absolute intensities of the reflections depend on the source intensity and counting time, in addition to the nature and kind of distribution of atoms in the unit cell. In the present work, a Philips 1729 diffractometer was mostly used for the characterization process. Philips-1729 diffractometer is based on the Bragg-Brentano reflection geometry. The Cu Kα emissions from sealed tube are used as the incident beam. In the former set up, the diffracted beam is monochromatised with a curved graphite single crystal. The Philips (PW-1729) diffractometer has a proportional counter (Argon filled) for the detection of X-rays. The X-ray tube rating was maintained at 30 kV and 20 mA in the Philips unit.

The data collection protocols often depend on the specific purpose of the data collections. In general a short time scan in the two-theta (2θ) range of 10 ° to 70 ° is sufficient for the identification of a well crystalline inorganic powder material. However, low symmetry samples and samples with poor crystallinity may need a slow scan. In most cases, data were collected in the 2θ ranges of 10 ° to 70 ° with a step width of 0.02 ° and time 1.25 sec. Before each measurement, Silicon was used for calibration of the instrument and then only data collection was made with the sample. By comparing the observed diffraction pattern with JCPDS (Joint Committee on Powder Diffraction Standards) data available for reported crystalline samples, fingerprinting of sample materials was normally done. The refinements are usually done by a least square method. The computer software used for this purpose was "Powder-X" [8]. However in the case of indium titanate the observed diffraction pattern was refined using the Riedvelt method [9]. The unit cell parameters are made free to adjust in the best way to fit the observed experimental data. The use and interpretation of the powder diffraction patterns are explained in several books [1, 6-8].

The broadening of an X-ray peak can occur due to smaller crystallite size or lattice strains from displacements of the unit cells about their normal positions. We briefly describe the two aspects below.

The approximate size of a crystal can be estimated from broadening of the X-ray peak by the Scherer's formula, if the crystal thickness is less than ~ 2000 Å. Thus for the crystalline oxides that were prepared, the approximate crystallite sizes were estimated using the Scherer's formula given as follows:

$$B(2\theta) = \frac{K\lambda}{L\cos\theta} \qquad \text{.....2.2}$$

where, L is the thickness of the crystal (in angstroms), λ the X-ray wavelength measured in angstrom (Å) units and θ (in radians) the Bragg angle, K is the Scherrer constant, generally taken as 0.9 for spherical crystals with cubic symmetry. The line broadening, B(2θ), is measured from the full width at half maxima (FWHM) of the peak. Its square is obtained from the difference between the square of the measured peak width of the sample and the square of the measured peak width of a peak of a standard material. Based on this concept of broadening of the XRD peak for the crystalline sample, the approximate crystallite size of the oxide powders were estimated.

Lattice strains arise from displacements of the unit cells about their normal positions. Often these are produced by dislocations, domain boundaries, grain-surface relaxation etc. Microstrains are very common in nanocrystalline materials. The peak broadening due to microstrain will vary as:

$$B(2\theta) = 4\varepsilon\frac{\sin\theta}{\cos\theta} \qquad \text{.....2.3}$$

Thus, combining equation 2.2 and 2.3 we have,

$$B(2\theta) = \frac{0.9\lambda}{L\cos\theta} + 4\varepsilon\frac{\sin\theta}{\cos\theta} \qquad \text{or,}$$

$$B(2\theta)\cos\theta = \frac{0.9\lambda}{L} + 4\varepsilon\sin\theta$$

i.e. plotting B(2θ) vs sinθ we can get the knowledge of both crystallite size and microstrain.

2.3.2 Surface area analysis

The surface area of a solid oxide catalyst is an important property from the catalytic point of view as heterogeneous catalysis is a surface phenomenon. The gas adsorption-desorption techniques are generally used to measure surface area of solid materials. BET method [10] (Brunauer, Emmett and Teller), which is the most commonly used procedure for determination of surface area, involves the following equation, known as the BET equation:

$$\frac{p}{v(p_0 - p)} = \frac{1}{v_m C} + \frac{C-1}{v_m C}\left(\frac{p}{p_0}\right) \qquad \text{.....2.4}$$

Where,

p = Adsorption equilibrium pressure

p_0 = Saturation vapour pressure of adsorbate at the adsorption temperature

v_m = Volume of adsorbate required for mono layer coverage

v = Volume of adsorbate adsorbed at equilibrium pressure p

C = Constant related exponentially to the heat of adsorption in the first layer (q_1) and heat of liquefaction of adsorbate (q_L) ; $C = e^{(q_1 - q_L)/RT}$

The constant C determines the shape of the isotherm. The higher the value of C, the more the isotherm tends to type-II, which is desirable for accurate determination of surface area. A plot of $p/(p_o-p)v$ against relative pressure p/p_o yields a straight line and from the slope $s = (C-1) / v_m C$ and intercept $I = 1/v_m C$, v_m can be calculated as follows.

$$v_m = \frac{1}{S+I} \qquad .....2.5$$

Thus the values of the specific surface area of sample can be derived by knowing the monolayer cross sectional area of adsorbate molecule and from slope and intercept, as described above. Thus, surface area is given by,

$$S = \frac{v_m N_A A_m}{W \times 22414} \times 10^{-20} \ (\mathrm{m}^2\ /\mathrm{g}) \qquad .....2.6$$

where, S = Specific Surface Area, N_A = Avogadro's number, v_m = Monolayer volume in ml at STP, W = Weight of the catalyst sample (g), A_m = Mean cross sectional area occupied by adsorbate molecule which is 16.2 $Å^2$ for nitrogen at 77 K.

For many practical purposes the BET equation (2.4) is generally fitted to the data over a range p/p_o = 0.05 - 0.3 as at higher p/p_o values complexity associated with multilayer adsorption and pore condensation may arise. In our study, Quantachome Autosorb-1 surface area analyzer was employed. Prior to surface area determination, samples were subjected to a pre-treatment at 300°C for ~ 2-3 h under vacuum with a liquid N_2 trap so as to remove impurities such as moisture.

An understanding of the surface area and porosity of an adsorbent can be achieved by the construction of an adsorption isotherm. When the quantity of adsorbate on a surface is measured over a wide range of relative pressures at constant temperature, the result is an adsorption isotherm. The adsorption is obtained point-by-point in the Autosorb-1 by admitting to the adsorbent, successive known volumes of adsorbate, by measuring the equilibrium pressure. Similarly, desorption isotherms can be obtained by measuring the quantities of gas removed from the sample as the relative pressure is lowered. All adsorption isotherms can be grouped into five types viz

Type I or Langmuir isotherms are concave to the P/P_0 axis and the amount of adsorbate approaches a limiting value as P/P_0 approaches 1. Type I physisorption isotherms are exhibited by microporous solids having relatively small external surfaces, for example, activated carbons and molecular sieve zeolites. The limiting uptake of adsorbate is governed by the accessible micropore volume rather than by the internal surface area.

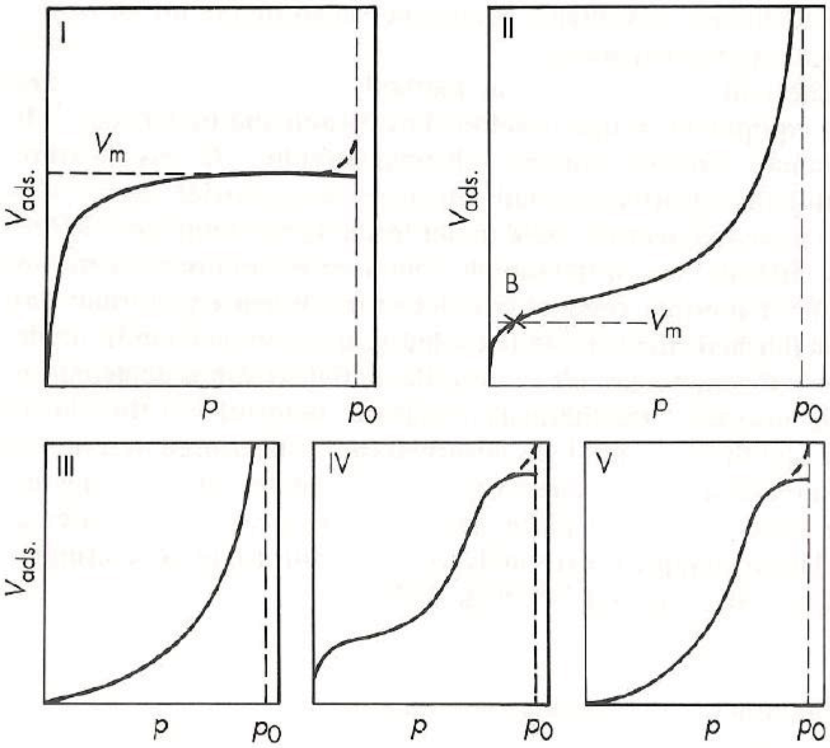

Fig. 2.2. Different adsorption Isotherms (TYPE I to V)

Type II isotherms are the normal form of isotherm obtained with a nonporous or macroporous adsorbent. This type of isotherm represents unrestricted monolayer-multilayer adsorption. Point B, the start of the linear central section of the isotherm, is usually taken to indicate the relative pressure at which monolayer coverage is complete.

Type III isotherm are convex to the P/Po axis over its entire range. Type III isotherm are rarely encountered. A well-known example is the adsorption of water vapor on nonporous carbons. The absence of a distinct point B on type III isotherm is caused by stronger adsorbate-adsorbate than adsorbate-adsorbent interactions.

Type IV isotherms are associated with capillary condensation in mesopores, indicated by the steep slope at higher relative pressures. The initial part of the type IV isotherm follows the same path as the type II.

Type V isotherms are uncommon, corresponding to the type III, except that pores in the mesopore range are present.

2.3.3 Scanning Electron Microscopy (SEM)

When a finely focused electron beam interacts with matter (specimen) several phenomena can take place viz.: (i) emission of secondary electrons (SE) (ii) back-scattering electrons (BSE) and (iii) transmission of electrons etc. which are depicted in Fig. 2.3.

In Scanning Electron Microscopy, the signals generated from the surface of the sample by secondary and back-scattered electrons are detected. Scanning microscope is comprise of the following systems: (i) electron optical system, (ii) specimen stage, (iii) display and recording system and (iv) vacuum system.

In SEM technique [11], the electrons from the electron source (a focused beam) are focussed across the surface of the sample. Electrons reflected by the surface of the sample and emitted secondary electrons are detected by the detecting system which then gives a map of the surface topography of the sample. It is useful for determining the particle size, crystal morphology, magnetic domains, surface defects etc. A wide range of magnifications can be achieved, the best resolution being about 2 nm. The samples (if non-conducting) may need to be coated with gold or graphite to stop charge building up on the surface. In scanning electron microscopy, the elements present in the sample also emit characteristic X-rays, which can be separately detected by a silicon-lithium detector, amplified and corrected for absorption and other effects, to give both qualitative and quantitative analysis of the elements present (for elements of atomic number greater than 11) in the irradiated particle, a technique known as energy dispersive analysis of X-rays (EDAX or EDX).

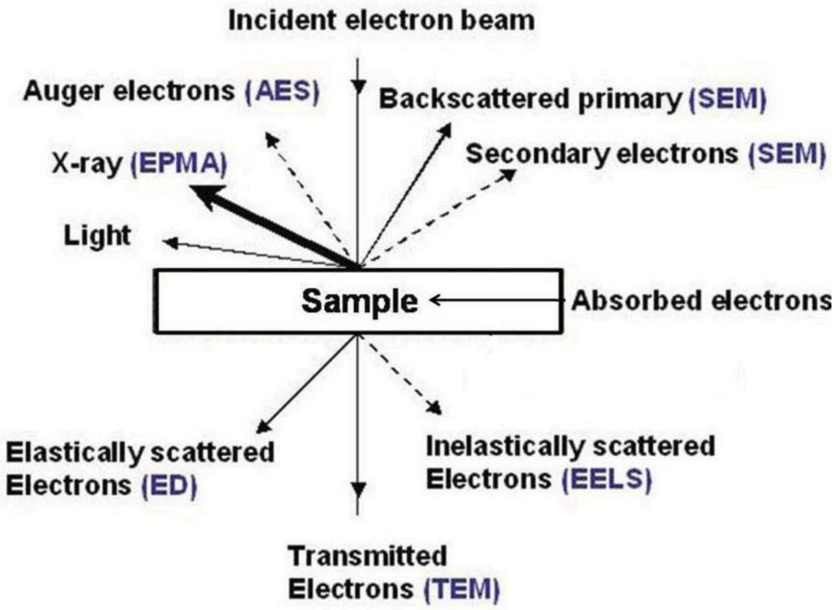

Fig. 2.3. Depiction of different phenomena occurring on interaction of electron beam with a solid sample

This technique of Scanning Electron Microscopy (along with EDX) was used to study the microstructure evolution (grain size, porosity, etc.) of the calcined metal oxide particles before and after use as a catalyst for sulphuric acid decomposition and also of the metal oxide photocatalysts. The instrument used was a Scanning Electron Microscope**,** Mirero, Korea, model- AIS2100. Conductive gold coating was applied on the sintered samples (if the metal oxide suffers from surface charge accumulation) using 6” d.c. sputtering unit, model 6-SPT, manufactured by M/s. Hind High Vacuum, Bangalore as and when necessary.

2.3.4 Transmission Electron Microscopy (TEM)

Transmission Electron Microscopy (TEM) is used to determine the morphology of particles (can detect particles upto 1 nm or even lower in case of High Resolution TEM). In TEM, a beam of highly focused electrons is directed towards a thin sample where the highly energetic incident electrons interact with the atoms in the sample, producing characteristic radiation and thus provide the necessary information for characterization of various materials. Information is obtained from both transmitted electrons (i.e. image mode) and diffracted electrons (i.e. diffraction mode). The image mode provides the information regarding micro-structural features whereas the diffraction mode is used for crystallographic information. The transmission electron microscopes are generally operated at voltages as high as 200 kV with a magnification of 300000 X. If the main objective is to resolve the finest possible details in specially prepared specimens, it is advantageous to use the shortest possible wavelength illumination (i.e., high voltage), an objective lens with very low aberrations and a microscope with extremely high mechanical and electrical stabilities, since high resolution requires both high instrumental resolving power and high image contrast. This special technique is termed as high-resolution transmission electron microscopy (HR-TEM) [12].

Low resolution transmission electron microscopy (TEM) images were collected with a Philips CM 200 microscope operating at an accelerating voltage of 200 kV. High resolution TEM (HR-TEM) images were taken with a FEI-Tecnai G-20 microscope operating at 200 kV. The samples were prepared by ultrasonicating the finely ground samples in ethanol and then dispersing on a carbon film supported on a copper grid. Electron micrographs presented in this study are bright field images.

A pin-shaped cathode heated up by passing the current produces the ray of electrons. A high voltage under ultra-high vacuum accelerates the electrons to the anode. The accelerated ray of electrons passes a drill-hole at the bottom of the anode. The lens-systems consist of an arrangement of electromagnetic coils. A condenser first focuses the ray and then it allows the ray to pass through the object. The object consists of a thin (< 200 nm), electron transparent, evaporated carbon film on which the powder particles were dispersed. After passing through the object, the transmitted electrons are collected by an objective. Thereby an image is formed, which is subsequently enlarged by an additional lens system. The images formed thereby are visualized on a fluorescent screen or it is documented on a photographic material.

The technique was used to characterize the synthesized nanocrystalline indium titanate powders in terms of their morphological features of primary particles like shape, size, size distribution and extent of aggregation. Also, the metal dispersion, particle size was analysed for both fresh and used Pt/Al_2O_3 catalysts using this technique.

2.3.5 Fourier Transform Infrared Spectroscopy (FTIR)

The infrared region of the electromagnetic spectrum encompasses radiation with wavelengths ranging from 1 to 1000 microns. From the standpoint of both application and instrumentation, this range is divided into three regions; Near IR (12500 – 4000 cm^{-1}), Mid IR (4000 – 200 cm^{-1}) and Far IR (200 – 10 cm^{-1}) [13]. The majority of analytical applications are confined to a portion of the middle region extending from 4000 to 400 cm^{-1} or 2.5 to 25 μm. The absorption spectra in the infrared region originate from the transitions between vibrational (along with rotational) levels of a molecule present in its ground electronic state upon irradiation with infrared radiation.

The atoms in a molecule are never stationary and a good approximation is to treat them as a combination of point masses held together by Hooke's law of forces. By classical mechanics it can be shown that the displacements of the masses from their mean positions are always the sum of the displacements due to a particular set of vibrations. If in these set of vibrations the masses are in phase and the motion of all the nuclei involved are such that the centre of gravity of the molecule remains unaltered, then such vibrations are known as the fundamental modes of vibration the molecule. Mostly, a normal mode is localized largely to a group within the molecule and hence corresponds to stretching or bending of one or few bonds only and hence associated with that particular functional group. Whether for the functional group or the entire molecule, the vibrations are universally classified either as stretching or as bending types. Stretching vibrations, which correspond to the oscillations leading to change in bond lengths, can be further sub-divided into symmetric or asymmetric stretching vibrations. Bending vibrations are characterized by continuously changing angle between the bonds and is further sub classified as wagging, rocking, twisting, or scissoring. Apart from fundamental modes a large number of vibrational absorptions overtones (multiple of fundamental modes, 2ν or 3ν etc), combination tones ($\nu_1 + \nu_2$, $\nu_3 + \nu_4$ etc.) and difference tones ($\nu_1 - \nu_2$, $\nu_5 - \nu_6$ etc.) can also be observed in a typical infrared absorbance spectrum of a molecule [14].

One of the primary requirements for vibrating molecules to interact with the oscillating electric field of the incident radiation and to undergo a transition between two vibrational energy levels is that the molecular dipole moment must change during the vibration. The intensity of the absorption is determined by the magnitude of this dipole moment change. Owing to symmetry, some of the vibrations in a molecule may not induce a change in dipole moment and hence are transparent to infrared radiations i.e. IR inactive.

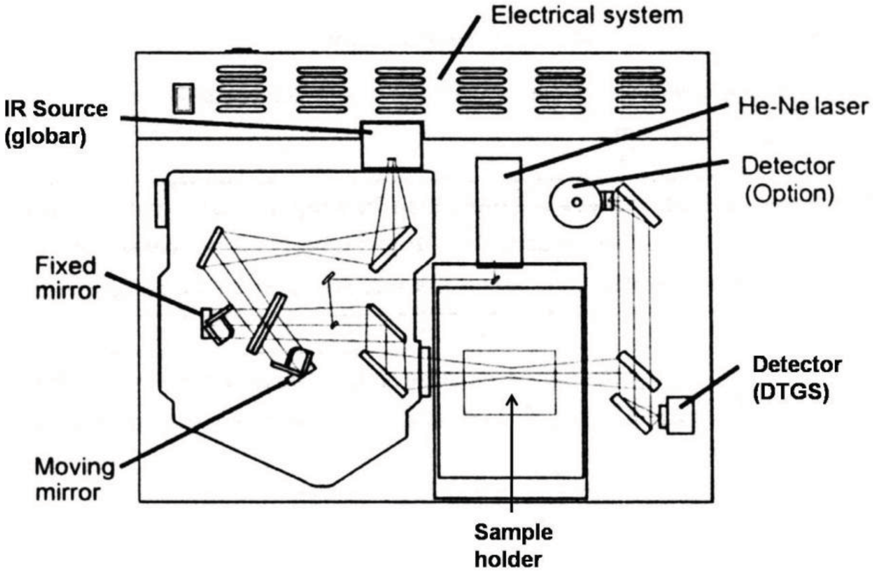

Fig. 2.4. Ray diagram of the FT/IR – 1600 instrument (JASCO make)

The instrument used in the present study was FT/IR – 600 model Fourier transform infrared spectrometer of JASCO (Japan). Fig. 2.4 depicts a typical ray diagram of this instrument. In this instrument, the light from a ceramic source (SiC) is collimated by a collimator mirror and introduced in to the Michelson interferometer, consisting of a beam splitter, fixed mirror and moving mirror. The beam splitter splits the beam into two equal parts – one part goes to the fixed mirror and the other towards the moving one. The movement of the moving mirror introduces a path difference between two beams and hence generates different interferograms consisting of different combination of wavelengths. The movement of the mirror is very precise and its speed decides the scan time and the resolution. The light passing through the interferometer is focused on the sample (placed in a holder) and the transmitted light is focused onto the detector. The detector used in current studies was DTGS (deuterated triglyceride sulphate) type. One complete scan gives an interferogram in terms of intensity with respect to time (in terms of the mirror movement). This interferogram, which is in time domain, is converted into frequency domain by a complicated mathematical treatment called as Fourier Transformation, hence yielding a spectrum of intensity change with respect to wavenumber. The function of the He-Ne laser is to provide alignment, measure precisely the optical path difference. 100 such scans were recorded for each sample to obtain spectra of low signal to noise ratio.

FT-IR spectra of the all the samples were recorded in the mid IR region (4000-400 cm^{-1}) of the samples prepared and used for catalytic use. For this purpose about 200 mg of dry KBr was mixed with ~6 mg of the sample and well grounded in a mortar pestle for homogenization. The mixture was then pressed into a transparent, thin pellet at 5 $tons/cm^2$. These pellets were used for IR spectral measurements.

2.3.6 Temperature Programmed Reduction/Oxidation/Desorption (TPR/O/D)

Temperature programmed reduction (TPR) and Temperature programmed oxidation (TPO) are the techniques which are highly sensitive and specific for redox property of the catalytically active species under reducing or oxidising conditions. Over past few years these methods have found application in study of both supported and unsupported catalysts.

The reaction between metal oxide MO (M having +2 oxidation state) and hydrogen can be represented by the general equation:

$$\mathrm{MO\,(s) + H_2\,(g) \longrightarrow M\,(s) + H_2O\,(g)} \qquad \text{.....}\mathbf{2.7}$$

The free energy change for the reduction ΔG° is negative for a number of oxides and thus for these oxides the reductions are thermodynamically feasible.

$$\Delta G = \Delta G^\circ + RT\ \log\left(\frac{P_{H_2O}}{P_{H_2}}\right) \qquad \text{.....}\mathbf{2.8}$$

The TPR experimental method is such that the water vapor is constantly swept from the reaction zone as it is formed. Thus, if P_{H_2O} is sufficiently low, at higher temperatures it is possible that the term RT log (P_{H_2O}/P_{H_2}) could be sufficiently negative to nullify a positive ΔG°. Hence, it is possible to obtain TPR profiles for oxides of vanadium, tin and chromium at higher reduction temperatures despite of their positive ΔG° values of 45, 50 and 100 kJ/mol respectively.

The process by which a sphere of metal oxide is reduced in a stream of flowing hydrogen has been explained on the basis of the kinetic studies either by nucleation model or by contracting sphere model [17, 18].

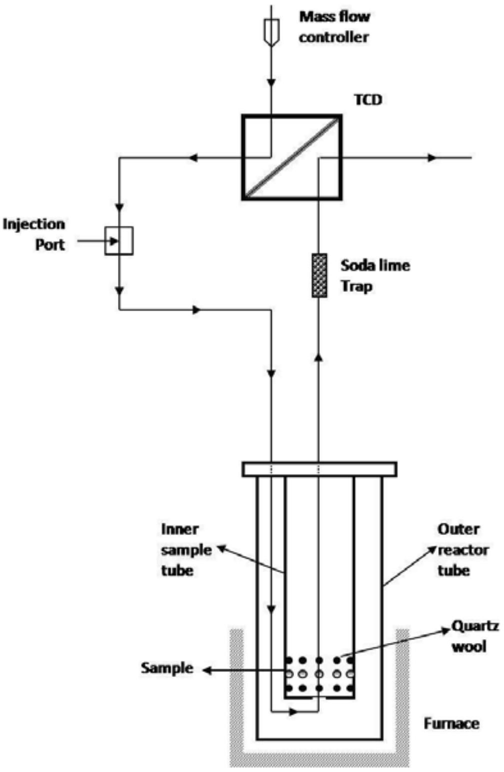

Fig. 2.5. Schematic for the TPDRO – 1100 instrument

The instrument used for TPD/TPR/TPO studies was TPDRO – 1100 of Thermoquest (Italy) make. Fig. 2.5 depicts a typical block diagram of the instrument used. In this instrument analysis is carried out at atmospheric pressure using continuous flow of inert or reactive gases. In a typical TPR experiment the sample is placed in the inner quartz reactor of a quartz reactor system which constitutes of two concentric tubes as shown in Fig. 2.5. Before start of actual analysis the sample is first pretreated under helium flow at 350 °C for 2 h. The reduction profile of the sample is thereafter recorded (cooling the sample after pre-treatment) by heating the sample at a fixed rate under the controlled flow of reactive gas mixture, i.e. 5% H_2 in Argon. A thermal conductivity detector (TCD) is employed to monitor the change in composition of reactive gas mixture with time or temperature ramp. Initially when the temperature and no reduction occur a steady baseline is obtained. As the reduction process begins the hydrogen concentration in effluent stream decreases and this change is recorded by TCD. The water formed during reduction process is removed from the flowing gas with the help of a soda lime trap (shown in Fig. 2.5) placed before the detector. Hence the signal obtained is primarily due to change in thermal conductivity of the flowing gas due to the consumption of hydrogen in the reduction phenomenon. The plot is generally intensity or signal in the TCD with respect to temperature. Peaks are observed in the plot due to the reduction process and the maxima of the peak correspond to the temperature at which maximum reduction takes place. The sample is cooled after completion of the analysis. This reduced sample can be removed for subsequent XRD analysis, in order to identify the reduced product. Alternatively, these samples can be used again for recording of a TPO profile. This facilitates the monitoring of the redox process in a particular sample. More than one TPR/TPO band is observed in case of a sample containing more than one kind of reducible species.

Redox behavior and reproducibility of the oxide samples viz, Fe_2O_3, Cr doped Fe_2O_3, spinel ferrites, indium titanates towards repeated reduction oxidation cycles was studied by recording temperature programmed reduction/oxidation (TPR/TPO) profiles on a TPDRO-1100 analyzer (Thermo Quest, Italy) under the flow of H_2 (5%) + Ar, alternatively, O_2 (5%) + He gas mixtures at a flow rate of 20 ml min^{-1}, in temperature range of 25-1000°C for TPR and up to 800°C for TPO at a heating rate of 6°C min^{-1}. The samples were pretreated at 350°C for about 2.5 h in helium, prior to recording of the first TPR run.

The O_2-TPD experiments for some catalyst oxides e.g. Fe_2O_3, Cr doped Fe_2O_3, spinel ferrites were also carried out on the TPDRO-1100 analyzer (Thermo Quest, Italy) instrument under the flow of carrier gas He at a flow rate of 20 ml min^{-1}, in temperature range of 150°-1000° C and at a heating rate of 10° C min^{-1}. The samples were pretreated at 350°C for about 2.5 h in helium, prior to recording of each TPD run.

2.3.7 X-Ray Photoelectron Spectroscopy (XPS)

X-ray photoelectron spectroscopy (XPS) is a semi-quantitative spectroscopic technique that measures the elemental composition, empirical formula, chemical state and electronic state (oxidation state) of the elements that exist within a material. XPS spectra are obtained by irradiating a material with a beam of aluminium or magnesium X-rays while simultaneously measuring the kinetic energy (KE) and number of electrons that escape from the top 1 to 10 nm of the material being analyzed. XPS requires ultra-high vacuum (UHV) conditions. XPS is also known as ESCA, an abbreviation for Electron Spectroscopy for Chemical Analysis. XPS detects all elements with an atomic number (Z) of 3 (lithium) and above. This limitation means that it cannot detect hydrogen (Z=1) or helium (Z=2).

A typical XPS spectrum is a plot of the number of electrons detected (Y-axis) versus the binding energy of the electrons detected (X-axis). Each element produces a characteristic set of XPS peaks at characteristic binding energy values that directly identify each element that exist in or on the surface of the material being analyzed. These characteristic peaks correspond to the electron configuration of the electrons within the atoms, e.g., 1s, 2s, 2p, 3s, etc. The number of detected electrons in each of the characteristic peaks is directly related to the amount of element within the area (volume) irradiated. It is important to note that XPS detects only those electrons that have actually escaped into the vacuum of the instrument. The photo-emitted electrons that have escaped into the vacuum of the instrument are those that originated from within the top 10 to 12 nm of the material. All of the deeper photo-emitted electrons, which were generated as the X-rays penetrated 1–5 micrometers of the material, are either recaptured or trapped in various excited states within the material.

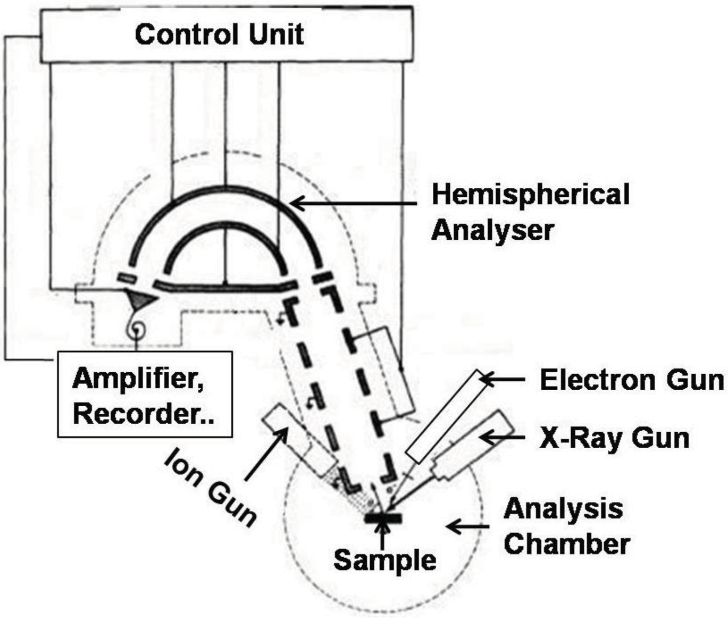

Fig. 2.6. Schematic of a XPS instrument

Monochromatic Al Kα X-rays are normally produced by diffracting and focusing a beam of non-monochromatic X-rays off of a thin disc of natural, crystalline quartz. The resulting wavelength is 8.3386 Å which corresponds to a photon energy of 1486.7 eV. The energy width of the monochromated X-rays is 0.16 eV, but the common electron energy analyzer (spectrometer) produces an ultimate energy resolution on the order of 0.25 eV which, in effect, is the ultimate energy resolution of most commercial systems. When working under practical conditions, high energy resolution settings will produce peak widths (FWHM) between 0.4-0.6 eV for various pure elements and some compounds. Non-monochromatic magnesium X-rays have a wavelength of 9.89 Å which corresponds to photon energy of 1253 eV. The energy width of the non-monochromated X-ray is roughly 0.70 eV, which, in effect is the ultimate energy resolution of a system using non-monochromatic X-rays. Non-monochromatic X-ray sources do not use any crystals to diffract the X-rays which allow all primary X-rays lines and the full range of high energy Bremsstrahlung X-rays (1–12 keV) to reach the surface.

A Thermo VG Clamp2 Analyzer based spectrometer using a radiation source of Mg Kα radiation was used to analyse the oxidation state of iron, oxygen and any sulphur present the surface of the fresh and spent Fe_2O_3 catalyst used for sulphuric acid decomposition reaction for 100h (Chapter 5).

2.3.8 Gas Chromatograph

A gas chromatograph is used for separation and quantification (with respect to a standard) of individual gases in a gaseous mixture. A gas chromatograph schematically shown in Fig. 2.9, uses a flow-through narrow tube known as the column, through which different chemical constituents of a sample pass in a gas stream (carrier gas, mobile phase) at different rates depending on their various chemical and physical properties and their interaction with a specific column filling, called the stationary phase. As the chemicals exit the end of the column, they are detected and quantified. The function of the stationary phase in the column is to separate different components, causing each one to exit the column at a different time on the basis of variable retention time. The carrier gas flow rate and the temperature can be suitably used to alter the order or time of retention.

In a GC analysis, a known volume of gaseous sample is injected into the injection port at the beginning of the column, usually using a syringe. As the carrier gas sweeps the analyte molecules through the column, the motion is inhibited by the adsorption of the analyte molecules either onto the column walls or onto packing materials in the column. The rate at which the molecules progress along the column depends on the strength of adsorption, which in turn depends on the extent of interaction between the molecule and on the stationary phase materials. Since each type of molecule has a different extent of interaction consequently a the rate of progression varies and thus, the various components of the analyte mixture are separated as they progress along the column and reach the end of the column at different times (retention time). A detector is used to monitor the outlet stream from the column determing both the time and amount of each component reaching the outlet.

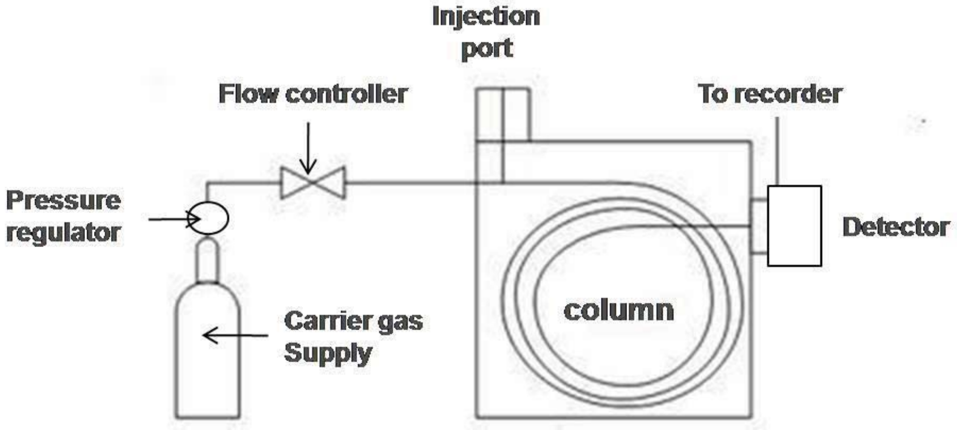

Fig. 2.7. Schematic of a typical Gas Chromatogram (GC)

The choice of carrier gas (*mobile phase*) and column material (stationary phase) both are important. The carrier gas should generally be inert to both the column bed material and the gases to be detected. Helium is inert and works with a greater number of detectors and is generally used as the carrier gas. The choice of carrier gas is vital from the point of view of detection in the thermal conductivity detector(TCD). In TCD the individual gases are detected based on the difference in thermal conductivity between the carrier gas and the individual gas. In case when we have to detect hydrogen (in case of photocatalysis) argon is used as a carrier gas as the thermal conductivity of helium and hydrogen are almost the same and so hydrogen cannot be detected in helium. The choice of material of the column or stationary phase is also important. Hydrogen is separated and detected in molecular sieve column while SO_2 in porapak.

A number of detectors are used in gas chromatography. The most common are the flame ionization detector (FID) and the thermal conductivity detector (TCD) that are used here. Both are sensitive to a wide range of components, and both work over a wide range of concentrations. While TCDs are essentially universal and can be used to detect any component other than the carrier gas (as long as their thermal conductivities are different from that of the carrier gas, at detector temperature), FIDs are sensitive primarily to hydrocarbons, and are more sensitive to them than TCD. However, an FID cannot detect water. Both detectors are also quite robust. Since TCD is non-destructive, it can be operated in-series before an FID (destructive), thus providing complementary detection of the same analytes. A gas chromatograph, (Netel Michro 9100, India) equipped with column Porapak-Q and with dual thermal conductivity and flame ionization detectors, was employed in temperature programming mode. Apart from that the reaction products were also analyzed over a period of about 3-5 h, at 30 to 45 minutes intervals. The reaction product in photocatalysis i.e. H_2 was analysed after every 2 h for a period of ~ 6-8 h using a gas chromatograph (Netel (Michro-1100), India) equipped with a thermal conductivity detector (TCD), molecular sieve column (4m length) with argon as carrier and it was employed in the isothermal temperature mode at 50°C oven temperature. For analysis of SO_2, the above mentioned gas chromatograph, which was also equipped with Porapak-Q (2 m length) column with thermal conductivity detector, was employed in programmed oven temperature mode (2 min hold at 80°C and then ramp at 20 °C to 200 °C and held for 5 mins at 200 °C).

2.3.9 Diffuse Reflectance Ultra Violet-Visible (DRUV-Vis) Spectroscopy

Ultraviolet (200-400 nm) and visible (400-800 nm) radiation are found towards the short wavelength, which lies between the X-rays and IR radiation of electromagnetic spectrum. Fig. 2.8 shows the whole electromagnetic spectrum. ΔE is defined as the difference in energy between an occupied orbital (ground state) and an empty (excited state) orbital. When the energy of the incoming photon matches ΔE, the photon is absorbed, and an electron from an occupied level is excited from its ground state to an empty excited state. This is an electronic transition and occurs in the UV-visible region of the electromagnetic spectrum [13, 19]. In general, this transition will occur between the highest occupied molecular orbital (HOMO) to the lowest unoccupied molecular orbital (LUMO).

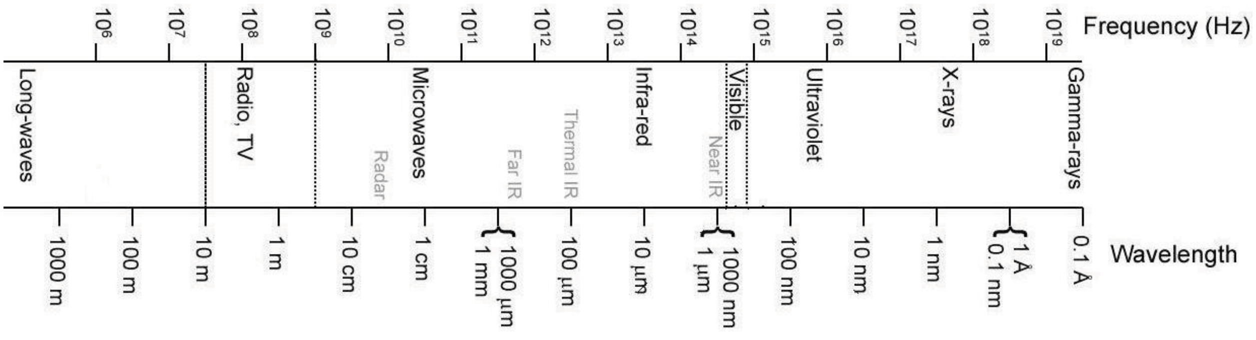

Fig. 2.8. The Electromagnetic Spectrum. Short wavelength corresponds to high frequency and high energy.

UV-Vis spectra tend to be broad in nature due to the fact that vibrational and rotational levels of the molecular orbitals are superimposed upon the electronic levels as shown in Fig.2.9. This broad nature makes their usefulness in identifying materials limited, but the technique is ideal for quantitative analysis of species in solution media.

In UV-Vis reflectance spectroscopy of solids (shown in Fig. 2.10) two types of reflection are encountered: specular or mirror like in which the angles of incidence and angle of reflection are identical and diffuse which is reflection from a matte structure – and this one serves the basis of reflectance spectroscopy [13]. It is an effective way for obtaining the UV-visible spectra directly on powdered sample resulting from scattering, transmission and absorption interactions. Reflectance is given by: Reflectance (%) = I_s/I_r x 100, where I_s is the intensity of the reflected beam and Ir the intensity of a reference standard usually barium sulphate. It is ideal for characterizing optical and electronic properties of many different materials such as ceramic powders, films, pigments etc.

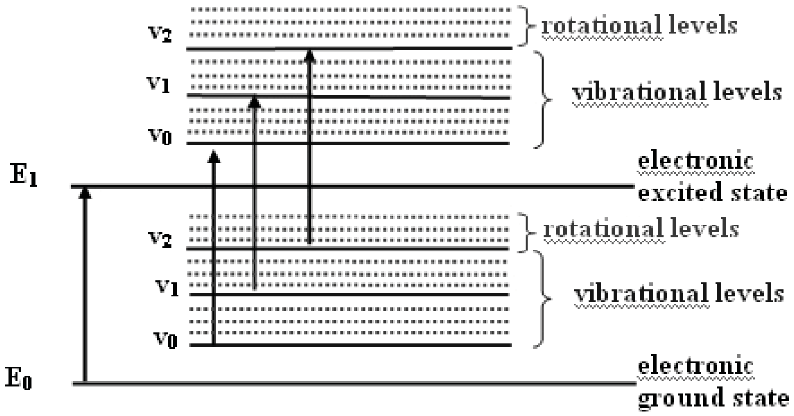

Fig. 2.9. Vibrational and rotational levels are superimposed on the electronic levels

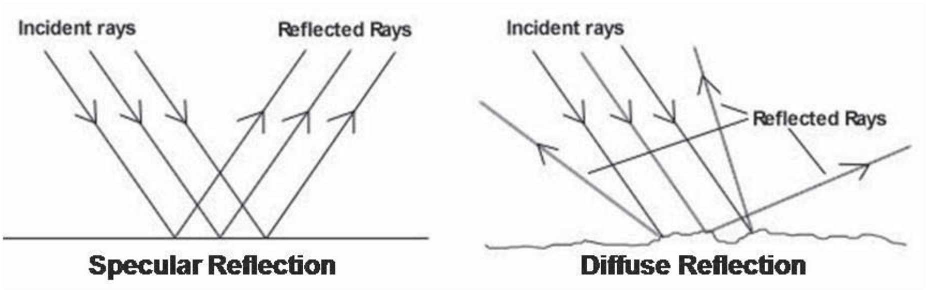

Fig. 2.10. Specular reflection on mirror like surface and diffuse reflection from a matte surface

Diffuse Reflectance UV-Vis Spectroscopy involves numerous light-sample interactions. Spectra may exhibit features associated with the transmission and/or reflection (external and/or internal) of UV-Vis radiation. Diffuse reflectance spectra of the semiconducting indium titanate oxides were recorded on a UV-visible spectrometer (JASCO model V-530 spectrophotometer). The light absorption characteristics of all the photocatalysts that have been prepared have been analysed by DRUV as it has a direct impact on the photocatalytic properties of the material. The DRUV spectra of all the indium titanate photocatalyst have been recorded and analysed in chapter 7 and 8.

2.3.10 Mossbauer Spectroscopy

The phenomenon of recoilless emission and resonance absorption of γ-rays by identical nuclei bound in solid is known as Mössbauer effect. Rudolph Mössbauer first discovered 'Mössbauer Effect' in 1957 in ^{191}Ir and received the Nobel Prize in Physics in 1961 for his work. What Mössbauer discovered is that when the atoms are within a *solid matrix* the effective mass of the nucleus is very much greater. The recoiling mass is now effectively the mass of the whole system, so if the gamma-ray energy is small enough the recoil of the nucleus is too low to be transmitted as a phonon (vibration in the crystal lattice) and so the whole system recoils, making the recoil energy practically zero: a *recoil-free event*. The relative number of recoil-free events (and hence the strength of the signal) is strongly dependent upon the gamma-ray energy and so the Mössbauer effect is only detected in isotopes with very low lying excited states. Similarly the resolution is dependent upon the lifetime of the excited state. These two factors limit the number of isotopes that can be used successfully for Mössbauer spectroscopy. The most used is ^{57}Fe, which has both a very low energy gamma-ray and long-lived excited state, matching both requirements well. Fig. 2.11 shows a simple Mössbauer spectrum from identical source and absorber.

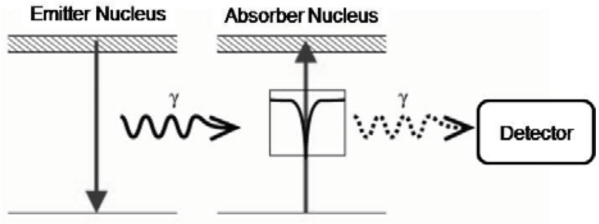

Fig. 2.11. Simple Mössbauer spectrum from identical source and absorber

Isomer shift arises due to different chemical environments at the emitting and absorbing nuclei. The isomer shift arises due to the non-zero volume of the nucleus and the electron charge density due to s-electrons within it. This leads to a monopole (Coulomb) interaction, altering the nuclear energy levels. Any difference in the s-electron environment between the source and absorber thus produces a shift in the resonance energy of the transition. This shifts the whole spectrum positively or negatively depending upon the s-electron density, and sets the centroid of the spectrum. As the shift cannot be measured directly it is quoted relative to a known absorber. For example ^{57}Fe Mössbauer spectra will often be quoted relative to alpha-iron at room temperature.

$$IS = \delta = \frac{4\pi}{5} Ze^2 R^2 \frac{\Delta R}{R}\left[|\Psi(0)|^2_{abs} - |\Psi(0)|^2_{sou} \right]$$

Here Ze is the positive charge of the nucleus, the term ΔR/R is the fractional change in the nuclear charge radius on the excitation and ΔR is the difference in the radii of the nuclear exited and ground states.

The isomer shift is useful for determining valency states, ligand bonding states, electron shielding and the electron drawing power of electronegative groups. For example, the electron configurations for Fe^{2+} and Fe^{3+} are $(3d)^6$ and $(3d)^5$ respectively. The ferrous ions have less s-electrons at the nucleus due to the greater screening of the d-electrons. Thus ferrous ions have larger positive isomer shifts than ferric ions. Even equivalent sites with different number of hydrogen neighbours and geometrical arrangements could be distinguished by their different IS values.

Nuclei in states with an angular momentum quantum number I>1/2 have a non-spherical charge distribution. This produces a nuclear quadrupole moment. In the presence of an asymmetrical electric field (produced by an asymmetric electronic charge distribution or ligand arrangement) this splits the nuclear energy levels.

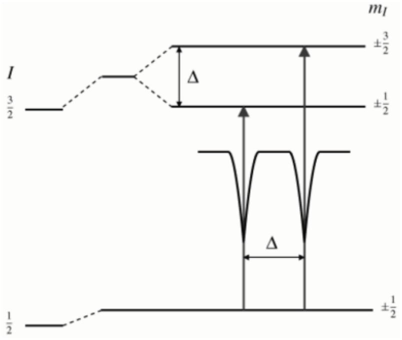

Fig 2.12. Quadrupole splitting for a 3/2 to 1/2 transition

In the case of an isotope with a I=3/2 excited state, such as ^{57}Fe or ^{119}Sn, the excited state is split into two substates $m_I=\pm1/2$ and $m_I=\pm3/2$. This is shown in Fig 2.12, giving a two line spectrum or 'doublet'. The extent of the splitting depends on the electron charge asymmetry. For ^{57}Fe the magnitude of the quadrupole splitting is given by

$$QS = \frac{1}{2}(e^2 q_{ZZ} Q)(1+\eta^2/3)^{\frac{1}{2}}$$

where q_{ZZ} is the principal component of the electric field gradient, η is asymmetry parameter = $(q_{ZZ} - q_{YY})/q_{ZZ}$. QS is highly sensitive function of charge state (high spin and low spin) as well as the nearest neighbor environment of the probe atom.

In the presence of a magnetic field the nuclear spin moment experiences a dipolar interaction with the magnetic field which is called as Zeeman splitting. There are many sources of magnetic fields that can be experienced by the nucleus. The total effective magnetic field at the nucleus, H_{eff} is given by:

$$H_{eff} = (H_{contact} + H_{orbital} + H_{dipolar}) + B_{applied}$$

the first three terms being due to the atom's own partially filled electron shells. $H_{contact}$ is due to the spin on those electrons polarising the spin density at the nucleus, $H_{orbital}$ is due to the orbital moment on those electrons, and $H_{dipolar}$ is the dipolar field due to the spin of those electrons.

This magnetic field removes the nuclear degeneracy and splits nuclear levels with a spin of I into (2I+1) substates, so that the m_I levels have energies given by

$$E_{ml} = -g_n \beta_n m_I H_{eff}$$

Where g_n is the electronic g factor or gyromagnetic ratio, β_n is the nuclear Bohr magneton and m_I is the component of nuclear spin I. Transitions between the excited state and ground state can only occur where m_I changes by 0 or 1. This gives six possible transitions for a 3/2 to 1/2 transition, giving a sextet as illustrated in Fig. 2.13, with the line spacing being proportional to H_{eff}.

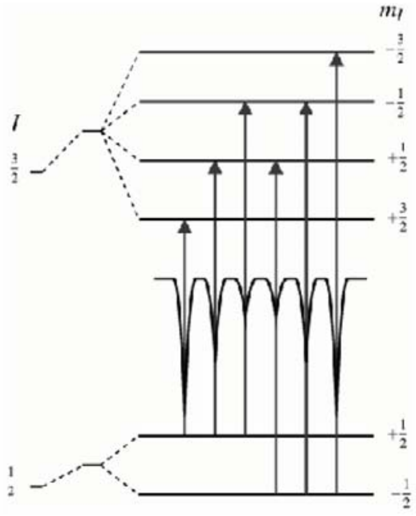

Fig 2.13. Magnetic splitting of the nuclear energy levels

The line positions are related to the splitting of the energy levels, but the line intensities are related to the angle between the Mössbauer gamma-ray and the nuclear spin moment. Thus a purely polycrystalline Fe-metal gives a symmetric six line spectrum (sextet), with intensities in the ratio 3:2:1:1:2:3 and the line separation gives a measure of hyperfine field at the nucleus. These interactions, Isomer Shift, Quadrupole Splitting and Magnetic Splitting, alone or in combination are the primary characteristics of many Mössbauer spectra.

In the present thesis ^{57}Co source embedded in the Rh matrix is used as a monochromatic source of γ-ray. Room temperature ^{57}Fe Mössbauer spectra were recorded using the 14.4 keV gamma ray energy, emitted from ^{57}Fe (produced from ^{57}Co by electron capture process), which is modulated by Doppler motion provided by constant acceleration mode. The spectrometer was calibrated with α-Fe and the isomer shift values given in this work are with respect to α-Fe. The experimental data were fitted by least square curve-fitting program. The Mössbauer spectra were recorded for the spinel ferrites to have a knowledge about the distribution of Fe^{+3} among the octahedral and tetrahedral sites in spinel ferrites (Chapter 4).

2.3.11 Evolved Gas Analysis

To understand the nature of stable species produced on the catalyst during decomposition of sulfuric acid, the spent catalyst samples were heated in the temperature range of 400-1000 °C at a heating rate of 10 °C/min and the evolved gases were analyzed by a QMS coupled to a TG-DTA, (model-SETSYS Evolution-1750, SETARAM). The schematic of the instrument is shown in Fig. 2.14 where it is shown that by coupling a gas analyser to a thermo analyser it is easier to identify the emitted vapors at different temperatures and understand the underlying mechanism. The gas analyzer used was a quadrapule mass spectrometer as shown in Fig. 2.15. An electrical quadruple field is formed between the 4 rods. Ions of varying mass are shot axially into the rod system at approximately equal energy and move through the rod system at uniform velocity. The applied quadrupole field deflects the ions in the X and Y directions, causing them to describe helical trajectories through the mass filter. Ions are separated by the m/e ration in the rod system and then detected at the detector.

Evolved gas analyser hyphenated with a Thermogravimetry set up (model-SETSYS Evolution-1750, SETARAM) was used to identify the gases evolved as the decomposition of the species present on the spent catalysts (used for sulfuric acid decomposition reaction). These thermal studies gave an idea about the relative stability of these species thus helping us in proposing a reaction scheme.

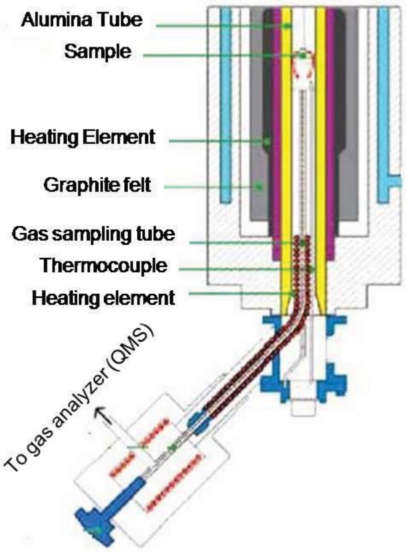

Fig. 2.14. Schematic of the coupling the thermo analyser (SETARAM – SETSYS Evolution-1750) to a gas analyser which is Quadruple Mass Spectrometer (QMS)

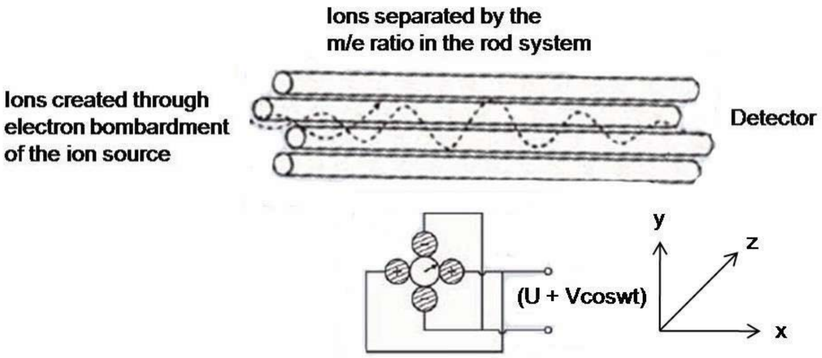

Fig. 2.15. A schematic representation of a quadruple mass analyzer (PFEIFFER Vacuum)

2.4 Catalytic activity evaluation for sulphuric acid decomposition

The catalytic reactors designed and developed for evaluation of catalytic activity for sulfuric acid decomposition are discussed here in details. Work was initiated in a continuous, flow through fixed-bed quartz reactor (30 cm long, 0.8 cm I.D) fabricated in quartz, where 2 g of catalyst was employed. A block diagram as well a photograph of the quartz setup used for the decomposition of H_2SO_4 is shown in Fig. 2.16. Sulfuric acid was kept in a glass cylindrical reservoir. The temperature of this reservoir was increased to ~338 °C and high purity nitrogen was bubbled through boiling sulfuric acid. The flowing nitrogen gas carried the acid vapors over the catalyst bed at a flow rate of 40 ml min^{-1}. To minimize condensation of the acid during its flow to the decomposition furnace from the boiler, the temperature of the in-between region was kept at 330°C. The samples of effluent gases were collected from the sampling port fitted with a septum. Each sample prior to activity measurements was given a pretreatment in N_2 flow for 3 h at 350°C.

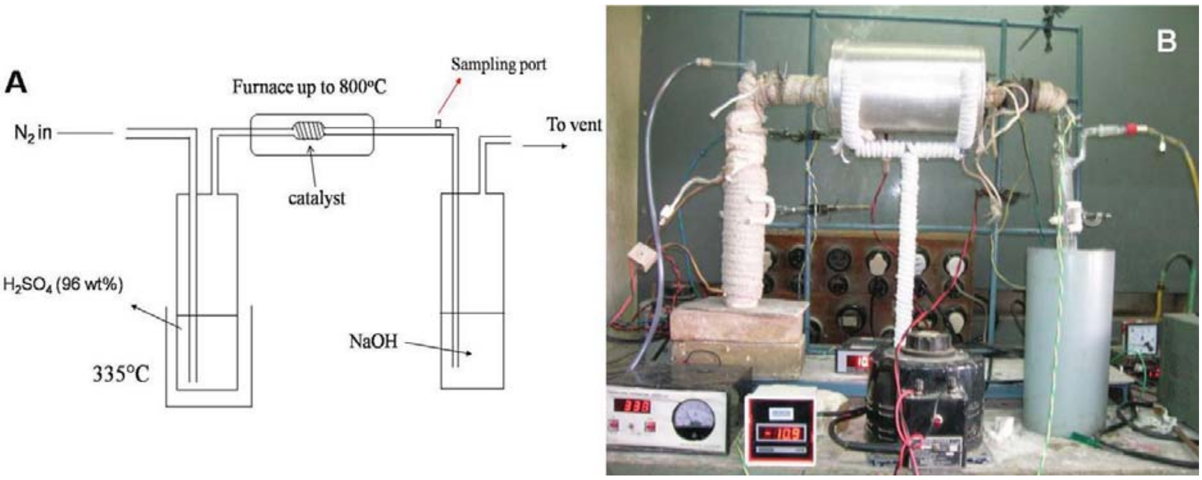

Fig.2.16. (A) Block diagram and (B) actual photograph of the quartz experimental set up developed initially for carrying out sulfuric acid decomposition reaction with 2 g powder catalyst

A gas chromatograph (Netel, model-Michro 9100) equipped with Porapak-Q column and a thermal conductivity detector, was used for the analysis of one of the reaction products SO_2, in programmed mode by injecting 500 μlit of the evolved gas from the outlet stream. A blank run was also performed, in which, acid was made to transfer from the sulfuric acid reservoir to the NaOH bubbler over an empty catalyst bed for 30 minutes at each temperature, in the temperature range of 400 – 800°C under similar conditions as above. The amount of acid collected in the bubbler was measured by titration with standardized NaOH solution, which led to the determination of the feed rate of sulphuric acid into the catalyst reactor. The catalytic activities of Fe_2O_3 and Chromium doped Fe_2O_3 prepared by solid state route was evaluated in this experimental setup and is discussed in chapter 3. But, some condensation of the acid occurred during its flow to the decomposition furnace from the boiler, although the temperature of the in-between region was kept at 330°C. This was rectified and another small scale experimental set up was indigenously developed for carrying out the catalytic activity measurements with 200 mg of the catalyst which also involved a flow through quartz reactor as shown schematically in Fig. 2.17.

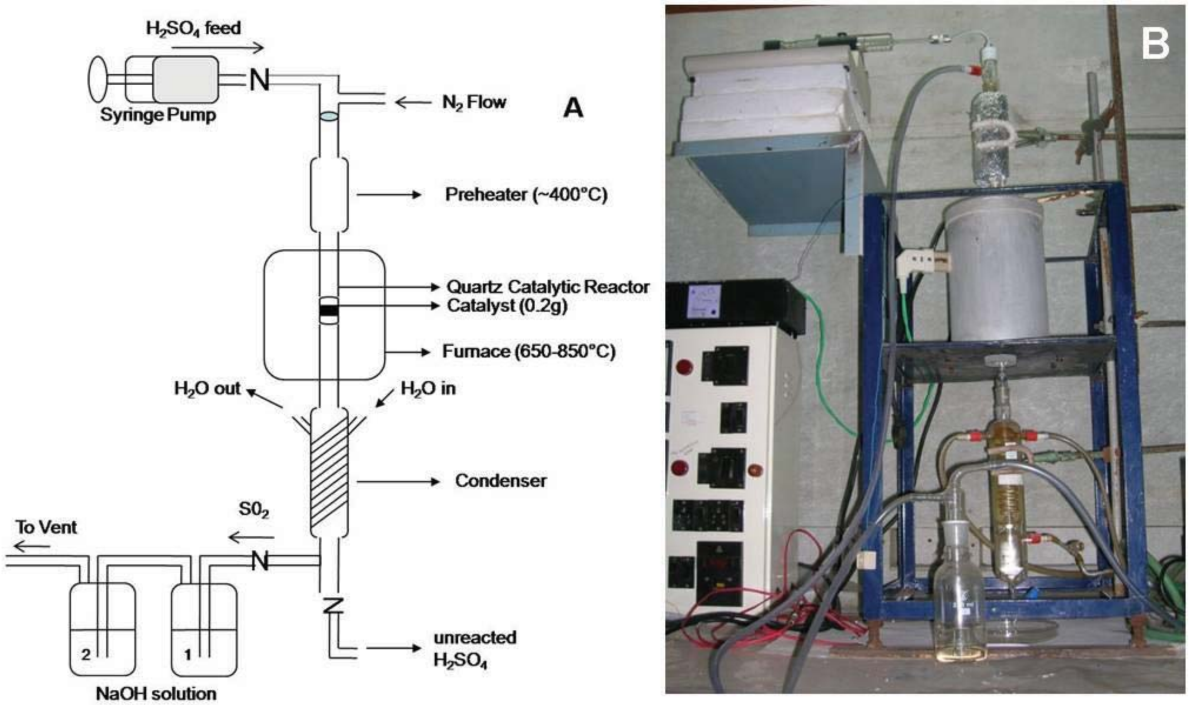

Fig. 2.17. (A) Block diagram and (B) the actual photograph of the small scale quartz experimental set up for carrying out sulfuric acid decomposition reaction with 200 mg powder catalyst

This modified experimental set up for carrying out the catalytic activity measurements involved a flow through quartz reactor as shown both schematically and actual photograph in Fig. 2.17. It was indigenously constructed of glass, quartz and Teflon tubing. A syringe pump, filled with concentrated sulfuric acid (98 wt.%, sp.gr = 1.84) was employed for controlled injection of sulfuric acid into the system and catalytic bed. Provision was made for N_2 to be used as a carrier. The acid pumped by the syringe at a flow rate of 0.05 ml min^{-1} were fed along with the carrier to a pre-heater kept at 400°C (heated by electrical heating tapes) to generate vapors of sulfuric acid. The acid vapors were then led to the catalytic reactor fabricated in quartz and kept inside a controlled electrically heated furnace at high temperature. A condenser was fitted downstream along with a liquid collector with tap. The gaseous products were passed through a NaOH solution and finally vented out. Fig. 2.17A shows the block diagram while Fig. 2.17B shows the actual picture of the experimental set-up for carrying oit sulfuric acid decomposition with 200 mg of powder catalysts.

In a typical experiment, the powder catalyst sample (200 mg) was loaded into the reactor at room temperature and a flow of nitrogen (HP) at a rate of 40 ml min^{-1} was initiated. The furnace temperature was increased to initial reaction temperature of 650 °C over a time interval of 1 h. Concentrated sulfuric acid (98 wt.%) was then pumped into the system (27.6 g acid g^{-1} h^{-1}) by syringe pump and it was carried by the carrier to the pre-heater, where the acid vaporized and then finally decomposed to SO_2, O_2 and H_2O over the catalyst bed. The unreacted SO_3 recombined with H_2O in the condenser downstream (the reaction between SO_3 and H_2O being spontaneous at room temperature, reverse of eqn. 1.6, Chapter 1) and was collected as a liquid solution. The gaseous products - SO_2 and O_2, along with carrier N_2 along with carrier were then passed through a NaOH solution, where SO_2 was trapped and the other gases vented. Product SO_2 was analyzed by measuring the decrease in concentration of the NaOH solution by titration with standardized sulfuric acid solution. 100 ml of 0.1 N NaOH solution was used to trap the product SO_2 for a 8 mins run. Similarly, the sulfuric acid collected downstream of the reactor (i.e., unreacted sulfuric acid) for the same time interval was determined by chemical titration with standardized NaOH solution. The percentage conversion of sulfuric acid to sulfur dioxide was calculated based on the product yield of SO_2 and is given by, SO_2 yield (%) = (No. of moles of SO_2 at outlet)/(No. of moles of H_2SO_4 at inlet). The catalytic activities were measured in the temperature range of 650 °C to 825 °C with an interval of 50°C and were held at each measuring temperature for 1 h.

Sulphuric acid decomposition reaction tests in an enhanced scale with granular or pellet catalysts were carried out in a quartz reactor with annular configuration as shown in Fig. 2.18. First, the experimental setup was indigenously designed which is shown in Fig.2.18A. The schematic representation is shown in Fig. 2.18B. The whole set-up consists of a sulfuric acid reservoir, a dual tube quartz catalytic reactor, condenser for unreacted sulfuric acid and a trap for analyzing one of the products SO_2. 98 wt.% sulfuric acid was tanked in the reservoir which was kept at a fixed height using an adjustable stand. The level of acid in the reservoir was kept constant throughout the experiments by adding sulfuric acid continuously using a burette. The quartz catalytic reactor consists of dual quartz tubes, with sulfuric acid accumulating at the bottom of the annular region and 20 g of catalyst being loaded at the top of the annular region and held on its position by a perforated quartz disc. The upper level of the acid in the annular zone remains constant as per the height of acid in the reservoir. The acid zone and the catalyst zone were heated separately by a two zone electrically heated furnace the temperature on the profile of the catalyst and the acid region being controlled and measured by thermocouples held on the surface of the quartz reactor. Several temperature profiles on the reactor surface were obtained by setting different temperatures of the acid zone (250 – 325 °C) and catalyst zone (550 – 950 °C). A typical temperature profile on the surface of the reactor on setting the catalyst zone temperature at 550 ° and 950 °C and the acid zone at 200 °C and 350 °C is shown in Fig. 2.18C. As seen from the temperature profile, the region in between the acid zone and catalyst zone acted as a preheater region and that the temperature in this region gradually increased from the acid boiler temperature to the catalytic decomposition temperature, thus minimizing acid condensation. The temperature at the catalyst zone remained almost constant.

To study the time dependent catalytic activity for 100 h, the acid boiler region was heated to temperature of ~ 325 °C and the catalyst region (with 20 g of catalyst pellet loaded) was heated in temperature of 800 °C. By fixing the temperature of the boiler region, an almost constant acid flux of ~ 0.63 ml of liquid sulfuric acid (weight hourly space velocity - WHSV of 3.4 g acid g^{-1} catalyst h^{-1}) was obtained as feed flow. The sulfuric acid accumulated at the annular region of the dual quartz tube, on attaining temperatures near to its boiling point (~ 334 °C), evaporated and reached the catalyst zone passing through the annular area in between the boiling and catalyst zone. In this zone in between the acid and catalyst zone in the annular region of the dual quartz tube, sufficient high temperatures were achieved to dehydrate H_2SO_4 to SO_3 (according to eqn 1.6, Chapter 1). SO_3 then passed through the catalyst bed held at a higher temperature undergoing decomposition (eqn 1.7, Chapter 1). This new design based on dual quartz tube can function as an integrated acid boiler, preheater and decomposer. This concept of a dual tube integrated catalytic reactor has no high temperature connections and so renders it free from acid corrosion and leakage a challenging issue in successful operation of sulfuric acid decomposition reaction [20, 21]. This type of reactors will be particularly useful for coupling with bayonet type heat exchangers, which are employed for high temperature reactions like selective catalytic reduction (SCR) [22, 23], coal gasification [24]. In fact, both theoretical and experimental studies to measure heat exchange efficiencies of bayonet type heat exchangers have being carried out for sulfuric acid decomposition recently by Nagarajan et al [25, 26] and Ma et al [27, 28]. Thus, successful operation of catalytic sulfuric acid decomposition in an integrated acid boiler, preheater and decomposer - dual tube quartz reactor, for more than 100 h in our experiments, will provides deep impetus in extending this concept to large scale catalytic reactor design and fabrication for bench scale demonstration experiments of sulfur based thermochemical cycles.

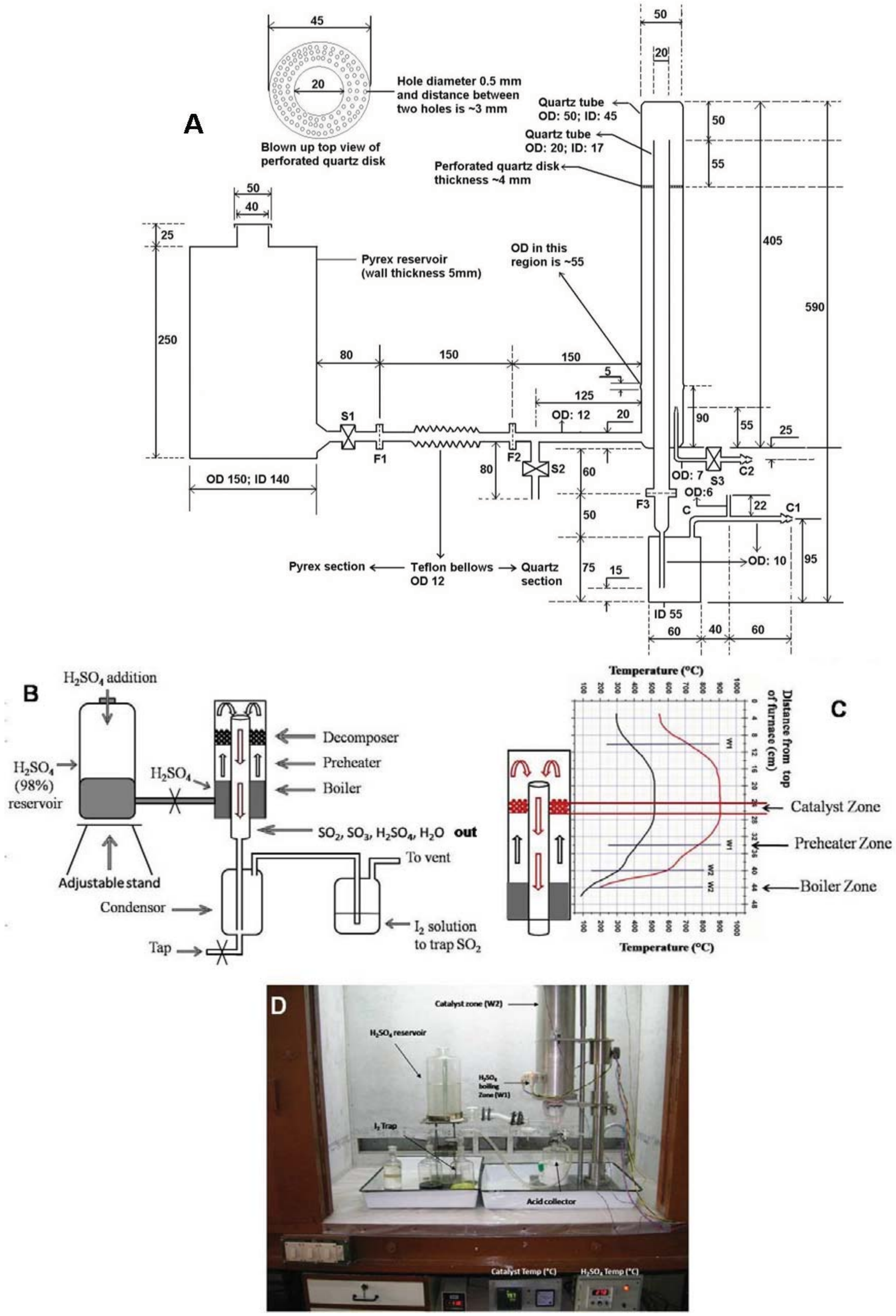

Fig. 2.18. (A) The indigenous design (B) the schematic diagram (C) the temperature profile of the two zone furnace and (D) the actual picture of the enhanced scale quartz experimental

set up for carrying out sulfuric acid decomposition reaction with 20 g granular catalyst. The temperature profile (C) on the surface of the reactor by setting the catalyst zone temperature at 550 ° (black line) and 950 °C (red line) and the acid zone at 200 °C and 350 °C.

During a typical temperature dependent catalytic run, the temperature of the catalyst zone was varied from 725 - 825 °C in step wise increments of 25 °C. The feed composed of sulfuric acid vapors of a constant flux generated by heating the acid boiler region at a constant temperature. The product analysis was done by chemical titrimetric method, the unreacted sulfuric acid being titrated after condensation and one of the products SO_2 was measured by trapping it in I_2 solution. 250 ml of 0.3 (M) I_2 solution was used to trap SO_2 for a 5 min run. Blank experiments in absence of any catalyst verified that homogeneous vapor phase reactions did not occur under these conditions.

In addition to the time dependent and temperature dependent catalytic activity, effect of variation of flux of sulfuric acid on the catalytic activity was also investigated. The sulfuric acid flux was varied by adjusting the temperature of the boiling zone of the integrated reactor. A post reaction ex-situ characterization of the spent catalyst was performed to check any deactivation, poisoning and to predict the most probable mechanism of the acid decomposition.

2.5 The Photoirradiator and photochemical reactors employed for photocatalytic hydrogen generation

Photocatalytic activity for hydrogen generation of indium titanate based oxides was evaluated in a rectangular quartz reactor of dimensions (10 x 2.1 x 2.1 cm^3), equipped with a sampling port provided with a septum through which gas mixture could be removed for analysis. 0.1 g of catalyst was kept in contact with water + methanol mixtures (total volume of 15 ml, 2:1 v/v %) for conducting the photocatalysis experiment. The reactor was then irradiated under water-cooled medium pressure mercury vapour lamp (Hg, Ace Glass Inc., 450W) placed horizontally in a chamber close to the lamp. The schematic of the UV-vis irradiator is shown in Fig. 2.19. The emission spectra of the medium pressure mercury lamp i.e. the light source is shown in Fig. 2.20. The lamp exhibits broad range emission spectra with maxima at both UV and the visible range (16% UV, rest is visible light).

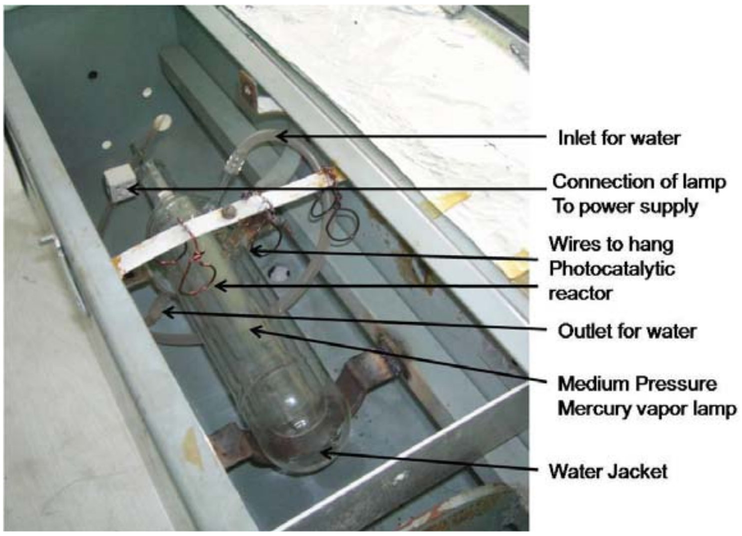

Fig. 2.19. The actual photograph of the UV-Visible Irradiation with housing

Fig. 2.21 displays the typical outer irradiation quartz assembly consisting of photoreactor and the light source along with water circulation jacket for cooling. The reaction products formed inside the photoreactor were analysed by injecting out gaseous samples from the sampling port provided with a septum, after every 2 h for a period of ~ 6-8 h. The analysis of the gaseous products was done using a gas chromatograph Netel (Michro-1100), India) equipped with a thermal conductivity detector (TCD), molecular sieve column (4m length) with argon as carrier and employed in the isothermal temperature mode at 50°C oven temperature.

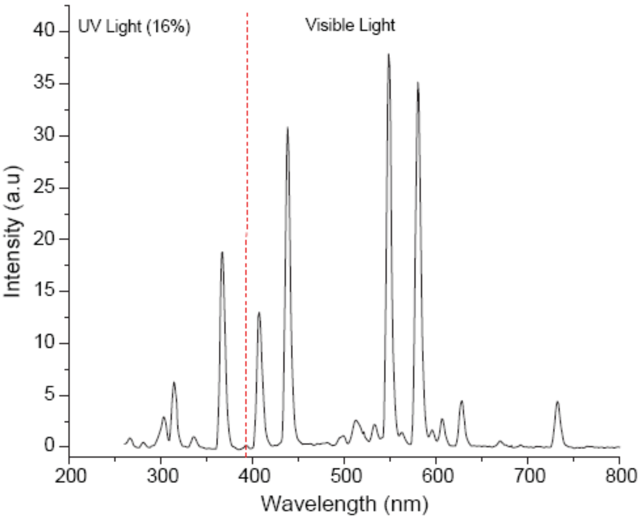

Fig. 2.20. Emission Spectra of the Photo-irradiator Lamp

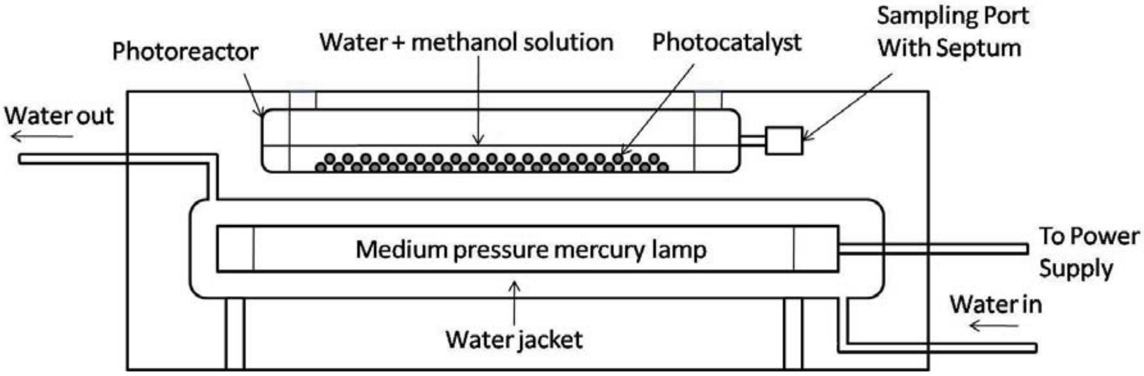

Fig. 2.21. Typical outer irradiation reaction assembly for evaluation of photoactivity of the samples for H_2 generation under UV-vis irradiation with medium pressure mercury lamp

References:

1. A. R. West in Solid state chemistry and its applications, John Wiley and Sons, p. 8, (1984)
2. S. Laurent, D. Forge, M. Port, A. Roch, C. Robic, L. V. Elst, and R. N. Muller, Chem. Rev. 108 (2008) 2064–2110.

3. K. C. Patil, S. T. Aruna, T. Mimani, Current Opinion in Solid State and Materials Science 6 (2002) 507–512.
4. S. R. Jain, K. C. Adiga, and V. R. Pai Verneker Combust. Flame 40 (1981) 71-79.
5. J. Rouxel, M. Tournoux and R. Brec, Mater. Sci. Forum: Soft Chemistry Routes to New Materials, Trans Tech Publication, Basle (1994) Vol. 152-153.
6. B. D. Cullity, "Elements of X-ray diffraction", Addison-Wilson Publishing Comp. Inc., USA (1959).
7. H. P. Klug and L. E. Alexander, "X-ray diffraction procedures", Wiley-Interscience Publication, New York (1974)..
8. L. V. Azaroff and M. J. Buerger, "The Powder Method in X-ray Crystallography", McGraw-Hill Book Comp., New York (1958).
9. WinPLOTR, J Rodrıguez-Carvajal, Laboratorie Leon Brillouin (CEA-CNRS), April 2005 (LLB-LCSIM).
10. S. Brunauer, P. Emmett and E. Teller, J. Amer. Chem. Soc., 60 (1938) 309.
11. R. W. Cahn, P. Haasen and E. J. Kramer, "Material Science and Engineering: Characterisation of Materials", VCH Publisher Inc., New York (1991).
12. D. B. William and C. B. Carter, "Transmission Electron Microscopy", Plenum Press, New York (1996).
13. A. Skoog in Principles of instrumental analysis, 3rd Edition, Saunders Golden Sunburst Series, Orlando, p. 315, (1985).
14. W. F. Pickering in Modern analytical chemistry, Marcel Dekker, Inc., New York, p. 153, (1971).
15. M. Che and A. J. Trench, Advan. Catal., 32 (1983) 2.
16. B. Smith in Infrared spectral interpretation – a systematic approach, CRC Press, Boca Raton, p. 165, (1999)

17. S. D. Robertson, B. D. McNicol, J. H. De Baas, S. C. Kloet and J. W. Jenkins, J. Catal., 37 (1975) 424.
18. T. Uda, T. T. Lin and G. W. Keulks, J. Catal. 62 (1980) 26.
19. Colin N. Banwell and E. M. McCash, Fundamentals of Molecular Spectroscopy, 4th Edition, Tata McGraw Hill Publishing Company Ltd. New Delhi (1995).
20. T. Takai, S. Kubo, T. Nakagiri, Y. Inagak, Int. J. Hydrogen Energy 36 (2011) 4689-4701.
21. N. Sakaba, S. Kasahara, K. Onuki, K. Kunitomi, Int. J. Hydrogen Energy 32 (2007) 4160-4169.
22. F. Castellino, S. B. Rasmussen, A. D. Jensen, J. E. Johnsson, R. Fehrmann, Appl. Catal. B: Environ. 83 (2008) 110–122.
23. Y. Zheng, A. Degn Jensen, J. E. Johnsson, J. R. Thøgersen, Appl. Catal. B: Environ. 83 (2008) 186–194.
24. T. O'Doherty, A. J. Jolly, C. J. Bates, Appl. Therm. Eng. 21 (2001) 1-18
25. V. Nagarajan, V. Ponyavin, Y. Chen, M. E. Vernon, P. Pickard, A. E. Hechanov, Int. J. Hydrogen Energy 33 (2008) 6445 – 6455.
26. V. Nagarajan, V. Ponyavin, Y. Chen, M. E. Vernon, P. Pickard, A. E. Hechanova, Int. J. Hydrogen Energy 34 (2009) 2543 – 2557.
27. T. Ma, M. Zeng, Y. Ji, H. Zhu, Q. Wang, Int. J. Hydrogen Energy 36 (2011) 3757-3768.
28. T. Ma, Yi-tung Chen, M. Zeng, Qiu-wang Wang, Appl. Therm. Eng. (2012), doi: 10.1016/j.applthermaleng.2012.01.032.

Chapter 3

Sulfuric acid decomposition in small scale over iron oxide and chromium doped iron oxide powder catalyst

3.1. Introduction

The catalytic decomposition of sulfuric acid to produce sulfur dioxide, oxygen and water is a topic currently gaining enormous importance as it can serve as thermal to chemical energy conversion step in all the sulfur based thermochemical cycles such as the sulfur–iodine thermochemical cycle [1], the hybrid sulfur cycle [2], and the sulfur–bromine hybrid cycle [3], for successful massive hydrogen production by water splitting. This aspect has been dealt and discussed in details in chapter 1. Thereafter, in chapter 1, we have given a brief review of the activities related to catalyst development for sulfuric acid decomposition that has taken place globally. Sulfuric acid decomposition comprises of the following two reactions in series:

$H_2SO_4\ (g) \rightarrow H_2O\ (g) + SO_3(g);\ \Delta H_0^{298} \sim 97$ kJ/mole .... (1.6)

$SO_3\ (g) \rightarrow SO_2\ (g) + 1/2O_2\ (g);\ \Delta H_0^{298} \sim 99$ kJ/mole …. (1.7)

Sulfuric acid can be decomposed to its anhydride SO_3 (Eqn.1.6) with or without a catalyst above 450 °C, while the decomposition of SO_3 (Eqn.1.7) has been known to be a catalytic reaction and is carried out at higher temperatures of 750-900 °C (Chapter1, section 1.6.1). Apparently only a few and partial kinetic data for the above process of sulfuric acid decomposition can be found in the literature. Both the activity and stability of the catalysts are major issues since sulfuric acid decomposition proceeds with a very slow kinetics, thermodynamically limited and occurs at high temperature (800-850 °C with a thermodynamic conversion of ~ 80 % at 800 °C) and have a very harsh chemical environment (steam, SO_2, SO_3, O_2). Mostly platinum based catalyst have been reported, but major concerns were raised during their use. The high temperature of the reaction causes the metal particles to agglomerate and grow and their overall surface area to decrease and deteriorate the catalytic activity [4]. Loss of active metal due to leaching and oxidation is also reported [5]. Lower cost, better chemical and thermal stability at relatively high temperature and satisfactory catalytic activity of metal oxides make them a valid alternative to noble metal based catalysts. Sulphuric acid decomposition being a very high temperature reaction with extreme harsh chemical environment, metal oxides can be successfully applied as catalysts taking advantage of their chemical and thermal stability. The performance of metal oxides for this reaction was initially investigated by Dokiya et al [6] followed by by Tagawa et al. [7]. However, the order of activity of metal oxides was controversial, since different results (order of activity: Pt ≈ Cr_2O_3> Fe_2O_3> CeO_2> NiO> Al_2O_3) were reported by them.

In recent years, focus on the synthesis of multi-metal oxide systems to fulfill the essential requirement of better chemical, thermal stability and modified catalytic properties has been emphasized. This subject is reviewed in several articles [8-10]. However, attempts towards mixed metal oxide systems for the sulfuric acid decomposition reaction, are very limited and have not been fully explored. The ionic radii of iron and chromium are very similar: 0.067 nm for Fe^{3+} and 0.064 nm for Cr^{3+} and their oxides are isostructural with rhombhohedral crystal structure. The structure of α-Fe_2O_3, α-Cr_2O_3 comprises of a hexagonal close packed array of oxygen ions with Cr and /or Fe ordered on two-thirds of the octahedral interstices giving rise to eight cations in the first neighbor sphere. The present study was taken up with an objective to develop certain Cr substituted Fe_2O_3 -based compositions which may serve as structurally stable and catalytically active materials for the sulfuric acid decomposition reaction. The present chapter reports the changes caused in the structural properties, redox behavior, stability and the catalytic activity of iron oxide - Fe_2O_3, arising due to Cr substitution at Fe-site. The $Fe_{2(1-x)}Cr_{2x}O_3$ (x= 0.0, 0.1, 0.2, 0.8, 0.9, and 1.0) samples were synthesized using solid state reaction. The sample characteristics were monitored by recording powder X-ray diffraction (XRD) patterns, surface area measurements and vibrational spectrums. The stability of substituted and unsubstituted samples towards repeated reduction and oxidation cycles have been monitored by multi temperature-programmed reduction/oxidation (TPR/TPO) cycles. Thermograms (TGA) of metal sulfate were used to explore the mechanistic aspect of sulphuric acid decomposition reaction. The catalytic activity was evaluated for sulfuric acid decomposition at various temperatures in the range of 500-1000°C as a function of Cr– substitution. The products were separated and quantitatively analyzed using gas chromatograph (GC) and were also identified by IR and Mass spectrometry. The unreacted sulfuric acid was analyzed by chemical titrimetric method.

3.2 Experimental

3.2.1 Catalyst preparation

Iron chromium binary mixed oxides ($Fe_{2(1-x)}Cr_{2x}O_3$: $0 \le x \le 1.0$) were synthesized via solid-state route employing AR grade Fe_2O_3 and Cr_2O_3 as starting materials. Samples were calcined initially at 650°C for 36 h and then at 700°C for 36 h with intermittent grinding and pelletization. For, homogeneous reaction, finally the samples were heated at 1000°C for 16 hours. The solid-state reaction involved is:

$$(1-x)\ Fe_2O_3 + x\ Cr_2O_3 = Fe_{2(1-x)}Cr_{2x}O_3 \quad .....(3.3)$$

3.2.2 Catalyst characterization

Powder XRD patterns for the synthesized samples and the used catalyst samples were recorded in 2θ range of 10-70 ° (step width 0.02° and step time 1.25 s) using a Philips X-ray Diffractometer (model 1729) equipped with nickel filtered Cu-K_α radiation. A Quantachrome

Autosorb-1 analyzer was employed for measurement of BET surface area by recording the nitrogen adsorption isotherms. The N_2-BET surface area of all the samples was found to be in range of 14-15 m^2g^{-1}. The FTIR spectra of the solid samples were recorded in KBr using a Jasco FTIR (model 610) in range of 400-4000 cm^{-1} with a resolution of 4 cm^{-1}. Redox behavior and reproducibility of the oxide samples towards repeated reduction oxidation cycles was studied by recording temperature programmed reduction/oxidation (TPR/TPO) profiles on a TPDRO-1100 analyzer (Thermo Quest, Italy) under the flow of H_2 (5%) + Ar, alternatively, O_2 (5%) + He gas mixtures at a flow rate of 20 ml min^{-1}, in temperature range of 25-1000°C for TPR and up to 800°C for TPO at a heating rate of 6°C min^{-1}. The samples were pretreated at 350°C for about 2.5 h in helium, prior to recording of the first TPR run.

3.2.3 Catalytic activity

Catalytic activities of the samples were evaluated for decomposition of sulfuric acid in temperature range of 400 – 800°C using 2 g of catalyst samples (40-80 mesh) in a continuous flow through fixed-bed quartz reactor (30 cm long, 0.8 cm I.D) at a space velocity of 1200 ml $g^{-1}h^{-1}$. A block diagram of the glass setup used for the decomposition of H_2SO_4 is given in fig. 2.16 in chapter 2. A gas chromatograph (Netel, model-Michro 9100) equipped with Porapak-Q column and a thermal conductivity detector, was used for the analysis of one of the reaction products SO_2, in programmed mode by injecting 500 micro-liter of the evolved gas from the outlet stream. A blank run was also performed, in which, acid was made to transfer from the sulfuric acid reservoir to the bubbler over an empty catalyst bed for 30 minutes at each temperature, in the temperature range of 400 – 800 °C under similar conditions as above. The amount of acid collected in the bubbler was measured by titration with standardized NaOH solution, which led to the determination of the feed rate of sulphuric acid into the catalyst reactor. Each catalyst was tested for activity for about 10 hours and then the stability of the catalysts was checked by recording the powder XRD patterns and FTIR spectrum of the used catalysts.

3.2.4 Identification of products by insitu IR and Mass spectrometry

The FTIR spectrum of the evolved gas SO_2 was recorded by introducing 10 ml of the gas from the outlet stream into a 25 ml evacuated gas cell using a Jasco FTIR (model 610). The mass spectrum of the evolved gas was recorded on quadrupole mass spectrometer of make *AngloScientific Instruments*, spectramass (model DAQ-100), U. K for analysis of decomposition product SO_2 gases.

3.3 Results and Discussion

3.3.1 XRD

The compounds α- Fe_2O_3 and α- Cr_2O_3 (mineral names haematite and eskolaite, respectively) are isostructural i.e., they belong to the same space group, having rhombhohedral symmetry R3c (no. 167). The XRD patterns of $Fe_{2(1-x)}Cr_{2x}O_3$ ($0.0 \leq x \leq 1.0$) samples, are shown in Fig. 3.1 as a function of Fe–content.

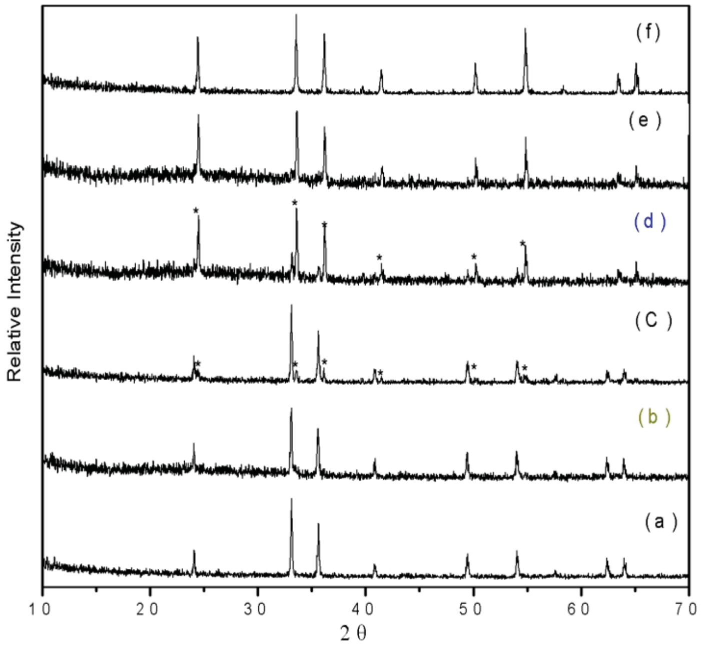

Fig. 3.1. XRD patterns of $Fe_{2(1-x)}Cr_{2x}O_3$; 2x = (a) 0, (b) 0.2, (c) 0.4, (d) 1.6, (e) 1.8 and (f) 2.

**XRD lines due to Cr_2O_3 phase*

The XRD pattern of unsubstituted sample (Fig. 3.1a) matches with the JC-PDS card No. 33-0664 corresponding to Hematite, Fe_2O_3 having lattice parameters a = 0.50356 (1) nm, c = 1.37489(7) nm, cell Vol = 0.30193 nm^3 and z = 6. The other extreme sample with x = 1.0 as represented by curve f matches with the reported XRD pattern of Cr_2O_3, eskolite, with cell parameters a = 0.495876(14) nm, c = 0.35942(7) nm, z = 6 and Vol = 0.28949 nm^3. The $Fe_{1.8}Cr_{0.2}O_3$ depicted by curve b has all lines corresponding to α-Fe_2O_3 phase and similarly Cr rich sample, $Fe_{0.2}Cr_{1.8}O_3$, (curve e), matches well with Cr_2O_3 phase. The additional lines due to other phases are absent. Thus indicating that dopant ion has formed a solution with the host oxide lattice. Thus, substituting either side upto 10% results in formation of solid solutions. The XRD pattern of composition with $Fe_{1.6}Cr_{0.4}O_3$ (curve c), shows close similarity with the pattern in Fig. 3.1a, and weak reflections attributable to a secondary phase (marked as *) are also visible. The intensities of XRD lines due to this secondary phase increased with further increase in Cr content as seen in curve d-f of $Fe_{2(1-x)}Cr_{2x}O_3$ substituted sample. The lines corresponding to secondary phase were identified and attributed to be of Cr_2O_3 phase. Thus Cr/Fe substitution in either oxide beyond 10% has resulted in mixed phases. This indicates that upto 10 % of either substitution, can be tolerated by both the oxide lattices, while further substitution is a mix of both phases. Both Fe^{3+} and Cr^{3+} are transition elements of same valence and ionic radii, still have limited tolerance for each other in their lattice. Thus, the nature of cation, its transport properties and diffusion characteristics play an important role in solid-state reaction.

3.3.2 FTIR

Infrared spectroscopy can be used to monitor chemical and structural changes in the mixed metal oxides. FTIR spectra of starting materials α-Fe_2O_3 and α-Cr_2O_3, and $Fe_{2x}Cr_{2(1-x)}O_3$ samples are shown in Fig 3.2. Table 3.1 shows the characteristic infrared absorption band positions (cm^{-1}) for various samples. The infrared spectrum of haematite has been extensively investigated by many researchers [11-13].

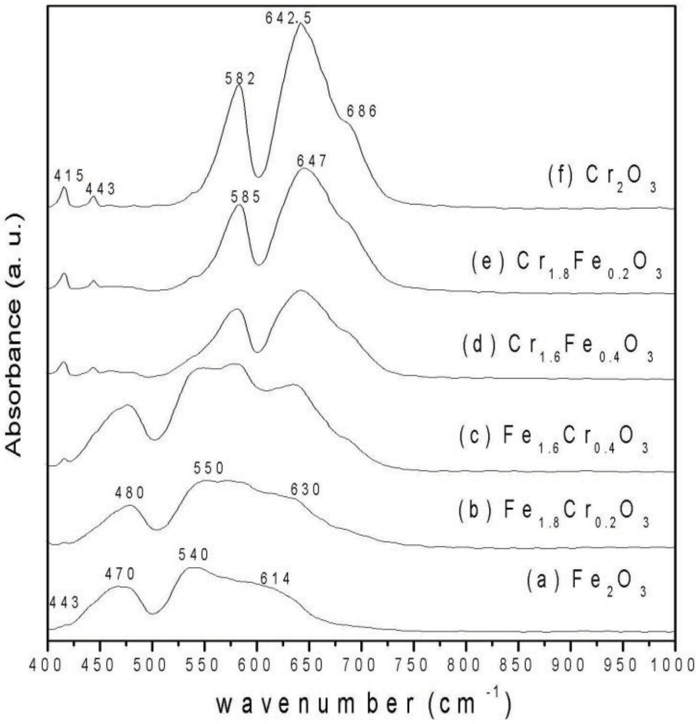

Fig. 3.2. IR spectra of $Fe_{2(1-x)}Cr_{2x}O_3$; 2x = (a) 0, (b) 0.2, (c) 0.4, (d) 1.6, (e) 1.8 and (f) 2

Table 3.1. Positions of the observed vibrational bands

* Bands could not be monitored as IR spectra were recorded in range of 400-4000 cm^{-1}.

Haematite [11, 12]	α-Fe_2O_3 (a)	$Fe_{1.8}Cr_{0.2}O_3$ (b)	$Fe_{1.6}Cr_{0.4}O_3$ (c)	$Fe_{0.4}Cr_{1.6}O_3$ (d)	$Fe_{0.2}Cr_{1.8}O_3$ (e)	α-Cr_2O_3 (f)
230*						
325*						
385*			416	415	415	415
440	443	466	466	443	444	443
470	470	480	478	480		
540	540	550	548	548	538.75	538
			586	586	583	582
			635	642	644	642.5
			683	684	685	686

McDevitt and Baun [11] published the characteristic infrared bands of haematite at 560, 480, 370 and 325cm^{-1}. Schwertmann and Taylor [12] suggested the characteristic bands at 540, 470 and 345 cm^{-1} in the low frequency region can be used as fingerprints in the identification of haematite. Differences in the location of the characteristic infrared bands of natural haematite can be ascribed to the presence of foreign ions in the haematite structure. In the present study the main characteristics of the FT-IR spectrum of Fe_2O_3 were two dominant infrared vibrational bands at 470 and 540 cm^{-1} with a well pronounced shoulder at 614 cm^{-1} and a weak IR band at 443 cm^{-1} as apparent from Table and curve "a" of Fig. 3.2. On the other hand in curve "f" prominent bands corresponding to 415, 443, 582, 642.5 and 686 cm^{-1} which matches with the reported IR spectra of commercial sample of Cr_2O_3 [13]. FTIR spectra of samples with compositions $Fe_{1.8}Cr_{0.2}O_3$ and $Fe_{0.2}Cr_{1.8}O_3$ are shown in curves "b" and "e" of Fig.3.2 which consists of bands exclusively due to Fe_2O_3 and Cr_2O_3 respectively. However, a shift in their IR bands as marked in curve "b' and suggested by Table 3.1 was observed. For instance, the dominant infrared bands at 470 and 540 cm^{-1} are shifted to 480 and 550 cm^{-1} respectively in $Fe_{1.8}Cr_{0.2}O_3$ sample. Also, the band at 550 cm^{-1} in $Fe_{1.8}Cr_{0.2}O_3$ sample was broadened along with shift in the shoulder at 630 cm^{-1} as compared to the original band at 540 cm^{-1} in Fe_2O_3 sample. The shift marks the microstructural defects generated in the structure of the respective oxides as a consequence to Cr/ Fe doping. Thus, IR spectra also support the formation of solid solution up to 20 % of Fe/Cr substitution in either oxide. In case of samples having value of x = 0.4 and 1.6 their IR spectra are shown by curves "c" and "d" in Fig. 3.2. Existence of the mixed phases, in these samples is evident from their IR spectra which consist of overlapping bands arising due to both Fe and Cr oxide phases. Evidently, FT-IR spectra of $Fe_{1.6}Cr_{0.4}O_3$ and $Fe_{0.4}Cr_{1.6}O_3$ sample indicate the transition between the structures (solid solutions) of α-Fe_2O_3 and α-Cr_2O_3, to mixed phases, with spectral characteristics of both the structures. These observations are thus in accordance with the inferences drawn from XRD results pertaining to the crystallographic phases of different compositions.

3.3.3 Temperature Programmed Reduction/Oxidation

Fig. 3.3 presents the reduction behavior of $Fe_{2(1-x)}Cr_{2x}O_{5-\delta}$ samples. As seen in Fig. 3.3 a, the TPR profile of Fe_2O_3 sample comprises of a prominent band with T_{max} at ~470°C and another broad band having T_{max} at ~705°C. The reduction onset temperature of the main band is at 330°C. The presence of two bands suggests the two reduction steps. Since Cr^{3+} is stable towards H_2 atmosphere up to 1000°C, as evident by Fig. 3.3, the reduction profile of these samples is attributed to reduction of $Fe^{3+} \rightarrow Fe^0$ species. It is reported that, the unsubstituted Fe_2O_3 shows three major peaks corresponding to three reduction steps: Fe_2O_3 to Fe_3O_4 at 400°C, Fe_3O_4 to FeO at 600°C and finally FeO to Fe metal at 720°C respectively [14]. In these samples the second and third peaks merge together to give a broad band at ~705°C. The T_{max} for the main band in TPR profiles of all samples are in range of 450-490°C. Earlier reports on other binary systems comprising of Fe/Al_2O_3 and Fe/TiO_2 systems show T_{max} at much higher temperature as compared to these Fe-Cr-O mixed oxide samples. Thus $Fe_{2(1-x)}Cr_{2x}O_3$ is catalytically more viable system as compared to other mixed oxide systems such as Fe-Al-O and Fe-Ti-O [14]. Fig. 3.4 presents the 3-4 successive TPR/TPO profiles recorded for both unsubstituted and substituted viz; Fe_2O_3 and $Fe_{2(1-x)}Cr_{2x}O_3$ samples respectively. Each TPR cycle is followed by a TPO run. In Fe_2O_3, as shown in Fig. 3.4a, the profiles of all four cycles are similar, but the TPR as a whole shifts to a higher temperature range in subsequent cycles.

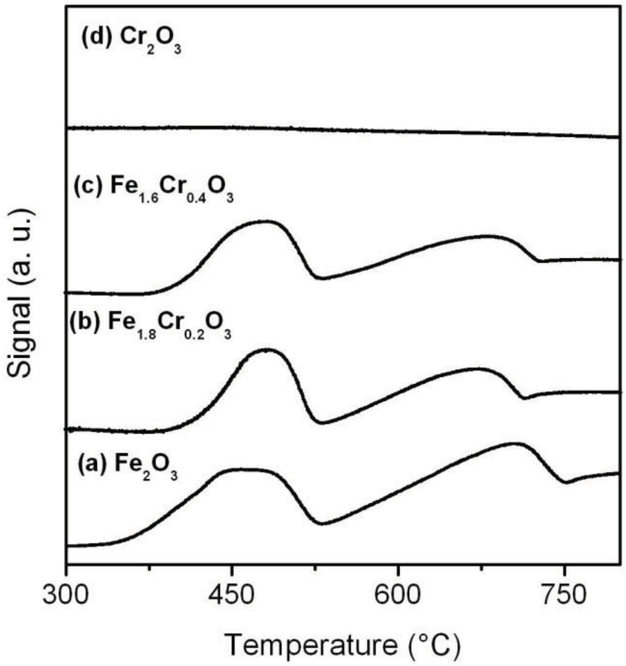

Fig. 3.3. Typical first TPR cycle of various samples

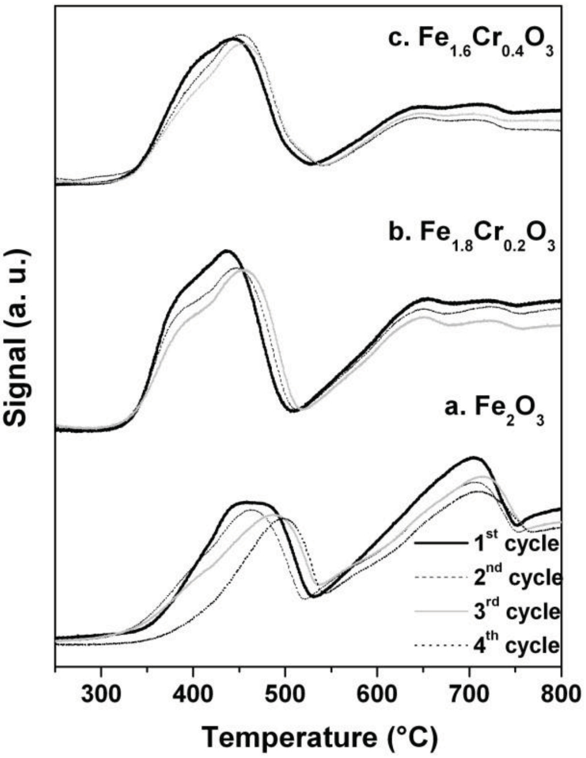

Fig. 3.4. Successive 4-5 TPR cycles of (a) Fe_2O_3 (b) $Fe_{1.8}Cr_{0.2}O_3$ and (b) $Fe_{1.6}Cr_{0.4}O_3$. Each TPR cycle is followed by a TPO run

However 20% substitution (Fig. 3.4 b) has resulted in reproducible behavior towards repeated TPR cycles thus minimizing the sintering effects observed in case of iron oxide,

Fe_2O_3 sample. Also, for consecutive cycles, shift in T_{max} is 12°C in case of $Fe_{1.8}Cr_{0.2}O_3$ in contrast to 50° in case of Fe_2O_3. Simple oxide catalysts faces main drawback of sintering when subjected to repeated cycles of reduction and oxidation and thus for every subsequent cycle the reduction temperature of Fe_2O_3 increases. Therefore, ease with which sample undergoes reduction decreases constantly, in multi cycle application and catalyst performance deteriotes after several cycles. Cr substitution helps in stabilizing active Fe_2O_3 component as evident by Fig. 3.4 (a,b) and minimizes the sintering effects. The multi component systems provide thermal and compositional stability to the oxide catalysts as amply exhibited by the mixed oxides of $Fe_{2(1-x)}Cr_{2x}O_3$. This indicates that every species in substituted sample, which are getting reduced in TPR are regenerated during oxidation cycle (TPO) thus giving rise to reproducible TPR profiles. Thus, Cr^{3+}/Fe^{3+} substitution has not only eased the reduction of simple oxide but also shows enhanced compositional stability towards multiple TPR/TPO cycles, as compared to unsubstituted sample.

3.3.4 Catalytic activity and identification of products using mass and IR spectrometry

The catalytic activities of various samples prepared in this study for the decomposition of sulphuric acid are shown in Fig. 3.5. Both substituted and unsubstituted iron oxide samples were found to be active for decomposition of sulfuric acid in temperature range of 600-800°C. The SO_2 yield, as measured with gas chromatograph increased with rise in temperature; the reaction onset temperature in all samples was ~ 600°C and maximum activity was obtained at ~ 800°C. It is pertinent to mention here that no SO_2 was produced under identical conditions in absence of a catalyst. The activity of catalyst samples was found to be stable upto 10 h run.

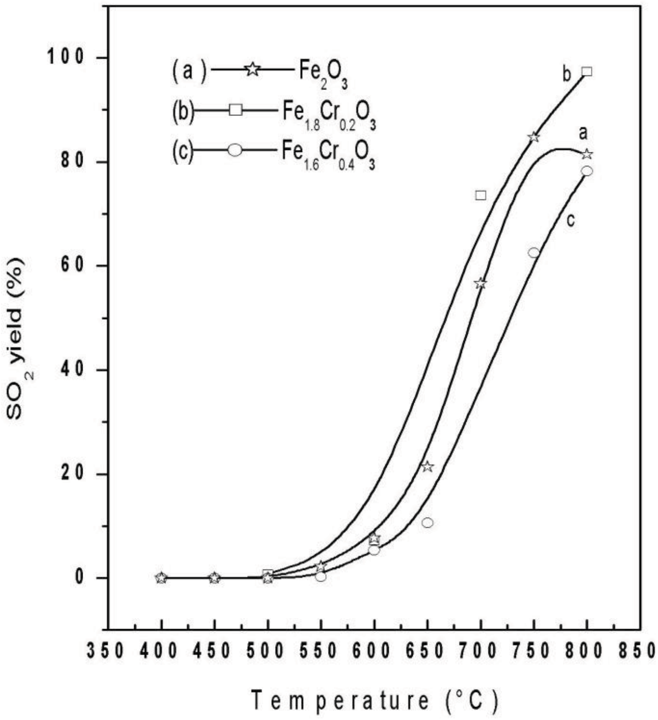

Fig. 3.5. Temperature dependent catalytic activity for decomposition of sulfuric acid reaction using samples: (a) Fe_2O_3, (b) $Fe_{1.8}Cr_{0.2}O_3$ and (c) $Fe_{1.6}Cr_{0.4}O_3$

Mass spectrometry and IR spectroscopy data further substantiated the GC results as shown in figs. 3.6 and 3.7. The intensity vs m/e ratio plot of various components of the gaseous effluents collected from the outlet of the catalytic reactor as a function of reaction temperature are shown in Fig. 3.6. Evidence of maximum yield of SO_2 at reaction temperature of 800°C and onset at 600°C is obtained from Fig. 3.6. Effluent stream at each reaction temperature was also analyzed by FTIR spectroscopy and typical spectra are plotted in Fig. 3.7. The increase in intensity for SO stretching bands in SO_2, with the increase in reaction temperature, in the IR spectrum of evolved gas using Fe_2O_3 as catalyst is shown in Fig. 3.7.

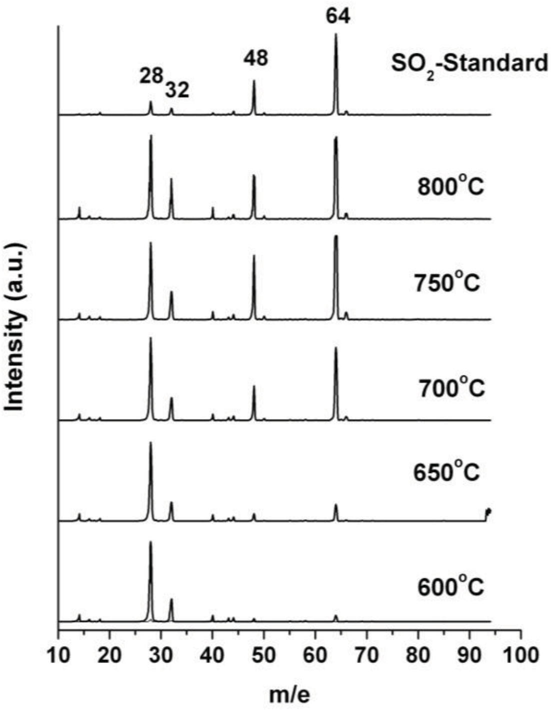

Fig. 3.6. Identification of SO_2 in effluent gases of sulfuric acid decomposition reaction at different reaction temperatures by mass spectrometry.

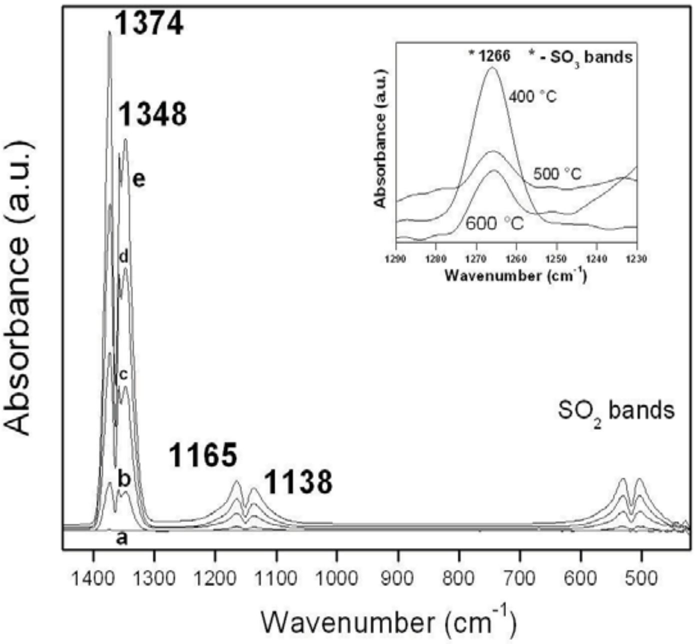

Fig. 3.7. FTIR spectra of effluent gases at different reaction temperatures resulting from sulfuric acid decomposition reaction using Fe_2O_3 catalyst (a) 500°C, (b) 600°C, (c) 650°C, (d) 700°C and (e) 800°C. Inset shows enlarged view of bands due to SO_3 with rise in temperature.

3.3.5 Stability of the oxide samples

Fig. 3.8 compares the XRD patterns of the oxide samples: fresh and spent in the sulfuric acid thermal decomposition reaction. The new lines marked as (*) in the XRD patterns of the used catalysts Fe_2O_3 and $Fe_{1.6}Cr_{0.4}O_3$ can be attributed to the formation of bulk metal sulfates (JCPDS. card No. 47-1774). The FTIR spectra (Fig.3.9) of the used catalysts confirm the formation of sulphate species as new lines appear in the range of 950-1250 cm^{-1}, which can be assigned to SO bond stretching in metal sulphates. Also intensity of bands due to M-O stretching in region of 700-400 cm^{-1} is significantly diminished thus indicating the bulk formation of $M\text{-}SO_4$ species in these samples. However, used sample of composition $Fe_{1.8}Cr_{0.2}O_3$ shows weak lines in the region of 950-1250 cm^{-1}, suggesting metastable formation of sulfate species at the surface of the oxide catalyst. The XRD patterns of the spent and fresh $Fe_{1.8}Cr_{0.2}O_3$ sample are identical as evident from curves c-d in Fig. 3.8. Thus deactivation of $Fe_{1.8}Cr_{0.2}O_3$ catalyst was not observed under the similar conditions as evident from XRD or IR results. Sample with solid solution of 20 % Cr in Fe_2O_3 lattice has not only enhanced reproducibility towards repeated reduction-oxidation cycles but also imparted stability to the oxide catalyst towards sulfuric acid decomposition reaction. As reported the comparison between the thermal analyses of metal sulfates and the activity of the corresponding metal oxides indicates that the metal sulfate formation rate as well as metal sulfate decomposition should be considered as the rate determining step for the SO_3 decomposition [14]. The following metal sulfate formation and decomposition route can be plausible for the SO_3 decomposition on metal oxides: the metal sulfate formation (oxidation: $MO + SO_3 \rightarrow MSO_4$) and the decomposition of metal sulfate ($MSO_4 \rightarrow MO_2 + SO_2$ and reduction: $MO_2 \rightarrow MO + 1/2O_2$). The presence of sulfate species on the used oxide samples such as Fe_2O_3 and $Fe_{1.6}Cr_{0.4}O_3$ supports the above mechanistic aspect.

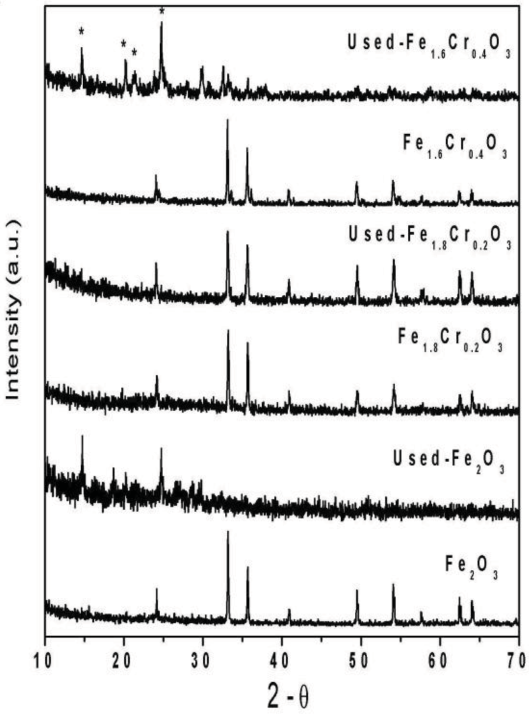

*Fig. 3.8. Powder XRD patterns of Fresh and used samples in catalytic decomposition of sulfuric acid decomposition reaction. * Lines due to $Fe_2(SO_4)_3$.*

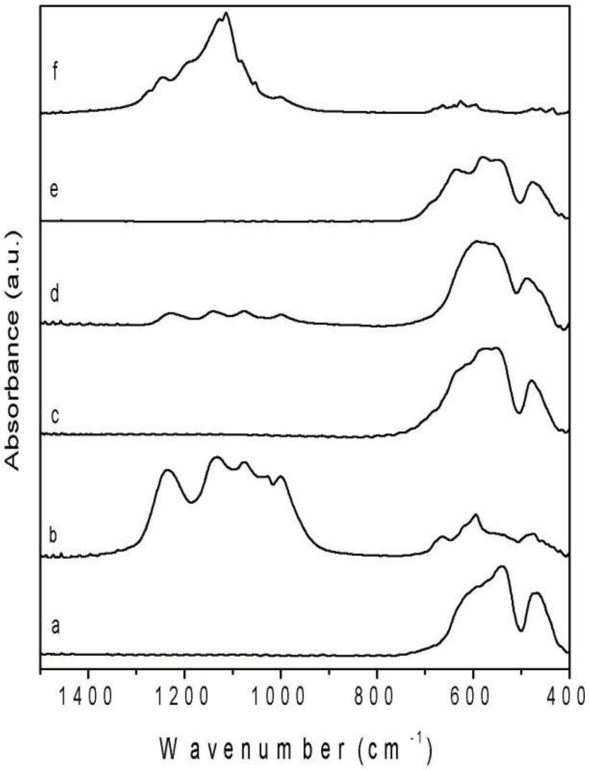

Fig. 3.9. FTIR spectra of fresh (a, c, e) and used (b, d, f) catalyst samples in KBr. (a,b), Fe_2O_3 (c,d) $Fe_{1.8}Cr_{0.2}O_3$ and (e,f) $Fe_{1.6}Cr_{0.4}O_3$.

The catalyst with composition, $Fe_{1.8}Cr_{0.2}O_3$ has regenerated its oxide identity after the reaction and suggests the formation of metastable sulfate species on the oxide surface during the reaction. It is reported that metal sulfate decomposition should be considered as the necessary conditions for the SO_3 decomposition. However, further investigations were required to completely elucidate the catalyst performance under sulfuric acid decomposition conditions and so this aspect have been dealt in great details over Fe_2O_3 and $Fe_{1.8}Cr_{0.2}O_3$ compositions.

3.4 Conclusion

All $Fe_{2(1-x)}Cr_{2x}O_3$ samples facilitated the thermal decomposition of sulfuric acid in temperature range of 550- 800°C much lower as compared to uncatalysed reaction. The maximum conversion was obtained at 800°C with the onset of formation of SO_2 at 600°C. Solid solution of 20 % Cr substitution in Fe_2O_3 lattice enhanced reproducibility towards repeated reduction-oxidation cycles. $Fe_{1.8}Cr_{0.2}O_3$ was found to be promising active and stable mixed oxide catalyst for the above reaction. The amount of SO_2 formed was found to increase with increase in reaction temperature as confirmed from Gas chromatography, FTIR and mass spectrometry. The presence of XRD and IR lines due to sulfate species on the used samples suggests their formation and decomposition as the rate determining step in the mechanism of SO_3-SO_2 conversion on oxides

References

1 J. H. Norman, G. E. Besenbruch, L. C. Brown, D. R. O'Keefe, C. L. Allen, General Atomic Company Report GA-A16713;1982.

2 L. E. Brecher, S. Spewock, C. J. Warde, Int J Hydrogen Energy 2(1) (1977) 7–15.

3 G. E. Beghi, Int J Hydrogen Energy 11(12) (1986) 761–771.

4 D. M. Ginosar, L. M. Petkovic, A. W. Glenn, K. C. Burch, Int. J. Hydrogen Energy 32(4) (2007) 482-488.

5 L. M. Petkovic, D. M. Ginosar, H. W. Rollins, K. C. Burch, P. J. Pinhero, H. H. Farrell, Appl. Catal. A, 338 (2008) 27-36.

6 M. Dokiya, T. Kameyama, K. Fukuda, Y. Kotera, Bull. Chem. Soc. Jpn. 50(10) (1977) 2657-2660.

7 H. Tagawa, T. Endo, Int J Hydrogen Energy 14(1) (1989) 11–17.

8 G. Busca, L. Lietti, G. Ramis, F. Berti, A review, Appl. Catal. B: Environ. 18 (1998) 1.

9 W. Ueda, C. L. Chen, K. Asakawa, Y. Moro-oka and T. Ikawa, J. Catal. 101 (1986) 369.

10 V. C. Belessi, C. N. Costa, T. V. Bakas, T. Anastasiadou, P. J. Pomonis, A. M. Efstathiou, Catal. Today, 59 (2000) 347.

11 N. T. McDevitt, and W. L. Baun, Spectrochim. Acta 20 (1964) 799.

12 U. Schwertmann, R. M. Taylor, Minerals in soil environments (soil science society of America, Inc., Madison, WI, 1977) p. 145.

13 M. Ristic, S. Popovic, S. Music, Materials Letters 16 (1993) 309-312.

14 Tae-Ho Kim, Gyeong-Taek Gong, B. G. Lee, Kwan-Young Lee, Hee-Young Jeon, Chae-Ho Shin, H. Kim, Kwang-Deog Jung, Appl. Catal. A: Gen. 305 (2006) 39-45.

Chapter 4

Sulfuric acid decomposition in small scale over spinel ferrite powder catalyst

4.1. Introduction

The global status and our approach of catalyst selection for sulfuric acid decomposition have been described comprehensively in Chapter 1. The high cost combined with deactivation on prolonged use of noble metal based catalysts, prompted us to investigate mixed oxide based systems which were having better thermal and redox properties and good catalytic activities. The potential of Fe_2O_3 and Cr doped Fe_2O_3 as catalyst for sulfuric acid decomposition was fully evident from the work presented in the preceding chapter. Catalysts with oxy anion of iron, crystallized into different crystal structure like spinels viz; AFe_2O_4 (A= Cu^{2+}, Co^{3+} and Ni^{2+}) were investigated to explore their suitability under harsh reaction conditions. Fe-based spinel oxides offer good thermal stability [1-2] and also interesting catalytic properties in several redox processes e.g. Fischer-Tropsch synthesis [2], CO_2 decomposition [3-4], NO_x decomposition [5], alkylation [6]. These properties of ferrospinels can be utilized in sulfuric acid decomposition which requires a catalyst which is active for the redox process and also stable under the high temperatures and extremely corrosive reactants and products. So, the present study was taken up with an objective to develop certain iron-based inverse spinel compositions which may serve as structurally stable and catalytically active materials for the sulfuric acid decomposition reaction. Three ferrospinels AFe_2O_4; (A = Co, Ni, Cu) were prepared by a gel-combustion technique [7-9] instead of the solid state method employed for the synthesis of iron oxides in chapter 3. Oxides prepared by this method give particles of better morphology and powder properties [10-12]. They were evaluated for sulfuric acid decomposition and the effect of A-site cation on the decomposition kinetics was compared. Also, the structural and surface modifications they undergo due to prolonged reaction with hot sulfuric acid vapors at very high temperatures (750-825 °C) were investigated on spent samples. Finally, we predict a mechanism for the decomposition reaction taking into consideration the characterization of the spent catalyst and draw a relationship between the physicochemical and catalytic properties of the spinel ferrites.

4.2. Experimental section

4.2.1. Preparation Ferrospinels (AFe_2O_4, A = Co, Ni, Cu) were synthesized by the glycine-nitrate gel combustion method. The stoichiometric quantities of starting materials, viz., $Cu(NO_3)_2 \cdot 6H_2O$, $Fe(NO_3)_3 \cdot 9H_2O$, $Ni(NO_3)_2 \cdot 6H_2O$, $Co(NO_3)_2 \cdot 6H_2O$ and glycine (NH_2CH_2COOH), were dissolved in 50 ml of distilled water keeping the fuel-oxidant molar ratio (1:4) so that the ratio of oxidizing to reducing valency is slightly less than unity according to the concept of propellant chemistry [13]. The amounts used for each cases are as: $CuFe_2O_4$: 2.5872 g of $Cu(NO_3)_2 \cdot 6H_2O$ + 8.6531 g of $Fe(NO_3)_3 \cdot 9H_2O$ + 3 g glycine; $NiFe_2O_4$: 2.9554 g of $Ni(NO_3)_2 \cdot 6H_2O$ + 8.2119 g of $Fe(NO_3)_3 \cdot 9H_2O$ + 3 g glycine and $CoFe_2O_4$: 2.9105 g $Cu(NO_3)_2 \cdot 6H_2O$ + 8.0804 g of $Fe(NO_3)_3 \cdot 9H_2O$ + 3 g glycine. The mixed nitrate-glycine solution was then slowly heated at 150 °C, with continuous stirring to remove the excess water. This resulted in the formation of a highly viscous gel (precursor). Subsequently, the gel was heated at 300 °C which led to auto-ignition with the evolution of the undesirable gaseous products, and formation of desired product in the form of foamy powder. Ultimately, the powder was calcined at two different temperatures (500 and 900°C) each for 12 h to obtain well crystalline powders of $CuFe_2O_4$, $CoFe_2O_4$, and $NiFe_2O_4$.

4.2.2. Characterization Powder XRD patterns for the synthesized samples and the spent catalyst samples were recorded in 2θ range of 10-70° (step width 0.02° and step time 1.25 s) using a Philips X-ray Diffractometer (model 1729) equipped with nickel filtered Cu-K_α radiation. A Quantachrome Autosorb-1 analyzer was employed for measurement of BET surface area by recording the nitrogen adsorption isotherms. The FTIR spectra of the solid samples were recorded in KBr disk using a Jasco FTIR (model 610) in range of 400-4000 cm^{-1} with a resolution of 4 cm^{-1}. Redox behavior of the oxide sample towards reduction oxidation cycles was studied by recording temperature programmed reduction/oxidation (TPR/TPO) profiles on a TPDRO-1100 analyzer (Thermo Quest, Italy) under the flow of H_2 (5%) + Ar, alternatively, O_2 (5%) + He gas mixtures at a flow rate of 20 ml min^{-1}, in temperature range of 25°-1000° C for TPR and up to 800°C for TPO at a heating rate of 6° C min^{-1}. The samples were pretreated at 350°C for about 2.5 h in helium, prior to recording of the first TPR run. The O_2-TPD experiments were also carried out on the TPDRO-1100 analyzer (Thermo Quest, Italy) instrument under the flow of carrier gas He at a flow rate of 20 ml min^{-1}, in temperature range of 150°-1000° C and at a heating rate of 10° C min^{-1}. The samples were pretreated at 350°C for about 2.5 h in helium, prior to recording of each TPD run. Mössbauer spectra have been obtained using a spectrometer operated in constant acceleration mode in transmission geometry. The source employed is ^{57}Co in Rh matrix of strength 50mCi. The calibration of the velocity scale is done using iron metal foil. The outer line width of calibration spectra was 0.29 mm/s. The Mössbauer data was analyzed using a least square fitting programme. The morphological features were analyzed by a Scanning Electron Microscope (Mirero, Korea, model- AIS2100). Prior to SEM examination, the samples were coated with a thin gold layer (~ 150 Å thick) so as to avoid the problem associated with charging. To understand the nature of stable species produced on the catalyst during decomposition of sulfuric acid, the spent catalyst samples were heated in the temperature range of 400-1000 °C at a heating rate of 10 °C/min and the evolved gases were analyzed by a QMS coupled to a TG-DTA, (model-SETSYS Evolution-1750, SETARAM).

4.2.3 Catalytic activity The experimental set up for carrying out the catalytic activity measurements involved a flow through quartz reactor which has been described and shown schematically in Fig. 2.17 in chapter 2. The actual picture of the setup during operation is also shown. In a typical experiment, the powder catalyst sample (200 mg) was loaded into the catalytic reactor at room temperature and a flow of nitrogen (HP) at a rate of 40 ml min^{-1} was initiated. The catalyst zone furnace temperature was increased to initial reaction temperature of 650 °C over a time interval of 1 h. Concentrated sulfuric acid was then pumped into the system (27.6 g acid g^{-1} h^{-1}) by syringe pump and it was carried by the carrier gas to the pre-heater, where the acid vaporized (~400 °C) and then finally decomposed to SO_2, O_2 and H_2O over the catalyst bed. The unreacted SO_3 recombined with H_2O in the condenser downstream and was collected as a liquid solution. The gaseous SO_2 and O_2 products along with carrier were then passed through a NaOH solution, where SO_2 was trapped and the other gases (O_2 and N_2) were vented. For analysis of product SO_2, the decrease in concentration of the NaOH solution was measured by titration with standardized sulfuric acid solution. Similarly, the sulfuric acid collected downstream of the reactor (i.e., unreacted sulfuric acid) was determined by chemical titration with standardized NaOH solution. The percentage conversion of sulfuric acid to sulfur dioxide was calculated based on the product yield of SO_2. The catalytic activities were measured in the temperature range of 650 °C to 825 °C with an interval of 50°C and were held at each measuring temperature for 1 h. The activity measurements were repeated for 3 times at each temperature and after the final measurement at 825 °C the supply of acid and the electric furnace were switched off. The spent catalytic samples after two such runs were collected and characterized ex situ by FTIR, SEM and evolved gas analysis.

4.3. Results and discussions

The crystallinity of the three ferrospinels $CuFe_2O_4$, $CoFe_2O_4$, $NiFe_2O_4$ prepared by glycine-nitrate gel combustion route and calcined at 800°C are confirmed by the powder XRD patterns shown in Fig. 4.1. The crystallite size as calculated from Scherrer equation and N_2-BET surface area are also listed in Table. 4.1. As shown in the Fig. 4.1 the peak position and relative intensity of all diffraction peaks for all the three samples are in close agreement with the standard diffraction data (JCPDS card no. 34-0425, 22-1086 and 10-0325 for copper, cobalt and nickel ferrite respectively). Copper ferrite crystallizes in tetragonal lattice while nickel and cobalt ferrite exhibits cubic crystal structure.

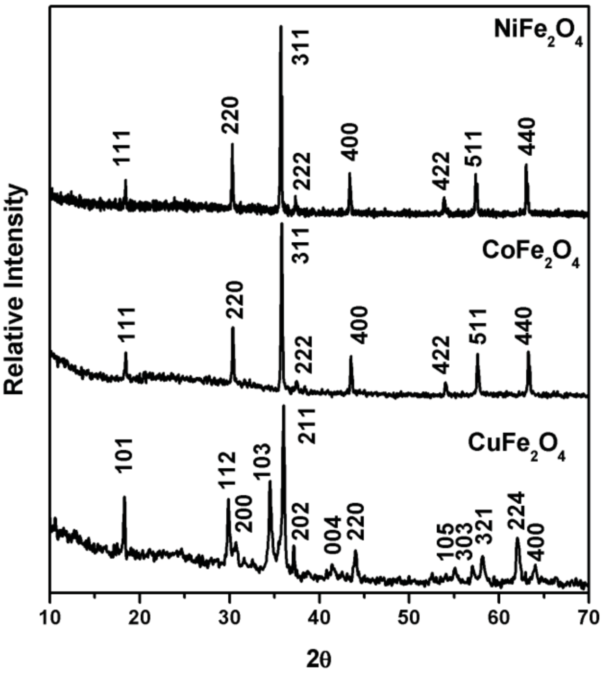

Fig. 4.1. XRD patterns of the ferrospinels prepared by gel combustion route and calcined at 900°C for 12 hrs

Table. 4.1. Crystallite size from Scherrer equation and BET surface area of the catalyst samples

sample	Crystallite size	Surface area
	nm	m^2/g
$CuFe_2O_4$	46.1	0.6
$CoFe_2O_4$	84.6	1.1
$NiFe_2O_4$	84.1	0.4

Mössbauer spectroscopy is an important tool to elucidate various properties of ferritic materials. Room temperature Mössbauer spectra of AFe_2O_4; (A = Co, Ni, Cu) is shown in Fig. 4.2. The Mössbauer spectra of the ferrospinels is fitted with two sextets (Zeeman patterns), corresponding to tetrahedral and octahedral sites, indicating that all three samples have inverse spinel structure and also indicating that samples are ferrimagnetic at the measured temperature. Results derived from Mössbauer spectra recorded at room temperature are given in Table 4.2, which gives the hyperfine values (H_f), isomer shift (δ), quadrupole splitting (Δ), linewidth (Γ) and proportional areas corresponding to tetrahedral and octahedral sites of Fe^{3+} ions in percentage for AFe_2O_4; (A = Co, Ni, Cu). Isomer shift (δ) values for AFe_2O_4; A = Co, Ni, Cu samples are 0.246-0.338 mm/s for tetrahedral (δ_{tet}) and 0.268-0.529 mm/s for octahedral (δ_{oct}) site. These results indicate that Fe is in Fe^{+3} high spin states [14-15]. The sextet which has lower field is related to tetrahedral site and the sextet which having higher field is related to octahedral site [16]. Quadrupole splitting values for AFe_2O_4; A = Co and Ni are nearly zero with respect to α-Fe, showing that Fe^{+3} ions are in cubic symmetry. $CuFe_2O_4$ octahedral site's quadrupole splitting value is 0.166 mm/s, which is comparatively higher and exhibits more distortion. This supports our XRD observations where we observed cubic crystal structure for both nickel and cobalt ferrite while tetragonal lattice was evident for copper ferrite. The magnetic interaction and cation distribution present in these systems influence the room temperature Mössbauer parameters. Mössbauer study confirms the occupancy of octahedral and tetrahedral sites by Fe^{+3} ions in all three samples AFe_2O_4; A = Co, Ni, Cu and so they exhibit the inverse spinel structure. The catalytic properties of ferrospinels crucially depend on the distribution of cations among octahedral and tetrahedral sites of the spinel [17] as only the octahedral sites are exclusively exposed in the crystallites and it is established that these octahedral cations are solely responsible for the catalytic activity [18]. So this determination of relative occupancy of the cations in the two sites by Mössbauer study would be highly imperative in elucidating the catalytic properties of these ferrospinels for sulfuric acid decomposition.

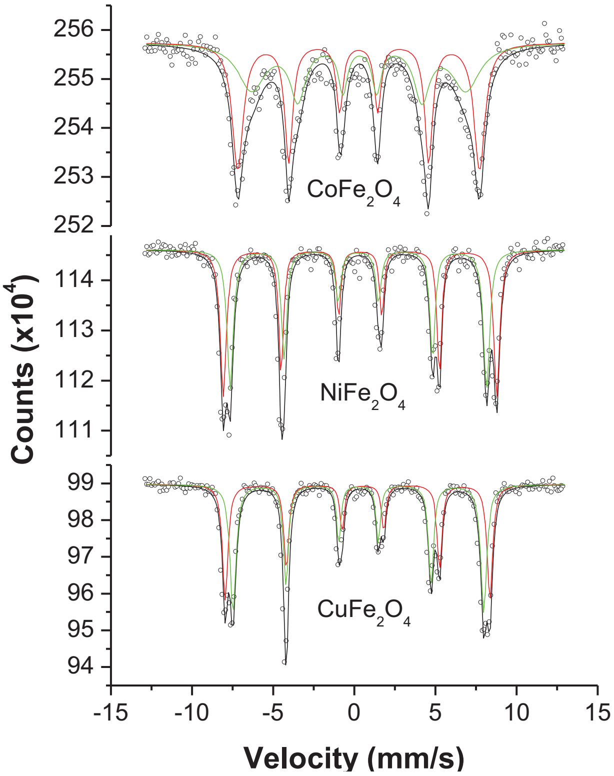

Fig. 4.2. Mossbauer spectra of the ferrospinels prepared by gel combustion route and calcined at 900°C for 12 hrs.

Table. 4.2. The hyperfine field (H_{hf}), isomer shift (δ), quadrupole splitting (Δ), line width (Γ) and areas in percentage of tetrahedral and octahedral sites of Fe^{3+} ions for MFe_2O_4; (M = Co, Ni, Cu) derived from Mössbauer spectra recorded at room temperature.

Sample	Iron sites	Isomer shift (δ)	Quadrupole splitting (ΔE_Q)	Hyperfine field (H_f)	Outer line width (Γ)	Area
		mm/s	mm/s	kG	mm/s	(%)
$CoFe_2O_4$	Sextet1(T)	0.338	0.035	410.5	2.0308	47.6
	Sextet2(O)	0.268	0.001	462.9	0.8217	52.4
$NiFe_2O_4$	Sextet1(T)	0.246	-0.003	490.8	0.4652	49.4
	Sextet2(O)	0.365	0.007	523.6	0.4489	50.6
$CuFe_2O_4$	Sextet1(T)	0.257	0.004	480.1	0.4476	55.0
	Sextet2(O)	0.529	0.166	506.8	0.4058	45.0

Spinels can be described by the general formula AB_2O_4, where A is a bivalent metal cation and B is a trivalent metal cation. The crystal structure consists of a hexagonal closed pack array of oxide ions with A cations occupying the tetrahedral holes and B cations occupying octahedral holes in a normal spinel, which can be represented as $(A^{2+})^{td}[B^{3+}]^{oct}{}_2O_4$. Spinel ferrites like the ones which we have prepared are in general inverse spinels. In inverse spinel the A cation preferably occupies the octahedral sites removing half of the B cations from the tetrahedral sites. So an inverse spinel can be represented in general as $(B^{3+})^{td}[A^{2+}B^{3+}]^{oct}O_4$. These two are extreme cases and in general when spinels are prepared by any soft chemical method an intermediate structure where there is a cationic distribution in between these two extreme structures are obtained. Mössbauer spectroscopy helps in evaluation of this so called degree of inversion of the inverse spinels ferrites. The exact cationic distribution at the tetrahedral and octahedral sites can be evaluated from the area under the curves for the two sextets. Areas in relative percentage in tetrahedral (A) and octahedral (B) sites for cobalt ferrite were evaluated to be 47.6% and 52.4%, respectively. It means the formula of composition will be $(Co^{+2}_{0.04}Fe^{+3}_{0.96})_A[Co^{+2}_{0.96}Fe^{+3}_{1.04}]_BO_4$, where $()_A$ and $[]_B$ indicate the tetrahedral (A) and octahedral (B) sites, respectively. Similarly the cation distribution for $NiFe_2O_4$ and $CuFe_2O_4$ was found to be $(Ni^{+2}_{0.02}Fe^{+3}_{0.98})_A[Ni^{+2}_{0.98}Fe^{+3}_{1.02}]_BO_4$ and $(Cu^{+2}_{0.9}Fe^{+3}_{1.1})_A[Cu^{+2}_{0.1}Fe^{+3}_{0.9}]_BO_4$, respectively. The magnetic interaction and cation distribution present in these systems influence the room temperature Mössbauer parameters.

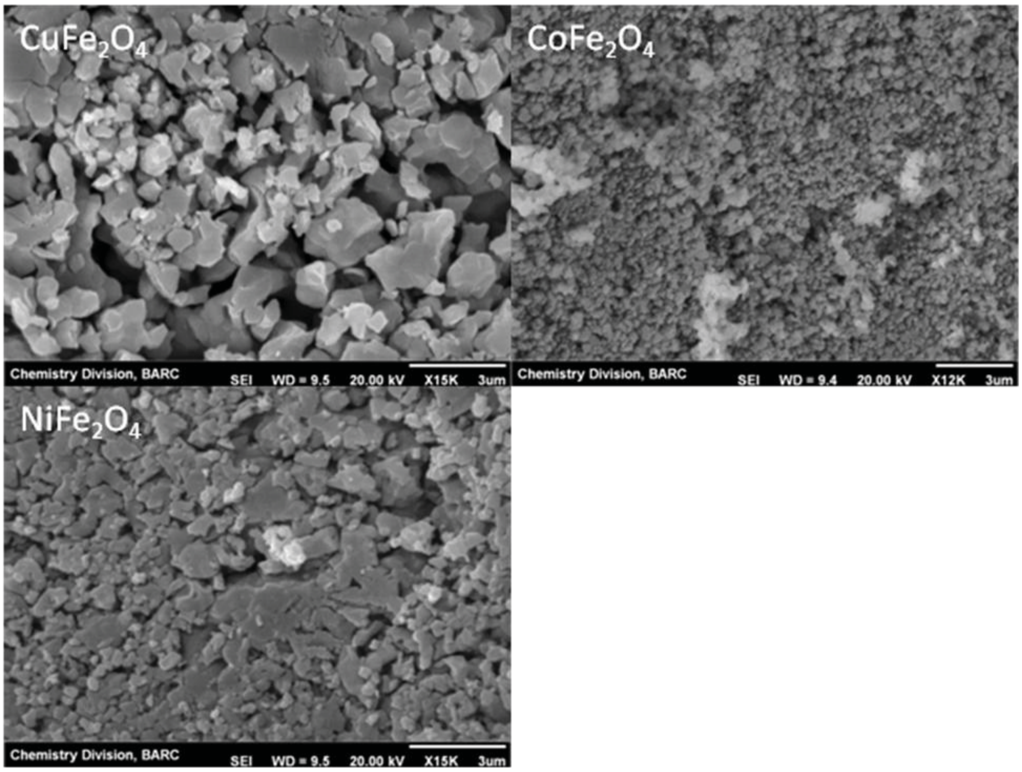

Fig. 4.3 Scanning Electron Micrograph image of the ferrospinel catalysts

Fig. 4.3 shows scanning electron microscope (SEM) images of 900°C-sintered ferrospinels. The images show the particles are well-defined with definite grain boundaries. The samples prepared by gel-combustion are generally porous but with high temperature sintering grain growth and densification occurs. The grain-to-grain connectivity is reflected in both cobalt and nickel ferrites with some air holes in case of copper ferrite even after high temperature sintering.

Temperature programmed reduction experiments were performed over the 900°C sintered ferrospinel catalysts to investigate their reduction behavior under conditions mentioned in experimental section. The great interest of these TPR studies is to establish correlations between the reducibilities of the spinels and reactivities for redox reactions like sulfuric acid decomposition. Here we present a very informative comparison of reducibilities of three spinel ferrites-Cu, Ni, Co. The first cycle TPR profiles of all these three catalysts are shown in Fig. 4.4. Copper ferrite exhibited a very sharp reduction peak having T_{max} at 400°C with onset at ~280°C and another very sluggish, broad and weak reduction peak with T_{max} at 610°C. The first prominent peak appearing at lower temperature can be ascribed to the bulk reduction of $CuFe_2O_4$. Generally $CuFe_2O_4$ is reduced in two steps, the first peak appearing at lower temperature is ascribed to the reduction of $CuFe_2O_4$ to metallic Cu and Fe_2O_3, the iron oxide being instantly reduced to Fe_3O_4. The second peak is due to the reduction of Fe_3O_4 to Fe via FeO [19]. In case of cobalt ferrite the reduction is inhibited to some extent with onset of reduction delayed to 330°C and a single very broad reduction band. Due to this broad pattern the elementary steps of Fe^{3+} and Co^{2+} reduction cannot be distinguished from the TPR curves, thus leading to the suggestion that the more easily reducible cations (in this case Co^{2+}) promote the reduction of iron cations which gets subsequently reduced [20-21]. Nickel ferrite showed a single reduction stage with initiation above 460°C and peaking at 645°C along with a shoulder at 760°C. This result is in agreement with the results of the reducibility studies of nickel ferrite by other authors [22-23] where they report a two step reduction. Thus the reduction temperature of the spinels increases in the order of $CuFe_2O_4 < CoFe_2O_4 < NiFe_2O_4$. If we compare the reducibility of the spinels, cobalt ferrite shows a 50°C delay in onset of reduction than copper ferrite while in case of nickel ferrite the onset temperature increased to an extent of ~ 180°C as was also observed by Shin et al in their comparative thermal analysis [3]. In our earlier study (chapter 3) we have carried out the TPR with iron oxide catalyst under similar conditions where the reduction of Fe^{3+} occurs in three steps to Fe^0 via Fe_2O_3 to Fe_3O_4 at 400°C, Fe_3O_4 to FeO at 600°C and finally FeO to Fe metal at 720°C respectively. Here, in the case of spinels the reduction of Fe^{3+} to metallic Fe^0 occurs relatively at a much lower temperature probably due to spillover effect. The A^{2+} (A= Cu^{2+}, Co^{2+}, Ni^{2+}) cation is reduced by hydrogen to the corresponding metals which "dissociates and activates the hydrogen" for reduction of the other cation Fe^{3+}. Here, it is evident that the activation of hydrogen in case of copper ferrite is the highest among the three samples. Since the BET-surface area is almost the same for all the three samples this difference in reducibility can be due to two prime reasons - first the ability of the characteristic metal atoms to dissosciate the hydrogen might be different and also the bulk crystal structure of copper ferrite being tetragonal i.e. of low symmetry, the diffusion and further reduction of metal ions is much faster as compared to the other two cubic oxides.

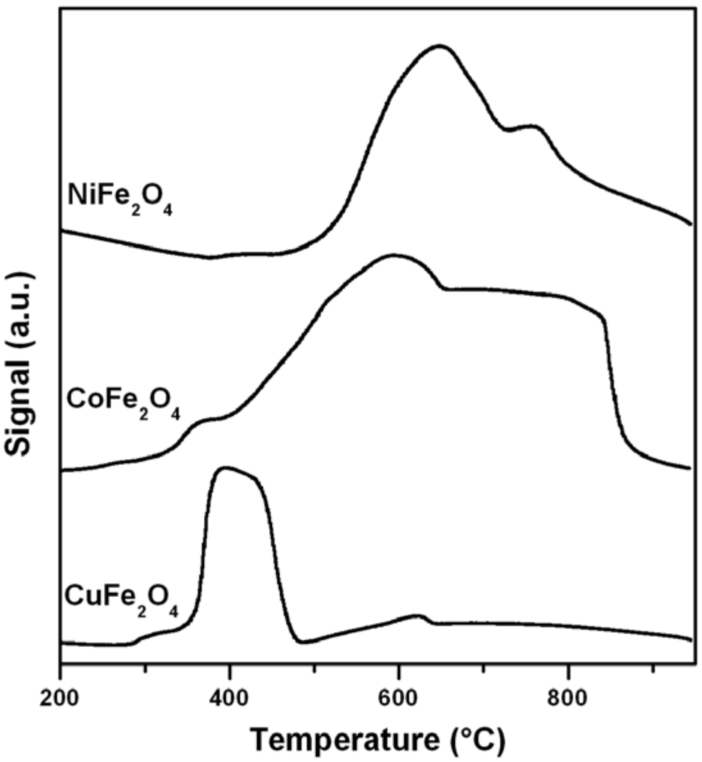

Fig. 4.4. Temperature programmed reduction profiles of the ferrospinel catalysts

A comparison of the temperature programmed desorption (TPD) profiles for the three inverse ferrospinels in the temperature range of 200°C to 1000°C is given in Fig. 4.5. The TPD patterns were recorded after a pretreatment of 2 hrs at 350°C to remove all surface adsorbed species. The TPD profiles exhibits peaks at very high temperature region due to desorption of lattice oxygen, although onset for desorption begins at as low as ~450°C for all the samples. Copper ferrite exhibits a two stage desorption with a broad low intensity band having an onset of desorption at 430°C and followed by a sharp desorption peak with maxima at ~940°C. Nickel ferrite shows a three step desorption beginning at ~422°C followed by two sharp peaks at ~490°C and 650°C and the a broad hump with maxima at 870°C. Oxygen desorption occurs in the cobalt ferrite sample in two steps having a small peak at 535°C and the prominent peak at 860°C. Thus the ease of lattice oxygen desorption from the three spinel ferrites decreases in the order $NiFe_2O_4$>$CoFe_2O_4$>$CuFe_2O_4$.

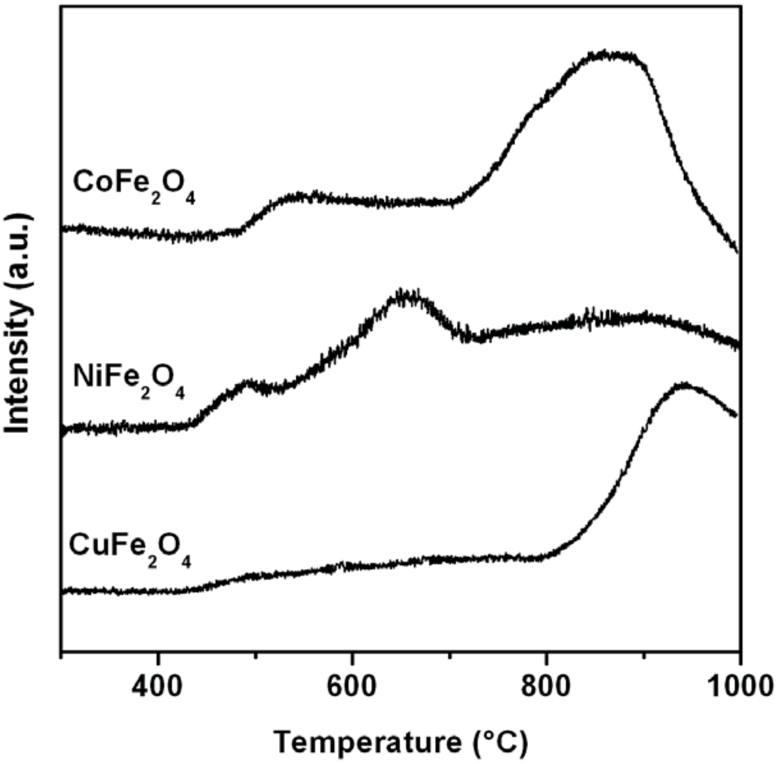

Fig. 4.5. Temperature programmed desorption profiles of the ferrospinel catalysts

The temperature dependent catalytic activities of the ferrospinels for sulfuric acid decomposition reaction in the temperature range of 650°C to 825°C are shown in Fig. 4.6. Catalytic activity of all the samples increases with temperature which is due to kinetic factors and this also shows that the catalysts perform well under the experimental conditions of high temperature and highly corrosive reactants and products. The onset temperature of sulfuric acid decomposition over all three ferrospinels were found to be very low (<650 °C). Initially the activity of NiFe$_2$O$_4$ was highest followed by CuFe$_2$O$_4$ and then CoFe$_2$O$_4$. This trend was evident till 750 °C but above this temperature CuFe$_2$O$_4$ exhibited the highest activity and approached towards the equilibrium SO$_2$ yield value (calculated from FACTSAGE thermodynamic software and represented by the dotted curve in Fig. 4.6) at higher temperatures. It is evident from Fig. 4.6 that the maximum activity is obtained for copper ferrite with a conversion of about ~ 78% at

800°C. Sulfuric acid decomposition in sulfur based thermochemical cycles is normally carried out at above 800 °C in a process reactor and so under the required process conditions copper ferrite is found to be the most active catalyst. The activity results were successfully reproduced twice within the limits of permissible errors. So, on the whole it can be concluded that among the three spinel ferrites investigated in this study copper ferrite is the most promising system for carrying out high temperature sulfuric acid decomposition. After two such activity runs the spent catalyst were collected and characterized by FTIR and EGA for evaluating the probable reasons in observation of the catalytic activity trend. It is pertinent to mention here that blank experiments in absence of catalysts verified that homogeneous vapor phase reactions did not occur under these conditions.

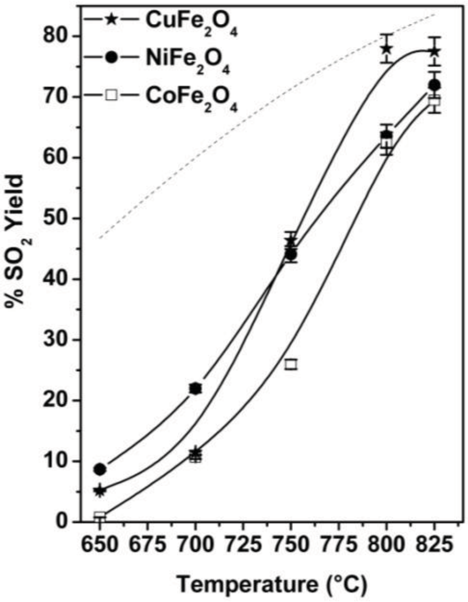

Fig. 4.6. Temperature dependent catalytic activity profiles of the three ferrospinel catalysts for H_2SO_4 *decomposition reaction. The dotted line represents the thermodynamic yield of* SO_2 *(calculated from FACTSAGE thermodynamic software)*

The XRD pattern of the fresh and spent copper ferrite catalyst, which showed the highest SO_2 conversion, are shown in Fig. 4.7. It is evident from the figure that even after use in two successive temperature dependent catalytic activity runs, there is no change in phase of the catalyst neither there are formation of any additional phases. Thus, the stability of the spinel phase for high temperature use in sulfuric acid decomposition can be confirmed from this aspect.

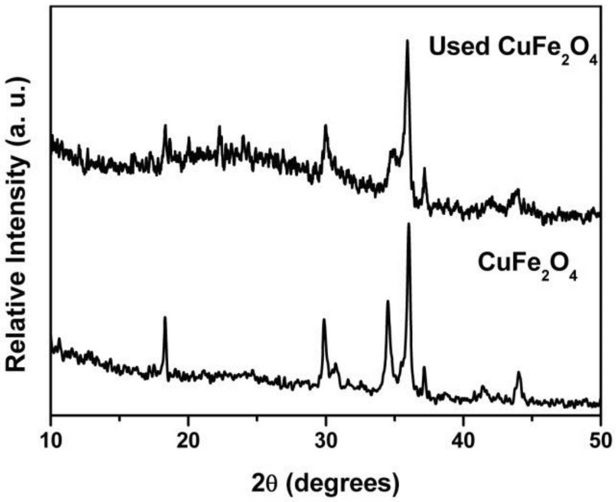

Fig. 4.7. XRD patterns of the fresh and spent $CuFe_2O_4$ catalyst

Fig. 4.8 shows the FTIR spectra of the three used ferrospinel catalyst samples in the 400-1500 cm^{-1} range. All the spent catalyst samples exhibits four prominent peaks in the 950-1200 cm^{-1} region which were absent in the freshly prepared samples. Presence of four prominent IR bands such as at 961, 996, 1163 and 1196 cm^{-1} for the spent $CuFe_2O_4$ is ascribed to ν_{S-O} vibrations of bidentate sulfate species. The peaks arise due to SO bond stretching in metal sulfates with the lowest wavenumber peak assigned to υ_1 stretching mode, while the higher three peaks are due to υ_3 mode. The presence of four bands is an indicative of C_{2v} symmetry and bidentate sulfate coordination, because a clear distinction between monodentate and bidentate coordination can be made, based on the number of observed bands - monodentate, C_{3v}, with three bands, and bidentate, C_{2v}, with four bands [24]. Sulfur–oxygen double bonds (i.e. SO) show a strong absorption band at 1381 cm^{-1} [25]. These FTIR spectra confirm the metal sulfate formation on these metal oxides. These metal sulfates are probably the transient intermediates of sulfuric acid decomposition to sulfur dioxide over these metal oxide catalyst.

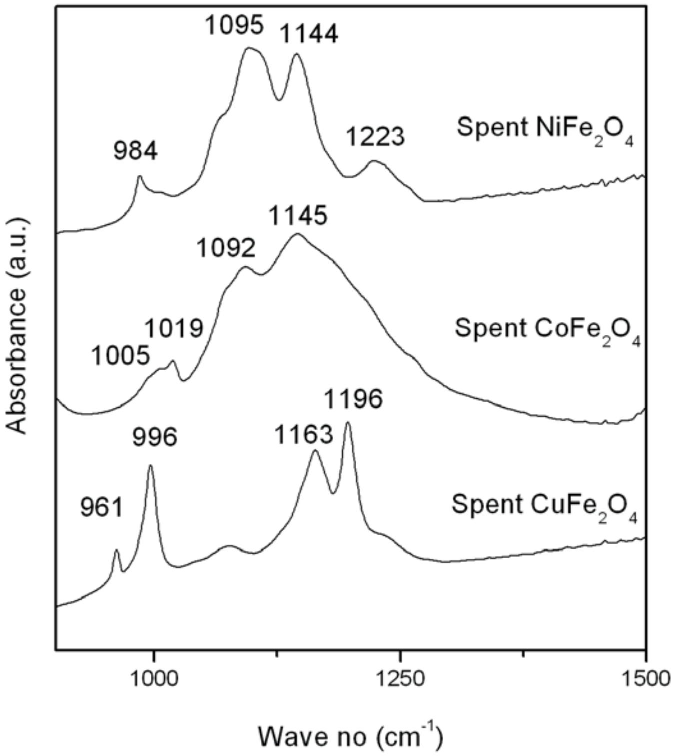

Fig. 4.8. FTIR spectra of the spent Cu, Ni and Co ferrospinel catalysts

The SEM images of the spent $CuFe_2O_4$ catalysts are shown in Fig. 4.9. Agglomeration of particles can be seen in Fig. 4.9. Patches of needle like crystals as shown in Fig. 4.9b were also visible on the surface of copper ferrite which can be probably attributed to the formation of crystals of metal sulfates. The electron map of the elements shown in Fig. 4.10 illustrates the uniform distribution of sulfur throughout the used catalyst in a particular region spread over ~ 1400 μm. This is probably due to the fact that metal sulfates are uniformly formed and decomposed leading to distribution of metal sulfates throughout the catalyst surface. Also SEM results showed the change in morphology of the samples due to ~12 hrs exposure to sulfuric acid vapors at high temperature.

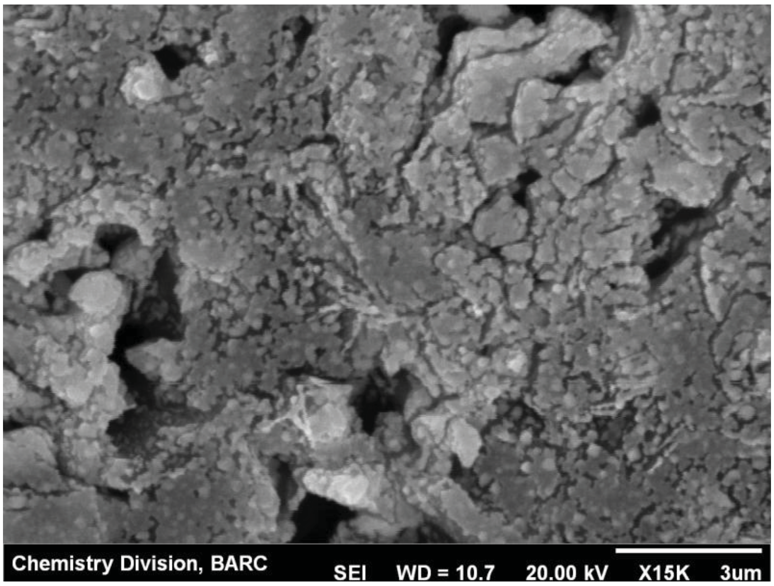

Fig. 4.9a. Scanning Electron Micrograph image of the spent $CuFe_2O_4$ catalyst after 10 h of exposure to sulfuric acid at high temperatures

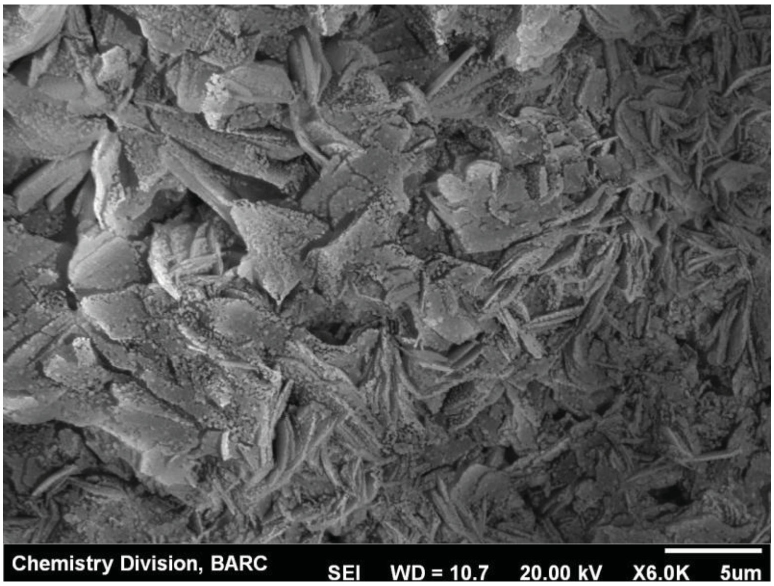

Fig. 4.9b. Scanning Electron Micrograph image of selected patches over the spent $CuFe_2O_4$ catalyst

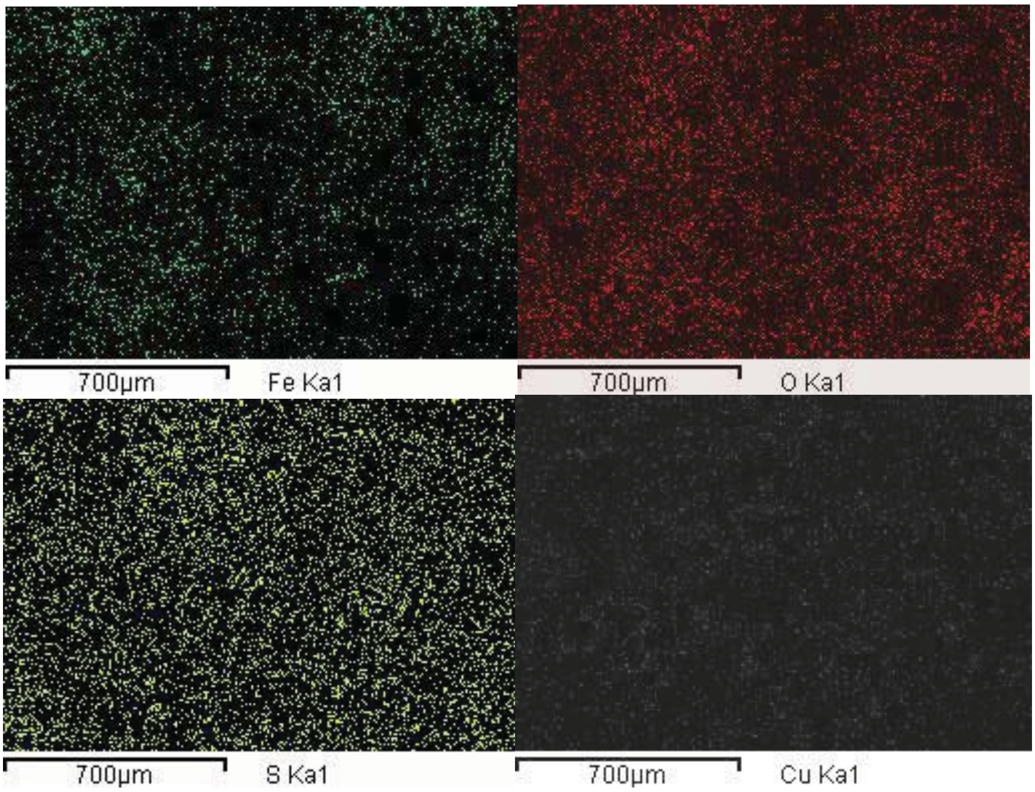

Fig. 4.10. Elemental maps of Fe, O, S and Cu on the surface of spent copper ferrite catalyst showing the distribution of sulfate species on the surface.

The spent catalyst was also subjected to evolved gas analysis experiments as a function of temperature. The evolved gases were detected using a quadruple mass spectrometer. A plot of intensity of evolved gas, having mass number 64 (SO_2), in the temperature range of 400-1000 °C is shown in Fig. 4.11. EGA analysis revealed that all the spent catalysts evolve SO_2 as a decomposition product of its sulfate as the temperature is increased. If we compare the decomposition temperature it is evident that the onset of SO_2 production occurs at lowest temperature for copper ferrite followed by nickel and cobalt ferrites. The temperature at which maximum SO_2 was evolved or the T_{max} also followed the same order. EGA of all the spent samples shows two peaks of SO_2 evolution, where first is low temperature peak with weak intensity whereas second is strongly intense peak occurs at relatively higher temperature. The first peak is attributed to desorption of SO_2 from surface sulfate species whereas second peak corresponds to evolution of SO_2 from decomposition of bulk metal sulfate. In case of Copper ferrite, the difference in temperatures of two peaks is minimal as compared to other catalysts suggesting that bulk metal sulfate is unstable resulting in facile decomposition of metal sulfates present in spent $CuFe_2O_4$ catalyst. Thus regenerability of catalyst follows the order same as the activity trend i.e; is maximum for $CuFe_2O_4$ > $NiFe_2O_4$ > $CoFe_2O_4$ with the completion of SO_2 liberation being ~ 700 °C for copper ferrite, ~ 775 °C for nickel ferrite and ~ 825 °C for cobalt ferrite.

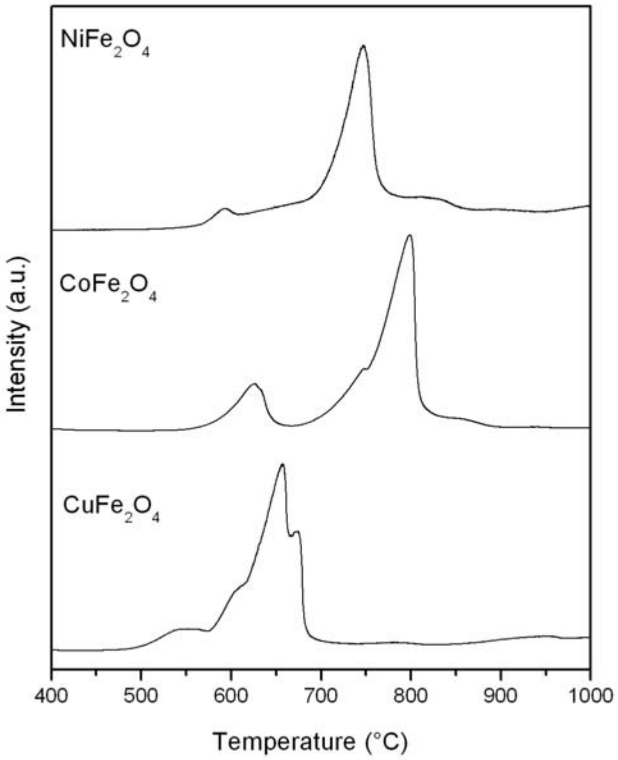

Fig. 4.11. Evolved gas analysis for mass no. 64 in mass spectrometer as a function of temperature of the spent spinel catalysts post sulfuric acid decomposition reaction.

4.4. Insights into most probable mechanism

From the ex-situ analysis of the spent catalyst samples we can get an insight into the mechanism of the high temperature sulfuric acid decomposition reaction. We have already discussed in chapter 1 that sulfuric acid decomposition is comprised of following two reactions in series:

H_2SO_4 (g) → H_2O (g) + SO_3(g) (~ 450 °C) ....(4.1)

SO_3 (g) → SO_2 (g) + 1/2O_2 (g) (800-900 °C) ….(4.2)

Also in the previous chapter (chapter 3) we saw that a metal sulfate formation and decomposition route can be a plausible mechanism for the SO_3 decomposition on metal oxides. Here in case of spinels, formation of bidentate metal sulfates was observed by FTIR spectra of the used catalyst. Again from the thermal decomposition experiments (EGA) we observed the evolution of SO_2 from the spent oxide catalyst samples, which must have come from the metal sulfates formed on the spent samples. Thus, metal sulfate formation and its subsequent decomposition can be a possible mechanism by which sulfuric acid decomposition proceeds. Sulfuric acid at high temperature (>450°C) will thermally decompose to produce sulfur trioxide and water vapor (eqn. 4.1). The catalyst will see these sulfur trioxide and moisture. The decomposition of SO_3 can then be proposed to occur in three steps as shown in scheme 4.4.1. Ferrospinels are generally n-type semiconductors which lose lattice oxygen on heating, causing anionic vacancies [17]. This process requires a reduction of the metal cations i.e $Fe^{3+} \Leftrightarrow Fe^{2+}$ and/or $A^{2+} \Leftrightarrow A^{+}$ (A = Co, Ni, Cu) to maintain electroneutrality in the system. This redox process of the metal cations will be highly dependent on the redox properties of the individual cations. A SO_3 molecule interacts with such a surface active site ([*]) which might probably be an oxygen vacant site on the metal oxide surface to form a bidentate surface sulfate species as shown in eqn. 4.3 in scheme. 4.4.1. Two bidentate surface complexes are possible; a chelating one with two oxygen atoms of the sulfate coordinating with the same metal atom (as shown in eqn. 1) or the two oxygen atoms coordinating with two different metal atoms forming a bridged structure. A bridged structure is possibly absent because a bridged bidentate sulfate structure exhibits the highest ν_3 frequency for SO stretching in the FTIR spectra at a much lower value (1160-1195 cm^{-1}) than that for a chelating bidentate sulfate (>1200 cm^{-1}) [26]. It is important to notice here that out of the four oxygens in a surface sulfate species three came from SO_3 and one from the metal oxide. The sulfate then undergoes decomposition producing SO_2 and the metal oxide as shown in eqn. 4.4. The reduced iron and copper, nickel or cobalt centers will be subsequently oxidized by the reduction of SO_3 to SO_2. Again, the redox couples $Fe^{3+} \Leftrightarrow Fe^{2+}$ and $A^{2+} \Leftrightarrow A^{+}$ plays a crucial role in here. Finally, the metal oxide liberates the oxygen (eqn. 4. 5).

The first step is thermodynamically favourable at lower temperatures (< ~780°C) as the Gibbs free energy of iron sulfate formation was calculated by Kim et al [27] and was found to be negative below ~ 780 °C and positive above this temperature. Still, at higher temperatures metastable sulfate formation is definitely possible on all metal oxide surfaces by surface adsorption phenomenon. The third step which is the evolution of oxygen is again a kinetically fast step. In SO_3 decomposition, lattice oxygen diffusion has a very little role to play, as the decomposition temperature being high (>750°C) the mobility of lattice oxygen of all the three oxides are comparable, so that after evolution of the SO_2 molecule from the surface active site an oxygen is liberated from another site, so that this step has very little kinetic implication. This is also reflected in the catalytic activity where, the order of liberation of lattice oxygen from the three spinel oxides by TPD is just the reverse of the activity trend at low temperature. But, at lower temperatures (<750°C) at low conversions, this step might become rate limiting as we see that at lower temperatures the order of catalytic conversions decreases in the order $NiFe_2O_4 > CuFe_2O_4 > CoFe_2O_4$. From the TPD profiles of the catalyst samples we observed that in case of nickel ferrite the onset temperature of lattice oxygen evolution was lowest among all and correspondingly SO_2 yield was also found to be higher at lower temperatures for the same. The second step or the metal sulfate decomposition step is most crucial as the nature of metal M plays an important role in deciding the rate of decomposition. In previous works [27, 28, 29 and chapter 3 of this thesis] the metal sulfate decomposition temperature has been proposed to be the rate determining step which is reflected here in spinel oxides as well, because from the evolved gas analysis results of the spent catalyst samples the temperature of evolution of SO_2 exactly matches with the order of catalytic activity at higher temperatures. Thus, the rate of metal sulfate decomposition dominates the catalytic decomposition of sulfur trioxide over the spinel oxide catalysts.

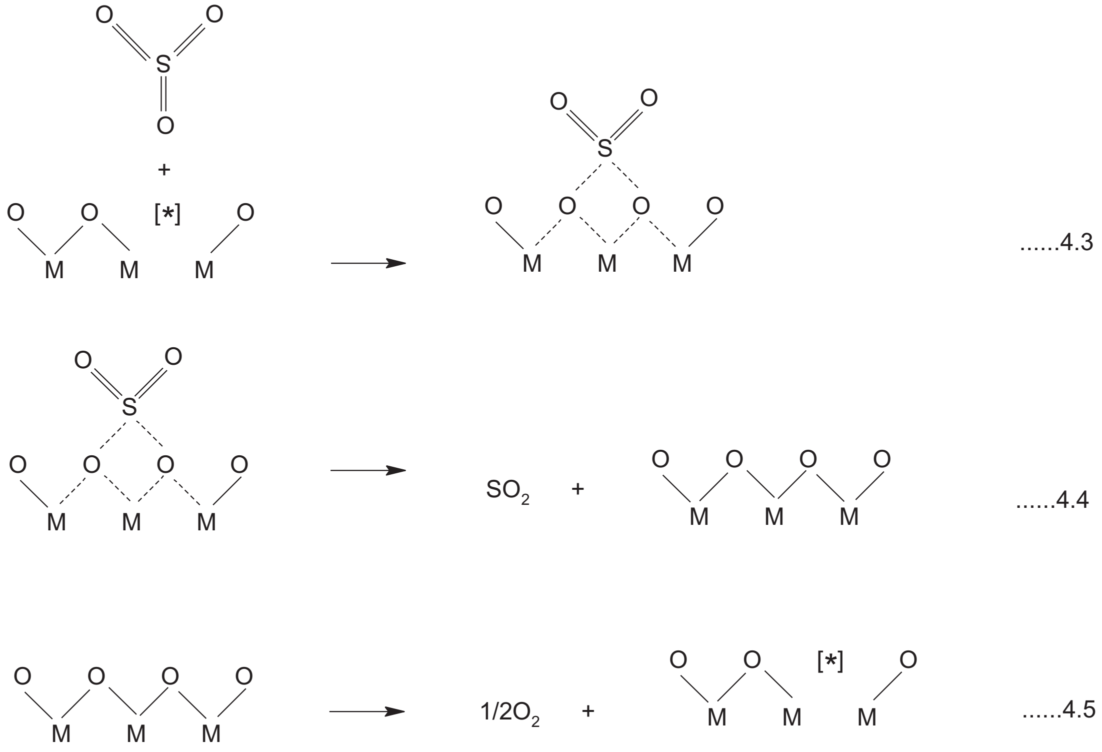

Scheme 4.4.1: A schematic presentation of proposed mechanism for sulfuric acid decomposition over spinel ferrites. [*] denotes surface active sites.

The decomposition of metal sulfate to SO_2 and oxygen involves the dissociation of two S-O bond instead of the direct S=O dissociation in gas phase reaction. Apparently it seems unfavorable but the thermal stability of the metal sulfates plays an important role here. The more thermally unstable the sulfate more it is prone to decompose by dissociating the two S-O bonds. Again, the strength of the S-O bond in the M-O-S linkage of the sulfate structure is decided by the nature of metal M. This is because in the bidentate sulfate structure possessing M–O–S linkage, the M electronegativity determines the iono-covalent character of the M–O bond, and consequently of the polarization of S-O bond. The more the electronegativity of M, more will be the covalent character of the M-O bond and weaker the S-O bond strength. Within our scenario of spinel ferrites, the electronegativity vary as $Fe^{3+} >> Cu^{2+} > Ni^{2+} > Co^{2+}$ [30]. Thus, by theoretical arguments the activity of the catalyst should follow the order: $CuFe_2O_4 > NiFe_2O_4 > CoFe_2O_4$. Indeed, our experimental results are in good agreement with the theoretical considerations. Although, spinel ferrites AFe_2O_4 (A = Co, Ni, Cu) being mixed oxides might not necessarily have shown the same trend as single oxides of A metal, but these ferrospinels being inverse there is a distribution of both A^{2+} and Fe^{3+} at the octahedral sites (Mössbauer results) regarded as the catalytically active sites [18]. In addition to the above, metal sulfate formation and decomposition (eqn, 4.3 and 4.4) over ferrospinel catalysts involves the working of two vital redox couples $Fe^{3+} \Leftrightarrow Fe^{2+}$ and $A^{2+} \Leftrightarrow A^{+}$ (A = Cu, Ni, Co). From the TPR results we observed that the reducibility of $CuFe_2O_4$ is much better than the other ferrites. In $CuFe_2O_4$ not only Cu^{2+} is highly reducible but the reducibility of Fe^{3+} is substantially improved. Thus our results show that all the ferrospinels are active formulations for sulfuric acid decomposition with copper ferrite being the most active catalyst which is ascribed to its improved redox properties and lower thermal stability of its sulfate.

4.5 Conclusion:

The single phasic crystalline spinel ferrites viz; $CuFe_2O_4$, $CoFe_2O_4$, $NiFe_2O_4$ were successfully prepared by gel combustion route and well characterized by various physico-chemical methods. The catalytic activities for these materials were evaluated for sulfuric acid decomposition reaction in an indigenously constructed flow through quartz reactor. All the spinel ferrites were found to be active for sulfuric acid decomposition reaction and they retained their catalytic activity for two successive temperature dependent catalytic runs. Mössbauer study confirmed the occupancy of Fe^{+3} in both octahedral and tetrahedral sites in all three spinel ferrite samples. Presence of bidentate surface sulfate complex, with two oxygen atoms of the sulfate coordinating with the same metal atom was revealed from *ex situ* FTIR spectra of the spent samples. The plausible mechanism as proposed from an *ex situ* catalyst investigation involves the metal sulfate formation and then decomposition followed with an oxygen evolution step, with the metal sulfate decomposition step playing the most crucial role in determining the reaction kinetics. Facile sulfate decomposition with lowest temperature of SO_2 evolution was observed in evolved gas analysis (EGA) over spent $CuFe_2O_4$ as compared to other ferrospinels. The lower decomposition temperature of the sulfates of copper ferrite is attributed to the higher electronegativity of Cu^{2+} as compared to Ni^{2+} and Co^{2+}, which renders the S-O bond in the mixed metal sulfate weaker than others and thus more susceptible to dissociation. In addition, the improved reducibility of Fe^{3+} and the Cu^{2+} cations in $CuFe_2O_4$ as compared to the Fe^{3+} and respective bivalent cation in $NiFe_2O_4$ and $CoFe_2O_4$ was evident from TPR results, which also promoted the sulfuric acid decomposition reaction. Here, both iron and copper cations could undergo facile redox reactions $Fe^{3+} \Leftrightarrow Fe^{2+}$ and $Cu^{2+} \Leftrightarrow Cu^{+}$ and the synergism between the two couples could be responsible for better decomposition rate. Based on the present findings it can be concluded that copper ferrite is the most promising catalyst for sulfuric acid decomposition reaction among the three ferrospinels investigated.

References:

1 V. Šepelák, L. Wilde, U. Steinike, K. D. Becker, Mater. Sci. Engg. A 375–377 (2004) 865–868.

2 E. de Smit and B. M. Weckhuysen Chem. Soc. Rev. 37(12) (2008) 2758–2781.

3 H. C. Shin, S. C. Choi, K. D. Jung, S. H. Han, Chem. Mater. 13 (2001) 1238-1242.

4 Y. Tamaura, M. Tabata Nature 346 (1990) 255-256.

5 G. Fierro, R. Dragone, G. Ferraris Appl. Catal. B 78 (2008) 183-191.

6 K. Lazar, T. Mathew, Z. Koppany, J. Megyeri, V. Samuel, S. P. Mirajkar, B. S. Rao and L. Guczi Phys. Chem. Chem. Phys. 4 (2002) 3530–3536.

7 S. Roy, S. Byaskh, M. L. N. Goswami, D. Jana, J. Subramanyam, Chem. Mater. 19 (2007) 2622.

8 R. D. Purohit, S. Saha, A. K. Tyagi, J. Nucl. Mater. 288 (2001) 7.

9 L. C. Pathak, T. B. Singh, S. Das, A. K. Verma, P. Ramachandrarao, Mater. Lett. 57 (2002) 380.

10 R. D. Purohit, B. P. Sharma, K. T. Pillai, A. K. Tyagi, Mater. Res. Bull. 36 (2001) 2711.

11 S. V. Chavan, A. K. Tyagi, J. Mater. Res. 19 (2004) 3181.

12 V. Bedekar, S. V. Chavan, A. K. Tyagi, J. Mater. Res. 22 (2007) 587.

13 S. R. Jain, K. C. Adiga, and V. R. Pai verneker, Combust. Flame 40 (1981) 71-79.

14 R. K. Selvan, V. Krishnan, C. O. Augustin, H. Bertagnolli, C. S. Kim, A. Gedanken Chem. Mater. 20 (2008) 429-439.

15 N. S. Gajhbhiye, S. Bhattacharya, G. Balaji, R. S. Ningthoujam, R. K. Das, S. Basak, J. Wiessmüller Hyperfine Intract. 165 (2005) 153-159.

16 W. B. Cross, L. Affleck, M. V. Kuznetsov, I. P. Parkin and Q. A. Pankhurst, J. Mater. Chem. 9 (1999) 2545-2552.

17 C. G. Ramankutty, S. Sugunan App. Catal. A 218 (2001) 39–51.

18 J. P. Jacobs, A. Maltha, J. G. H. Reintjes, J. Drimal, V. Ponec, H. H. Brongersma, J. Catal. 147 (1994) 294-300.

19 K. Faungnawakij, Y. Tanaka, N. Shimoda, T. Fukunaga, R. Kikuchi, K. Eguchi, Appl. Catal. B 74 (2007) 144–151.

20 E. Manova, T. Tsoncheva, D. Paneva, I. Mitov, K. Tenchev, L. Petrov Appl. Catal. A 277 (2004) 119–127.

21 E. Manova, T. Tsoncheva, C. Estourne`s, D. Paneva, K. Tenchev, I. Mitov, L. Petrov Appl. Catal. A 300 (2006) 170–180.

22 Y. Cesteros, P. Salagre, F. Medina, J. E. Sueiras Chem. Mater. 12 (2000) 331-335.

23 E. Manova, T. Tsoncheva, D. Paneva, J. L. Rehspringer, K. Tenchev, I. Mitov, L. Petrov, Appl. Catal. A, 317 (2007) 34–42.

24 S. J. Hug. J. Coll. Int. Sci. 188 (1997) 415–422.

25 S. K. Samantaray, K. M. Parida, J. Mater. Sci. 38 (2003) 1835-1848.

26 T. Yamaguchi, T. Jin, K. Tanabe J. Phys. Chem. 90 (1986) 3148-3152.

27 Kim TH, Gong GT, Lee BG, Lee KY, Jeon HY, Shin CH, et al. Appl Catal A Gen 2006;305(1):39–45.

28 B. M. Nagaraja, K. D. Jung, B. S. Ahn, H. Abimanyu, K. S. Yoo Ind. Eng. Chem. Res. 48 (2009) 1451–1457.

29 V. Barbarossa, S. Bruttib, M. Diamantia, S. Saua, G. De Mariab, Int J Hydrogen Energy 31 (2006) 883-890.

30 K. Li and D. J. Xue Phys. Chem. A 110 (2006) 11332-11337.

31 M. Eibschütz, S. Shtrikman, D. Treves, Phys. Rev. 156 (1967) 562.

Chapter 5

Sulfuric acid decomposition in enhanced scale with iron oxide based granular catalysts

5.1. Introduction

We have seen earlier in chapter 1, that the catalytic decomposition of sulfuric acid to produce sulfur dioxide, oxygen and water is a topic currently gaining enormous importance as it can serve as thermal to chemical energy conversion step in all the sulfur based thermochemical cycles such as the sulfur–iodine thermochemical cycle [1], the hybrid sulfur cycle [2], and the sulfur–bromine hybrid cycle [3], for successful massive hydrogen production by water splitting. We also discussed about the problems of using noble metal based catalysts e.g.dispersed platinum catalyst due to its deactivation on prolonged use by sintering, oxidation, active metal loss or substrate sulfation. So, we proposed to work with oxide based catalyst for this reaction and with an aim of working in this direction we initially started with chromium doped iron oxide as catalyst for the above application, where we found that 10% chromium doping helped in increasing the activity of iron oxide (Chapter 3). We have also reported the catalytic properties of three spinel ferrites AFe_2O_4 (A= Cu^{2+}, Co^{3+} and Ni^{2+}) among which copper ferrite was the most promising catalyst by virtue of its superior redox properties and lower decomposition temperature of its sulfate (Chapter 4). The present study was aimed at developing iron oxide based catalyst for sulfuric acid decomposition that can operate in extreme conditions as posed in the actual reactor conditions. In most of the reported studies (as discussed in chapter 1-section 1.6 and 1.8) catalysts in powder form were used in sulfuric acid streams in which an inert gas carrier was used.

In the current study, Fe_2O_3 and $Fe_{1.8}Cr_{0.2}O_3$ catalysts were prepared by co-precipitation in contrast to conventional solid state reaction used in our previous study (Chapter 3), to obtain powders with better morphology. Besides, in almost all of the reported studies (Global status review, Chapter 1, section 1.8) and our previous studies in small scale (Chapter 3, 4) the catalysts were employed in powder form and sulfuric acid vapors were passed over the catalyst along with a carrier gas. Also, the amount of catalyst used for the studies were very low (say upto 2 g), so extrapolation at an engineering scale was not possible. The preferred physical form of a practical heterogeneous catalyst used for gas phase reactions in industries in a fixed bed reactor is usually macroparticulate, i.e. consisting of granules or pellets or spheres of suitable size (3-25 mm) so that there is sufficient space between the particles for the gases to flow freely (minimum pressure drop across the reactor and at the same time minimum channeling or catalyst bypass) [4]. So, for a practical application approach, the two screened oxides that showed good initial promise as catalyst for sulfuric acid decomposition - iron oxide and 10% chromium doped iron oxide, were investigated in pelletized form for the said reaction in an enhanced scale – using 20 g of catalyst. Catalytic activity was evaluated in absence of any carrier gas or diluents and under the flow of vapors of concentrated sulfuric acid (~98 %) alone so that the catalytic decomposer operates in extreme conditions as posed in the actual reactor conditions. To ensure the above aspect, experiments were performed in an indigenously designed and fabricated dual tube quartz catalytic reactor which served as an integrated boiler, preheater and decomposer having no high temperature connections (Fig. 2.17, Chapter 2). The concept of this dual-tube type of catalytic reactor can also be enhanced to an engineering scale for pilot plants. Again, for practical purpose the chief criteria for a successful catalyst are (i) its ability to perform the task required of it efficiently under suitable conditions of pressure and temperature; (ii) its initial cost and (iii) its life under operating conditions. So, the catalytic activity was evaluated as a function of reaction variables e.g. time, temperature and acid flow rate to completely assess the catalytic performance. Subsequently, the spent catalyst sample was analyzed ex-situ by physicochemical and spectroscopic techniques to understand the reaction mechanism and investigate any deactivation phenomenon which might be occurring at the molecular level.

5.2 Experimental

5.2.1. Preparation Fe_2O_3 and $Fe_{1.8}Cr_{0.2}O_3$ were prepared by co-precipitation method. Calculated amounts of nitrate precursors of iron and chromium were dissolved separately in deionized water. To prepare the doped material the two solutions were mixed together while in case of Fe_2O_3 only iron nitrate was used.

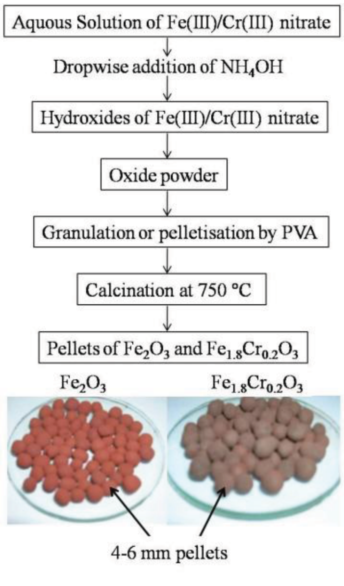

Scheme 5.1 Scheme for the preparation of granular iron oxide catalysts

Dilute aqueous ammonia was gradually added dropwise to the aforementioned solutions under vigorous stirring until precipitation was complete (pH 8.5). The precipitate gels thus obtained were further aged overnight and filtered off. The resulting cakes were oven-dried at 100 °C for 12 h and then shaped into spherical beads of 4-6 mm in diameter with the help of binder polyvinyl alcohol. Finally the spherical pellets were calcined at 750 °C for 12 h in air which also ensured complete removal of the binder. The heating and cooling rates were maintained at 5 °C/min. A scheme for the preparation of the granular catalyst is shown in scheme 5.1.

5.2.2. Characterization The catalyst samples were characterized before and after 100 h use by various techniques. Powder XRD patterns were recorded in 2θ range of 10-70° (step width 0.02° and step time 1.25 s) using a Philips X-ray Diffractometer (model 1729) equipped with nickel filtered Cu-K_α radiation. A Quantachrome Autosorb-1 analyzer was employed for measurement of BET surface area by recording the nitrogen adsorption isotherms. The FTIR spectra of the solid samples were recorded in KBr using a Jasco FTIR (model 610) in range of 400-4000 cm^{-1} with a resolution of 4 cm^{-1}. Redox behavior of the oxide sample towards reduction oxidation cycles was studied by recording temperature programmed reduction/oxidation (TPR/TPO) profiles on a TPDRO-1100 analyzer (Thermo Quest, Italy) under the flow of H_2 (5%) + Ar, alternatively, O_2 (5%) + He gas mixtures at a flow rate of 20 ml min^{-1}, in temperature range of 25-1000°C for TPR and up to 800°C for TPO at a heating rate of 6°C min^{-1}. The samples were pretreated at 350°C for about 2.5 h in helium, prior to recording of the first TPR run. Mössbauer spectra have been obtained using a spectrometer operated in constant acceleration mode in transmission geometry. The source employed is ^{57}Co in Rh matrix of strength 50mCi. The calibration of the velocity scale is done using iron metal foil. The outer line width of calibration spectra was 0.29 mm/s. the Mössbauer data was analyzed using a least square fitting programme. The morphological features were analyzed by a Scanning Electron Microscope (Mirero, Korea, model- AIS2100). Prior to SEM examination, the samples were coated with a thin gold layer (~ 150 Å thick) so as to avoid the problem associated with charging. To analyze the surface elemental composition and valence state of ions in the catalysts, X-ray photoelectron spectroscopy (XPS) was employed. A Thermo VG Clamp2 Analyzer based spectrometer using a radiation source of Mg KR radiation (1253.6 eV, 30mA × 8 kV) was used for these studies. As an internal reference for the absolute binding energy, a C 1s peak of 284.6 eV was used. To understand the nature of stable species produced on the catalyst during decomposition of sulfuric acid, the spent catalyst samples were heated in the temperature range of 400-1000 °C at a heating rate of 10 °C/min and the evolved gases were analyzed by a QMS coupled to a TG-DTA, (model- SETSYS Evolution-1750, SETARAM).

5.2.3 Catalytic activity Sulfuric acid decomposition reaction tests were carried out in a quartz reactor with annular configuration as shown in Fig. 2.18 (Chapter 2). The reactor consists of dual quartz tubes, with sulfuric acid accumulating at the bottom of the annular region and catalyst being loaded at the top of the annular region and held on its position by a perforated quartz disc. The acid and the catalyst are heated by a two zone electrically heated furnace the temperature on the profile of the catalyst and the acid region being controlled and measured by thermocouples held on the surface of the quartz reactor. The acid boiler region was heated to temperatures varying between 250-325°C and the catalyst region was heated in temperature range of 725 – 825°C for evaluation of the catalytic activity. The temperature profile of the reactor showed that the region in between the acid and catalyst acted as a preheater region and that the temperature in this region gradually increased from the acid boiler temperature to the catalytic decomposition temperature, thus minimizing acid condensation. This new design based on dual quartz tube can function as an integrated acid boiler, preheater and decomposer and the absence of high temperature connections renders it free from acid corrosion and leakage.

To study the time dependent catalytic activity for 100 h, the acid boiler region was heated to temperature of ~ 325 °C and the catalyst region was heated in temperature of 800 °C. By fixing the temperature of the boiler region an almost constant acid flux of ~ 0.63 ml of liquid sulfuric acid or a weight hourly space velocity (WHSV) of 3.4 g acid g^{-1} catalyst h^{-1} was obtained as feed flow. The sulfuric acid accumulated at the annular region of the dual quartz tube on attaining temperatures near to its boiling point (~ 334 °C) evaporated and reached the catalyst zone passing through the annular area in between the boiling and catalyst zone. In this zone in between the acid and catalyst zone in the annular region of the dual quartz tube, sufficient high temperatures were achieved to dehydrate H_2SO_4 to SO_3. SO_3 then passed through the catalyst bed held at a higher temperature undergoing decomposition. This new design based on dual quartz tube can function as an integrated acid boiler, preheater and decomposer. This concept of a dual tube integrated catalytic reactor has no high temperature connections and so renders it free from acid corrosion and leakage a challenging issue in successful operation of sulfuric acid decomposition reaction. This type of reactors will be particularly useful for coupling with bayonet type heat exchangers (Chapter 2). Thus, successful operation of catalytic sulfuric acid decomposition in an integrated acid boiler, preheater and decomposer - dual tube quartz reactor for more than 100 h in our experiments for each catalyst will provides deep impetus in extending this concept to large scale catalytic reactor design and fabrication for bench scale demonstration experiments of sulfur based thermochemical cycles.

In addition to the temperature dependent catalytic activity time dependent reference tests were also performed at atmospheric pressure and at a WHSV of 3.4 g acid g^{-1} catalyst h^{-1} with 20 gm of the spherical catalysts for 100 h. Again, catalytic activity based on varied sulfuric acid flux was performed by varying the sulfuric acid flux (0.2 $mlmin^{-1}$ to 10 $mlmin^{-1}$) by adjusting the temperature of the boiling zone of the integrated reactor. A post reaction ex-situ characterization of the spent catalyst was performed to check any deactivation, poisoning and to predict the most probable mechanism of the acid decomposition.

5.3 Results and Discussion

5.3.1 Catalytic activity for Sulfuric acid decomposition

The decomposition of sulfuric acid is a highly endothermic reaction and occurs only at very high temperatures. The temperature dependent catalytic activities for the decomposition of sulfuric acid over iron oxide and chromium doped iron oxide catalysts are shown in Fig 5.1 A. Both Fe_2O_3 and $Fe_{1.8}Cr_{0.2}O_3$ samples were found to be active for decomposition of sulfuric acid in temperature range of 700-825°C. Catalytic activity of both the samples increased with rise in temperature which is due to kinetic factors. From the temperature dependent catalytic activity (Fig. 5.1 A) we can clearly see that at lower temperatures < 775 °C, the catalytic activity of the doped sample is much higher than the undoped Fe_2O_3. But, at higher temperatures > 775 °C, the catalytic curves for the two oxide is similar in shape with the doped catalyst showing slightly higher activity as compared to the pristine Fe_2O_3. The SO_2 yield as measured with chemical titrimetric method increased with rise in temperature with a maximum activity of 76 % and 82 % for Fe_2O_3 and $Fe_{1.8}Cr_{0.2}O_3$ at ~ 825°C. The equilibrium product yield theoretically calculated is indicated in red curve in Fig. 2A. The experimental points for the doped catalysts are close to equilibrium above 750 °C. It is pertinent to mention here that no SO_2 was produced under identical conditions in absence of a catalyst.

The time dependent product yield of SO_2 obtained in the experiments that lasted for 100 h is shown in Fig. 5.1 B. It is evident from the figure that there is negligible deterioration in the catalyst performance during 100 h run at a sulfuric acid flux of ~ 0.63 ml/min for both the samples. So, the catalysts are stable under the experimental conditions of high temperature and highly corrosive reactants and products. This result implies that these catalysts can have a good catalytic activity for a long term. However the SO_2 yield was higher for the Cr doped samples than the pristine Fe_2O_3 throughout the 100 h run.

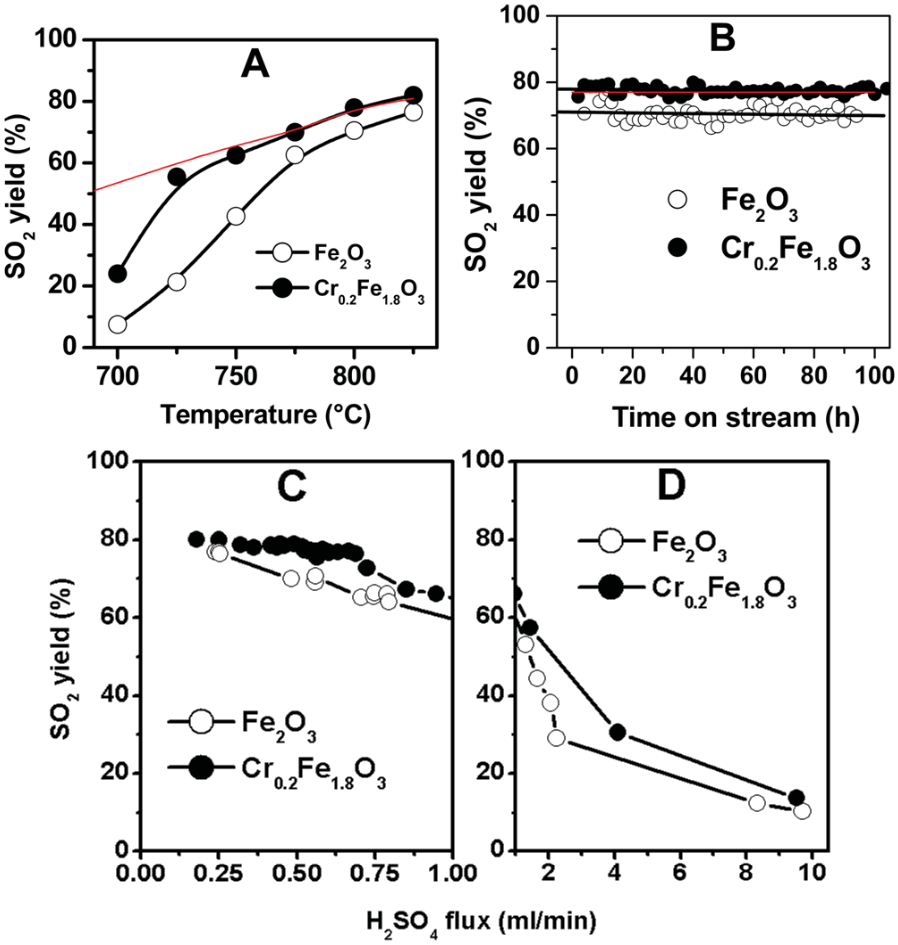

Fig. 5.1. The catalytic activities of Fe_2O_3 and $Fe_{1.8}Cr_{0.2}O_3$ for sulfuric acid decomposition; (A) temperature dependent catalytic activities at a H_2SO_4 flux of ~ 0.63 ml/min (WHSV of 3.4 g acid g^{-1} catalyst h^{-1}); (B) catalytic activity for 100 h time on stream at 800 °C at a H_2SO_4 flux of ~ 0.63 ml/min (WHSV of 3.4 g acid g^{-1} catalyst h^{-1}); (C and D) The effects of sulfuric acid flux on the product yield at 800 °C. The calculated equilibrium product yields are shown in red curve in (A) and (B).

The effects of sulfuric acid flux on the product yield are shown in Fig. 5.1 C and 5.1 D. At lower flux in the range of 0.2-1ml/min H_2SO_4 the decomposition rate decreases linearly but when the acid flux crosses ~ 2 ml/min a drastic drop in the product yield is noticed.

After the time dependent experiments for 100 h were over the spent catalyst pellets were collected and analyzed for any obvious change in structure, morphology or oxidation states as compared with the unused ones. The analysis of the fresh and spent catalyst along with the catalytic activity results were taken into account to predict the most probable mechanism of sulfuric acid decomposition and also the reason for improved performance of the Cr doped catalyst.

5.3.2 Characterization of the fresh and the spent catalysts

Fig. 5.2 shows the XRD patterns of the fresh and spent catalyst samples recovered after 100 h of exposure to sulfuric acid decomposition. The XRD pattern of fresh Fe_2O_3 and 10 % Cr doped Fe_2O_3 prepared by co-precipitation method matches with the JC-PDS card No. 33-0664 corresponding to Hematite, Fe_2O_3. From the comparison of the XRD patterns of the oxide samples from Fig 5.2, it is evident that even after exposure of the catalyst for 100 h in sulfuric acid stream at 800 °C there is no obvious change in phase and neither there is formation of any additional phases for both the samples. Thus we can conclude that the catalyst is having sufficient phase stability even after exposure to harsh catalytic reaction environment for sufficiently long duration. Table-1 lists the lattice parameters, crystallite size from Scherrer equation, BET surface area of the fresh and used Fe_2O_3 and $Fe_{1.8}Cr_{0.2}O_3$ catalyst samples. The BET surface area of the two fresh catalysts (Fe_2O_3 ~17 m^2gm^{-1} and $Fe_{1.8}Cr_{0.2}O_3$ ~ 18 m^2gm^{-1}) are comparable. The decrease in BET surface area on catalytic use for sulfuric acid decomposition reaction at high temperature, of both the pristine and doped catalysts can mostly be attributed to sintering and surface sulfate formation. The lattice parameters and cell volume of all the samples were generated from Powderx Indexing programme [5]. The ionic radii of iron and chromium are very similar: 0.067 nm for Fe^{3+} and 0.064 nm for Cr^{3+} [6] and their oxides are isostructural with rhombohedral crystal structure. The structure of α-Fe_2O_3, α-Cr_2O_3 comprises of a hexagonal close packed array of oxygen ions with Cr and/or Fe ordered on two-thirds of the octahedral interstices giving rise to eight cations in the first neighbor sphere.

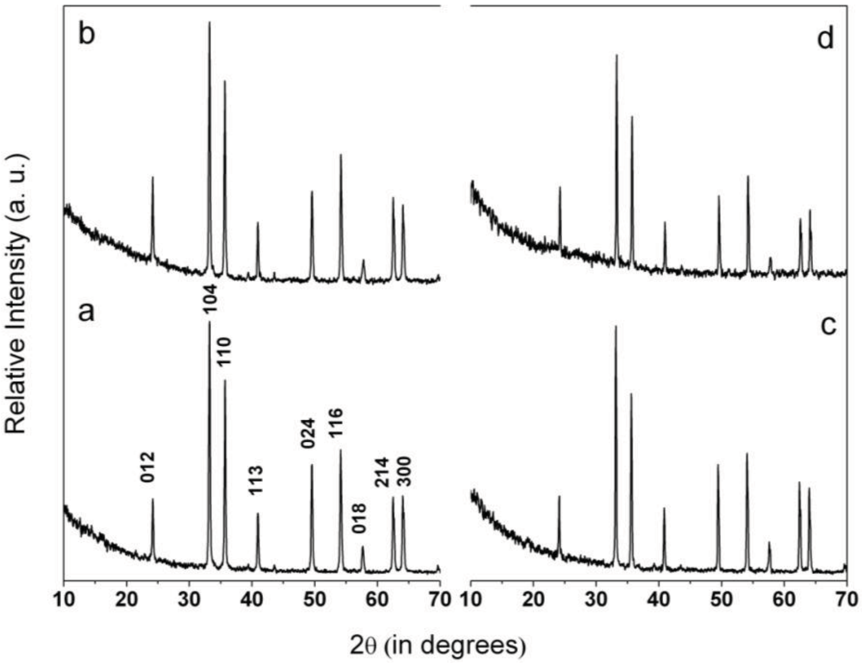

Fig. 5.2. The XRD pattern of the (a) fresh Fe_2O_3 and (b) $Fe_{1.8}Cr_{0.2}O_3$ catalysts which indicates the formation of solid solution of 10% chromium in Fe_2O_3 lattice. The spent (c) Fe_2O_3 and (d) $Fe_{1.8}Cr_{0.2}O_3$ catalysts does not show any phase change or formation of any additional phases.

Table.5.1:Lattice parameters, crystallite size and BET surface area of the catalyst samples

Sample	a	b	c	Volume	Crystallite Size	BET Surface Area
	(nm)	(nm)	(nm)	(nm^3)	(nm)	(m^2gm^{-1})
Fe_2O_3 (JCPDS card no.33-0664)	5.035	5.035	13.74	301.93	-	-
Fe_2O_3 fresh	5.02879	5.02879	13.74658	301.060	49.5	17
Fe_2O_3 Used	5.03969	5.03969	13.74633	302.361	66.5	13
$Fe_{1.8}Cr_{0.2}O_3$ fresh	5.03276	5.03276	13.70485	300.619	46.5	18

$Fe_{1.8}Cr_{0.2}O_3$ Used	5.03560	5.03560	13.69734	300.794	74.4	3

From Table 5.1 it is evident that the lattice parameters of Fe_2O_3 are in well agreement with those listed in the JC-PDS card No. 33-0664 corresponding to Hematite, Fe_2O_3. On Cr^{3+} doping at Fe^{3+} sites there is a slight decrease in lattice parameters of $Fe_{1.8}Cr_{0.2}O_3$ than Fe_2O_3 due to a minor decrease in ionic radii of the substituting ion.

Figure 5.3 shows the X-ray photoelectron spectroscopy (XPS) survey spectrum of the Fe_2O_3 catalyst. As can be seen from the spectrum, the main elements detected include only Fe and O. The XPS spectra (slow scan) were also recorded for the Fe 2p, O 1s and S 2p regions before and after catalytic activity cycle and are presented in Fig 5.4.

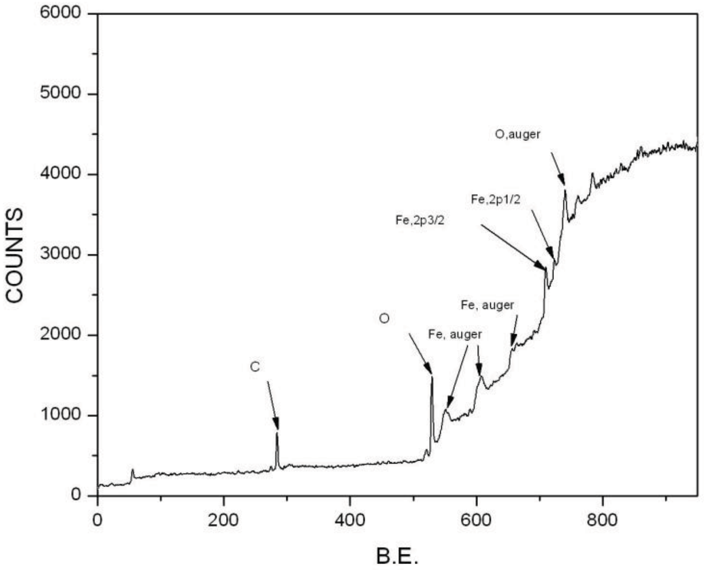

Fig. 5.3. X-ray Photoelectron survey scan of the calcined Fe_2O_3 catalyst (fresh) prepared by precipitation method

The binding energy of the Fe $2p_{3/2}$ in the catalyst before reaction was determined to be 709.5 ev which after the 100 h of reaction is determined to be 711.4, which is very close to that for the unused catalyst. This suggests that Fe is present in Fe^{3+} state [7] in both the fresh and used iron oxide catalysts, but due to formation of some surface sulfate species a shift towards higher binding energy is noticed in the spent catalyst. The O 1s peak as shown in fig. 5.4-B, exhibits a shift in the higher binding energy region from 529.35 to 530.28 ev. This shift towards higher binding energy can be attributed to oxygen present in a surface sulfate species [8]. However, a more accurate assessment of the presence of sulfates in the surface can be obtained using the sulfur 2p spectra [9].We observe a prominent peak at 169 ev which is specific for sulfur present as sulfates [7]. These results from XPS study of this sample indicate that the catalyst itself is very stable even after 100 h of reaction with no change in the valence state of Fe [10].

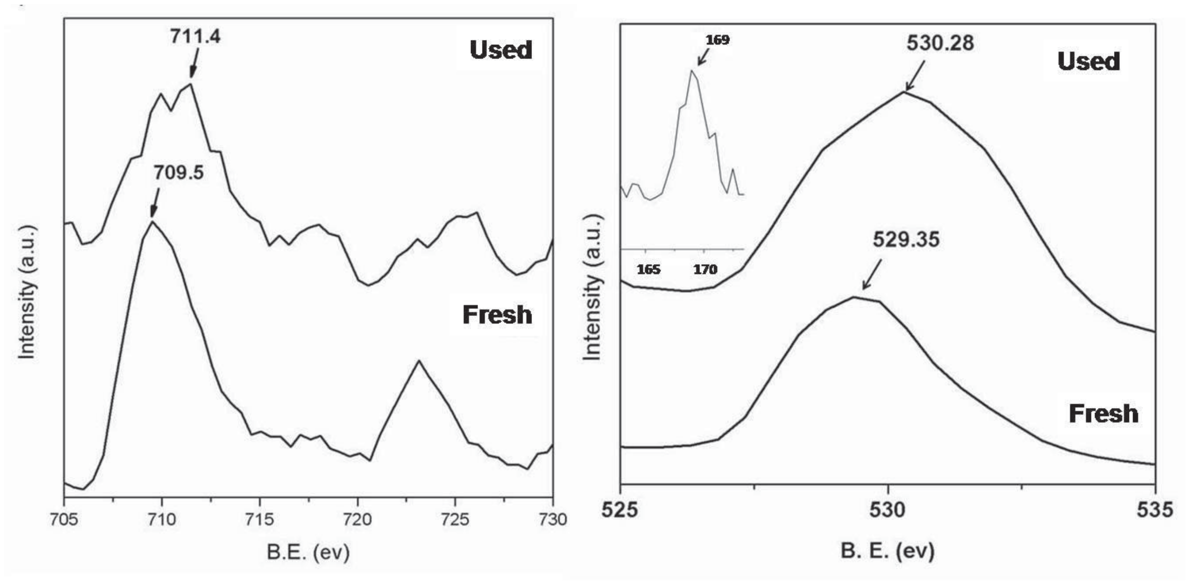

(A) (B)

Fig. 5.4. Spectra (A) is the Fe-2p X-ray Photoelectron spectra (XPS) of the fresh Fe_2O_3 *before reaction and of spent* Fe_2O_3 *collected after 100 h use in high temperature sulfuric acid decomposition reaction. Spectra (B) shows the O-1s XPS spectra of the fresh and the spent* Fe_2O_3 *catalyst. Inset shows the S-2p peak present in the spent catalyst.*

Infrared spectroscopy can be used to monitor chemical and structural changes in the mixed metal oxides. A comparison of the FTIR spectra of the fresh and spent catalyst samples is shown in Fig. 5.5. The prominent infrared absorption bands (cm^{-1}) observed for

Fe_2O_3 catalyst are at 470 cm^{-1} and 540 cm^{-1} with a well pronounced shoulder at 591 cm^{-1}. McDevitt and Baun [11] published the characteristic infrared bands of hematite at 560, 480, 370 and 325cm^{-1}. Schwertmann and Taylor [12] suggested the characteristic bands at 540, 470 and 345 cm^{-1} in the low frequency region can be used as fingerprints in the identification of hematite. Since our measurements were made in between 400-4000 cm^{-1}, we could not record the lower wave number peaks. But, peaks at 479 cm^{-1} and 560 cm^{-1} in Fe_2O_3 are in good agreement with hematite structure, the higher wave number peak being due to Fe-O bond stretching and the lower one due to Fe-O-Fe deformation [13, 14]. In the chromium doped sample $Fe_{1.8}Cr_{0.2}O_3$ the peak positions are slightly shifted towards higher wave number region and appear at 575 cm^{-1} and 493 cm^{-1} along with a shoulder at 457 cm^{-1}. The shift marks the microstructural defects generated in the structure of the iron oxide as a consequence to Cr doping. Also, since Cr is substituted at Fe sites, Cr-O-Fe bonds will be present in $Fe_{1.8}Cr_{0.2}O_3$ in addition to Fe-O-Fe bonds, thus decreasing the reduced mass and consequently increasing the peak position, as the IR wave number and reduced mass are inversely related. Further, all the peak positions are altered in the used samples as compared to the corresponding fresh ones indicating changes in the microstructure on catalytic use.

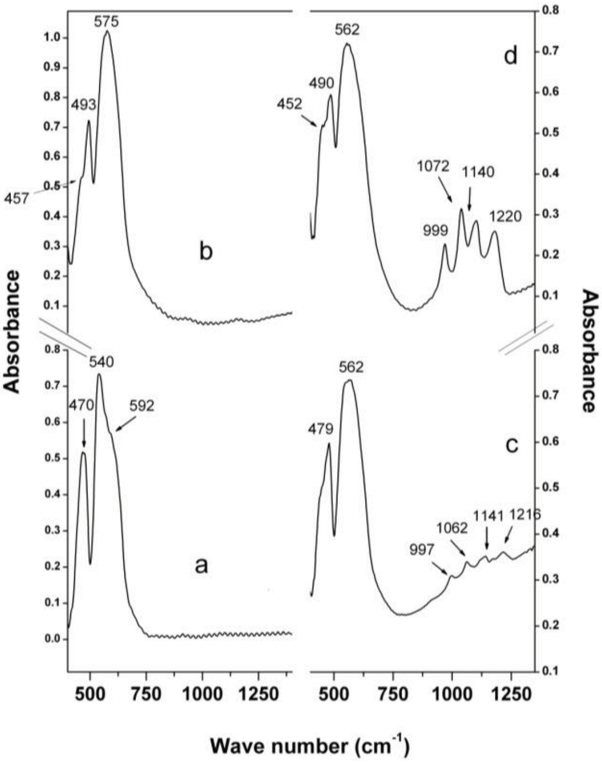

Fig. 5.5. The FTIR spectra of the fresh Fe_2O_3 and $Fe_{1.8}Cr_{0.2}O_3$ catalysts are shown in spectra a and b respectively. The FTIR spectra of the (c) spent Fe_2O_3 and (d) $Fe_{1.8}Cr_{0.2}O_3$ catalysts show four characteristic peaks in the 900-1250 cm^{-1} region which is characteristic of SO stretching in bidentate metal sulfates.

To further stress upon this fact, we mention that additional peaks appear at the range of 1000–1200 cm^{-1} in both the used catalysts which can be assigned to SO bond stretching in metal sulfates. Formation of ferric sulfate was confirmed by XPS but information about the structure of the surface sulfate species was obtained from FTIR spectra of the spent catalyst samples. The spent Fe_2O_3 catalyst exhibited characteristic small peaks at 997, 1062, 1141 and 1216 cm^{-1}, while used $Fe_{1.8}Cr_{0.2}O_3$ exhibited peaks at 999, 1072, 1140 and 1220 cm^{-1} (Fig. 5.5) which is an indicative of C_{2v} symmetry and bidentate sulfate coordination, because a clear distinction between monodentate and bidentate coordination can be made, based on the number of observed bands (monodentate, C_{3v} , with three bands, and bidentate, C_{2v} , with four bands) [15]. The peaks arise due to SO bond stretching in metal sulfates with the lowest wave number peak assigned to υ_1 stretching mode while the higher three peaks are due to υ_3 mode. Sulfur–oxygen double bonds (i.e. SO) show a strong absorption band at 1381 cm^{-1} [16]. Thus, the FTIR spectra of the spent catalyst samples confirm the presence of sulfates and that the sulfates are consistent with bidentate coordination. These metal sulfates are probably the transient intermediates of sulfuric acid decomposition to sulfur dioxide over these metal oxide catalyst. We can also observe from Fig. 4 that the intensity of the FTIR peaks for the sulfate species in the 950 – 1250 cm^{-1} region, is more on the doped catalysts indicating the presence of sulfates in higher amounts in $Fe_{1.8}Cr_{0.2}O_3$ than Fe_2O_3.

The temperature programmed reduction profile of the fresh and spent Fe_2O_3 catalyst is shown in Fig. 5.6. The TPR profile of fresh Fe_2O_3 sample comprises of a prominent band with T_{max} at ~520°C and another broad band with onset of 615°C and having T_{max} at ~ 815°C due to the reduction of $Fe^{3+} \rightarrow Fe^0$ species in three reduction steps: Fe_2O_3 to Fe_3O_4, Fe_3O_4 to FeO and finally FeO to Fe metal. In these samples the second and third peaks merge together to give a broad band at ~815°C. In the spent catalyst sample the reduction profile also shows a two step profile but the first peak is of reasonably higher intensity with T_{max} at ~577°C. This higher intensity is due to increased hydrogen consumption which can be attributed to reaction of surface sulfate species with hydrogen. The reduction of iron sulfate proceeds in hydrogen atmosphere giving hydrogen sulfide [17, 18], and if we consider eqn. 5.4 as the reduction phenomenon then we see that for 1 mole of ferric sulfate to reduce completely to iron, 15 moles of hydrogen will be consumed (eqn. 5.1-5.4) in contrast to 3 moles of hydrogen for reduction of 1 mole of Fe_2O_3 to Fe (eqn. 5.1-5.3).

$3Fe_2O_3 + H_2 = 2Fe_3O_4 + H_2O$ ...5.1

$2Fe_3O_4 + 2H_2 = 6FeO + 2H_2O$ ...5.2

$6FeO + 6H_2 = 6Fe + 6H_2O$ ...5.3

$Fe_2(SO_4)_3 + 12H_2 = Fe_2O_3 + 3H_2S + 9H_2O$ ...5.4

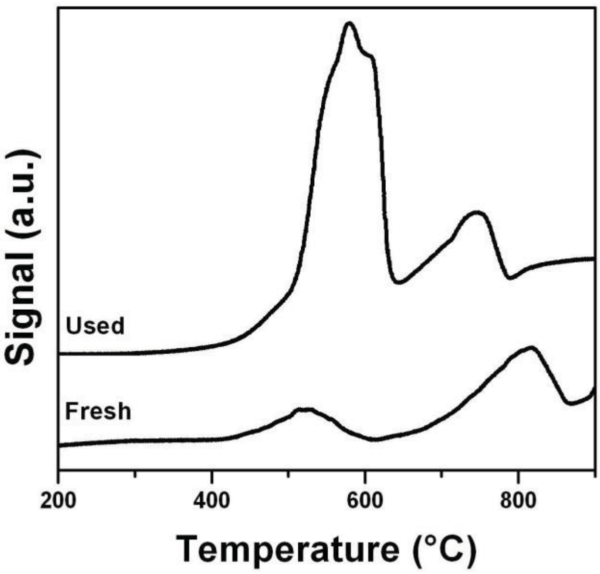

Fig. 5.6. Temperature programmed reduction profile of the fresh and spent Fe_2O_3 *catalysts*

The spent catalyst was also subjected to an evolved gas analysis experiments as a function of temperature and the evolved gases were detected using a quadruple mass spectrometer. Since the spent catalyst was having surface sulfate species, we attempted to track the decomposition profile of this surface sulfate. Ferric sulfate decomposes at higher temperature to form SO_2 and the formation and decomposition of this sulfate was proposed to be the most probable mechanism in our earlier studies (Chapter 3 and 4). Iron oxide catalyst on exposure to SO_3 vapors will form surface sulfate species, but if the temperature of the iron oxide catalyst is higher than the decomposition temperature of iron sulfate, the sulfate becomes a metastable one and the sulfate will quickly decompose to form SO_2. Thus SO_3 decomposition to SO_2 is proposed to follow this concerted mechanism of surface metal sulfate formation and decomposition. The formation of bulk ferric sulfate and its decomposition can be represented by eqn. 5.5 and 5.6 respectively. The temperature of formation of this SO_2 as a decomposition product of sulfate from the spent catalyst sample was pursued by the evolved gas analysis of the spent catalysts. A plot of intensity of evolved gas, having mass number 64 (SO_2), in the temperature range of 250-1000 °C is shown in Fig. 5.7. EGA analysis revealed that both the spent catalysts evolve SO_2 as a decomposition product of its sulfate as the temperature is increased and the pattern of decomposition is similar. If we compare the decomposition temperature it is evident that, the temperature at which maximum SO_2 was evolved or the T_{max} was lower for the chromium substituted sample-suggesting lower temperature decomposition of its surface sulfate. In case of Fe_2O_3, the SO_2 evolution peak is broader and peaking at higher temperatuer suggesting slower kinetics of decomposition of the sulfate than the substituted oxide. Another interesting observation which is evident from the EGA curves is that the amount of SO_2 evolved is much higher in case of $Fe_{1.8}Cr_{0.2}O_3$ that Fe_2O_3.

$Fe_2O_3 + 3SO_3 = Fe_2(SO_4)_3$ ...5.5

$Fe_2(SO_4)_3 = Fe_2O_3 + 3SO_2 + 1.5O_2$ ...5.6

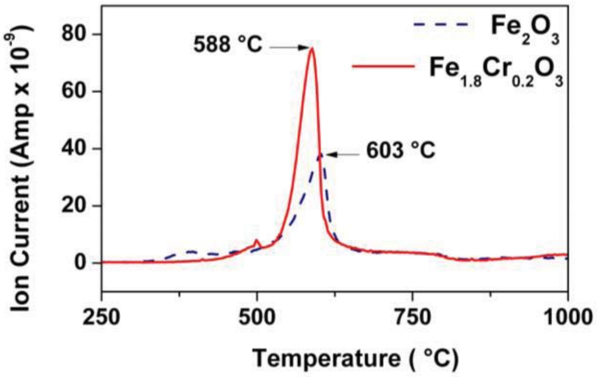

Fig. 5.7. Evolved gas analysis for mass no. 64 in mass spectrometer as a function of temperature of the spent Fe_2O_3 and $Fe_{1.8}Cr_{0.2}O_3$ catalysts post 100 h performance in sulfuric acid decomposition reaction.

The microstructure evolution during this 100 h reaction process can be observed in Fig 5.8 and 5.9 by the Scanning Electron Micrograph of the fresh and used Fe_2O_3 catalyst pellets. Fig 5.8 A shows the clean spherical Fe_2O_3 surface of the unused pellet having a diameter of ~ 5 mm while Fig 5.8 B exhibits the development of cracks on the surface of the spherical catalyst pellets as a result of catalyzing the high temperature sulfuric acid decomposition for 100 h. Agglomeration and grain growth are evident from fig 5.8 C and 5.8 D, where we observe that the ~ 100 nm particles in the unused catalyst grows to 250 – 500 nm. Fig. 5.9 shows the SEM of the used Fe_2O_3 catalyst at different locations and at various magnifications. Although, agglomerated particles of iron oxide were visible on majority of the surface of the used catalyst (as was obvious in Fig. 5.8 B), Fig. 5.9 A show that at certain locations numerous needle shaped crystals were formed which can be attributed to ferric sulfate crystals. One specific location is shown in Fig. 5.9 B where we clearly observe both ferric sulfate crystals and agglomerated ferric oxide particles. The microstructural characteristics were similar in the chromium doped samples. Fig. 5.10 shows the surface morphology of the fresh and used catalyst surfaces of the Cr doped sample. Grain growth and agglomeration is clearly evident from Fig. 10A and 10B while Fig. 10C shows elongated sulfate crystals at a cracked site on the surface of the catalyst pellet. From these SEM images in can be concluded that particle agglomeration is a major phenomenon due to 100 h catalytic runs at high temperature of ~ 800 °C. Also, formation of elongated concentrated crystals at surface sites were evident in small concentration i.e. discontinuity of sulfate concentration exist all over the catalyst surface.

From the SEM micrographs of the spent catalysts it is evident from that particle agglomeration due to sintering at high temperature is more severe on the pristine sample. For both the fresh catalysts the average particle size were ~ 100 nm which increased to ~ 200-400 nm (majority of particles) in the spent Fe_2O_3 in comparison to ~ 150-300 nm in the doped sample. Thus, presence of chromium helps in prevention of sintering in Fe_2O_3 which was observed from our TPR results in our earlier study (chapter 3). Thus, it is expected that the formation of surface sulfate might play a role in the larger decrease in the BET surface area of the spent catalyst in case of $Fe_{1.8}Cr_{0.2}O_3$. In this regard we would like to refer the FTIR spectra of the used catalysts in Fig. 5.5, from where it is evident that the intensity of the sulfate species is more on the doped catalysts indicating the presence of sulfates in higher amounts in the doped catalyst. This fact was further confirmed by our Evolved Gas Analysis results (Fig. 5.7) which showed grater evolution of SO_2 from the doped catalyst than the pristine one. Thus, from the SEM, FTIR and EGA results we can infer that the larger decrease in BET surface area of spent $Fe_{1.8}Cr_{0.2}O_3$ sample than Fe_2O_3 is primarily due to surface sulfate formation.

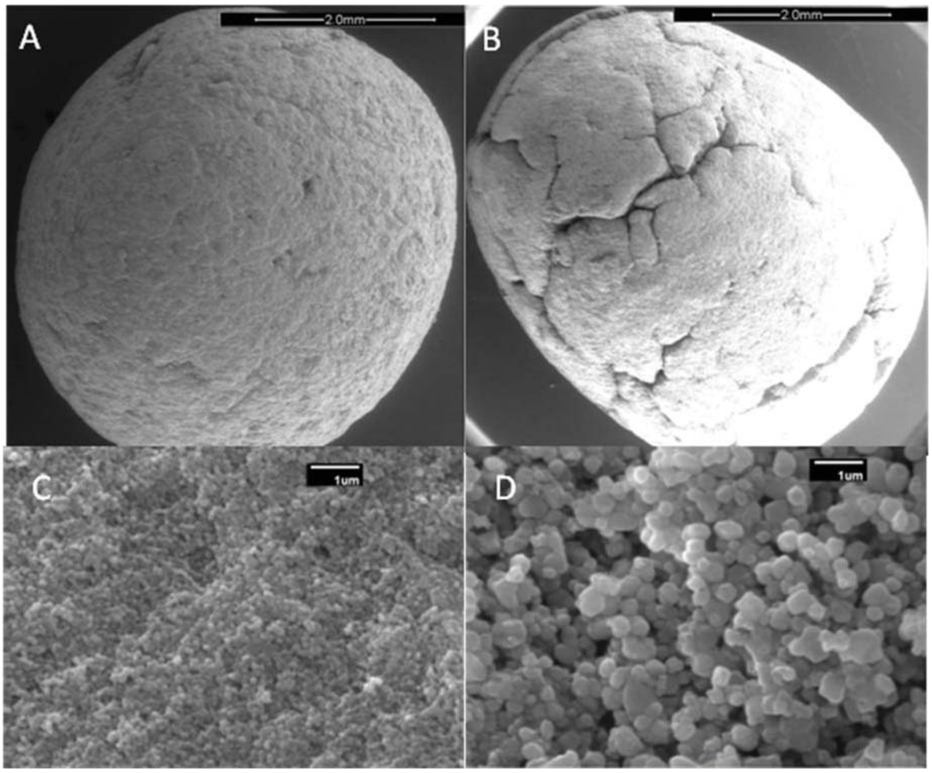

Fig. 5.8. Scanning Electron Micrographs of (A & C) of fresh Fe_2O_3 before reaction and (B &D) of spent Fe_2O_3 collected after 100 h use in high temperature sulfuric acid decomposition reaction

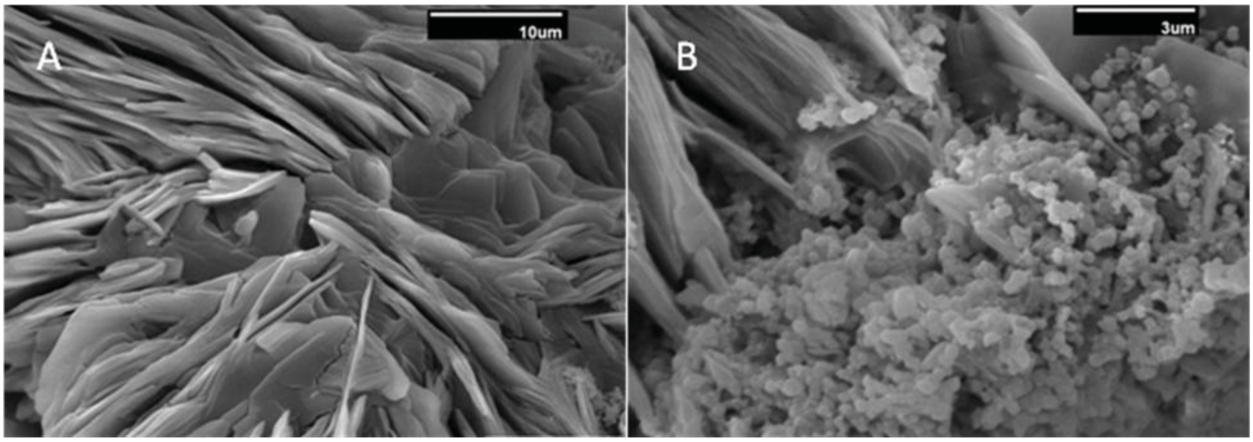

Fig. 5.9. Scanning Electron Micrographs of the used Fe_2O_3 catalyst at different locations and at various magnifications

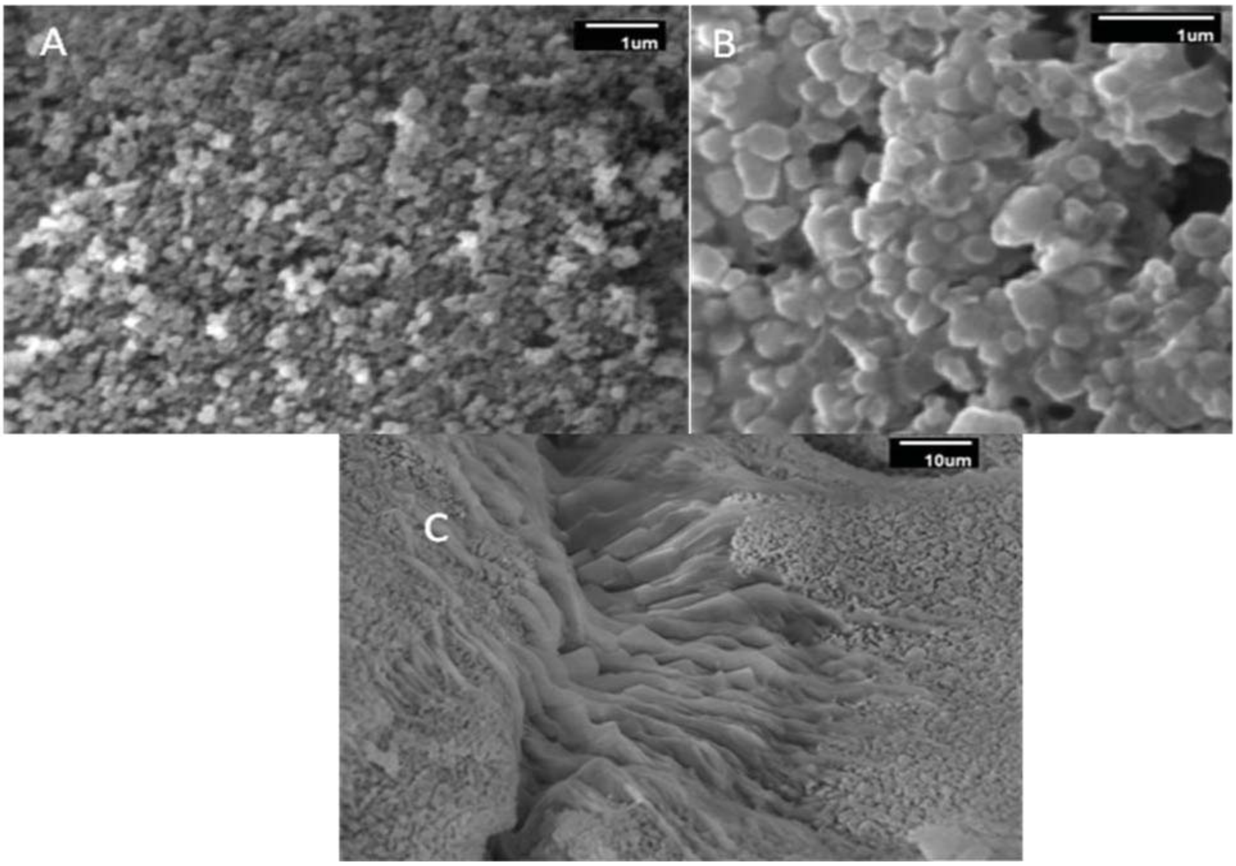

Fig. 5.10. Scanning Electron Micrographs of of fresh $Fe_{1.8}Cr_{0.2}O_3$ (A) before reaction and (B & c) of spent $Fe_{1.8}Cr_{0.2}O_3$ sample collected after 100 h use in high temperature sulfuric acid decomposition reaction

From the ex-situ analysis of the spent catalyst samples we can throw an insight into the mechanism of the high temperature sulfuric acid decomposition reaction. We have discussed in our previous chapter (Chapter 3) that a metal sulfate formation and decomposition route can be a plausible mechanism for the SO_3 decomposition on iron and chromium doped iron oxides. Further, our earlier investigation (Chapter 4) with ferrospinel catalysts for sulfuric acid decomposition helped us to propose a three step model for the decomposition reaction over metal oxides. From the spent catalyst investigations carried out in this work, it can be said that on use for sulfuric acid decomposition reaction, iron oxide catalyst showed evidence of formation of metal sulfates on the surface which again undergoes thermal decomposition producing SO_2. On the basis of our present findings, we suggest the most probable mechanism of sulfuric acid decomposition over doped and undoped iron oxide catalysts in scheme 5.2, which is in accordance to our previous findings. Sulfuric acid at high temperature (>450°C) will thermally decompose to produce sulfur trioxide (SO_3) and moisture (H_2O) (eqn. 5.7). In absence of catalysts these gas phase SO_3 molecules reacts and decompose producing SO_2 and O_2 (eqn. 5.8) as follows:

$H_2SO_4\ (l) \rightarrow H_2O\ (l) + SO_3(g)\ \ (\sim 450\ °C)$ .... (5.7)

$SO_3\ (g) \rightarrow SO_2\ (g) + 1/2O_2\ (g)\ \ (800\text{-}\ 900\ °C)$ …. (5.8)

The oxide catalyst will see these sulfur trioxide and moisture. A SO_3 molecule interacts with such a surface active site ([*]) which might probably be an oxygen vacant site on the metal oxide surface. The generation of this type of active sites (shown in eqn. 5.9 in scheme. 5.2) process requires a reduction of the metal cations i.e $Fe^{3+} \Leftrightarrow Fe^{2+}$ to maintain electroneutrality in the system. Transition metal oxides like Fe_2O_3 are generally n-type semiconductors which lose lattice oxygen on heating, causing anionic vacancies [11], thus oxygen vacant site are available on the catalyst surfaces at high temperatures. These oxygen surface oxygen deficient sites acts as active sites in Fe_2O_3 catalyst even for Fischer-Tropsch synthesis [12].

This process occurs can be treated as a reduction of surface as the reduction of metal ion $M^{x+} \Leftrightarrow M^{(x-1)+}$ is a necessity. The SO_3 molecule generated from sulfuric acid at high temperatures then interacts with these surface active sites to form a bidentate surface sulfate species as shown in eqn. 5.10 in scheme. 5.2. It is important to notice here that out of the four oxygens in a surface sulfate species three came from SO_3 and one from the metal oxide. The sulfate then undergoes decomposition producing SO_2 and the metal oxide as shown in eqn. 5.11 in scheme. 5.2. The reduced metal (M) centers will be subsequently oxidized by the reduction of SO_3 to SO_2. Here also, the redox couples $M^{x+} \Leftrightarrow M^{(x-1)+}$ e.g. $Fe^{3+} \Leftrightarrow Fe^{2+}$ plays a crucial role. Again, the metal oxide liberates the oxygen (eqn. 5.9) from any other surface site and this process is kinetically fast by virtue of the high lattice oxygen mobility in iron oxides. Thus these three steps go on as a concerted mechanism and the decomposition of sulfuric acid proceeds catalytically over iron oxide surfaces. We observed the formation of bidentate metal sulfates from FTIR spectra of the used catalyst of both doped and undoped samples. Again from the thermal decomposition experiments (EGA) we observed the formation of SO_2 from the spent oxide catalyst samples, which must have come from the metal sulfates formed on the spent samples. Thus, metal sulfate formation and its subsequent decomposition can be a possible mechanism by which sulfuric acid decomposition proceeds. The decomposition of SO_3 can be then proposed to occur in three steps as shown in scheme 5.1 over doped and pristine iron oxides.

The first step (eqn 5.9 scheme 5.2) which is the evolution of oxygen has very little kinetic implication since the decomposition temperature being very high (>750°C) the mobility of lattice oxygen of many transition metal oxides are comparable, so that after evolution of the SO_2 molecule from the surface active site an oxygen is liberated from any other site. The second step (eqn 5.10 scheme 5.2) is thermodynamically favorable at lower temperatures (<~ 750°C) as the Gibbs free energy of iron sulfate formation was calculated by

Kim et al [14] and was found to be negative below ~ 780 °C and positive above this temperature. Still, at higher temperatures metastable sulfate formation is definitely possible on all metal oxide surfaces by surface adsorption phenomenon and its rate will depend on the number of surface active sites. But, the next step of SO_2 formation by surface metal sulfate decomposition (eqn 5.11 scheme 5.1) will be governed by the decomposition temperature of the metal sulfate i.e. lower the decomposition temperature faster will be the kinetics of this step. This step or the metal sulfate decomposition step is most crucial as the nature of metal M plays an important role in deciding the rate of decomposition.

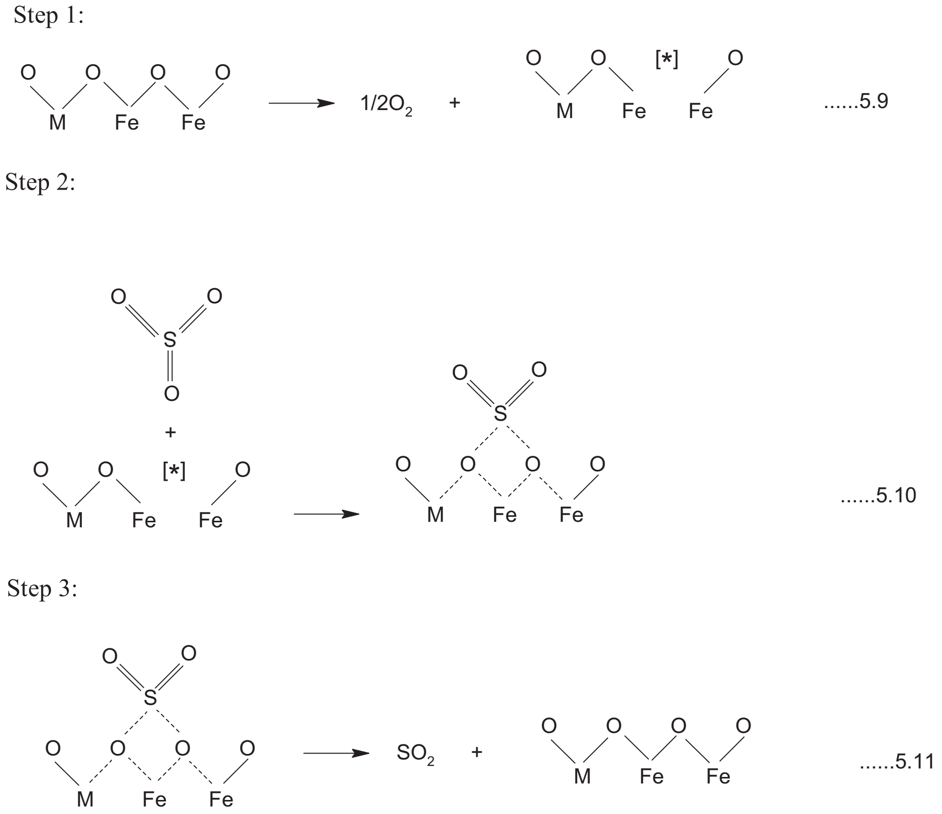

Scheme 5.2: A schematic presentation of proposed mechanism for sulfuric acid decomposition over spinel ferrites. [*] denotes surface active sites.

From the temperature dependent catalytic activity (Fig. 5.1A) we can clearly see that at lower temperatures < 775 °C, the catalytic activity of the doped sample is much higher than the undoped Fe_2O_3. This increased catalytic activity of the doped sample can be attributed to mainly two factors. Firstly, as the EGA experiments showed that the rate of decomposition of the sulfates on the used catalyst is faster from the chromium doped sample the SO_2 evolution will be more facile on the doped oxide than the pristine one. Secondly, the metal sulfate formation and decomposition (eqn 5.9 and 5.10 in scheme 5.1) over iron oxide catalysts involves the working of the vital redox couple $Fe^{3+} \Leftrightarrow Fe^{2+}$. From the TPR results in our earlier work (Chapter 3) we observed that the solid solution of 10 % Cr substitution in Fe_2O_3 lattice has enhanced reproducibility towards repeated reduction-oxidation cycles. Thus working of the redox couple $Fe^{3+} \Leftrightarrow Fe^{2+}$ is more facile in the chromium doped sample. Thus our results show that both Fe_2O_3 and Cr-doped Fe_2O_3 are active formulations for sulfuric acid decomposition without showing any visible deactivation in long term activity runs. The Cr-doped Fe_2O_3 was found to be more active catalyst which is ascribed to its lower thermal stability of its sulfate, improved redox properties and probably more number of catalytic active sites.

5.4. Conclusion

Fe_2O_3 and 10% Cr doped Fe_2O_3 catalyst pellets or granules were tested as catalyst for sulfuric acid decomposition reaction for 100 h at 800 °C and a sulfuric acid flux of 0.63 ml/min (WHSV of 3.4 g acid g^{-1} catalyst h^{-1}), in an indigenously constructed quartz dual tube catalytic reactor which served as an integrated boiler, preheater and decomposer. No decrease in catalytic activity was observed during this long term experiment, although the doped sample exhibited slightly higher catalytic activity throughout. However, in the temperature dependent catalytic runs, the Cr-doped sample showed much higher intrinsic activity at lower temperatures (< 775 °C). Both the catalyst exhibited a loss in catalytic activity when subjected to very high flow of sulfuric acid of 2-10 ml/min. From the ex-situ analysis of the spent catalyst samples the most probable mechanism of the high temperature sulfuric acid decomposition reaction was proposed, which involves metal sulfate formation and then decomposition followed with an oxygen evolution step. The enhanced catalytic activity of Cr-doped Fe_2O_3 was ascribed to its lower thermal stability of its sulfate and improved redox properties.

References:

[1] D. O'Keefe, C. Allen, G. Besenbruch, L. Brown, J. Norman, R. Sharp, K. McCorkle, Int. J. Hydrogen Energ. 7 (1982) 381-392.

[2] L. E. Brecher, S. Spewock, C. J. Warde, Int. J. Hydrogen Energ. 2 (1977) 7-15.

[3] G. E. Beghi, Int. J. Hydrogen Energ. 11 (1986) 761-771.

[4] G. C. Bond, Principles of Catalysis, London Chemical Society, London (1972).

[5] V. S. Jakkal: Powderx: A Fortran software for refining the unit cell parameters from the powder diffraction pattern, Private communication.

[6] F. Magalhaes, M. C. Pereira, S. E. C. Botrel, J. D. Fabris, W. A. Macedo, R. Mendonc¸ R. M. Lago, L.C.A. Oliveira, Applied Catalysis A: General 332 (2007) 115–123.

[7] Handbook of X-ray Photoelectron Spectroscopy; Perkin-Elmer Corp. Physical Electronics Division: New York, 1992.

[8] Diane R. Milburn, Robert A. Keogh, Ram Srinivasan, Burtron H. Davis, Applied Catalysis A: General 147 (1996) 109-125.

[9] S. Richardson, D. J. Vaughan, Mineralogical Magazine, April 1989, Vol. 53, pp. 223-9.

[10] D. R. Milburn, R. A. Keogh, D. E. Sparks, B. H. Davi , Applied Surface Science 126 (1998)11–15.

[11] N. T. McDevitt, and W. L. Baun, Spectrochim. Acta 20 (1964) 799.

[12] U. Schwertmann, R. M. Taylor, Minerals in soil environments (soil science society of America, Inc., Madison, WI, (1977) p. 145.

[13] K. K. Kartha, M. R. Pai, A. M. Banerjee, R. V. Pai, S. S. Meena and S. R. Bharadwaj, J. Molec. Catal. A 335 (2011) 158–168.

[14] J. D Kubicki, K. W Paul and D. L Sparks, Geochemical Transactions 9 (2008) 4.

[15] S. J. Hug J. Coll. Int. Sci. 188 (1997) 415–422.

[16] S. K. Samantaray, K. M. Parida, J. Mater. Sci. 38 (2003) 1835-1848.

[17] Lei Ma, J. Li, Rui Ke, and L. Fu, J. Phys. Chem. C 115 (2011) 7603–7612.

[18] J. D. Henao, B. Wen, and W. M. H. Sachtler J. Phys. Chem. B 109 (2005) 2055-2063.

[19] A. Atkinson and R. I. Taylor J. Phys. Chem. Solid 46(4) (1985) 469-475.

[20] S. Li, W. Ding, G. D. Meitzner and E. Iglesia J. Phys. Chem. B 106 (2002) 85-91.

[21] T. Yamaguchi, T. Jin, K. Tanabe J. Phys. Chem. 90 (1986) 3148-3152.

[22] Tae-Ho Kim, Gyeong-Taek Gong, B. G. Lee, Kwan-Young Lee, Hee-Young Jeon, Chae-Ho Shin, H. Kim, Kwang-Deog Jung, Appl. Catal. A: Gen. 305 (2006) 39–45.

Chapter 6

Performance of Pt/Al_2O_3 catalyst for sulfuric acid decomposition in comparison to iron oxide based catalysts

6.1 Introduction

Earlier results of our investigations (chapter 3-5) have shown effectiveness (chemical and thermal stability and high catalytic activity) of iron oxide based catalysts for decomposition of sulfuric acid both in powder form at a small scale and in pellet form at an enhanced scale. In the present chapter we report the catalytic activities of a commercial Pt (~0.5 wt.%) /Al_2O_3. Such a study was essential from the view point of the conclusion from our previous works that iron based oxide catalyst can be a suitable substitute to noble metal based catalysts for sulfuric acid decomposition reaction. Development of a suitable catalyst for sulfuric acid decomposition stands to be a crucial issue today primarily because of three reasons. Firstly, the kinetics of the reaction is slow so product conversion is low in absence of a catalyst. But, the reaction environment is extremely hostile like high temperatures, presence of aggressive chemicals, including sulfur oxides, high temperature steam and oxygen, so both activity and stability of the catalysts are important. Finally, sulfuric acid decomposition is the thermal to chemical energy conversion step in sulfur based thermochemical cycles for hydrogen generation, which are proposed to be prospective large scale water splitting processes in future using either nuclear or solar heat. We have already reviewed the current global status of catalyst research and development for sulfuric acid decomposition reaction (chapter 1 Section 1.8).

Pt metal based catalysts have been extensively employed as catalysts for sulfuric acid decomposition. Some of the reports include supported platinum catalysts such as (Pt/Al_2O_3, Pt/TiO_2 and Pt/ZrO_2) [1], Pt/TiO_2 (rutile) [2], ($Pt/BaSO_4$) [3] and theoretical studies on supported metal particles (Pd, Pt, Rh, Ir, and Ru supported on titania) [4]. In the demonstration studies on a closed-cycle hydrogen production by the thermochemical water-splitting iodine–sulfur process, JAERI mentions about the use of a (catalyst bed of platinum) [5], while GA reported the use of Pt/ZrO_2, Pt/TiO_2, $Pt/BaSO_4$ and $Pt/A1_2O_3$ for sulfuric acid decomposition reaction [6]. But there are major concerns regarding the use of Pt-based catalysts. The prime factor is the ever rising demand and increasing cost of noble metals which make them less preferred for any catalytic applications when a cheaper and suitable alternative exist. Other concerns with supported noble metals are the problems of leaching in present of the corrosive acidic catalytic environment. Besides, prolonged use at high temperatures results in sintering of the metal particles and a decrease in active metal area and consequent deactivation. Oxidation of the noble metal has also been reported under the reaction conditions of sulfuric acid decomposition [6]. Substrate sulfation is also a deactivation phenomenon for supported noble metals for the acid decomposition reaction as reported by Norman et al [6]. Detailed account of the reaction mechanism is given by Golodates [7], where it is suggested that reaction mechanism proceeds via an adsorption and dissociation of SO_3 at the surface active sites which are the active noble metal centre via the intermediate formation of adduct [$SO_2.O$] on the metal centre.

So, to evaluate the catalytic performance of a Pt-based catalyst under similar environment under which we evaluated the iron oxide based catalysts we studied the catalytic properties of a commercial Pt/Al_2O_3 for sulfuric acid decomposition reaction. The catalytic decomposition of sulfuric acid on the Pt (~0.5 wt.%)/Al_2O_3 catalyst was evaluated both in powder form at a small scale and in pellet form at an enhanced scale. The catalytic activity of Pt /Al_2O_3 pellets were evaluated as a function of temperature (700 °C – 825 °C), flow rate of sulfuric acid (0.2 – 3.5 mlmin^{-1}) and time (100 h). The results are compared with iron oxide catalyst. The physicochemical properties of both the fresh and used alumina-supported Pt catalyst were investigated using BET surface area measurement, hydrogen chemisorption, X-ray powder diffraction, Fourier Transform Infrared Spectroscopy, Scanning Electron Microscopy and transmission electron microscopy to evaluate the stability of the catalyst under the reaction environment.

6.2 Experimental

The Pt (0.5 wt.%)/Al_2O_3 catalyst samples were characterized before and after 100 h use by various techniques. First, the Pt content was evaluated using ICP-AES technique after microwave digestion of the powders in conc. HNO_3-HCl. Powder XRD patterns were recorded in 2θ range of 10-70° (step width 0.02° and step time 1.25 s) using a Philips X-ray Diffractometer (model 1729) equipped with nickel filtered Cu-K_α radiation. A Quantachrome Autosorb-1 analyzer was employed for measurement of BET surface area by recording the nitrogen adsorption isotherms. The FTIR spectra of the solid samples were recorded in KBr using a Jasco FTIR (model 610) in range of 400-4000 cm^{-1} with a resolution of 4 cm^{-1}. The morphological features were analyzed by a Scanning Electron Microscope (Mirero, Korea, model- AIS2100). Prior to SEM examination, the samples were coated with a thin gold layer (~ 150 Å thick) so as to avoid the problem associated with charging.

The catalytic activity of the powdered Pt (~0.5 wt.%)/Al_2O_3 samples were evaluated in the small scale experimental quartz setup which has been described and shown schematically in Fig. 2.17 in Chapter 2. The actual picture of the setup during operation is also shown. In a typical experiment, the powder catalyst sample (200 mg) was loaded into the catalytic reactor at room temperature and a flow of nitrogen (HP) at a rate of 40 ml min^{-1} was initiated. The catalyst zone furnace temperature was increased to initial reaction temperature of 650 °C over a time interval of 1 h. Concentrated sulfuric acid was then pumped into the system (WHSV ~ 27.6 g acid g^{-1} h^{-1}) by syringe pump and it was carried by the carrier to the pre-heater, where the acid vaporized (~400 °C) and then finally decomposed to SO_2, O_2 and H_2O over the catalyst bed. The unreacted SO_3 recombined with H_2O in the condenser downstream and was collected as a liquid solution. The gaseous SO_2 and O_2 products along with carrier were then passed through a NaOH solution, where SO_2 was trapped and the other gases (O_2 and N_2) were vented. For analysis of product SO_2, the decrease in concentration of the NaOH solution was measured by titration with standardized sulfuric acid solution. Similarly, the sulfuric acid collected downstream of the reactor (i.e., unreacted sulfuric acid) was determined by chemical titration with standardized NaOH solution. The percentage conversion of sulfuric acid to sulfur dioxide was calculated based on the product yield of SO_2. The catalytic activities were measured in the temperature range of 650 °C to 825 °C with an interval of 50°C and were held at each measuring temperature for 1 h. The activity measurements were repeated and after the final measurement at 825 °C the supply of acid and the electric furnace were switched off.

The catalytic properties of pellets of Pt/Al_2O_3 samples were also evaluated in a quartz reactor with annular configuration as shown in Fig. 2.18 (chapter 2). The catalytic activity of 20 g of Pt (~0.5 wt.%)/Al_2O_3 pellets (4-6 mm) were evaluated in the said catalytic reactor as a function of temperature (700 °C – 825 °C) and time (100 h) at a sulfuric acid flux 0.63 mlmin^{-1} (WHSV of 3.4 g acid g^{-1} catalyst h^{-1}). The catalytic activity was also evaluated as a function of flux of sulfuric acid in the range of 0.2 – 3.5 mlmin^{-1}. The product analysis was done by chemical titrimetric method. The evaluation procedure was same as that adapted for iron oxide based catalysts in chapter 5.

6.3 Results and discussion

The temperature dependent catalytic activity of Pt (~0.5 wt.%) /Al_2O_3 catalyst in powder form carried out in the small scale catalytic reactor (Fig. 2.17 in Chapter 2) at a WHSV of 27.6 g acid g^{-1} h^{-1} is shown in Fig. 6.1. The catalytic activity increased with an increase in temperature. For comparison the catalytic activity of Fe_2O_3 powder prepared by precipitation technique (the catalyst prepared and evaluated in Chapter 5) is also shown.

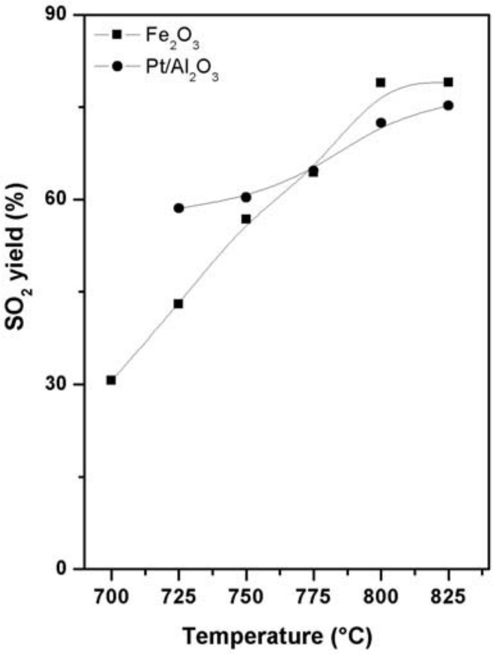

Fig. 6.1. Comparison of temperature dependent catalytic activity of Pt/Al_2O_3 with Fe_2O_3 in small scale reactor with 0.2 g powder catalyst at a WHSV of ~ 27 g acid g^{-1} cat h^{-1}

Catalytic activity of both the samples increases with temperature, Fe_2O_3 showing maximum SO_2 yield of ~ 79% at 825 °C. At lower temperatures in the range of 725 – 750 °C the SO_2 yield for the supported noble metal catalyst was found to be higher than that of Fe_2O_3 while at higher temperatures in the range of 800 – 825 °C the catalytic activities of the two catalysts were comparable. It is pertinent to mention here that blank experiments in absence of catalysts verified that homogeneous vapor phase reaction did not occur under these conditions. Thus, Fe_2O_3 can be a good substitute for noble metal catalysts for sulfuric acid decomposition reaction at temperatures of 750 °C and above. Since, the operation temperatures of the high temperature nuclear reactors would be high (>800 °C), Fe_2O_3 can be considered as a suitable catalyst for sulfuric acid decomposition.

The temperature dependent catalytic activity of the Pt/Al_2O_3 pellets employed in the dual quartz tube catalytic reactor (Fig. 2.18 in Chapter 2) at a WHSV of ~3.4 g acid g^{-1} h^{-1} (flow of 0.63 $mlmin^{-1}$ of liquid sulfuric acid over 20 g of catalyst bed) is shown in Fig. 6.2A. The SO_2 yield increased with the increase in temperature with the maximum reaching to ~ 83 % at 825 °C. For the sake of comparison the catalytic activities of both Fe_2O_3 and $Fe_{1.8}Cr_{0.2}O_3$ pellets are also shown in the Fig. 6.2. We can see from the Fig. that the temperature dependent catalytic activity of Pt/Al_2O_3 pellets is almost similar to $Fe_{1.8}Cr_{0.2}O_3$ pellets.

To test the stability of the catalyst pellets of Pt/Al_2O_3 for a longer duration 100 h time on stream run was also conducted at 800 °C (WHSV of ~3.4 g acid g^{-1} h^{-1}) as was carried out for the doped and undoped iron oxide pellets (Chapter 5). Comparison of the SO_2 conversion obtained during the 100 h run (with measurements at 2 h interval) for all the three catalysts is shown in Fig. 6.2 B. Contrary to the results obtained for the oxide catalysts the Pt-catalysts showed a minor decrease in activity during this longer duration activity measurements. The catalytic activity decreased from a SO_2 conversion of ~ 80 % to ~ 73 %. But, in the case of the oxide catalysts any such decrease in catalytic activity was not noticed during the 100 h run at 800 °C.

The catalytic activity as a function of flow rate of sulfuric acid was also carried out and is shown in Fig 6.2 C. A decrease in catalytic activity is visible for all the three catalysts with an increase in flux of liquid sulfuric acid from 0.2 $mlmin^{-1}$ to 2.5 $mlmin^{-1}$.

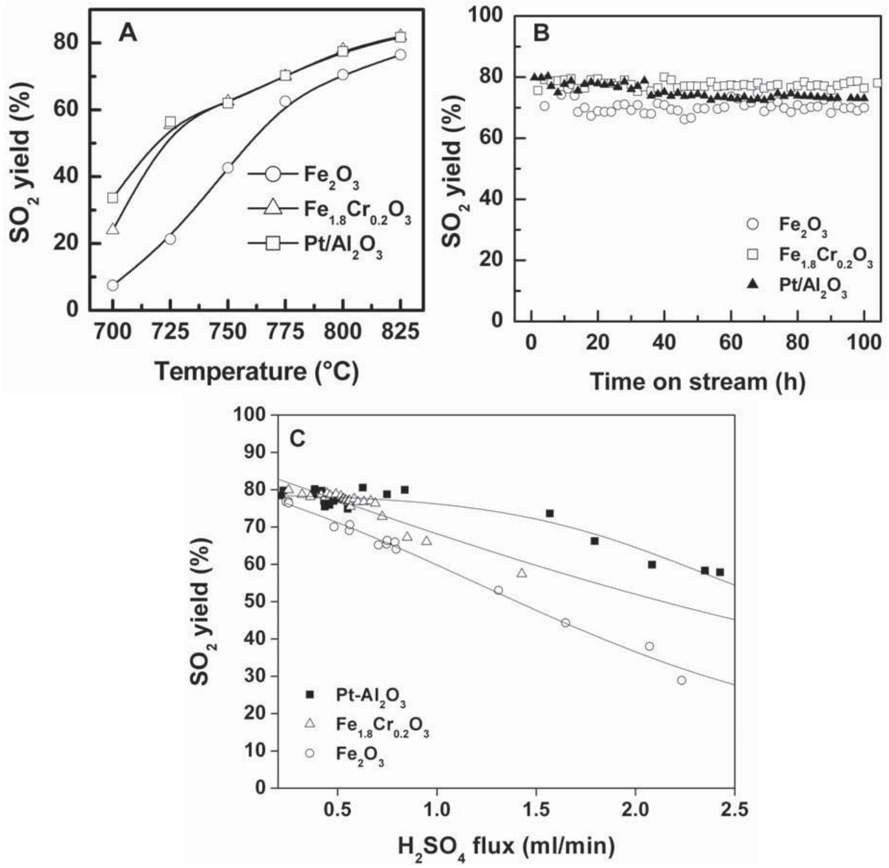

Fig. 6.2. Comparison of catalytic performance of pellets (4-6 mm diameter) of Pt/Al_2O_3 with Fe_2O_3 and $Fe_{1.8}Cr_{0.2}O_3$ for sulfuric acid decomposition with 20 g catalyst in the dual quartz tube integrated boiler, preheater and decomposer. (A) Temperature dependent catalytic activity at WHSV of 3.4 g acid g^{-1} catalyst h^{-1} (acid flux 0.63 $mlmin^{-1}$) (B) catalytic activity with respect to time on stream for 100 h at 800 °C with WHSV of 3.4 g acid g^{-1} catalyst h^{-1}(acid flux 0.63 $mlmin^{-1}$)and (C) catalytic activity as a function of flux of sulfuric acid from 0.2 to 2.5 $mlmin^{-1}$

The fresh Pt (~0.5 wt.%) /Al_2O_3 catalyst before carrying out the catalysis experiments was characterized for composition, structure and morphology by various techniques. The catalyst after 100 h use was collected and also well characterized. The results were compared to analyze the obvious changes occurring to the Pt/Al_2O_3 sample on catalytic use and is presented below.

Fig. 6.3 shows the photograph of the fresh and the spent catalyst samples.

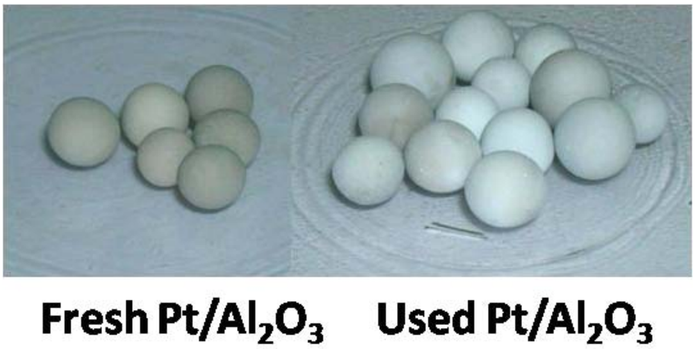

Fig. 6.3. Photograph of the fresh and spent (used) catalyst pellets

Table 6.1 summarizes the results obtained for metal loading (ICP-AES), BET-surface area, H_2-uptake (pulsed chemisorptions) for the fresh and the spent Pt (~0.5 wt.%) /Al_2O_3 catalyst. The commercial catalyst was found to have a Pt-metal loading of 0.47 wt.% and on catalytic use for more that 100 h for sulfuric acid decomposition there was a decrease in metal content to 0.44 wt.%. The BET-surface area of the fresh catalyst was found to be 261 m^2g^{-1} and on use the surface area decreases to 145 m^2g^{-1}. Drastic decrease in H_2-uptake from pulsed chemisorptions experiments was observed. The fresh catalyst shows an uptake of 17.2 $\mu molg^{-1}$ which corresponds to a very good dispersion of 71 % (H/Pt = 1). The value decrease abruptly in the spent catalyst.

Table 6.1. Characteristics of the fresh and used Pt /Al_2O_3 *catalysts*

Sample	Pt metal content (@)	BET surface Area (#)	H_2 uptake (#)	Dispersion
	Wt %	m^2g^{-1}	$\mu molg^{-1}$	
Fresh Pt/Al_2O_3	0.47	261	17.2	0.71
Used Pt/Al_2O_3	0.44	145	0.3	0.01

The adsorption-desorption isotherms for the fresh and the spent catalyst are shown in Fig. 6.4. First none of the isotherms are similar to the so called Type I isotherms encountered for microporous samples indicating the absence of any major amount of small pores in the alumina support. The fresh catalyst shows a Type IV isotherm generally encountered for mesoporous samples. This indicates the mesoporous nature of the alumina support of the fresh catalyst. The hysteresis indicates the presence of cylindrical pores. Significant change in the porosity occurs due to catalytic use for 100 h at 800 °C, with the spent catalyst showing a major change in the adsorption-desorption isotherm (Fig. 6.4). The isotherm for the spent catalyst is convex but not completely convex throughout which is generally encountered for non-porous or macroporous solids with weak adsorptions. Also hysteresis in the adsorption-desorption isotherm is absent. These results definitely indicate a reduction in porosity of the support alumina which is further supported by the observation of the decrease in surface area.

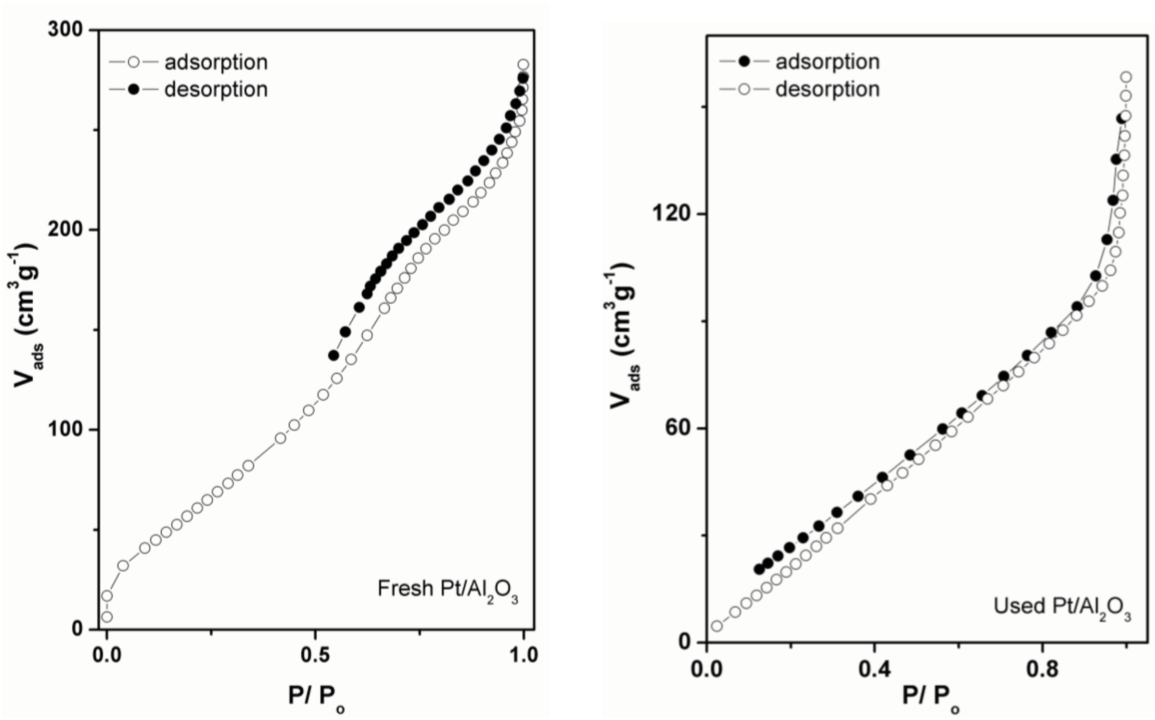

Fig. 6.4. Adsorption-Desorption isotherms for the fresh and the spent Pt/Al_2O_3 *catalyst*

Fig. 6.5 shows the powder X-ray diffraction pattern of the fresh and the used Pt/Al_2O_3 catalyst. The fresh sample consists mainly of three phases – AlO(OH) phase (JCPDS card No. 211307) peak position marked by "$" in the Fig. 6.5, γ-Al_2O_3 phase (JCPDS card No. 290063) peak position marked "&"and the Pt phase (JCPDS card No.) peaks marked by "#" in Fig.6.5. Thus we see that the powder XRD pattern of the sample is able to identify even the minority phase of ~0.47 wt. % of Pt in the alumina sample. The peak due to γ-Al_2O_3 phase at 2θ position of 39.52 ° and that due to Pt phase at 39.76 ° can be resolved (marked in Fig. 6.5). We observed that the alumina sample contains a considerable amount of AlO(OH) phase in addition to the γ-Al_2O_3 phase. This oxy-hydroxide phase AlO(OH) commonly termed as boehmite is generally the precursor to γ-Al_2O_3 phase and completely converssts to the alumina phase at higher temperatures [8-10]. The powder X-ray diffraction pattern of the used catalyst sample is quite interesting. The used sample shows evidence of both the γ-Al_2O_3 and Pt phases identified in the fresh catalyst but the AlO(OH) phase disappeared. Besides, $Al_2(SO_4)_3$ phase was detected in the spent sample (peaks marked by *). Thus, alumina reacts with the reactant SO_3 at high temperatures generating the aluminum sulfate phase. Metal sulfates were detected in minor amounts (sulfate detected not in XRD but in FTIR-Chapter 5) in the spent doped and undoped iron oxide catalysts, but it was found that it decomposes at the reaction temperature (EGA results –Chapter 5). Thus, metal sulfates were proposed to be the reaction intermediates i.e. the sulfates were metastable species formed at the high reaction temperature (temperatures where the metal sulfate is supposed to decompose forming SO_2) and its formation and decomposition was the mechanism of sulfuric acid decomposition. But the $Al_2(SO_4)_3$ here are stable species and does not decompose at the reaction temperature, and so we notice prominent peaks of its phase in the XRD pattern and hence this is a case of substrate sulfation as noticed by Norman et al [6]. The reactant reacts with the substrate forming stable aluminumm sulfate phase. In addition to these phases that are present in the used catalyst, many other alumina phases have been generated which prominently includes the κ-Al_2O_3, δ-Al_2O_3, θ-Al_2O_3 and α-Al_2O_3 phases. The phase transformation of aluminas is itself a topic of great interest and is well studied and still pursued [11-14]. The detailed powder XRD investigation of the different phases of alumina has been carried out by Santos et al [14], where it is shown that boehmite undergoes phase transformations with an increase in temperature the sequence being boehmite to gamma to delta to theta to alpha phase. We obtained the κ-Al_2O_3 phase additionally. Again, phase transformation of γ-Al_2O_3 to α-Al_2O_3 was observed above 1000 °C by Legros et al [15-16]. But in our case the time becomes an important factor- significantly high of 100 h sufficient for partial formation of α-Al_2O_3 phase. Thus prolonged use (100 h) at a temperature of ~ 800 °C converts the γ-Al_2O_3 and the AlO(OH) phases to other phases of alumina. Any sort of phase transformations of the support alumina has a significant impact on the catalytic properties of alumina supported metal catalysts [17], in some cases reported as being the major cause for deactivation [18] while in others the phase of the alumina used has a major impact on catalyst stability [19].

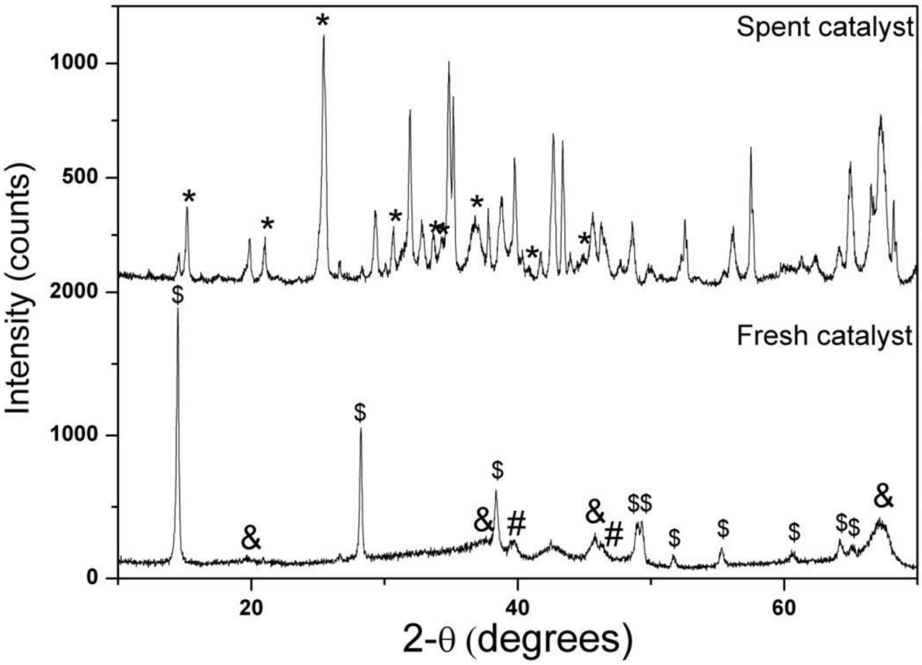

*Fig. 6.5. Powder XRD patterns of the fresh and spent Pt/Al_2O_3 catalyst $ - AlO(OH) phase; & - γ-Al_2O_3 phase; # - Pt phase; * - $Al_2(SO_4)_3$ phase*

The FTIR spectra of the fresh and the spent Pt/Al_2O_3 catalyst are shown in Fig. 6.6 and the results supports our XRD findings. The characteristic FTIR peaks in the 500-750 cm^{-1} i.e. 621 cm^{-1} and 721 cm^{-1} are assigned to the vibrations of AlO_6 present in boehmite [8] and the 895 cm^{-1} shoulder due to the presence of γ-AlO_4 [20]. All these peaks are combined characteristic of γ-Al_2O_3 and boehmite [8]. But these peaks are not clearly visible in the spent sample. The 1072 cm^{-1} peak is due to the presence of δ(OH) in boehmite [8] and are absent in the spent sample supporting our XRD observations. The spent catalyst on the other hand shows peaks in the 1100 cm^{-1} to 1325 cm^{-1} due the S-O stretching frequencies present in sulfates.

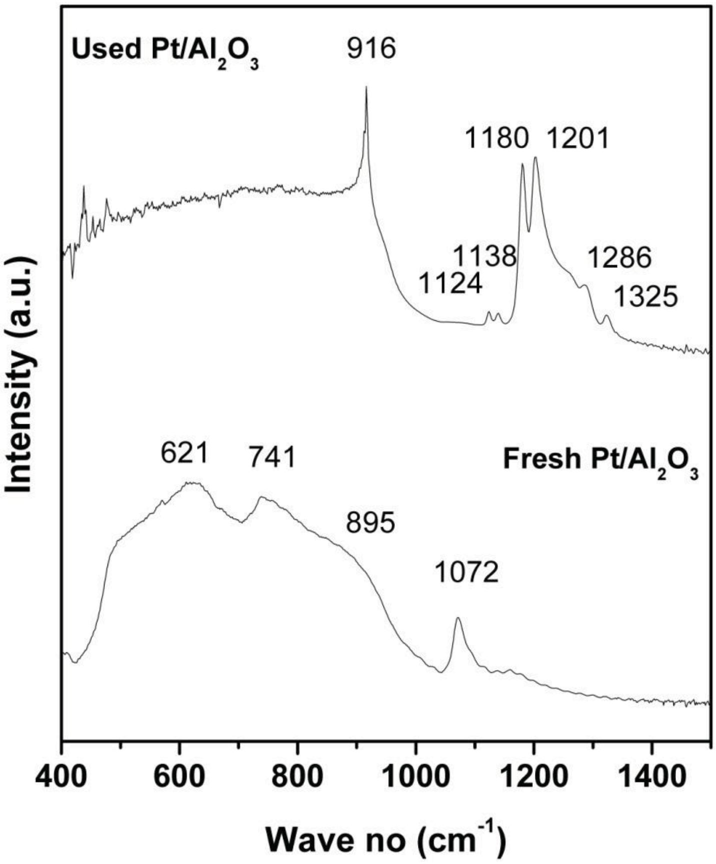

Fig. 6.6. FTIR spectra of the fresh and spent Pt/Al_2O_3 catalyst

The Scanning electron micrograph images of the fresh and spent Pt/Al_2O_3 catalyst are shown in Fig. 6.7. The size (5 mm diameter) and the spherical shape of the pellets can be seen in Fig. 6.7. The SEM image of the fresh catalyst shows the alumina particles having very large variation both in size (100 nm to 10 μm) and shape. The grain boundaries are clearly visible. In contrast the spent catalyst does not exhibit clear grain boundaries and particles are not distinct. Thus sintering and densification of the support alumina is indicated.

This densification process causes a reduction in porosity which supports our earlier observation in the N_2 adsorption-desorption isotherms. Thus on prolonged catalytic use the microstructure of the surface undergoes major changes – sintering and densification of alumina occurs along with a reduction in porosity and the sulfate phase formed is also dense. The sintering and densification of porous or nanocrystalline powders is generally observed on prolonged heating at higher temperature and this topic has been studied in great details and comprehensively reviewed [21-23]. The EDX spectra of the samples are also shown in Fig. 6.7. The spectra indicate the presence of O, Al and Pt in the fresh catalyst while S is present additionally in the spent samples. This S obviously comes from the $Al_2(SO_4)_3$ phase detected in the spent catalyst sample.

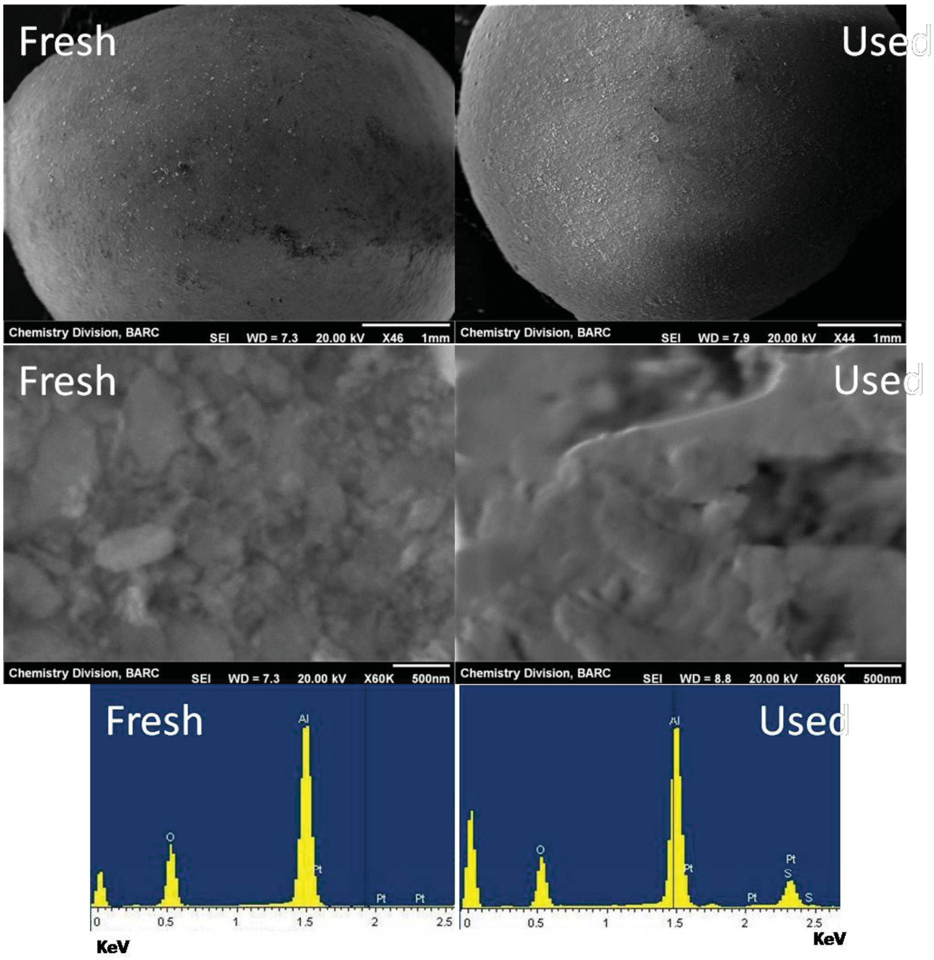

Fig. 6.7. SEM-EDX images of the fresh and spent of the Pt/Al_2O_3 catalyst

The morphological characters of the fresh and spent Pt/Al_2O_3 catalyst samples were further evaluated by TEM. Fig. 6.8 exhibits the dispersion of the Pt particles on the fresh commercial Pt/Al_2O_3 along with the EDS image and the particle size distribution. We can observe from the images that very fine Pt particles are uniformly distributed over the larger alumina grains. Due to z-contrast the Pt particles appear as darker dots over the alumina grains in the bright field TEM images. The Pt particles are highly monodisperse of the order of ~ 2-3 nm. The histogram of the size distribution of the Pt-particles shows the narrow distribution of particle size. The EDS pattern is also shown which depicts the presence of Pt. The high resolution TEM image along with the magnified view of a selected portion of the HRTEM image is shown in Fig. 6.9. The metal support interaction is evident from this image. Also the shape and size of the Pt nano particles are more distinctly viewed from these images. It is clear that in addition to the spherical particles some different shaped particles are seen (marked and magnified). The crystallinity of the support is visibly understood from the lattice fringes present but the lattice spacings of the Pt-particles are not clearly seen.

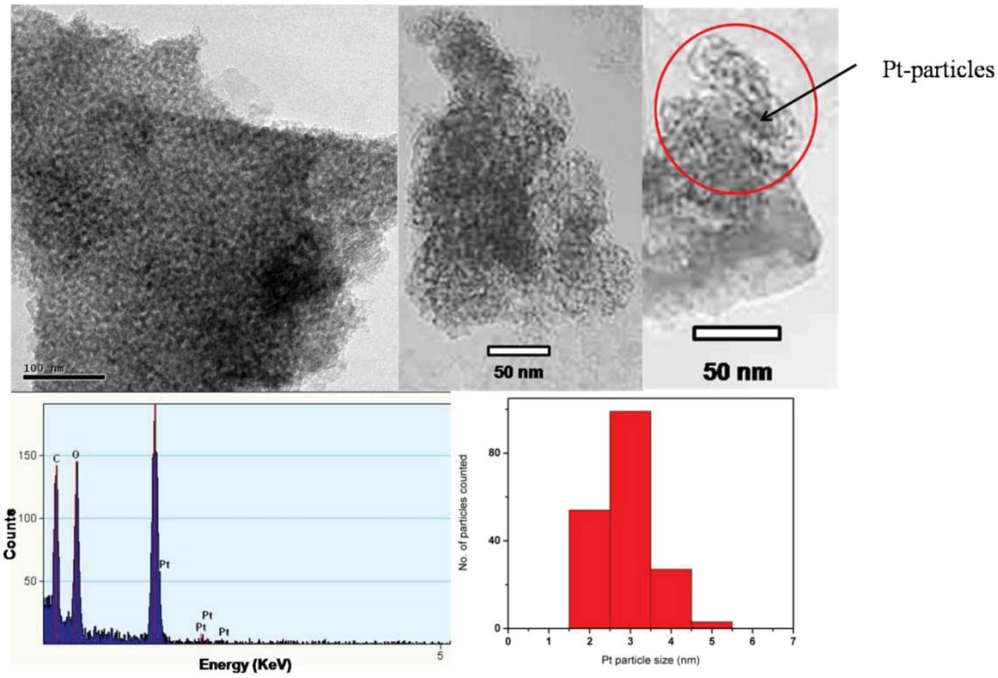

Fig. 6.8. TEM-EDS images of the fresh Pt/Al_2O_3 catalyst along with the particle size distribution

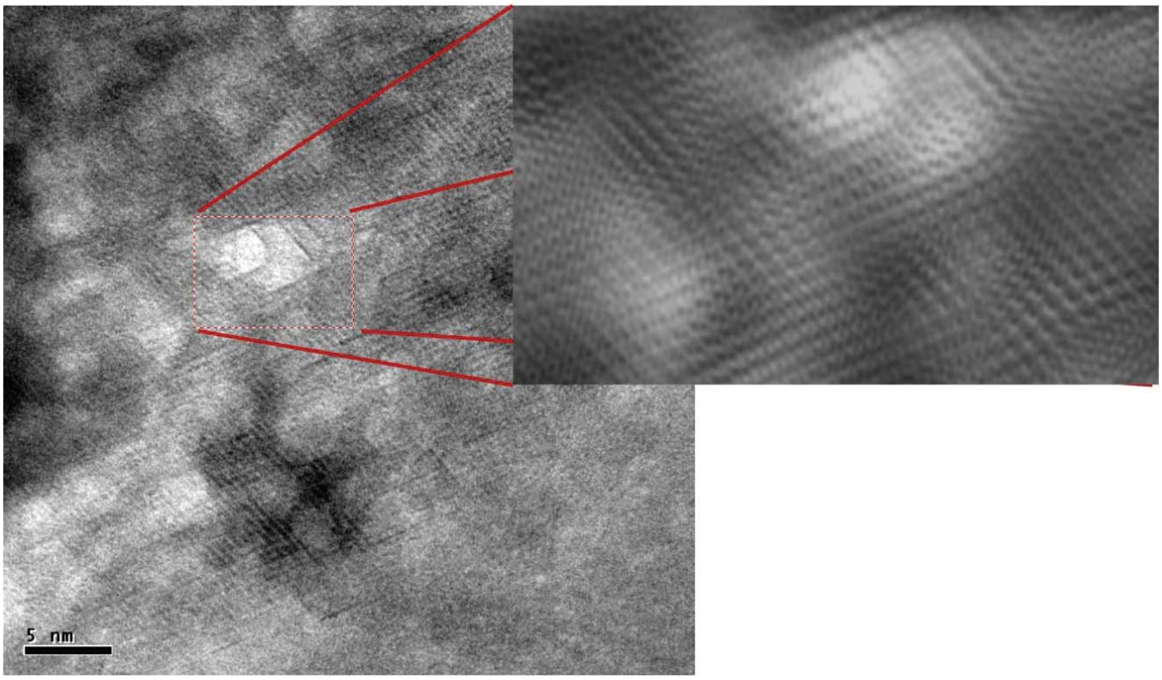

Fig. 6.9. HRTEM image of the fresh Pt/Al_2O_3 *catalyst along with a magnified view of a selected portion (rectangular box outlined)*

The agglomeration of the Pt-particles on use for sulfuric acid decomposition at high temperatures is clearly visible from the TEM images of the used catalyst samples shown in Fig. 6.10. The morphological changes of the platinum metal particles are distinctly visible. Metal particle agglomeration results in very poor dispersion of platinum along the support. Platinum agglomerates of varied shape and size are now non-uniformly scattered over the support grain. To strengthen this aspect further TEM images were recorded at different regions of the copper grid on which the used sample was dispersed. One such typical result is shown in Fig. 6.11 where we can observe a Pt particle of the order of 80 nm. The EDS spectra show the presence of Al, Pt, O and even S.

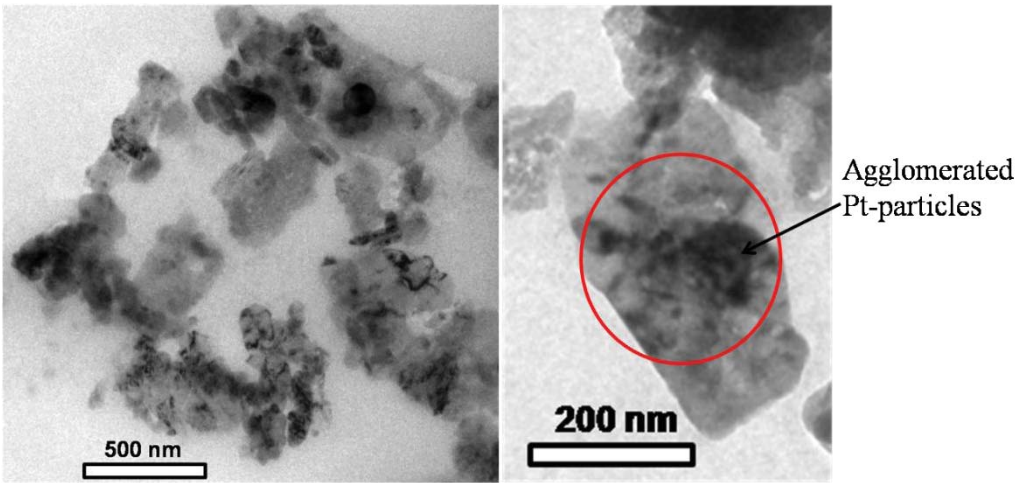

Fig. 6.10. TEM images of the used Pt/Al_2O_3 *catalyst*

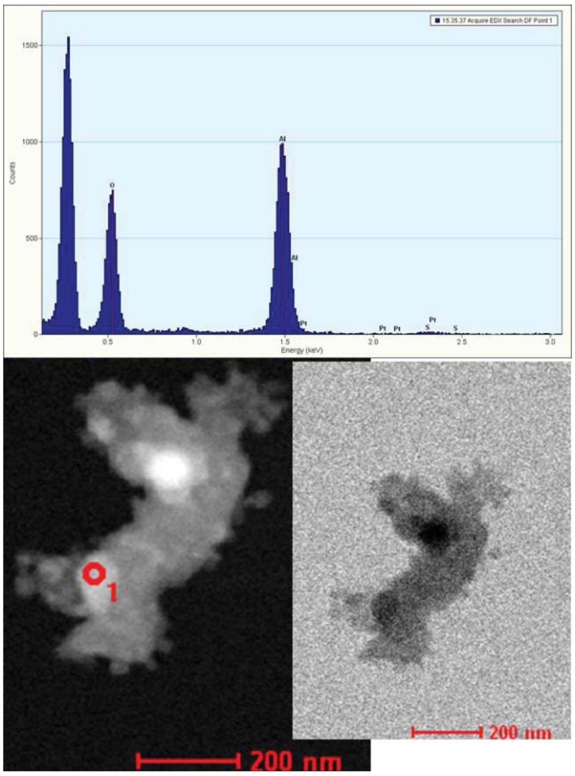

Fig. 6.11. Dark and bright field TEM image of a chosen grain of the used Pt/Al_2O_3 *catalyst along with EDS of a selected region (*O_1*) showing Pt- particles of size of 80 nm.*

Thus the ex-situ characterization provides light on the changes in physical and chemical properties of the Pt/Al_2O_3 catalyst pellets due to use for sulfuric acid decomposition under harsh catalytic environment (high temperature, steam, corrosive oxides of sulfur and oxygen). The surface area of the catalyst decreases along with a decrease in H_2 uptake in pulsed chemisorptions experiments. A reduction in porosity of the support was observed both by nitrogen adsorption desorption isotherm and SEM. Aluminum sulfate stable phase was detected in the powder X-ray diffraction pattern of the spent catalyst which was further verified by FTIR. Finally the platinum metal particle agglomeration was observed from the TEM images. Thus, surface area reduction, substrate sulfation, porosity loss and metal particle agglomeration are the major physicochemical changes observed for Pt/Al_2O_3 catalyst due to use in sulfuric acid decomposition at 800 °C for 100 h.

6.4 Conclusion

Commercial Pt (~0.5 wt.%)/Al_2O_3 pellets (4-6 mm diameter) were employed as catalysts for sulfuric acid decomposition reaction under similar conditions used earlier with iron oxide and chromium doped iron oxide pellets. The SO_2 yield increased with the increase in temperature for the Pt/Al_2O_3 pellets at a WHSV of ~3.4 g acid g^{-1} h^{-1} (flow of 0.63 $mlmin^{-1}$ of liquid sulfuric acid over 20 g of catalyst bed) with the maximum reaching to ~ 83 % at 825 °C. The SO_2 yield for of Pt/Al_2O_3 pellets is similar to $Fe_{1.8}Cr_{0.2}O_3$ pellets employed earlier, (Chapter 5) throughout the temperature range of 700 °C to 825 °C. In a typical 100 h catalytic run at 800 °C and a WHSV of ~3.4 g acid g^{-1} h^{-1}, the Pt/Al_2O_3 catalyst suffered a decrease in SO_2 yield from 80 % to 73 %. But any such decrease in catalytic activity was not observed for the iron oxide pellet catalyst earlier (Chapter 5). To investigate the probable cause for this decrease both the fresh and the spent catalyst was analyzed for structure and morphology by various techniques viz. ICP-AES, H_2-pulsed chemisorptions, N_2-BET-surface area, N_2-adsorption-desorption isotherm, powder XRD, FTIR, SEM and TEM. Reduction in N_2-BET-surface area, alumina substrate sulfation, reduction in porosity of support alumina, phase transformation of the alumina support and metal particle agglomeration are the major physicochemical changes observed for Pt/Al_2O_3 catalyst due to use in sulfuric acid decomposition at 800 °C for 100 h. Since the reaction proceeds via adsorption and dissociation of SO_3 at the surface active sites which are the active noble metal centres the metal particle agglomeration is supposed to be playing the major role in the deactivation noticed for the supported platinum catalyst.

The outcome from our investigations of both the oxide based catalyst and the conventional supported noble metal catalyst (Chapter 3, 4, 5 and 6) is that the $Fe_{1.8}Cr_{0.2}O_3$ composition stands best among all the catalyst investigated. On the basis of the overall results obtained from our studies we recommended the $Fe_{1.8}Cr_{0.2}O_3$ catalyst for use in the Sulfur-Iodine demonstration facility at Chemical Technology Division, an engineering division in BARC, who has taken up the task of demonstration of the sulfur-iodine cycle at a laboratory scale in quartz with a target H_2 generation rate of 150 lph.

References:

1. D. M. Ginosar, L. M. Petkovic, A. W. Glenn, K. C. Burch Int. J. Hydrogen Energy 32(4) (2007) 482-488.
2. L. M. Petkovic, D. M. Ginosar, H. W. Rollins, K. C. Burch, P. J. Pinhero, H. H. Farrell, Appl. Catal. A 338 (2008) 27-36.
3. B. M. Nagaraja, K. D. Jung, B. S. Ahn, H. Abimanyu, K. S. Yoo Ind. Eng. Chem. Res. 48 (2009) 1451–1457.
4. S. N. Rashkeev, D. M. Ginosar, L. M. Petkovic, H. H. Farrell, Catal. Today 139(4) (2009) 291–298.
5. S. Kubo, H. Nakajima, S. Kasahara, S. Higashi, T. Masaki, H. Abe et al. Nucl. Eng. Des. 233 (2004) 347–354.
6. J. H. Norman, G. E. Besenbruch, L. C. Brown, D. R. O'Keefe, C. L. Allen General Atomic Company Report GA-A16713;1982.
7. G. I. Golodates, Heterogeneous catalytic reaction involving molecular oxygen, Elsevier Science Publisher

8. Seung-Moon Kim, Yun-Jo Lee, Jong Wook Bae, H.S. Potdar, Ki-Won Jun, Appl. Catal. A: Gen. 348 (2008) 113–120.
9. R. Vidruk, M. V. Landau, M. Herskowitz, V. Ezersky, A. Goldbourt, J. Catal. 282 (2011) 215–227.
10. Y. Liu, Fei-Yang Huang, Jian-Mei Li, Wei-Zheng Weng, Chun-Rong Luo, Mei-Liu Wang, Wen-Sheng Xia, Chuan-Jing Huang, Hui-Lin Wan, J. Catal. 256 (2008) 192–203.
11. Y. Wang, K. Shih, X. Jiang, Ceram. Int. 38 (2012) 1879–1886.
12. R. S. Zhou, R. L. Snyder, Acta Crystallogr. B 47 (1991) 617–630.
13. Y. Wang, C. Suryanarayana, J. Am. Ceram. Soc. 88 (2005) 780–783.
14. P. Souza Santos, H. Souza Santos, S.P. Toledo, Mater. Res. 3(4) (2000) 104-114.
15. C. Legros, C. Carry, P. Bowen, H. Hofmann, J. Eur. Ceram. Soc. 19 (1999) 1967.
16. C. Legros, F. Herbst, S. Lartigue-Korinek, C. Carry, P. Bowen, Rev. Metall. 99 (2002) 1073.
17. N. Jiang, K.S.R. Rao, M.-J. Jin, S.-E. Park, Appl. Catal. A: Gen. (2012), doi:10.1016/j.apcata.2012.03.001
18. Seon-Ju Park, Jong Wook Bae, Gyu-In Jung, Kyoung-Su Ha, Ki-Won Jun, Yun-Jo Lee, Hae-Gu Park, Appl. Catal. A: Gen. 413– 414 (2012) 310– 321.
19. M. G. Álvarez, M. Plísková, A. M. Segarra, F. Medina, F. Figueras, Appl. Catal. B: Environ. 113– 114 (2012) 212– 220.
20. G.K. Priya, P. Padmaja, K.G.K. Warrier, A.D. Damodaran, G. Aruldhas, J. Mater. Sci. Lett. 16 (1997) 1584–1587.
21. M.N. Rahaman, Ceramic Processing and Sintering, Marcel Dekker, New York, 2003.
22. S.-J.L. Kang, Sintering, Densification, Grain Growth and Microstructure, Elsevier, Amsterdam, 2005.

23. R. Haim, M. Levin, A. Shlayer, C. Estournes, Adv. Appl. Ceram. 107 (2008) 159.

Chapter 7

Indium Titanate as a Photocatalyst for Hydrogen Generation

7.1. Introduction

Efficient photocatalytic hydrogen generation from water which involves the conversion of solar energy into hydrogen assisted by semiconductor photocatalysts, is one of the most promising technologies for the future energy solutions because hydrogen can potentially be generated in a clean and sustainable manner [1-4]. It is attractive as it provides a viable solution for energy and environment based issues arised due to depleting fossil fuels and evolution of green house gases. In the search for efficient photocatalysts under visible light for hydrogen generation from water, a variety of semiconductors based on TiO_2, tantalates, titanates nitrides, niobates sulphides, oxysulfides, oxynitrides, have been extensively studied and have been reviewed in details in chapter 1 (section 1.11) of this thesis and also in several articles [1-4]. In fact, the work done by Maeda et al [5] using GaN:ZnO solid solutions still stands as the most active photocatalyst for water splitting reaction under visible light. The quantum efficiency of overall water splitting on this catalyst was found to be about 2.5% at 420–440 nm, which is about an order of magnitude higher than the earlier reported activity of photocatalysts used in overall water splitting under visible light. Similarly $Cr_xRh_{2-x}O_3$/GaN:ZnO [6] and Ru/$SrTiO_3$:Rh-$BiVO_4$ [7] photocatalysts respond to about 500 nm for overall water splitting thus approaching the required target in terms of wavelength but the quantum yield (30% in terms of quantum yield) is quite low [4]. Hence, the development of new and superior photocatalyst materials is still a major issue.

A variety of ternary metal oxide semiconductors based on niobates, tanatalates and titanates, such as $InTaO_4$, $NaTaO_3$, $Bi_2Ti_2O_7$, and $La_2Ti_2O_7$ have been extensively studied [8-12]. A common structural feature of all these photocatalysts is the presence of $[BO_6]$ (B= Ti, In, Nb, Ta, etc.) octahedral moiety, which are considered to be active motifs for hydrogen generation reaction. The In_2TiO_5 is composed of the octahedral $[TiO_6]$ and $[InO_6]$ motifs, containing both early-transition metal (d_0) and p-block metal (d_{10}), where the $[InO_6]$ octahedra in the crystal structure are considered to favour the mobility of charge carriers and elevate the photocatalytic activity. Up to now, very few studies have been reported on In_2TiO_5 as a potential photocatalyst. Gaewdang et al. [13] studied the luminescent properties and structure details of indium titanate. Wang et al. [14] evaluated the photocatalytic activity of bulk In_2TiO_5 for methyl orange degradation. Photoactivity of vanadium-doped In_2TiO_5 semiconductors synthesized by the ceramic route was investigated by Shah et al. [15].

In this chapter we report the studies carried out on In_2TiO_5 as a prospective photocatalyst material for photocatalytic hydrogen generation from water. The syntheses of In_2TiO_5 have been carried out by conventional solid state method to obtain well crystalline particles and also nanocrystalline In_2TiO_5 have been prepared by solvothermal and polyol methods. The detailed crystallographic structure of In_2TiO_5 was obtained from Rietveld refinement of the X-Ray diffraction pattern. The synthesized samples have been well characterized by various instrumental techniques and finally we have evaluated the thermophysical properties and photocatalytic activities for hydrogen generation from water. Electronic structure and density of states for bulk In_2TiO_5 have been calculated by TB-LMTO method. Photocatalytic activity of the indium titanate prepared by different methods for hydrogen generation under UV-visible irradiation (16% UV + visible) was studied and compared with the bulk In_2TiO_5 as well as TiO_2 (P25) photocatalyst. The effect of structure on photoactivity was also discussed.

7.2 Experimental and Theoretical Methods

7.2.1 Synthesis of Catalyst

7.2.1.1 Solid State Synthesis

Mixed oxides with nominal composition In_2TiO_5were synthesized through ceramic route by mixing reactant oxides in appropriate stoichiometry as depicted by following equation:

$In_2O_3 + TiO_2 \rightarrow In_2TiO_5$

The pellets of homogeneous mixtures were calcined, first at 650°C followed by high temperature calcination at 800°, 1000°C and finally at 1250°C for 24 h, with intermittent grindings so as to ensure the uniformity and the completion of the reaction.

7.2.1.2 Polyol synthesis

Indium titanate was prepared by polyol method by hydrolysis of indium chloride and titanium chloride in ethylene glycol under reflux for 5 hours. Stoichiometric quantities (2:1) of Indium (0.6889 g, 6 mmol) and titanium (0.1436 g, 3 mmol) metal were separately dissolved in minimum amount of concentrated hydrochloric acid. To remove excess of acid water was added to the solution and boiled and this process was repeated 4 times. The solutions after cooling were added separately to 20 ml of ethylene glycol and then mixed together to make the total volume to ~ 40 ml. The mixed solution was heated to 100 °C. To this solution urea (2 g) dissolved in 40 ml of ethylene glycol was added and a clear solution was obtained. The temperature of this solution was then raised to ~ 170 °C and then maintained at this temperature for 5 h for completion of hydrolysis. After cooling to room temperature the white precipitate was separated from the suspension by centrifugation. The precipitate was washed several times with acetone and ethanol and then dried in the oven at 120 °C. The sample was then calcined at 900 °C for 4 h to obtain nanocrystalline In_2TiO_5.

7.2.1.3 Solvothermal synthesis

In(acac)$_3$ (99.99 %, Aldrich), Ti(IV) isopropoxide (97 %, Aldrich) and benzyl alcohol (> 98%, Fluka) were used as received. In a typical procedure, In(acac)$_3$ (0.50 g, 1.21 mmol) and Ti(IV) isopropoxide (0.176 g, 0.62 mmol) were dissolved in 40 ml of benzyl alcohol. After vigorously stirring for 15 minutes, the colorless solution was transferred to a Teflon cup in a stainless-steel-lined autoclave. The autoclave was maintained at 220 ^{o}C for 48 h. After cooling to room temperature, the resulting off-white product was collected by centrifugation, thoroughly washed with chloroform and methanol and finally dried in vacuum for 4 h at room temperature. The product so obtained was calcined at 400 ^{o}C for 16 h to remove all the organic impurities. After calcining, a white color product was obtained and this product was used for photoactivity and other measurements. Further, the product obtained after heating at 400 ^{o}C was subjected to XRD as a function of temperature to see the phase formation process of the In_2TiO_5 nanoparticles.

7.2.2 Characterization

Powder XRD patterns of indium titanate obtained by different methods were recorded in 2θ range of 10-70° using a Philips X-ray Diffractometer (model X'Pert pro) equipped with nickel filtered Cu-K_α radiation at 40 kV and 30 mA. The powder HT-XRD patterns were also recorded in the same instrument for solvothermal sample. Rietveld profile refinement was employed to extract the lattice parameters of the well crystalline In_2TiO_5 sample prepared by solid state and solvothermal methods (phase observed in HT-XRD pattern recorded at 1000°C). Whereas, LeBail refinement, was used to model the XRD profile with broad peaks to get the accurate cell parameters of In_2TiO_5 nanoparticles obtained at 400°C.

Low resolution transmission electron microscopy (TEM) images were collected with a Philips CM 200 microscope operating at an accelerating voltage of 200 kV. High resolution TEM (HR-TEM) images were taken with a FEI-Tecnai G-20 microscope operating at 200 kV. Scanning electron microscopy (SEM) images were taken using a Tescan Vega MV 2300T/40 microscope. Chemical composition of the samples was determined by energy dispersive X-ray analysis (EDS) using an INCA Energy 250 instrument coupled to Vega MV2300T/40 scanning electron microscope. N_2- Brunauer-Emmett-Teller surface areas were measured with Quantachrome Autosorb-1 analyzer using nitrogen as the adsorbing gas.

Diffuse reflectance spectra were recorded on a UV-visible spectrometer (JASCO model V-530 spectrophotometer).). Band gap was estimated by Kubelka-Munk calculation using indirect transition.

7.2.3 TB/LMTO method

Self-consistent scalar relativistic TB-LMTO method within atomic sphere approximation (ASA) was employed, which also included the so-called 'combined correction' term [16-18]. The potential is calculated using the density functional prescription under the Local density approximation (LDA). Von Barth-Hedin parametrization of the exchange-correlation potential was employed for this purpose. The tetrahedron method of Brillouin zone (k-space) integration was used. Spin-averaged LDA calculations were performed on unit cell of In_2TiO_5, containing 64 atoms (16 In, 8 Ti, 40 O atoms). It should be pointed out here that inspite of the fact that the TB-LMTO-ASA method does not include spin-orbit effects, which may become important for heavier elements ($Z > 50$), the method is well-known to produce qualitative features of the band structure quite accurately.

7.2.4 Photocatalytic Activity

Photocatalytic activity was evaluated in a rectangular quartz reactor of dimensions (10 x 2.1 x 2.1 cm^3), equipped with a sampling port provided with a septum through which gas mixture could be removed for analysis. 0.1 g of catalyst was kept in contact with water + methanol mixtures (total volume of 15 ml, 2:1 v/v %) for conducting the photocatalysis experiment. The reactor was then irradiated horizontally in a chamber close to a water-cooled medium pressure mercury vapour lamp (Hg, Ace Glass Inc., 450W). The typical outer irradiation quartz assembly consisting of photoreactor and the light source along with water circulation jacket is shown in Fig. 2.21 (Chapter 2). The lamp exhibits broad range emission spectra (Fig. 2.20 Chapter 2) with maxima at both UV and the visible range (16% UV, rest is visible light). The reaction products were analysed after every 2 h for a period of ~ 6-8 h using a gas chromatograph (Netel (Michro-1100), India) equipped with a thermal conductivity detector (TCD), molecular sieve column (4m length) with argon as carrier was employed in the isothermal temperature mode at 50°C oven temperature. The intensity of the light source was measured using a calibrated precision lux meter (cal-Light 400).

7.3 Results

7.3.1 Powder XRD

7.3.1.1 Solid State method synthesized In_2TiO_5

Fig. 7.1 shows the powder XRD patterns of In_2TiO_5 which matches well with that of orthorhombic In_2TiO_5 (JCPDS card No.30-0640, space group Pnma). To determine the detailed crystal structure under investigation Rietveld refinement of the diffraction patterns were carried out. The accurate unit cell parameters as obtained from Rietveld refinement results are a = 7.238(2) Å, b = 3.496 (1) Å, c = 14.877(5) Å, and V = 376.47(2) Å^3. The values are in good agreement with the reported ICDD values for bulk In_2TiO_5 (JCPDS card no.: 30-0640). The calculated pattern from Rietveld refinement for indium titanate and the difference pattern between the calculated and observed patterns are also shown in Fig. 7.1. The reliability factor obtained for the indium titanate Rietveld refinement is a κ^2 of 2.89.

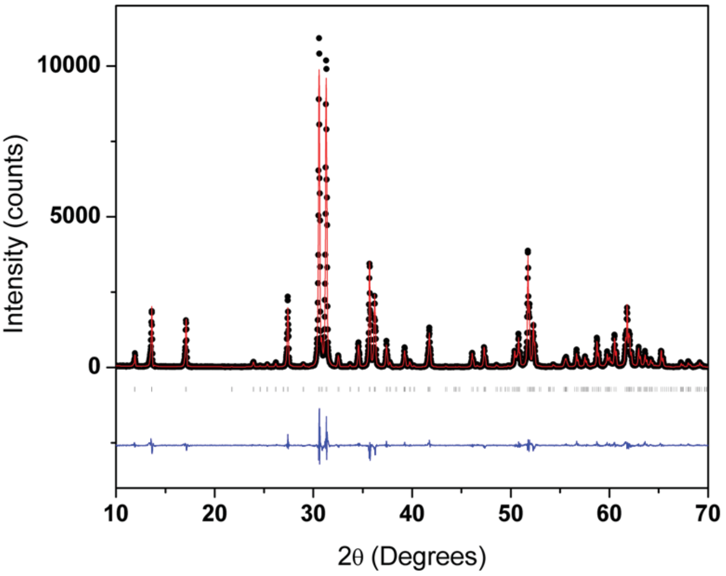

Fig. 7.1. Rietveld refined profiles of X-ray diffraction data of In_2TiO_5. The dots represent the observed data, while the solid line through dots is the calculated profile, and vertical tics represent Bragg reflections for the phase. The difference pattern is also shown below the vertical tics.

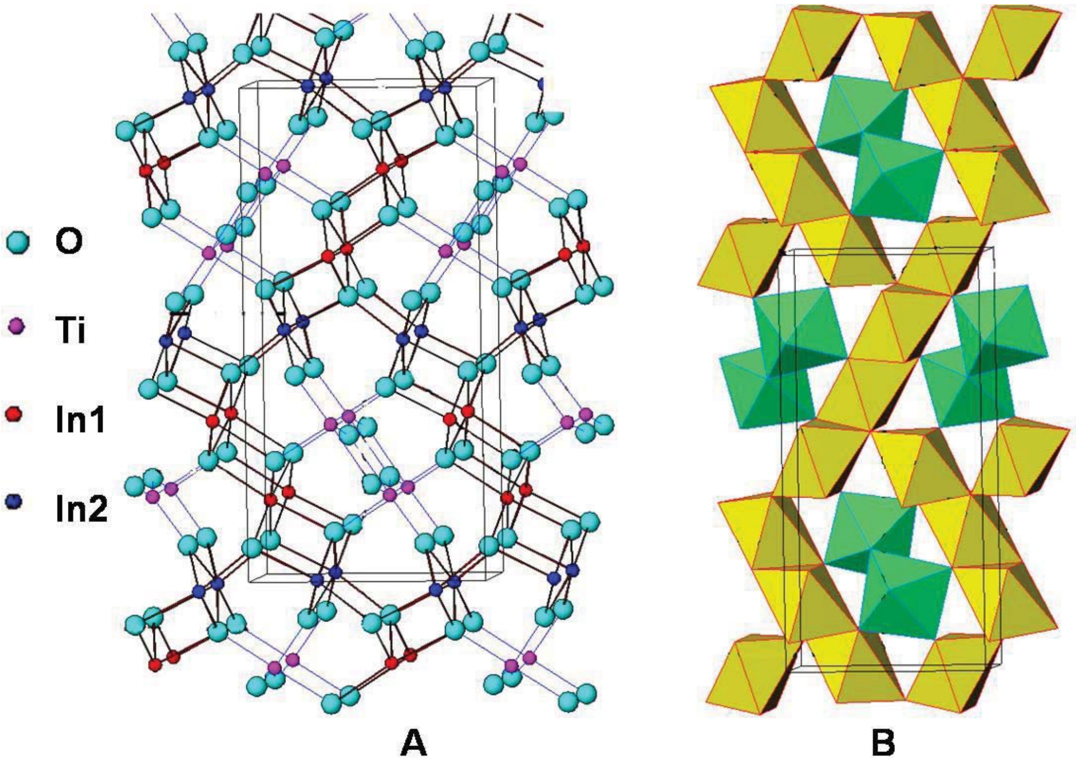

Fig. 7.2 The (A) structure of In_2TiO_5 as derived from the Rietveld refinement of the XRD pattern, also showing the unit cell. The (B) structure showing the polyhedral arrangement, with the yellow octahedra being that of InO_6 while the green octahedra that of TiO_6

The crystal structure as derived from the refinement is shown in Fig. 7.2. The unit cell consists of four formula units i.e. the unit cell formula is $In_8Ti_4O_{20}$. All the 32 atoms and their co-ordinates in a unit cell as derived from the Rietveld results are listed in Table 7.1. The structure contains two types of Indium atoms (In1 and In2). Each indium atom forms an InO_6 octahedral unit and so two types of InO_6 units are present in In_2TiO_5. Both the types of InO_6 octahedral units are independently edge shared and form infinite chains. The Ti atoms also form distorted TiO_6 octahedral units. The InO_6 octahedral units are corner shared with the TiO_6 octahedral units.

Table. 7.1 All atoms in In_2TiO_5 unit cell

Atom no.	Type		Crystal coordinates			Symmetry
			x	y	z	
1	In1	49	0.09881	0.25	0.0841	1
2	In1	49	0.40119	0.75	0.5841	2
3	In1	49	0.59881	0.25	0.4159	3
4	In1	49	0.90119	0.75	0.9159	4
5	In2	49	0.3288	0.75	0.23942	1
6	In2	49	0.1712	0.25	0.73942	2
7	In2	49	0.8288	0.75	0.26058	3
8	In2	49	0.6712	0.25	0.76058	4
9	Ti	22	0.10262	0.25	0.42414	1
10	Ti	22	0.39738	0.75	0.92414	2
11	Ti	22	0.60262	0.25	0.07586	3
12	Ti	22	0.89738	0.75	0.57586	4
13	O1	8	0.24766	0.25	0.32514	1
14	O1	8	0.25234	0.75	0.82514	2
15	O1	8	0.74766	0.25	0.17486	3
16	O1	8	0.75234	0.75	0.67486	4
17	O2	8	0.34031	0.25	0.49766	1
18	O2	8	0.15969	0.75	0.99766	2
19	O2	8	0.84031	0.25	0.00234	3
20	O2	8	0.65969	0.75	0.50234	4
21	O3	8	0.36692	0.25	0.15011	1
22	O3	8	0.13308	0.75	0.65011	2
23	O3	8	0.86692	0.25	0.34989	3
24	O3	8	0.63308	0.75	0.84989	4
25	O4	8	0.05667	0.75	0.17294	1

26	O4	8	0.44333	0.25	0.67294	2
27	O4	8	0.55667	0.75	0.32706	3
28	O4	8	0.94333	0.25	0.82706	4
29	O5	8	0.06528	0.75	0.45378	1
30	O5	8	0.43472	0.25	0.95378	2
31	O5	8	0.56528	0.75	0.04622	3
32	O5	8	0.93472	0.25	0.54622	4

7.3.1.2 In_2TiO_5 via polyol mediated synthesis

The XRD pattern of the In_2TiO_5 sample synthesized by polyol method and calcined at 900 °C is shown in Fig. 7.3. Similar to the solid state method the sample crystallized in orthorhombic unit cell of In_2TiO_5.

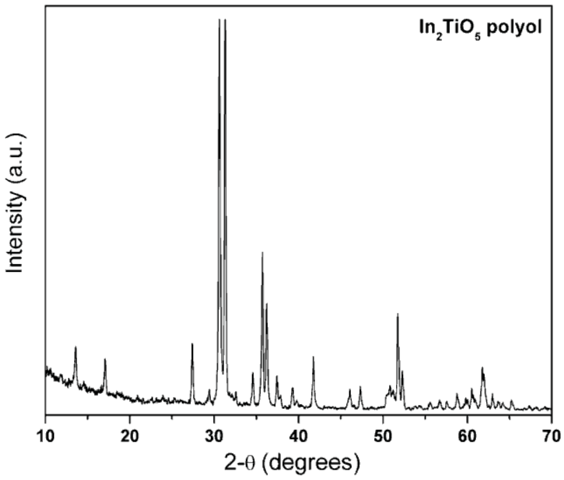

Fig. 7.3. Powder X-ray diffraction pattern of In_2TiO_5 *sample prepared by polyol method and calcined at 900 °C.*

7.3.1.3 In_2TiO_5 by Solvothermal method

Fig. 7.4a displays the room temperature powder X-ray diffraction (XRD) pattern of the synthesized white product obtained after annealing at 400 °C for 16 hours. The broad reflections observed in the pattern reveal the presence of nanosized crystallites. The peak positions observed closely match with the orthorhombic phase of In_2TiO_5 and there is no indication for the presence of any other crystalline phases like oxides of indium or titanium, indicating that the product is pure crystalline indium titanate. The broadened XRD pattern observed could not be refined with the structural model of In_2TiO_5 considering the size and strain broadening parameters. Hence the profile was modeled by LeBail refinement to get the accurate unit cell parameters and the values are *a* = 7.183(2) Å, *b* = 3.494 (1) Å, *c* = 14.922(5) Å, and V = 374.6(2) Å^3. The values are in good agreement with the reported ICDD values for bulk In_2TiO_5.

HT-XRD patterns (Fig. 7.4) of the product have also been recorded to observe the effect of annealing temperature on crystal growth of the In_2TiO_5 phase. Here the as-synthesised product obtained by solvothermal method after heating at 400 ^{o}C for 16 h, was subjected to XRD as a function of temperature. The irreversible formation of In_2TiO_5 phase is indicated by XRD pattern of the cooled sample (Fig. 7.4g) which is identical to the pattern observed for well crystalline In_2TiO_5 phase corresponding to the one recorded at 1000°C (Fig. 7.4f). Due to the expansion of unit cell at high temperature, a shift towards the lower 2θ values is observed in the XRD reflections recorded at 1000 °C (Fig. 7.4f) as compared to that at room temperature (Fig. 7.4g). The reflections observed in Fig. 7.4g can be indexed according to the orthorhombic phase of In_2TiO_5 (space group Pnma (62), JCPDS card no. 82-0326). The extracted values of lattice parameters for the crystalline In_2TiO_5 sample obtained from the Rietveld profile refinement are *a* = 7.2344(2) Å, *b* = 3.4986(1) Å, *c* = 14.0408 (5) Å, and V = 376.81(2) Å^3.

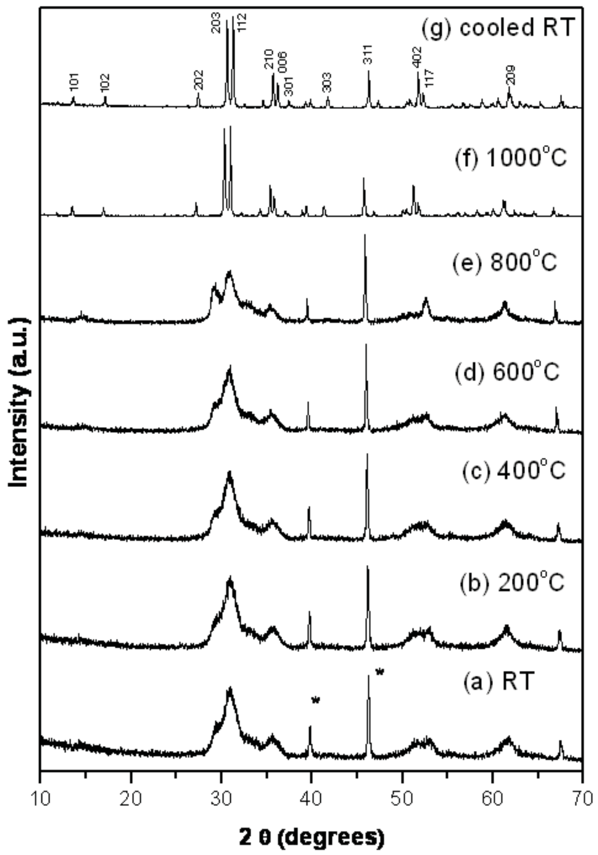

*Fig. 7.4. HT-XRD (high temperature XRD) patterns obtained after heating In_2TiO_5 nanoparticles at different temperatures (a-f) upto 1000°C. A room temperature XRD pattern of the cooled sample is also shown (g). * Peaks due to Platinum sample holder.*

7.3.2. Morphological features (N_2-BET, SEM and TEM)

7.3.2.1 Solid State method synthesized In_2TiO_5

The N_2-BET surface area of the samples synthesised by solid state method was as expected very low (~ 4 m^2g^{-1}) owing to the high temperature calcinations employed for long duration for phase formation. The Scanning Electron Microscopic (SEM) image of the solid state method prepared catalyst is shown in Fig. 7.5. We can see the particles have a faceted structure with clear grain boundaries. The sizes of the particles are large in the range of ~ 1-3 μm.

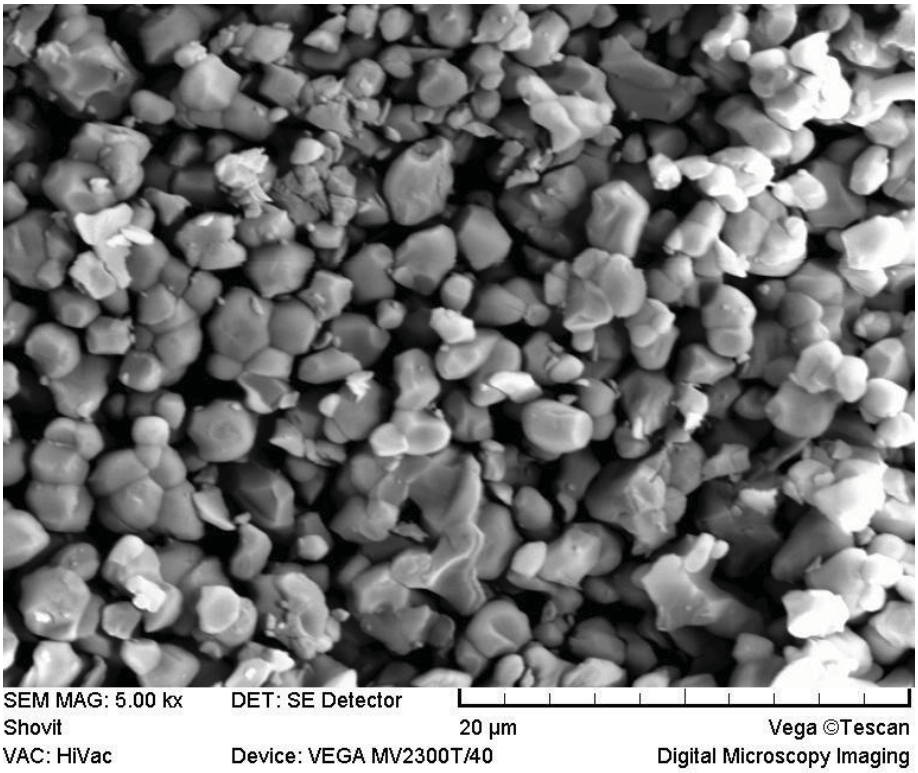

Fig. 7.5 Scanning Electron Micrograph image of the In_2TiO_5 *sample prepared by solid state method*

7.3.2.2 Polyol method synthesized In_2TiO_5

The N_2-BET surface area of the samples synthesised by polyol method increases to 12 m^2g^{-1} owing to solution method employed and the lower temperature of calcination (900 °C as compared to 1250 °C). The Scanning Electron Microscopic (SEM) image (Fig. 7.6) of the polyol mediated synthesized In_2TiO_5 show highly monodisperse particles of uniform size and shape. The grain boundaries are well also visible. The sizes of the particles are in the range of ~ 150 nm. Thus it is evident that the morphological properties of In_2TiO_5 significantly improve in the samples prepared by a polyol mediated method than by solid state method. The, surface area increases, the particle size decreases and also the distribution of size of the particles are also narrowed.

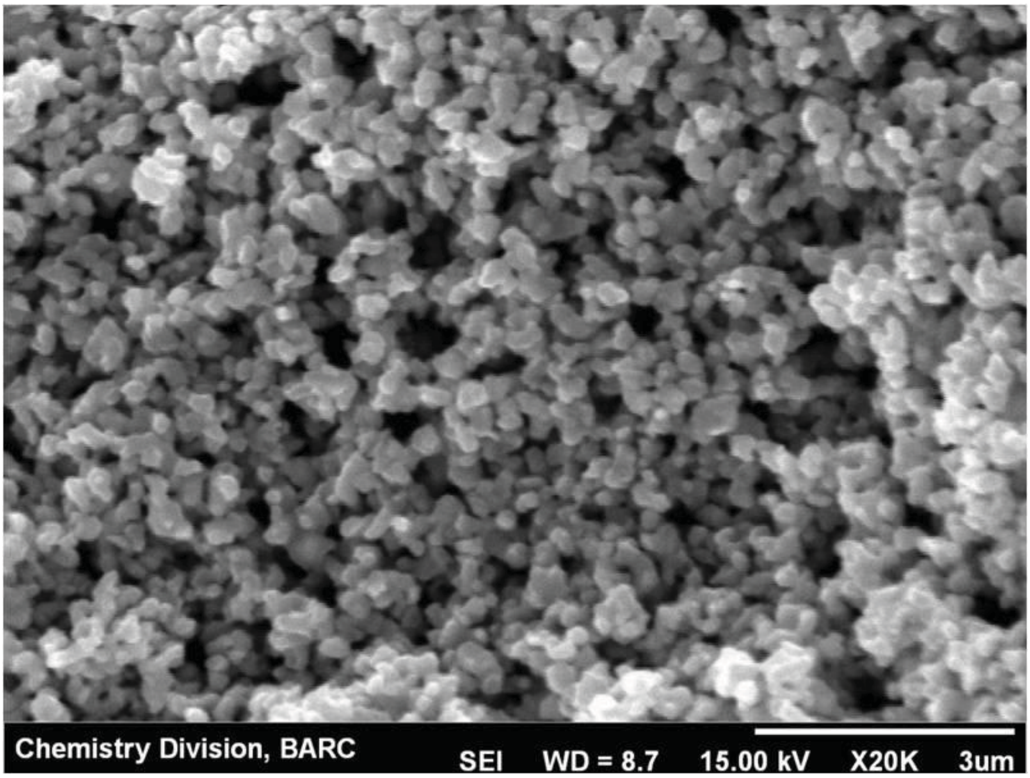

Fig. 7.6. The Scanning Electron Micrograph image of In_2TiO_5 prepared by polyol method and calcined at 900 °C for 5 h

The morphological characteristics of In_2TiO_5 nanoparticles have also been investigated by transmission electron microscopy (TEM). The TEM and High resolution TEM (HRTEM) images for the indium titanate synthesized by polyol method and calcined at 900 °C for 6 h are shown in Fig. 7.7. A representative low-resolution image of a single particle is shown in Fig. 7.7a exhibits that the structure of the particle is facetated and of ~ 100 nm in size. Since, the TEM image is of the calcined sample the size is of higher order, but the crystallinity is also high which can be seen from the HRTEM images. The lattice fringes corresponding to the 101 plane can be identified in the High Resolution Transmission Electron Microscopy (HRTEM) image of the particles.

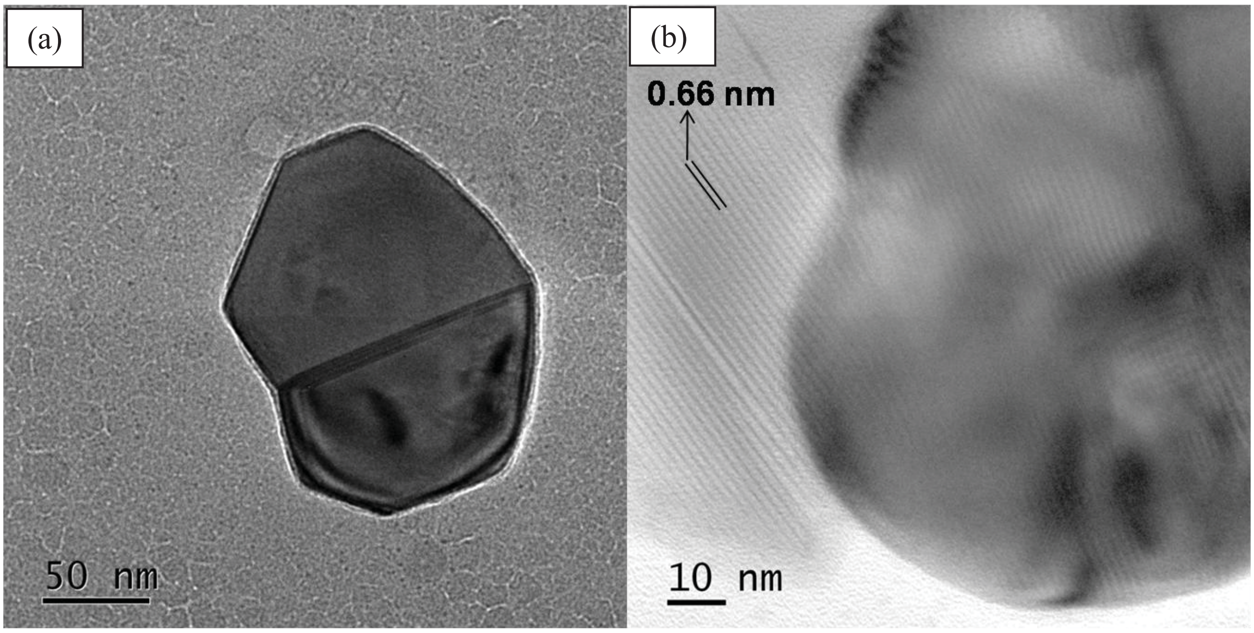

Fig. 7.7. The (a) Transmission Electron Micrograph image and the (b) HRTEM image of In_2TiO_5 *prepared by polyol method and calcined at 900 °C for 5 h.*

7.3.2.3 In_2TiO_5 synthesized by solvothermal method

Nitrogen sorption measurements were applied to determine the surface area of the assynthesied In_2TiO_5 nanoparticles prepared by solvothermal route. The BET surface area of the sample was found to be 60 m^2g^{-1}. After calcination of nanoparticles of In_2TiO_5 at 800°C the surface area of the sample decreased to 38 m^2g^{-1}. This value is significantly higher than that of bulk In_2TiO_5 sample which was obtained at 1250°C (4 m^2g^{-1}) or that of In_2TiO_5 particles prepared by polyol route and calcined at 900 °C (12 m^2g^{-1}). P25 TiO_2 degussa has a surface area of 56 m^2g^{-1}.

The surface morphology and the chemical composition of the In_2TiO_5sample prepared by solvothermal route and annealed at 800 °C were determined by scanning electron microscopy (SEM) and energy dispersive X-ray spectroscopy (EDS) respectively, and the results are shown in Fig. 7.8. The particles are quite uniform in size and spherical in shape. The observed average atom% values from the data collected at three different locations are well in agreement with expected values for In_2TiO_5 within experimental error (expected atom %: In, 25; Ti, 12.5; O, 62.5; observed: In, 23.65; Ti, 12.83; O, 62.57) (Fig, 7.8b).

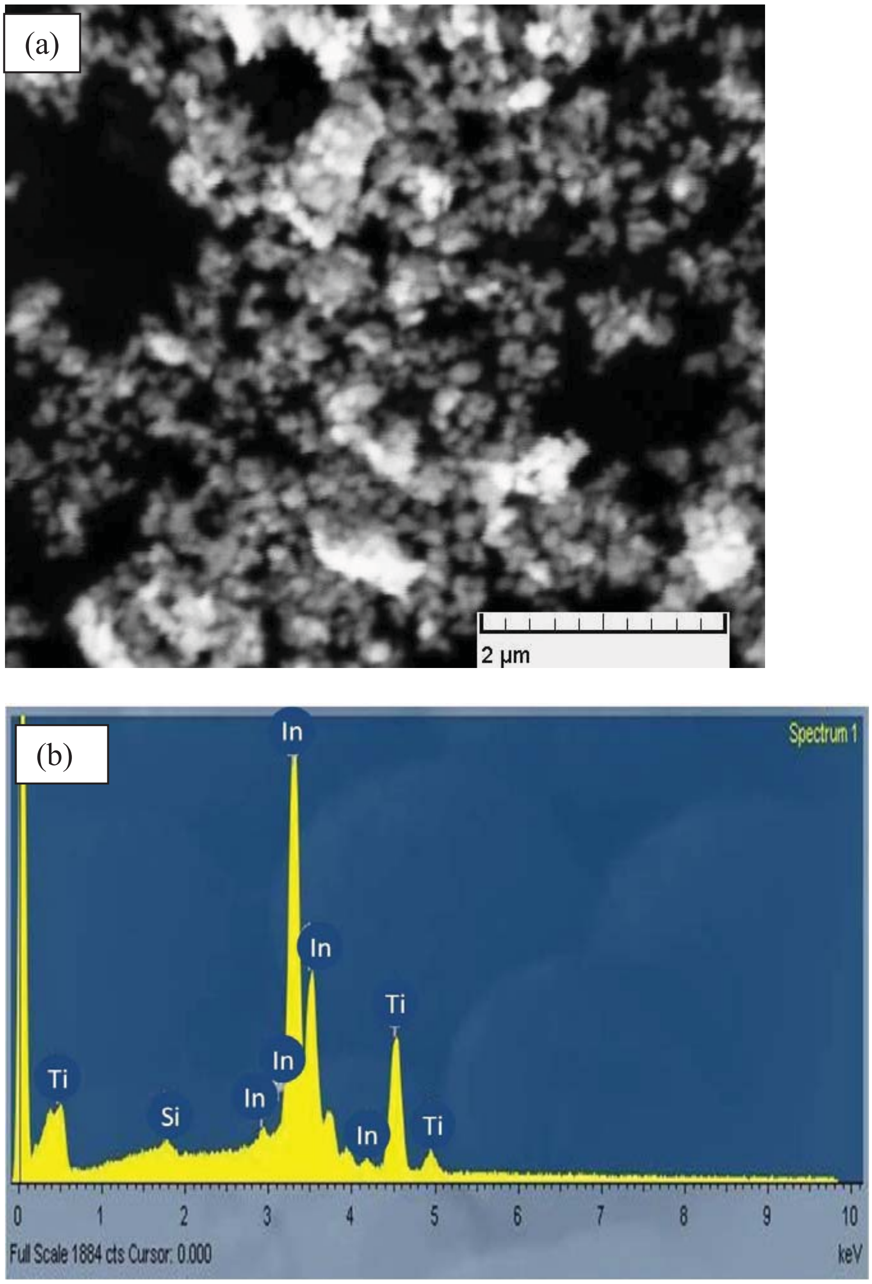

Fig. 7.8. The morphology and chemical composition of the In_2TiO_5 *nanoparticles prepared by solvothermal route and calcined at 800°C as determined by recording (a) SEM images (b) Energy dispersive X-ray spectroscopic data.*

The morphological characteristics of In_2TiO_5 nanoparticles prepared by solvothermal route have been investigated by transmission electron microscopy (TEM). The TEM results are for the indium titanate nanoparticles obtained after calcining the as synthesized product at 400 ° C for 16 h. A representative low-resolution image is shown in Fig. 7.9a. Due to lack of any stabilizing surfactants, the particles are agglomerated but it is still possible to determine the diameters of the particles which are in the range 5-8 nm. A single particle with distinguishable grain boundaries and clear lattice fringes could be discerned within agglomerate as seen in high-resolution image (Fig. 7.9b). A magnified view of the marked particle is shown in Fig. 7.9c. By measuring the interplanar spacing and angular relationship with the generated structure, the presence of orthorhombic In_2TiO_5 was confirmed. The inset of Fig 7.9c shows the oriented view of the lattice. Selected area electron diffraction (SAED) shown as inset in Fig. 7.9a can be indexed according to orthorhombic In_2TiO_5. Thus, both HRTEM and SAED studies confirm the high crystallinity of the In_2TiO_5 nanoparticles.

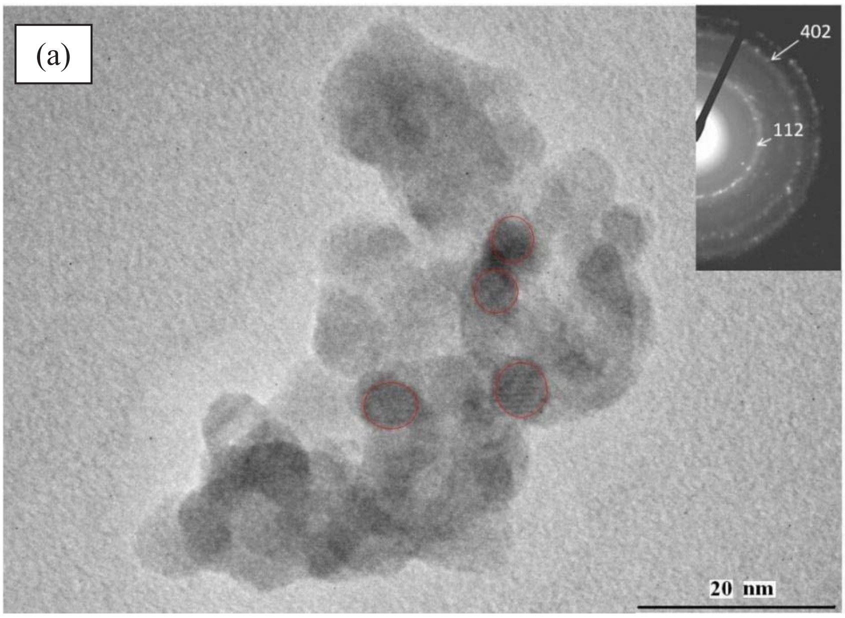

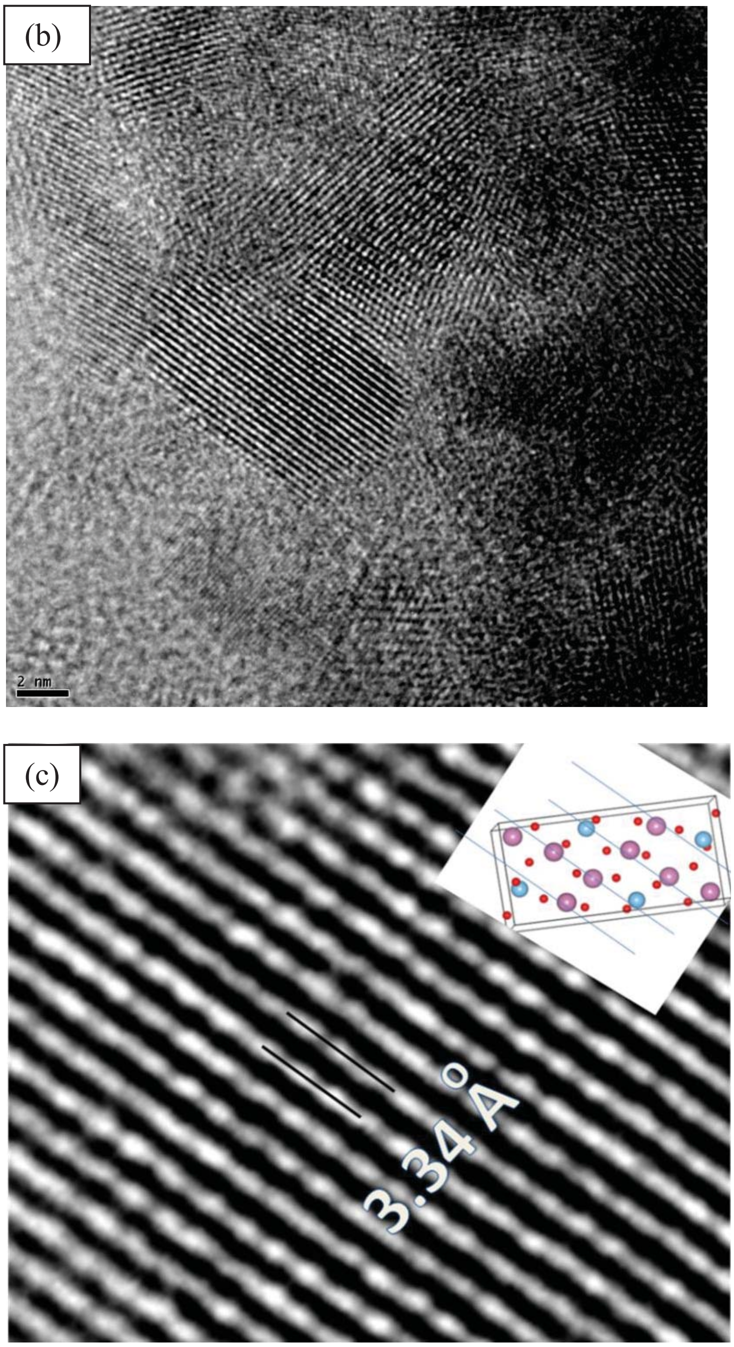

Fig. 7.9. TEM (a), HRTEM (b) of In_2TiO_5 nanoparticles. SAED pattern for the nanoparticles is shown as the inset in Fig. 3a and (c) magnified view of lattice planes marked in (b).

Thus we can conclude from the investigation of the morphological characteristics of the In_2TiO_5 samples prepared by different routes that nanoparticles with excellent powder properties of high surface area, low particle size with uniform distribution has been obtained for the samples prepared by solvothermal method.

7.3.3. DRUV-visible spectra

It is a well-known fact that the light absorption by a semiconducting material and the migration of the light-induced electrons and holes are the key factors controlling the photocatalytic reaction. The photoabsorption properties of the In_2TiO_5 samples prepared by different routes viz. solid state, polyol and solvothermal methods detected by diffuse-reflectance UV-visible spectroscopy (DRUV-visible) are illustrated in Fig. 7.10. It is evident that all the samples absorb in the visible region of the UV-visible spectrum. Band gap was estimated by Kubelka-Munk calculation and was found to be 3.02 eV for that of bulk In_2TiO_5 prepared by solid state method, 3.1 eV for that of samples prepared by polyol method and 3.25 eV which is largest for the nanoparticles synthesized by solvothermal method. Thus, we observe a progressive blue shift in the band gap of the materials as the powder properties of the In_2TiO_5 is modified from bulk type in the solid state samples to solvothermal route synthesized nanoparticles of high surface area.

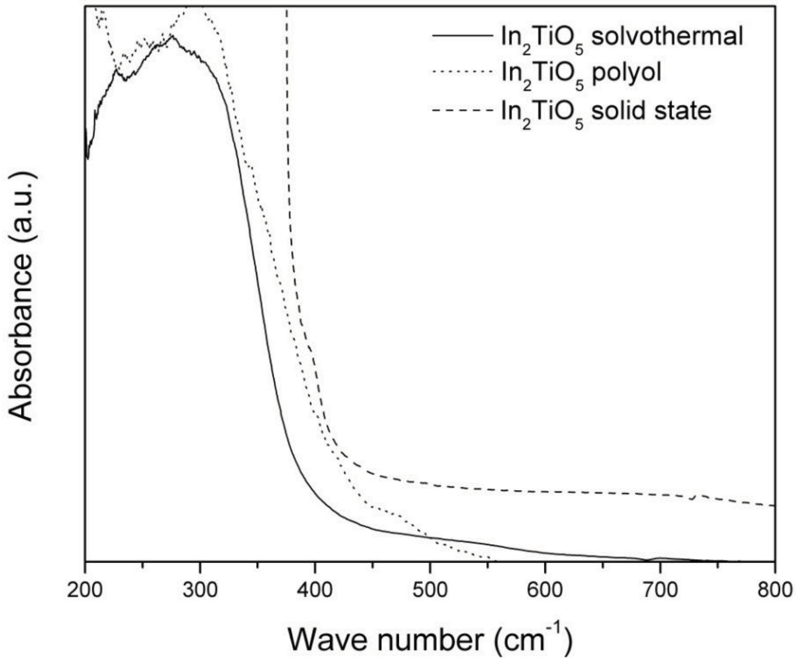

Fig. 7.10 Diffuse reflectance UV-visible spectra of In_2TiO_5 sample prepared by different routes

7.3.4 Electronic Structure

The electronic structure of In_2TiO_5 samples were calculated using TB-LMTO code in order to clarify the distribution of valence states of Ti, In, O atoms near Fermi level and identify the band structure of In_2TiO_5. Fig. 7.11 show the calculated band structure of In_2TiO_5, while Fig. 7.12 shows the total as well as site- and *l-projected* partial density of states (DOS) for In_2TiO_5. As expected, the LDA band structure of In_2TiO_5 (Fig. 7.11) shows all the features identical to that reported by Wang et al [14] using the same TB-LMTO method. The lowest unoccupied state (LUMO) are found at Γ-point (0, 0, 0) whereas the highest occupied state (HOMO) are found between points S and X; Y and Γ; R and U in the valence band not at Γ-point as shown in Fig. 7.11. Thus, In_2TiO_5 have indirect band gap between the LUMO and HOMO as revealed from Fig. 7.11. There are two indirect bands in range of 1.6 to 3.0 eV above the fermi level, which mainly consists of In 5s orbitals. The calculated E_g (band gap) of 1.6 eV is not consistent with the optical band gap (3.02 eV). The valence band consists of mainly O-2*p*, Ti-3*d* and In-5*p* and In-4*d* states (Fig. 7.12), while the conduction band is comprised of Ti-3*d*, In-5*s* and In-5*p* states. The In-4*d* states in the valence band show a sharp peak near the Fermi level representing their localized nature. The strong optical transitions are due to flat bands from valence band to conduction band (Fig. 7.11) and these are found along S to X point and R to U point and T to Y-point and R to S-point. The transition from highest occupied states to the unoccupied states between T and Y or between S and R, respectively, exhibits a gap about 3.20 eV, which is closer to the observed value (3.02 eV for solid state samples). The O 2p states contribute considerably to the Density of states near Fermi level, whereas the Ti 3d and 4s just make the contributions above the Fermi level. Indium 5s states are of large dispersion with rather small DOS, thus indirect band gap of 1.6 eV is not flat band to flat band transition, hence is less probable.

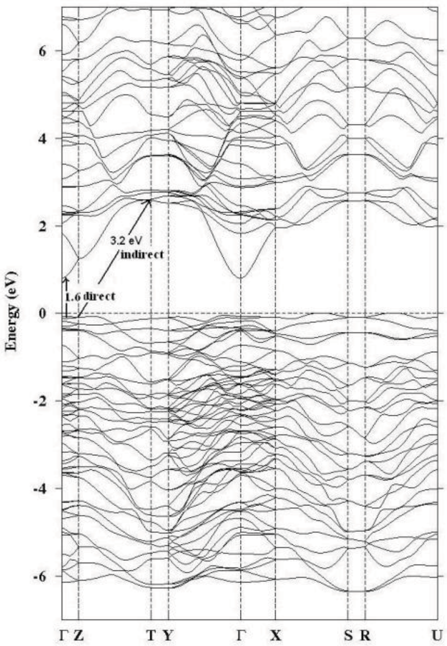

Fig. 7.11. Band Structure of In_2TiO_5 along high-symmetry Γ (0,0,0), X(0.25,0,0), Y(0,0.5,0), Z(0,0,0.125), S(0.25,0.5,0), R(0.25,0.5,0.125), T(0,0.5,0.125) and U(0.25,0.0,0.125) directions.

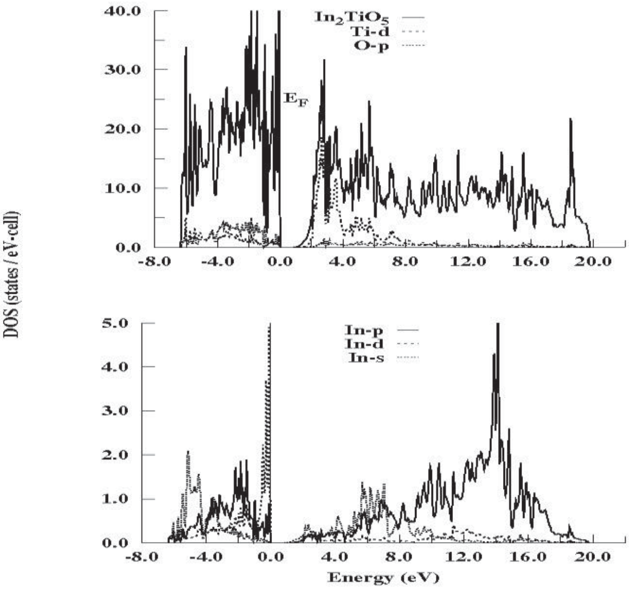

Fig. 7.12. Total and site- and angular momentum-projected partial density of states for In_2TiO_5 showing valence band to be mainly composed of O-p, Ti-d and In-p,d, states.

Band calculations on In_2TiO_5 reveal that the large dispersion of In 5s states, and the optical indirect transition are in favor of photon energy storage and electron-hole separation to benefit the photocatalytic activity of In_2TiO_5. This model study is also useful in understanding the performance of similar photocatalysts.

7.3.5 Photoactivity

Fig. 7.13 shows the results of H_2 evolution from water-methanol mixture (2:1) using indium titanate nanoparticles prepared by solvothermal method (surface area 38 m^2g^{-1}), indium titanate prepared by polyol method (surface area 12 m^2g^{-1}), bulk Indium titanate prepared by solid state synthesis (surface area 4 m^2g^{-1}), and commercial TiO_2 (P25, surface area 56 m^2g^{-1}) without any co-catalyst. It is clearly seen from the Fig. 7.13 that all the In_2TiO_5 photocatalysts prepared are active for hydrogen generation from water-methanol mixture under UV-visible light irradiation. Also, the hydrogen yield increases as a function of time as observed for a period of 6 h. Thus, the In_2TiO_5 compositions are suitable mixed oxides for being photocatalytically active for hydrogen generation. The trend of photocatalytic activity for hydrogen generation being: In_2TiO_5 (solvothermal) > TiO_2 (P25) > In_2TiO_5 (polyol) > Bulk In_2TiO_5 (solid state synthesis) (Fig. 7.13). The decreasing order of activity of the prepared photocatalysts follows the decreasing order of surface area of the prepared samples. The indium titanate nanoparticles prepared by solvothermal method having the highest surface area among the three prepared photocatalyst, showed considerably enhanced photoactivity and yielded ~2600 μmoles g^{-1} of H_2 in 6 h as compared to ~1400 and ~ 760 μmoles g^{-1} of H_2 in 6 h generated by indium titanate prepared by polyol and solid state methods (having lower surface areas) respectively.

We further wanted to compare the catalytic activity of indium titanate with the standard commercially available photocatalyst which is P25 degussa TiO_2. TiO_2 (P25) had a surface area of ~ 56 m^2g^{-1}, and gave a hydrogen yield of ~ 1500 μmoles g^{-1} in 6 h. Even the solvothermally synthesised indium titanate had a lower surface area than P25 degussa titania (other indium titanate sample having much lower surface area). But, still the solvothermally prepared indium titanate showed a hydrogen yield of ~ 2600 µmoles g^{-1} in 6 h, which is much higher than the titania standard.

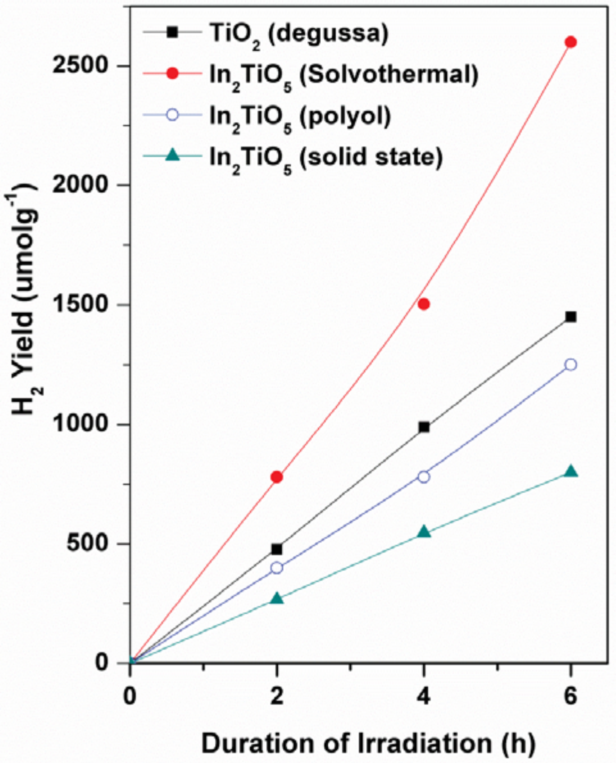

Fig. 7.13. Photocatalytic activity of In_2TiO_5 *prepared by various methods for hydrogen generation. Reaction conditions: 0.1 g catalyst, 10 ml distilled water, 5 ml methanol. Light source; UV-visible medium-pressure mercury lamp (Hg, Ace Glass Inc., 450W) surrounded with water circulation jacket to absorb IR irradiation.*

The intrinsic stability of indium titanate nanoparticles in the course of the photocatalytic experiment was confirmed by recording XRD of the sample after photoillumination. The XRD patterns obtained were the same as those before irradiation.

The high photocatalytic activity of In_2TiO_5 can be attributed to its favourable electronic structure and crystal structure and this aspect is discussed below.

7.4 Discussion

Indium titanate, In_2TiO_5, was successfully prepared by solid state synthesis and its crystal structure was well characterised by powder XRD and then Rietveld refinement of the pattern. Thus we can emphasize the role of crystallinity and crystal structure, wherein, it is revealed that as compared to nanoparticles of TiO_2 (P25), the orthorhombic nanocrystalline In_2TiO_5 has a more favourable crystal structure for the photocatalytic generation of H_2. $InTi_2O_5$ has a three-dimensional tunneling structure, built by octahedra [InO_6] and [TiO_6] octahedral moieties. The InO_6 octahedral units were edge shared and formed infinite chains while the InO_6 and TiO_6 octahedra were corner shared. A comparison of the Ti-O bond distance/angle in octahedra [TiO_6], the density and crystal packing factor of In_2TiO_5 and TiO_2 is shown in Table 7.2.

Table 7.2. Comparison of the octahedra [TiO_6], density and crystal packing factor of In_2TiO_5 and TiO_2

Name of the compound	Bond distance Ti–O (Å)	Bond angle O–Ti–O (°)	Crystal packing factor (%)
In_2TiO_5 (our results)	1.8087, 1.8230 (×2), 2.0323, 2.0386, 2.1853	73.53–179.52	68.0
Anatase TiO_2 (1)	1.964 (×2),1.937 (×4)	77.64–179.98	70.2
Rutile TiO_2 (1)	1.988 (×2), 1.944 (×4)	80.86–180.00	76.6

The comparison (Table-7.2) reveals that the coordination environment of Ti in In_2TiO_5 is more open and flexible than that in TiO_2 – by virtue of the more distorted TiO_6 octahedral units and a lesser value of the crystal packing factor. This is a well established fact from structure–activity correlations that photocatalysts with more open structures are more catalytically active [1, 13, 14, 19, and 20]. In addition to the more favorable characteristics of the TiO_6 polyhedra, another advantage In_2TiO_5 possesses is the presence of infinite chains of edge shared InO_6 octahedral units. The presence of such octahedral InO_6 polyhedra in the crystal structure has been found to have a positive effect on the photocatalytic properties in some compounds like $InNbO_4$ [22], $InTaO_4$ [11, 22-23] or even $AgInW_2O_8$ [24] and In_6WO_{12} [25]. This is by virtue of the fact that the presence such polyhedral units which are either edge or corner shared forming infinite chains will help in charge transfer to the surface which is an important requirement for a proper photocatalyst [11, 21-22]. The characteristics of the $[InO_6]$ octahedra in In_2TiO_5 as derived from the reitveld refinement results i.e. the In-O bond distances/angle are shown in Table 7.3 and also compared with the reported values of some other representative photocatalyst containing the InO_6 polyhedra. Even the In-O bond distances suggest the more flexible InO_6 geometry in In_2TiO_5 than $InTaO_4$ or $InNbO_4$.

Table. 7.3. Characteristics of $[InO_6]$ octahedral in In_2TiO_5 and some other photo catalyst

Name of the compound	Bond distance In1–O (Å)	Bond distance In2–O (Å)	Bond angle O–In1–O (°)	Bond angle O–In2–O (°)
In_2TiO_5 (our results)	2.1748, 2.2127 (x2), 2.2145 (x2), 2.2316	2.1024, 2.2040, 2.2130 (x2), 2.2421 (x2)	75.56-176.37	76.01-171.9
$InTaO_4$ [22]	2.13 (x2), 2.13 (x2), 2.20 (x2)	*	99.2 (O-In-O)	
$InNbO_4$[22]	2.099 (x2), 2.151 (x2), 2.235 (x2)	*	98.6(O-In-O)	

* *Crystal structure has only one type of In atom*

Further, band calculations on In_2TiO_5 revealed large dispersion of In 5s states, and the presence of an optical indirect transition. Upon photoabsorption in the semiconducting indium titanate the electron goes to the largely dispersed In 5s states and by virtue of the presence of chains of InO_6 octahedra are transferred to the surface kinetically fast, where chemical reaction occurs resulting in hydrogen production. The presence of the optically indirect transition restricts the electron-hole recombination to a certain extent. Thus, both the crystal structure and band structure are in favor of photon energy storage and electron-hole separation to benefit the photocatalytic activity of In_2TiO_5. The light absorption properties of indium titanate were evaluated by recording the DRUV-visible spectrum, which revealed a band gap of 3.02 ev for bulk solid state sample. To obtain better powder properties by increasing the surface to volume ratio of indium titanate photocatalyst, attempts were made to prepare nanoparticles of indium titanate using polyol and solvothermal methods. The samples obtained from both the methods were well characterised for structure, morphology and light absorption properties using powder XRD, SEM, TEM, N_2-BET surface area and DRUV-visible spectra. Samples prepared by both the methods crystallised in single phase indium titanate structure. The powders obtained from solvothermal method had the highest surface area and smallest particle size. The band gap were estimated to be 3.2 ev for solvothermal, 3.1 ev for polyol. All the photocatalyst were found to be active for hydrogen generation reaction with the order of activity being: In_2TiO_5 (solvothermal) > TiO_2 (P25) > In_2TiO_5 (polyol) > Bulk In_2TiO_5 (solid state synthesis). The order of activity of the indium titanate powders followed the same order of surface are or particle size which was found to be: In_2TiO_5 (solvothermal) – minimum particle size and maximum surface area – 38 m^2 g^{-1} > In_2TiO_5 (polyol) – intermediate particle size and surface area – 12 m^2 g^{-1} > Bulk In_2TiO_5 (solid state synthesis) – highest particle size and negligible surface area. The solvothermally prepared indium titanate sample having a surface area of 38 m^2 g^{-1} showed a hydrogen yield of ~ 2600 μmoles g^{-1} in 6 h, much higher than the P25 degussa TiO_2 (surface area 56 m^2 g^{-1}) which showed an yield of ~1500 μmoles g^{-1} in 6 h. Thus, the high photocatalytic activity of In_2TiO_5 is thus attributed to its favourable electronic structure and crystal structure.

7.5 Conclusion

Single phasic In_2TiO_5 photocatalysts were successfully prepared by solid state, polyol and solvothermal methods. The samples were well characterized for structure, morphology and light absorption properties by XRD (Rietveld refinement of its pattern), N_2-BET surface area, SEM, TEM and DRUV techniques. All the samples were photocatalytically active for hydrogen generation reaction from water-methanol mixtures. The high photocatalytic activity of In_2TiO_5 is attributed to its favourable electronic structure and crystal structure.

References:

1. A. L. Linsebigler, G.Lu, J. T. Yates Jr, Chem. Rev. 95 (1995) 735.
2. A.J. Esswein, D. G. Nocera,; Chem. Rev. 107 (2007) 4022-4047.
3. K. Maeda, K. Domen, J. Phys. Chem. C 111 (2007) 7851.
4. A. Kudo, Y. Miseki, Chem. Soc. Rev. 38 (2009) 253–278.
5. K. Maeda, K. Teramura, D. Lu, T. Takata, N. Saito, Y. Inoue, K. Domen, Nature 440 16 March 2006.
6. K. Maeda, K. Teramura, K. Domen, J. Catal. 254 (2008) 198.
7. H. Kato, M. Hori, R. Konta, Y. Shimodaira and A. Kudo, Chem. Lett. 33, (2004) 1348.
8. S. M. Ji, P. H. Borse, H. G. Kim, D. W. Hwang, J. S. Jang, S. W. Bae and J. S. Lee, Phys. Chem. Chem. Phys. 7 (2005) 1315
9. M. Machida, T. Mitsuyama, K. Ikeue, S. Matsushima and M. Arai, J. Phys. Chem. B 109, 7801 (2005).
10. H. Kato and A. Kudo, J. Phys. Chem. B. 105 (2001) 4285.
11. Z. Zou, J. Ye, K. Sayama and H. Arakawa, Nature 414 (2001) 625.
12. X. Shu, J. He and D. Chen, Ind. Eng. Chem. Res. 47 (2008) 4750

13. T. Gaewdang, J.P. Chaminade, P. Gravereau, A. Garcia, C. Fouassier, P. Hagenmuller, R. Mahiou, Mater. Res. Bull. 28 (1993) 1051.
14. W. D. Wang, F. Q. Huang, C. M. Liu, X. P. Lin, J. L. Shi, Mater. Sci. Eng. B. 139 (2007) 74.
15. P. Shah, D. S. Bhange, A. S. Deshpande, M. S. Kulkarni, N. M. Gupta, Mater. Chem. Phys. 117 (2009) 399.
16. O. K. Andersen, O. Jepsen, Phys. Rev. Lett. 53 (1984) 2571.
17. O. K. Andersen, O. Jepsen, D. Glötzel in "Highlights of Condesed Matter Theory", eds. F. Bassani, F. Fumi and M. Tosi, North-Holland, New York (1985).
18. O. Jepsen; O. K. Andersen, Z. Phys. Condens. Matter 97 (1995) 35.
19. D. W. Kim, N. Enomoto, Z. Nakagawa, K. Kawamura, J. Am. Ceram. Soc. 79 (1996) 1099.
20. X.P. Lin, F.Q. Huang, W.D. Wang, Y.M. Wang, Y.J. Xia, J.L. Shi, Appl. Catal. A, 313 (2006) 218.
21. Junwang Tang, Zhigang Zou, Jiang Yin, Jinhua Ye Chem. Phys. Lett. 382 (2003) 175–179.
22. Z. Zou, J. Ye, H. Arakawa, Chem. Phys. Lett. 332 (2000) 271-277.
23. Hsiang-Chen Chen, Hung-Chi Chou, and Jeffrey C.S. Wu and Hsin-Yu Lin, J. Mater. Res., 23(5) (2008) 1364.
24. J. Tang, Z. Zou, and J. Ye, J. Phys. Chem. B 107 (2003) 14265-14269.
25. H. Zhang, X. Chen, Z. Li, L. Liu, T. Yu and Z. Zou, J. Phys.: Condens. Matter 19 (2007) 376213.

Chapter 8

Substituted Indium Titanates - Enhanced Photocatalytic Hydrogen Generation and Favorable Redox Properties

8.1 Introduction

In the previous chapter (Chapter 7) we have seen the suitability of indium titanate as a photocatalyst for hydrogen generation by virtue of its proper band gap and photocatalytic activity for hydrogen generation. First principle investigations revealed the band structure showing the distribution of valence states of the constituent atoms near the Fermi level of the indium titanate. The band gap of bulk indium titanate was also estimated from DRUV experiments and was found to be 3.02 ev. Both the bulk and nano indium titanate were photoactive for hydrogen generation from water-methanol mixture. The interesting photoactivity results on pristine indium titanate prompted us to investigate the effect of transition metal like Ni^{2+} on the photocatalytic properties of indium titanate as transition metals with partly filled d-orbital (e.g. Ni^{2+}, Cr^{3+}, Fe^{3+}) are known to add impurity levels near the conduction band of titanates thereby decreasing its band gap and increasing its photoactivity [1-4]. It is a well-known fact that the light absorption by the material and the migration of the light-induced electrons and holes are the key factors controlling a photocatalytic reaction (Chapter 1), which is related to the electronic structure characteristic of the material [1-4]. The ionic radius of Ni^{2+} (0.69 Å) being much smaller than that of In^{3+} (0.81 Å), substituting In^{3+} by Ni^{2+} should reduce the volume of the InO_6 octahedra, and hence the cell volume in $InTiO_5$. This should in turn affect the direct metal-metal bonding in the crystal, with the In-In distance shortened, resulting in profound alterations of the electronic properties of the compounds and consequent modifications in the photocatalytic properties [5]. So, in the present Chapter, we report the A-site substitution of Ni^{2+} induced effects on the photocatalytic behavior of indium titanate. For this purpose, $In_{2(1-x)}Ni_{2x}TiO_{5-\delta}$ ($0.0 \leq x \leq 0.2$) mixed oxide catalysts were synthesized using solid-state reaction and characterized by powder X-ray diffraction (XRD), the light absorption properties was studied by recording the DRUV spectra and finally the photocatalytic splitting of water was investigated under UV-visible light irradiation. The photocatalytic activity was also compared with other A- (Nd) and B- site (Fe, Cr) doped indium titanates to compare the effect of dopant to indium titanate lattice.

The redox properties of the Ni substituted indium titanates were also studied. The important considerations in designing an oxide catalyst are its thermal, chemical stability, reducibility and oxidizability. So, it is imperative to study their interesting physicochemical properties the knowledge of which finds them utilized in suitable applications. The thermal and chemical stability and redox behavior of these titanates would play a vital role in determining their catalytic properties for various redox processes (even photocatalytic redox reactions).

8. 2. Experimental:

8.2.1Material Synthesis

Mixed oxides with nominal composition, $In_{2(1-x)}Ni_{2x}TiO_{5-\delta}$, for $0.0 \leq x \leq 0.2$, were synthesized through ceramic route using pre-dried In_2O_3, TiO_2 and NiO (99.99% purity) as starting materials, mixing them in appropriate stoichiometry as depicted by following equation:

$$(1-x)In_2O_3 + TiO_2 + 2xNiO \rightarrow In_{2(1-x)}Ni_{2x}TiO_{5-\delta}$$

The pellets of homogeneous mixtures were calcined at 900 °C for 24 h, 1000 °C for 24 h and finally at 1250°C for 12h, with intermittent grindings so as to ensure the uniformity and the completion of the reaction.

8.2.2 Catalyst Characterization

The Powder XRD patterns were recorded on a Philips diffractometer (model PW 1710), equipped with a graphite monochromator and Ni-filtered Cu-K_α radiation. Structural analysis has been done by using Rietveld refinement program Fullprof-2005 [6]. First of all, the background parameters and scale factor were adjusted. The background was fitted with sixth order polynomial. The diffraction peak profile was fitted with Pseudo-Voigt profile function and then the FWHM parameters were adjusted. No absorption parameter was considered during refinement. Subsequently, individual thermal parameters were refined. Finally, positional parameters were refined. Consequently, individual cell parameters with position of individual atoms in the Ni-substituted In_2TiO_5 crystal lattice were derived. Band gap measurements of all semiconductor oxide samples was estimated by recording their Diffuse reflectance UV-Visible spectra using spectrophotometer of JASCO model V-530, Japan, scanned in range of 200-1000 nm at the scanning speed of 200 nm/min.

8.2.3 Redox properties

Redox behavior of catalyst was studied by recording temperature programmed reduction/oxidation (TPR/TPO) profiles on a TPDRO-1100 analyzer (ThermoQuest, Italy) in temperature range of 25-1100 °C under the flow of H_2(5%)+Ar, gas mixtures at a flow rate of 20 ml min^{-1}, with a heating rate of 6 Kmin^{-1}. The samples were pretreated at 350°C for about 2.5 hrs in helium, prior to recording of the first TPR run. A thermal conductivity detector (TCD) is employed to monitor the change in composition of reactive gas mixture with time. The water formed during reduction process was removed from the flowing gas by the help of a soda lime trap placed just before the detector. Hence the signal obtained was primarily due to change in thermal conductivity of the flowing gas by consumption of hydrogen. The amount of hydrogen consumed by the sample during a TPR run corresponded to the area under the TPR profile. The calibration factor (μmoles of H_2 per mV of TCD signal) for the H_2 was calculated using the standard sample. This factor has been employed in all the substituted samples and the experimental amount of H_2 consumed was obtained. The calculated value of H_2 consumed by the sample was compared with the experimental value. XPS studies were carried out on electron spectrometer using Mg-Kα X-rays (hν=1253.6 eV) as the primary source of radiation. The appropriate corrections for charging effect were made with the help of a C 1s signal appearing at 285.1 eV.

8.2.4 Photocatalytic activity

The photocatalytic activities of the samples were carried out under irradiation of a medium-pressure mercury lamp (Hg, Ace Glass Inc., 450W) placed in an outer irradiation–type quartz cell surrounded with water circulation jacket to absorb IR irradiation. The rectangular quartz cell ($2.1 \times 2.1 \times 8$ cm^3) was equipped with sampling and evacuation ports and placed horizontally in a chamber close to a water-cooled medium pressure mercury vapor lamp (400 W) (shown in Fig. 2.21, Chapter 2). The said lamp exhibits very broad range emission spectra having maxima at both UV and the visible range with the UV part being only 16% of the whole spectra (shown in Fig. 2.20, Chapter 2). The catalyst (0.1g) was suspended in distilled water (10 ml) and methanol (5ml). The reaction mixture was evacuated and irradiated under the medium pressure mercury lamp. After irradiation, the amount of Hydrogen evolved was analyzed by gas Chromatograph (TCD, Molecular sieve, 5m length and Ar carrier). The number of photons falling on the reaction cell or flux of the light was determined by a calibrated light flux meter (Cal light 400), where the flux observed in horizontal geometry was 19 x 10^4 lux or 278.2 watts/m^2.

8.3 Results and discussions

8.3.1. XRD

Table-8.1 lists the abbreviations and phases identified from XRD patterns of all the $In_{2(1-x)}Ni_{2x}TiO_{5-\delta}$, ($0.0 \leq x \leq 0.2$) samples prepared by solid state method. Henceforth, in this Chapter, the samples will be designated by their abbreviations. The XRD patterns of all samples were recorded and analyzed. Fig. 8.1 shows the powder XRD patterns of In_2TiO_5 and corresponding patterns observed due to aliovalent substitution of Ni^{2+} in place of In^{3+} at A-site. The XRD pattern of x = 0, composition matches well with that of orthorhombic In_2TiO_5 (JCPDS card No.30-0640, space group Pnma). The XRD patterns of ITN05 ($In_{1.95}Ni_{0.05}TiO_{5-\delta}$) and ITN1 ($In_{1.9}Ni_{0.1}TiO_{5-\delta}$) compositions match with the XRD patterns of unsubstituted indium titanate sample as shown in Fig. 8.1. Thus, lower extent of Ni substitution resulted in single phase material comprised of In_2TiO_5 phase due to formation of solid solution of Ni with the lattice of the parent compound. However, for the nickel doped indium titanates, the peaks are shifted slightly towards higher 2-θ values as compared to those of the pristine samples, which is attributed to the decrease in lattice spacings due to substitution of smaller Ni^{2+} ions in place of larger In^{3+} ions. On further Ni substitution i.e. samples having Ni content $x \geq 0.1$ in $In_{2(1-x)}Ni_{2x}TiO_{5-\delta}$ a very low intensity line (marked with #) was observed which corresponds to the 100 % peak of NiO (JCPDS card No.47-1049). Thus for these compositions in addition to parent phase there was segregation of unreacted NiO phase in very small proportion. Moreover, for samples having higher Ni content i.e. $x \geq 0.15$, a third phase of $NiTiO_3$ (JCPDS card No.33-0960, peaks marked with *) was observed in addition to the unreacted nickel oxide phase (Fig.

8.1). It is pertinent to mention here that the presence of a small amount of these secondary phases in the samples, as mentioned above, was taken into consideration for Rietveld analysis. The reliability factors of the Rietveld refinement of the substituted and unsubstituted indium titanates, κ^2, were within the range of 2.8 to 3.6.

Table-8.1 Identification of phase in $In_{2(1-x)}Ni_{2x}TiO_{5-\delta}$, $(0.0 \leq x \leq 0.2)$ samples and their abbreviations.

Nominal Composition	Ni content (x in $In_{2(1-x)}Ni_{2x}TiO_{5-\delta}$)	Abbreviation	Phase identification by XRD and weight fraction (in %) of each phase calculated from Reitveld refinement
In_2TiO_5	0.00	ITO	In_2TiO_5 (100)
$In_{1.95}Ni_{0.05}TiO_{5-\delta}$	0.025	ITN05	In_2TiO_5 (100)
$In_{1.9}Ni_{0.1}TiO_{5-\delta}$	0.05	ITN1	In_2TiO_5 (100)
$In_{1.8}Ni_{0.2}TiO_{5-\delta}$	0.1	ITN2	In_2TiO_5 (97.3) & NiO (2.7)
$In_{1.7}Ni_{0.3}TiO_{5-\delta}$	0.15	ITN3	In_2TiO_5 (97.19), NiO (1.28) & $NiTiO_3$ (1.52)
$In_{1.6}Ni_{0.4}TiO_{5-\delta}$	0.2	ITN4	In_2TiO_5 (94.76), NiO (2.48) & $NiTiO_3$ (2.76)

To determine the crystal structure under investigation and to confirm the site of dopant cation Ni^{2+} in the crystal lattice Rietveld refinement of the diffraction patterns were carried out and the results are shown in Fig. 8.2. The detailed crystal structure of the parent In_2TiO_5 phase has already been discussed in Chapter 7. The substituted samples were found to be iso-structural with the parent indium titanate phase and Ni^{2+} was found to substitute only at one of the 4c In^{3+}

site. The typical variation in cell parameters and cell volume as a function of nickel content in $In_{2(1-x)}Ni_{2x}TiO_{5-\delta}$ ($0.0 \le x \le 0.2$) phases in indium titanate samples, as deduced from the Rietveld analysis of corresponding powder XRD reflections, is shown in Fig. 8.3. As seen in Fig. 8.3d, the cell volume decreases as a function of nickel content (x in $In_{2(1-x)}Ni_{2x}TiO_{5-\delta}$) as long as $x \le 0.15$. Thereafter, the cell expands when Ni content $x = 0.2$. Also, the decrease in cell volume is large from $x = 0$ to $x = 0.05$ and then there is a small linear decrease upto $x \le 0.15$. The lattice parameters *a, b* and *c* also show a similar trend. Due to incorporation of smaller cation Ni^{2+} by substitution of a larger cation In^{3+} there is a linear decrease in the values of cell parameters and cell volume upto $x \ge 0.15$. Thereafter, the impurity phase of $NiTiO_3$ also appears and increases its volume fraction significantly with further increase in Ni-content. The offset from linearity and then an increase in lattice parameters can be explained from the segregation of this impurity phase. Although, the occupancy of Ni^{2+} increases with doping but the parent lattice has a maximum capacity to substitute a large cation by a smaller cation as the structure destabilize by such a substitution and when the maximum capacity for such substitution exceeds, secondary phases appear keeping the parent crystal phase as the major phase. Such, segregation of secondary phases and its growth, due to substitution of In^{3+} by Ni^{2+} in oxide lattices was also observed in $InTaO_4$ by Zou et al [5].

As discussed in Chapter 7, the presence of InO_6 and TiO_6 polyhedra in the In_2TiO_5 lattice has a marked effect on the charge transport properties and consequently on photocatalytic properties. The perturbation of these polyhedral units due to substitution of Ni was also evaluated from the Rietveld refinement results and is tabulated in Table 8.2. We can see from Table 8.2 the shrinkage of both the Ti-O and In2-O bond distances in the TiO_6 and InO_6 which is in accordance to the decrease in cell parameters with Ni-doping shown in Fig. 8.3. The decrease in bond distances in the polyhedral can have a profound influence on the photocatalytic properties. This can be understood from the point of view that since the edge shared TiO_6 and InO_6 polyhedral assist in charge conduction to the surface the reduced distances can enhance this rate of charge transfer to the surface and increase the photoactivity of the semiconductor photocatalyst.

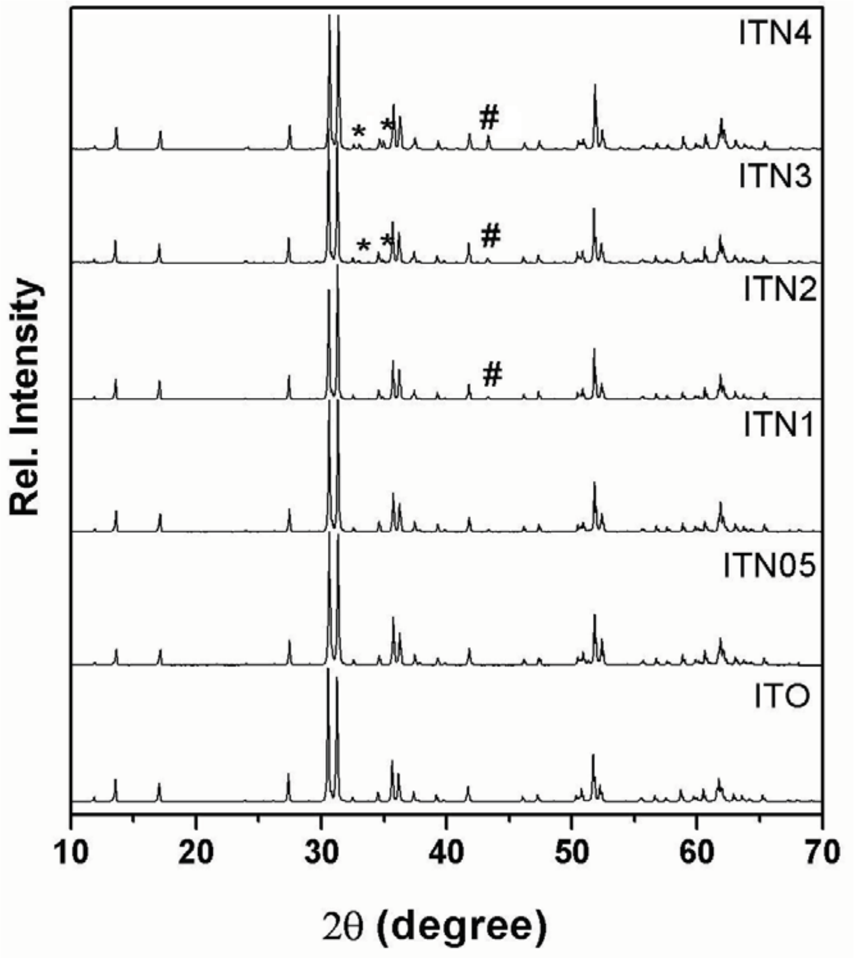

Fig. 8.1. XRD patterns of $In_{2(1-x)}Ni_{2x}TiO_{5-\delta}$*samples, # indicates peaks due to unreacted NiO phase and * indicates the peaks arising from* $NiTiO_3$ *phase.*

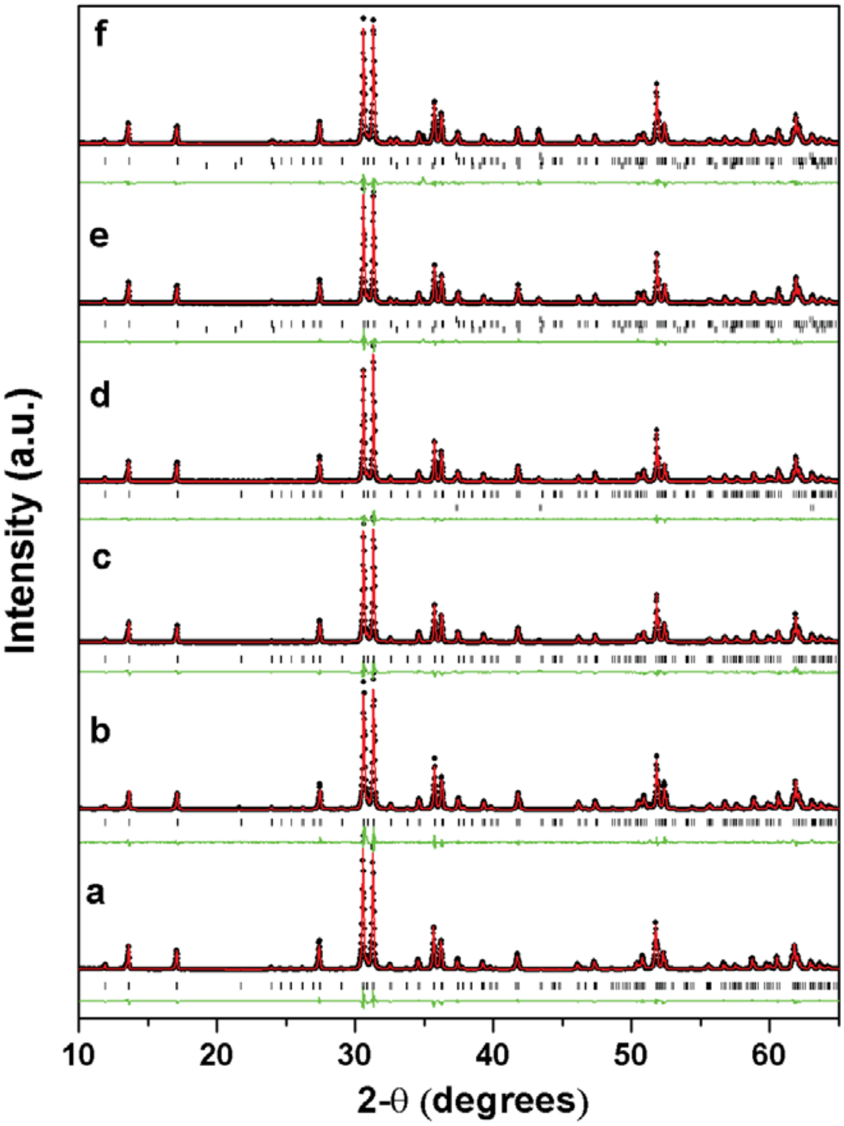

Fig. 8.2. Rietveld refined profiles of X-ray diffraction data of $In_{2(1-x)}Ni_{2x}TiO_{5-\delta}$ *samples, where x = a) 0.0, b) 0.025, c) 0.05, d) 0.1 e) 0.15 and f) 0.2. The dots represent the observed data, while the solid line through dots is the calculated profile, and vertical tics represent Bragg reflections for the phase. The difference pattern is also shown below the vertical tics in each case.*

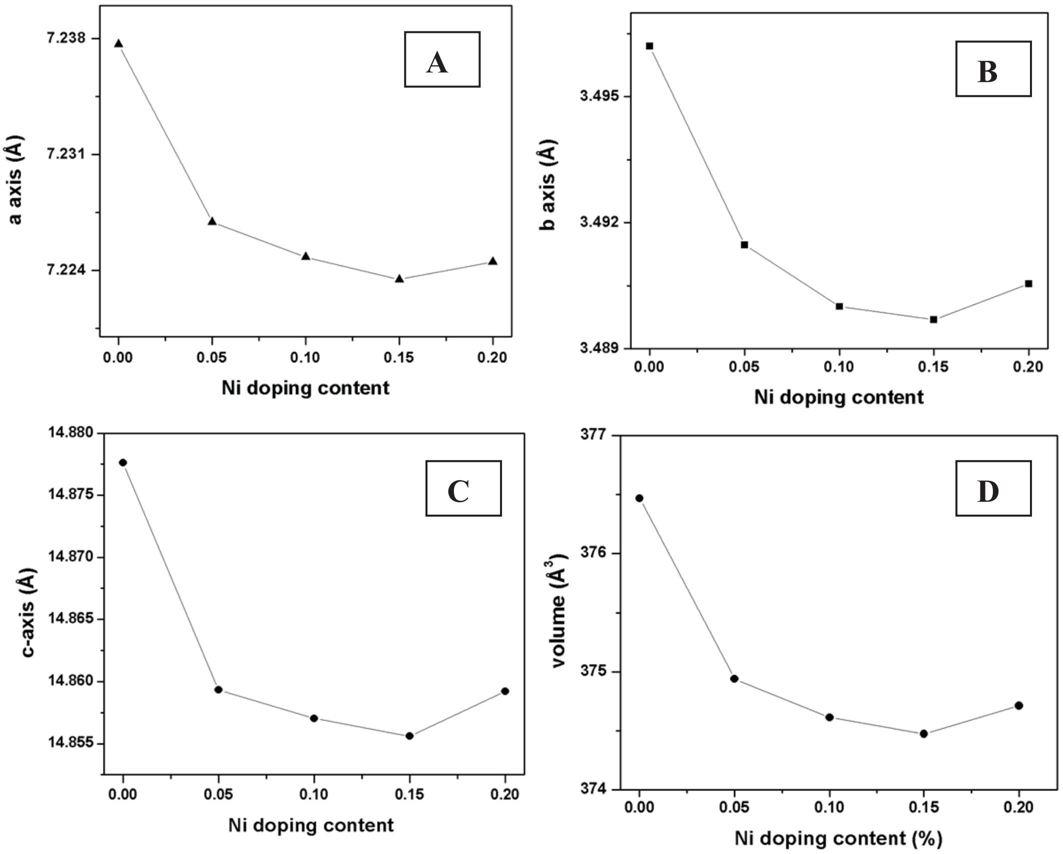

Fig. 8.3. Changes in crystal structure with doping where A, B and C are the variation of lattice parameters with Ni doping and D shows Ni-content dependence of the cell volume

Table-8.2. Selected bond distances and angles in TiO_6 and InO_6 polyhedra

Name of phase	Ti-O distances	In1-O distances	In2-O distances	O-In-O angles	O-Ti-O angles
	Å	Å	Å	degrees	degrees
In_2TiO_5	1.8087 1.8230 (×2), 2.0323 2.0386 2.1853	2.1748 2.2127 (x2) 2.2145 (x2) 2.2316	2.1024 2.2040 2.2130 (x2) 2.2421 (x2)	75.56-176.37 (O-In1-O), 76.01-171.9 (O-In2-O)	73.53-179.52
$In_{1.9}Ni_{0.1}TiO_{5-\delta}$	1.8049 (x2) 1.8291 2.0390 2.0569 2.3077	2.2000 2.2005 2.2133 (x2) 2.2445 (x2)	2.0709 2.1418 2.2003 (x2) 2.2017 (x2)	76.73-175.95 (O-In1-O), 74.56-172.76 (O-In2-O)	75.35-179.95

$In_{1.8}Ni_{0.2}TiO_{5-\delta}$	1.8494 (x2) 1.8563 1.9655 2.0686 2.1688	2.1275 2.1958 2.2237 (x2) 2.2430 (x2)	2.0552 2.1398 2.1836 (x2) 2.2381 (x2)	77.70-178.87 (O-In1-O), 75.43-174.00 (O-In2-O)	70.86-178.40
$In_{1.7}Ni_{0.3}TiO_{5-\delta}$	1.7928 (x2) 1.8826 2.0205 2.0263 2.3201	2.1839 2.1920 (x2) 2.2203 (x2) 2.2353	2.1731 2.1192 2.1745 (x2) 2.2041 (x2)	75.24-175.04 (O-In1-O), 73.59-171.09 (O-In2-O)	76.80-177.74
$In_{1.6}Ni_{0.4}TiO_{5-\delta}$	1.7839 1.9740 1.8276 (x2) 2.0604 2.2250	2.1921, 2.1900, 2.3299, 2.2148, 2.1921, 2.2148.	2.0862 2.1739 2.1946 (x2) 2.2246 (x2)	74.91-173.92 (O-In1-O), 75.32-173.95 (O-In2-O)	72.97-177.18

With these modifications in the crystal structure of In_2TiO_5 by Ni-doping, we were interested to investigate the effect of doping on both the photocatalytic properties and redox properties of indium titanate. First we depict the results of photocatalytic properties then the redox properties.

8.3.2 Redox properties

The typical first temperature programmed cycle (TPR) of substituted samples and unsubstituted sample are shown in Fig. 8.4. The TPR profile of unsubstituted, In_2TiO_5 sample as seen in Fig. 8.4 comprises of a prominent band with onset at ~625 °C and extending beyond 1000 °C. This indicated the predominant reduction of one of the species, identified to be In^{3+}, in the temperature range of 600-1100 °C over other reducible species in In_2TiO_5 sample. The temperature maximum (T_{max}) of the reduction bands corresponds to ~1070 °C. However, Ni^{2+} substitution at In^{3+} site has induced considerable changes in the reduction profile of indium titanate. In case of compositions having higher content of Ni, viz., ITN2 and ITN4, TPR profiles (Fig. 8.4), exhibit two-three weak bands in low temperature range of 450-800 °C in addition to main reduction band. The presence of these bands is probably attributed to reduction of $Ni^{2+} \rightarrow Ni^0$ along with reduction of In^{3+}. At the same time, the T_{max} of the individual peaks was found to be lower in the case of substituted samples. For instance, we observe the lowering of T_{max} around by 80 °C for ITN4 in Fig. 8.4, as compared to the TPR profile of an un-substituted phase. Also the onset reduction temperature of 625 °C in unsubstituted phase has considerably decreased by Ni substitution as shown in Fig. 8.4.

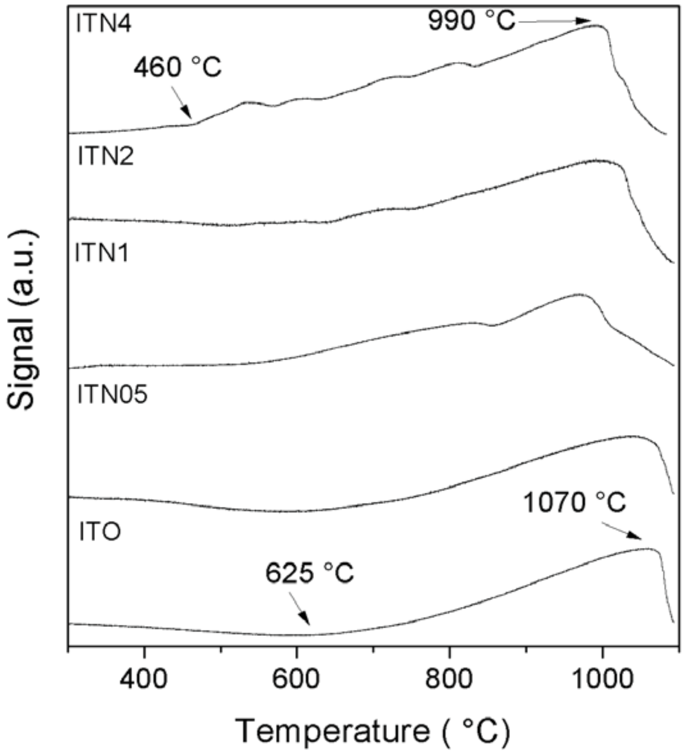

Fig. 8.4. Typical first TPR cycle of $In_{2(1-x)}Ni_{2x}TiO_{5-\delta}$ samples as a function of Ni substitution

The TPR profile as a whole has shifted to lower temperature as a result of Ni substitution. Thus, Ni^2 substitution has undoubtedly facilitated the reduction of In_2TiO_5 phase. These changes in the TPR profiles can be ascribed to the nonstoichiometry and imperfections generated in the single phased compositions as a result of A -site substitution.

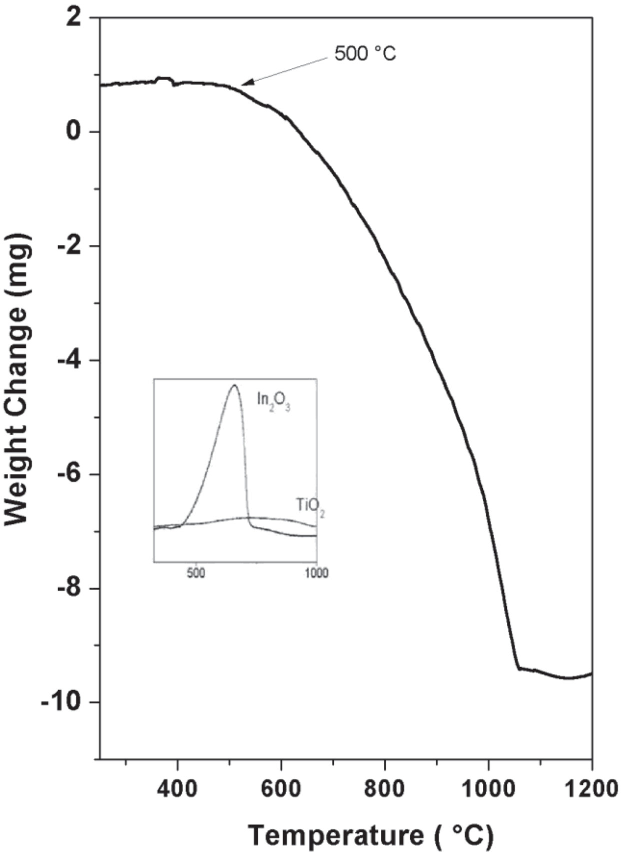

Fig. 8.5. Thermogram plot of ITN4 composition recorded in H_2 (5%) + Ar atmosphere. Inset exhibiting TPR profiles of In_2O_3 and TiO_2.

Both substituted and unsubstituted samples did not show any weight loss in TG when recorded in O_2 (5%) + Ar, thus indicating that all substituted $In_{2(1-x)}Ni_{2x}TiO_{5-\delta}$ oxide samples are stable in air upto 1000 °C. So the $In_{2(1-x)}Ni_{2x}TiO_{5-\delta}$, (x = 0.0-0.4) samples once formed, do not pick up either moisture or CO_2, and are thermally stable compositions till 1000 °C. Although, in O_2 (5%) + Ar atmosphere these compositions are stable whereas in H_2 (5%) + Ar, the corresponding TG exhibits substantial weight loss. A representative TG-DTA plot of ITN4 in H_2 (5%) + Ar atmosphere is shown in Fig. 8.5. The weight loss in TG plot starts above ~ 500 °C and continues upto ~ 1050 °C in the 20 % Ni-substituted sample. As revealed by temperature programmed reduction profiles (Fig. 8.5) of these oxides, we can infer that this weight loss is due to reduction of these oxides in H_2 atmosphere. Mainly the weight loss is attributed to reduction of species, In^{3+} and Ni^{2+}, to In^0 and Ni^0 respectively. The evidence of the above inference comes from temperature programmed reduction profiles of In_2O_3 and TiO_2 oxides. TPR profiles of In_2O_3 and TiO_2 reactant oxides (exhibited as inset in Fig. 8.5) suggests that In^{3+} species reduces above 600 °C with T_{max} at 670 °C, whereas TiO_2 does not reduce upto 1000 °C recorded in the range of 25-1000 °C under H_2 flow (5 % H_2 in Ar).

8.3.2.1*Ex situ* characterization of reduced residue samples

Fig.8.6 shows the XRD patterns of reduced residue of In_2TiO_5, ITN2 and ITN4 samples obtained after recording TPR. In the reduced In_2TiO_5 and ITN2 samples the presence of prominent lines at $2\theta = 32.98^\circ$, 39.2° conforms to reported pattern of In^0 (JC-PDS No.05-0642). Other strong lines at 27.44°, 36.08° and 54.32° match well with rutile TiO_2 phase (JC-PDS No.21-1276). Thus, both metallic indium and rutile titania were present in these two reduced samples. There was no other phases present in the reduced In_2TiO_5 sample. No prominent additional lines were also observed in the reduced ITN2 sample, except for a weak hump at 41.2°. This peak can be attributed to the formation of an alloy of Ni and In namely δIn_3Ni_2 (JCPDS No. 070298). The small amount of nickel present in the sample was initially reduced at a lower temperature with an onset at ~ 450 °C and subsequently In^{3+} was also reduced (refer fig. 8.4). The reduced metallic nickel then reacted with the reduced In metal to form the In-Ni alloy. An interesting feature was observed in the XRD pattern of reduced ITN4 sample. The intensity of the peaks due to reduced Indium metal was reduced drastically, along with the appearance of prominent lines (marked by *) at $2\theta = 28.9$, 41.0, 41.3 and 59.8. These peaks are attributed to the presence of δIn_3Ni_2 phase. Remaining line in the residue were at $2\theta = 41.5^\circ$. An alloy formation of Ni-Ti is indicated by this peak as $2\theta = 41.57^\circ$ corresponds to 100% peak due to reflection from 511 plane of Ti_2NI alloy (JCPDS No. 180898). This suggests that Ti^{4+} an otherwise stable cation towards reduction got reduced within 1100 °C. The formation of Ni-Ti alloy on reduction of ITN4 sample is quite plausible as revealed by the XRD pattern (Fig. 8.6), as secondary phase of $NiTiO_3$, also got reduced along with major indium titanate phase. This new phases possibly would have facilitated the reduction of Ti^{4+} along with reduction of Ni^{2+}. Any of the lines in the spent samples do not match with the reported XRD pattern of Ni metal alone (JC-PDS. No. 04-0850). So, Ni metal formed by reduction was very active and reacted with other reduced phases to form alloys. Further, the presence of Ni facilitated the reduction of In^{3+} as the T_{max} of the individual peaks due to reduction of In^{3+} was found to be lowered in the case of substituted samples. In addition to this, the otherwise non-reducible cation Ti^{4+} also got reduced in the 20% substituted sample which might probably be due to autocatalytic effect of Ni^{2+}. This phenomenon can be referred to as an incident of hydrogen spillover in mixed metal oxide. The Ni metal initially formed by reduction of the cation was active enough to dissociate and activate the hydrogen, which in turn could even reduce Ti^{4+} cation in addition to facilitating the reduction of In^{3+}. It could also be suggested that the extent of reduction of Ti^{4+} and subsequent alloy formation would depend on the content of secondary phase. In ITN2 sample In^{3+} was replaced partially by Ni^{2+} and the reduced Ni metal facilitated the reduction of In^{3+} cation and then an alloy formation took place. This fact is evident from the TPR curve where the whole reduction pattern including T_{max} for reduction of In^{3+} shifts to lower temperature. Further in the ITN4 sample the reduction of partially substituted Ni^{2+} cation generated Ni metal which dissociated and activated the hydrogen which eased the reduction of In^{3+} cation and also reduced Ti^{4+}. This process of reduction of Ti^{4+} if continued would have resulted in the reduction of all Ti^{4+} but the formation of the Ti_2Ni alloy prevented further hydrogen activation and that further reduction of the Ti^{4+} was hindered. So, only partial reduction of Ti^{4+} was feasible. The presence of $NiTiO_3$ phase might have assisted the above process. Thus, Ni substitution at In-site of In_2TiO_5 had a drastic effect on the reduction behavior of indium titanates. TPR results in conjunction with XRD studies reveal the reduction of $In^{3+} \rightarrow In^0$, while Ni^{2+} facilitated the reduction of otherwise non-reducible cation Ti^{4+} and resulted in formation of Ni-Ti alloy (Ti_2Ni).

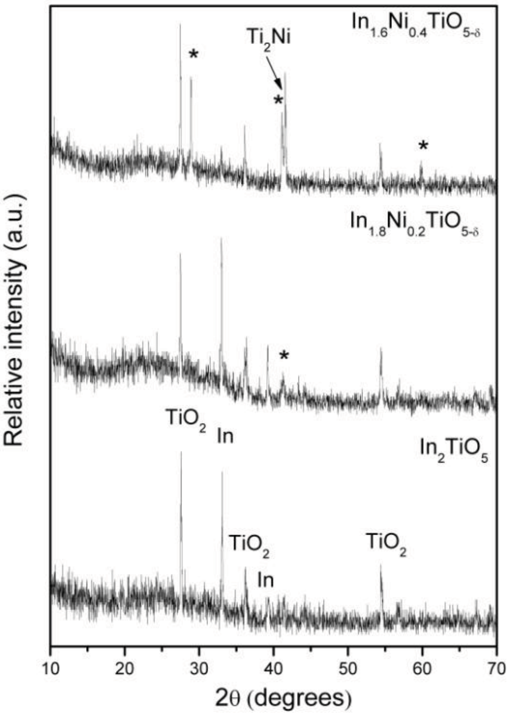

*Fig. 8.6. XRD patterns of spent $In_{2(1-x)}Ni_{2x}TiO_{5-\delta}$samples after recording TPR in H_2(5%) + Ar atmosphere of ITO, ITN2 and ITN4 compositions. The peaks due to δIn_3Ni_2 alloy are marked by *.*

In Fig. 8.7 a-b, the X-ray photoelectron (XPS) spectrum of fresh, and completely reduced ITN4, sample are shown, which were recorded in order to identify the oxidation states of indium and titanium metal ions present in the spent samples after the reduction. Table-8.3 lists the elements identified and their oxidation states in the fresh and reduced samples. The binding energies at 445.9 eV and 457.5 eV corresponding to In ($3d_{5/2}$) and Ti ($2p_{3/2}$) which matches with the reported binding energies for In in +3 and Ti in +4 oxidation state present in fresh ITN4 sample as shown in Figs. 8.7a and 8.7b. But, the binding energy at 445.9 eV as observed in the fresh sample in Fig. 8.7a is shifted to lower binding energies of 444.1 eV in completely reduced ITN4 sample. XPS spectra suggest the existence of indium in +3 oxidation state in the fresh sample and In(0) in completely reduced sample. The changes in oxidation states of Ti present in the fresh and reduced sample are shown in Fig. 8.7b. In the reduced sample, in addition to major peak at 457.5 eV a shoulder is observed at 453.7 eV coresponding to Ti(0) state. The appearance of this shoulder peak confirms the reduction of Ti^{4+} to Ti metal during the temperature programmed reduction (TPR) experiments. In addition, in Figure 8.7a, a shoulder appears at higher binding energy in the XPS spectra of Indium ion for the fresh sample, but it completely disappears in the spectra recorded after the complete reduction. The appearance of shoulder is attributed to the interaction of In^{3+} with other ions present in the compound. Thus as process of reduction proceeds, the interaction of Indium with other ions decreases or it gets segregated out from the sample. However, presence of In^{1+} in the reduced sample is not observed. Intensity of In (3d) peak is considerably increased in Fig 8.7a, after complete reduction as compared to fresh sample. Thus, ITN4, sample on reduction, deposits the metallic Indium on the surface and hence the peak intensity due to Indium on surface increases. It is well known that the catalytic properties of a sample are sensitive to its surface composition; therefore this observation may play a crucial role in deciding its performance for redox reactions. The XPS results in accordance with TPR and thermogravimetry results suggests the formation of metallic Ti(0) along with Ti^{+4} and In (0) when ITN4, was reduced in H_2 upto 1100 °C whereas unsubstituted In_2TiO_5 did not reveal any reduction of Ti^{4+} species. Thus presence of Ni influenced the reduction behavior of Ti^{4+} species present in the sample by activating H_2 molecules.

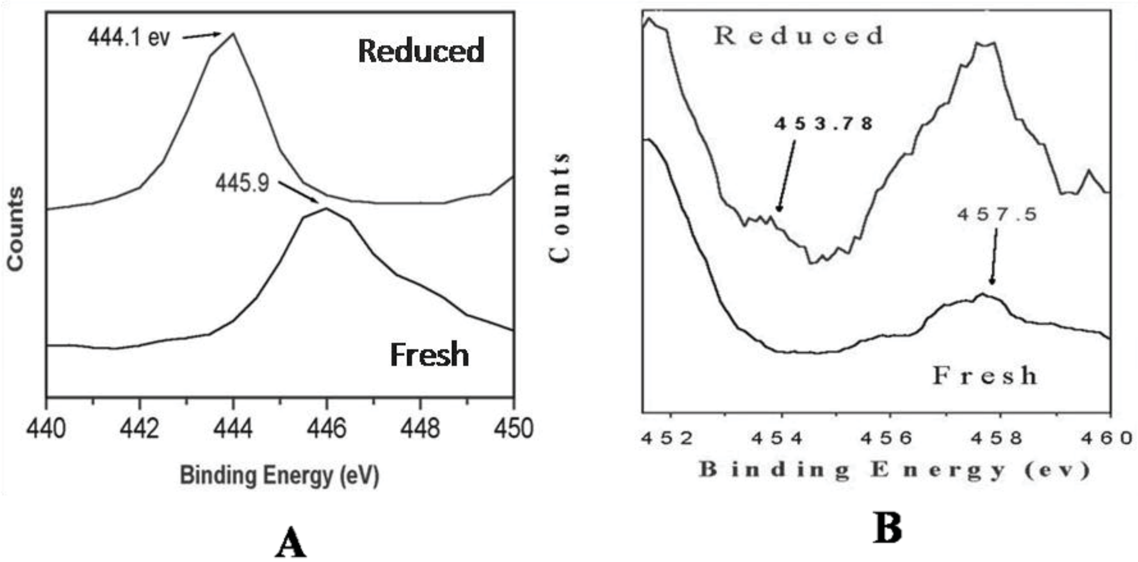

Fig. 8.7. Binding energies of different metal ions in partially reduced sample of ITN4 obtained after recording TPR up to 1000 °C of (a) In (3d), (b) Ti (2p).

Table. 8.3: Representative XPS binding energy values of different elements in ITN4 samples□ obtained before and after the first TPR cycle in temperature range of 25-1100 °C.

BE of XPS Signal (eV)				
Before TPR			After TPR	
elements	In $3d_{5/2}$	Ti $2p_{3/2}$	In $3d_{5/2}$	Ti $2p_{3/2}$
B.E	445.9	457.5	444.1	457.5, 453.7
Oxidation state	+3	+4	0	+4, 0
	In^{3+}	No peak due to Ti^0 metal	In^0	Ti^{4+}, Ti^0

8.3.2.2 Discussion

The reduction of $In_{2(1-x)}Ni_{2x}TiO_{5-\delta}$ oxide samples is represented by following equation:

$$In^{3+}_{2(1-x)}Ni^{2+}_{2x}Ti^{4+}O_{5-\delta}\,(s)+(3-\delta)H_2\,(g) \xrightarrow{490\text{-}1100°C} 2(1-x)In^{0}(s) + 2xNi^{0}(s) + Ti^{4+}O_2(s) + (3-\delta)H_2O(g)$$

Table 8.4. H_2 consumption data of $In_{2(1-x)}\,Ni_xTiO_{5-\delta}$ samples□ obtained from the first TPR cycle in temperature range of 25-1100 °C.

Sample composition [*]	Calculated	Experimental [#]	Residue as identified by XRD
In_2TiO_5	8390	8404	In^0 & TiO_2 rutile
$In_{1.95}Ni_{0.05}TiO_{5-\delta}$	8396	9009	
$In_{1.9}Ni_{0.1}TiO_{5-\delta}$	8401	8358	
$In_{1.8}Ni_{0.2}TiO_{5-\delta}$	8412	9528	In, TiO_2 & δIn_3Ni_2
$In_{1.7}Ni_{0.3}TiO_{5-\delta}$	8424	10514	
$In_{1.6}Ni_{0.4}TiO_{5-\delta}$	8436	10153 [$]	In, TiO_2, δIn_3Ni_2 & Ti_2Ni

[*] stoichiometry determines δ as *x*. [#] TCD signal for manual injection of standard hydrogen has been used for calibration to find out the H_2 consumption. [$] is the difference observed in experimental values (higher) of H_2 consumed as compared to calculated values is attributed to reduction of Ti^{4+} metal ions to Ti metal driven by presence of Ni^{2+} ions.

H_2 consumption data calculated as well as that observed from the areas under TPR peak, for all samples for the first reduction cycle (TPR) is listed in Table-8.4. The comparison shows that except for ITN1 for all other samples experimental values are higher than calculated values. This discrepancy increases with increase in Ni content as observed from the Table-8.4. It can be explained on the basis of autocatalytic reduction of the samples in the presence of Ni^{2+} cations. Ti^{4+} cation is stable in H_2 upto 1000 °C in TiO_2 samples as evident from inset of Fig. 8.5. As such, to obtain the TPR profiles of some simple oxides, TiO_2 and Cr_2O_3, are difficult because the standard approximate free energy change (ΔG° in KJ/mol) for the process: $MO + H_2 \rightarrow Metal + H_2O$ are respectively ~ 220 and ~140 [7]. However for $In_{2(1-x)}Ni_{2x}TiO_{5-\delta}$ samples, in addition to the normal nucleation and growth process, during reduction the presence of Ni^{2+} in even a minor amount modifies the reduction. Ni metal initially formed by reduction dissociates and activates hydrogen. This hydrogen then reacts and reduces the oxide (even Ti^{4+}). This phenomenon is termed as hydrogen spillover. In oxide catalysts the presence of metal cations, which after reduction generates the active metal that can dissociate and activate the hydrogen for facilitating an otherwise difficult reduction phenomenon. It is reported [8-9] that hydrogen spillover can be broken into three primary steps: (i) dissociative chemisorption of gaseous H_2 on a transition metal catalyst; (ii) migration of H atoms from the catalyst to the substrate and (iii) diffusion of H atoms on substrate surfaces and/or in the bulk materials. In this case the metallic Ni formed after reduction is the transition metal catalyst. The substrate is the remnant oxide from which Ni^{2+} cation gets eliminated and then the reduction of bulk In^{3+} occurs by diffusion of H-atoms into the remnant oxide material and thus the reduction profile shifts to lower temperature. Diffusion of H atoms and subsequent reduction of Ti^{4+} is definitely easier in $NiTiO_3$ that the indium titanate phase so we observe higher amount of Ti^{4+} reduction in the sample. This is further corroborated by the TPR results where we observe increased hydrogen consumption discrepancy with an increase in Ni content. Alloy formation of the transition metal catalyst Ni with In and Ti prevented further reduction of Ti^{4+} but In^{3+} being reducible was completely reduced. Such phenomenon of hydrogen spillover has been noticed over nickel metal used as catalyst in hydrogen storage materials like activated carbon, where hydrogen spillover is mainly responsible in increasing the storage capacity [10]. Recently, pioneering studies by Yang et al revealed novel processes to store substantial quantities of hydrogen via hydrogen spillover [11-13].

8.3.3 Photocatalytic properties

8.3.3.1 DRUV

Figure 8.8 illustrates the light absorption properties of $In_{2(1-x)}Ni_{2x}TiO_{5-\delta}$ ($0.0 \le x \le 0.2$), showing that the UV-visible absorption spectra of these compounds are characteristic of photocatalysts able to respond to UV-visible light. It is also evident from Fig. 8.8, that with the substitution of Ni, there is a progressive red shift in the absorption pattern of the titanates. The band gap of these compounds can be estimated from plots of the square root of Kubelka-Munk functions F(R) versus photon energy. One of the most characteristic features is that the bandgap is narrowed with Ni doping. This decrease in band gap is considered largely to be a consequence of the presence of Ni 3d level. The Nickel 3d levels might sit at a forbidden level in the band gap of indium titanate and fuction as an impurity level, lowering the effective band gap. The bandgap change in Ni-doped compounds is generally to internal transitions in a partly filled Ni d shell [5, 14]. Some authors [5, 14] support this fact by the appearance in the Ni-doped compounds of an ultraviolet-visible absorption band at 420-520 nm. But, it is not established how a Ni d-d internal transition can play a role in photoactivity. In our case such internal transitions were not noticed but the overall shift of the band edge towards higher wavelength was evident. The smaller bandgap will anyway facilitate excitation of an electron from the valence band to the conduction band in the doped oxide semiconductors, thus increasing the photoresponse and is expected to increase photocatalytic efficiency of the material.

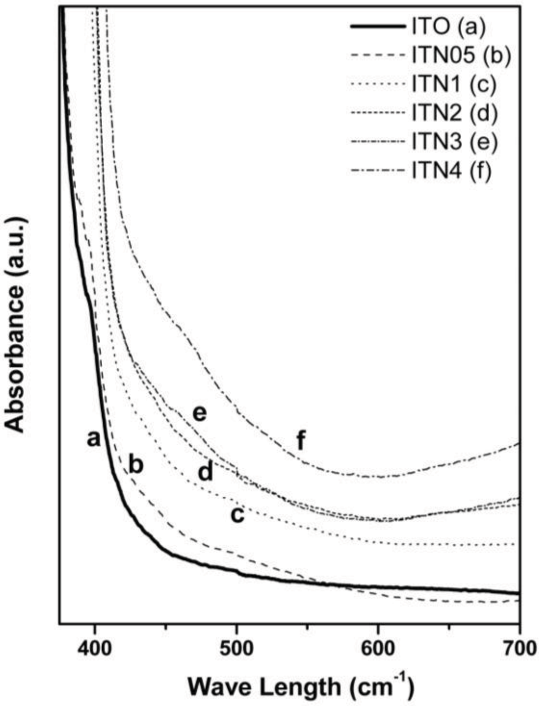

Fig. 8.8. DRUV spectra of the indium titanate samples which shows a progressive red shift in absorbtion with an increase in Ni content

8.3.3.2 Photoactivity

Results of photo-activity of unsubstituted In_2TiO_5 and Ni substituted Indium titanates, $In_{2(1-x)}Ni_{2x}TiO_{5-\delta}$ ($0.0 \le x \le 0.2$) samples for hydrogen generation by water splitting in presence of methanol as a sacrificial agent, under UV-vis irradiation are shown in Fig. 8.9. The hydrogen yield was found to increase with irradiation time for all the samples upto an experiment of 6 h. It is observed from Fig. 8.9 that the 10% doped sample having composition $In_{1.8}Ni_{0.2}TiO_{5-\delta}$ exhibited highest photoactivity. The pristine indium titanate sample was significantly photoactive for hydrogen generation but the rate decreased initially with low Ni substitution upto $x < 0.1$ but on further substitution the rate increased showing highest photoactivity at $x = 0.2$

followed by a drastic decrease on further increase in Ni content. Our present work clearly demonstrates the fact that indium titanate is able to generate hydrogen photocatalytically by water splitting in presence of sacrificial agent methanol. Further, Ni doping modifies the photoactivity to a great extent. On Ni-doping the photoactivity for hydrogen generation increases initially and the reaches a maximum at 10% doping and the again falls with the highest Ni-content sample of 20 % doping showing lower activity than the base ITO itself.

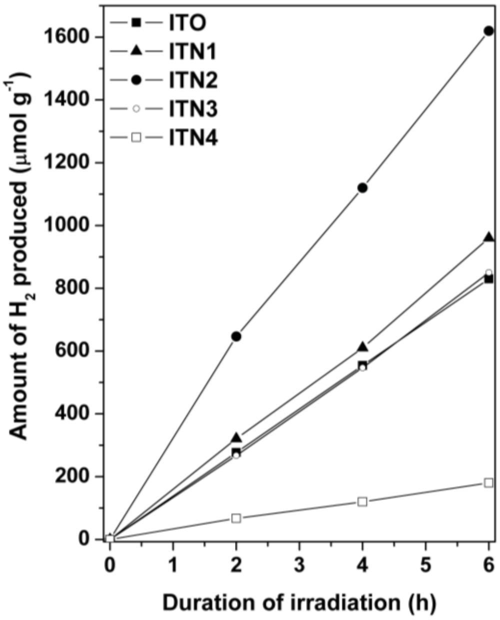

Fig. 8.9. The time dependent H_2-yield from water-methanol solution using different indium titanate samples. Reaction conditions: 0.1 g catalyst, 10 ml distilled water, 5 ml methanol. Light source; UV-visible medium-pressure mercury lamp (Hg, Ace Glass Inc., 450W) surrounded with water circulation jacket to absorb IR irradiation.

The increase in photocatalytic activity can be attributed to a decrease in band gap of indium titanate on Ni-doping. The smaller bandgap as seen from DRUV result facilitated the photoinduced electron excitation from the valence band to the conduction band in the doped oxide semiconductor, thus increasing the photocatalytic activity of the material. But, Ni-doping had an effect on the crystal structure as well which has been depicted in the XRD and Reitveld refinement results. The formation of secondary phase NiO was seen in ITN2 sample but it was not detrimental to the photocatalytic activity. Further substitution of Ni resulted in formation of other phase $NiTiO_3$ which could have a negative effect on photoactivity of indium titanate. The combination of a proper band gap and crystal structure was present in the ITN2 sample for having the highest photocatalytic activity among these semiconductor oxides.

The results are compared with other A-site and B-site cationic doped samples in indium titanate In_2TiO_5 ($A = Nd^{3+}$; $B = Fe^{3+}$ and Cr^{3+}; extent of doping 10 % - all prepared by solid state route) as shown in Fig 8.10. Among all the catalysts, 10% Nd substituted indium titanate photoctalysts was found to be the most active under UV-vis irradiation. A site substitution with Nd^{3+} ions yielded hydrogen typically in range of ~1600 μmoles/g in 4 h as compared ~ 1100 μmoles g^{-1} for Ni^{2+} substituted sample. B site doped with Fe/Cr ions showed much lower photoactivity. The higher photoactivity of Nd substituted samples can be attributed again on the basis of band structure and crystal structure. The band structure contribution comes from the role played by 4f orbital of Nd in the band structure of In_2TiO_5 which is much more prominent than those of 3d orbitals of Ni. Further Nd substitution was an isovalent substitution at A-site creating negligible anionic vacancies or defects as compared to an aliovalent Ni substitution. As we have discussed in Chapter 1 that defect in the crystal lattice can acts as sites for electron-hole recombination thus decreasing photocatalytic activity.

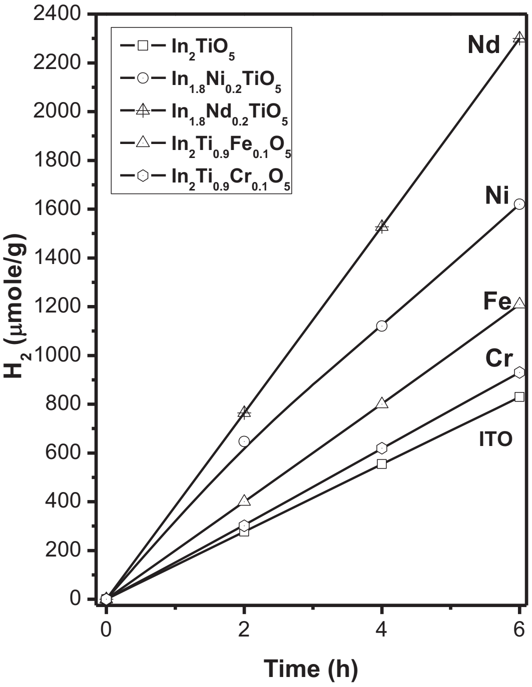

Fig. 8.10. Photocatalytic activity of substituted indium titanate samples. H_2 *yield is plotted as a function of time over* In_2TiO_5, $In_{1.8}Nd_{0.2}TiO_5$, $In_{1.8}Ni_{0.2}TiO_{5-\delta}$, $In_2Ti_{1-x}M_xO_{5-\delta}$ *(M =* Fe^{3+} *and* Cr^{3+}*; x = 0.2), photocatalyst samples.Reaction conditions: 0.1 g catalyst, 10 ml distilled water, 5 ml methanol. Light source; UV-visible medium-pressure mercury lamp (Hg, Ace Glass Inc., 450W) surrounded with water circulation jacket to absorb IR irradiation.*

8.4. Conclusion

A-site substitution by a divalent Ni^{2+} cation at In^{3+} site of In_2TiO_5 resulted in single phase compositions at low extent of substitution (upto 5%), biphasic at a higher substitution (10%) with very low impurity phase of unreacted NiO and triphasic at even higher Ni content (15-20%), having very low concentrations of NiO and $NiTiO_3$ phase. Highly crystalline phase of indium titanate was obtained which on Ni doping at the In site exhibited lattice contraction. The redox properties, were investigated by recording temperature programmed reduction in temperature range of 450-1100 °C in all the samples. Ni substitution induced considerable ease in reducibility (T_{max}) of substituted samples as compared to In_2TiO_5 phase. The substitution-induced non-stoichiometry and the microstrucural defects may cause the distortion in the lattice, thus facilitating the reduction of oxides. The interesting observation was the reduction of otherwise non-reducible cation Ti^{4+}, in the 20% substituted sample, ITN4. Ni metal initially formed by the reduction of Ni^{2+} dissociate and activate the hydrogen which eased the In^{3+} reduction and even facilitated the reduction of Ti^{4+}. The optical measurements showed that Ni-doping induced a lowering in band gap of these semiconductor oxides. All the samples were active for hydrogen generation by water splitting in presence of methanol as a sacrificial agent, under sunlight type irradiation. The photocatalytic activity increased with Ni-doping with the $In_{1.8}Ni_{0.2}TiO_{5-\delta}$ sample showing the highest rate of hydrogen evolution. This increase in photocatalytic activity can be attributed to the favorable crystal structure i.e. reduction in cell parameters and bond distances and better light absorption properties. Further increase in Ni-doping reduced the rate of hydrogen evolution probably due to segregation of secondary phases and also an increase in non-stoichiometric defects.

References:

1. A. L. Linsebigler, G. Lu, and John T. Yates, Jr., Chem. Rev. 95 (1995) 735-758.
2. A. J. Esswein and D. G. Nocera, Chem. Rev. 107 (2007) 4022-4047.
3. A. Kudo and Y. Miseki, Chem. Soc. Rev. 38 (2009) 253–278.
4. K. Maeda and K. Domen, J. Phys. Chem. C 111 (2007) 7851-7856.
5. Z. Zou, J. H. Ye, K. Sayama, H. Arakawa, Nature 414 (2001) 625–627.
6. WinPLOTR, J Rodrıguez-Carvajal, Laboratorie Leon Brillouin (CEA-CNRS), April 2005 (LLB-LCSIM).

7. N. W. Hurst, S. J. Gentry, and A. Jones, Catal. Rev.-Sci. Engg., 24(2) (1982) 233-309.
8. H. Cheng, L. Chen, A. C. Cooper, X. Sha and Guido P. Pez, Energy Environ. Sci. 1 (2008) 338–354.
9. W. C. Conner, Jr. and J. L. Falconer, Chem. Rev. 95 (1995) 759-708.
10. M. Zielinski, R. Wojcieszak, S. Monteverdi, M. Mercy, M. M. Bettahar, Int. J. Hyd. Energ. 32 (2007) 1024 – 1032.
11. H. Chen and R. T. Yang, Langmuir, DOI: 10.1021/la100172b.
12. Y. W. Li and R. T. Yang J. Phys. Chem. B. 110 (2006) 17175-17181.
13. R. T. Yang and Y. Wang J. Am. Chem. Soc. 131(12) (2009) 4224-4226.
14. Dare-Edwards, M. P., Goodenough, J. B., Hammett, A. and N. D. Nicholson, J. Chem. Soc. Faraday Trans. 77 (1981)643-661.

Chapter 9

Conclusion and scope for future work

The studies carried out in this thesis have contributed significantly to both fundamental understanding and development of heterogeneous catalysis for the major goal of hydrogen generation. Thermochemical water splitting by sulfur based thermochemical cycles which are proposed to be large scale hydrogen generation processes in future utilizing nuclear or solar energy were investigated. This thesis contributes significantly to the development of catalysts for sulfuric acid decomposition: the most high temperature step in these sulfur based thermochemical cycles (Chapter 3, 4, 5 and 6). One more route of hydrogen generation which was explored in this thesis is photocatalytic hydrogen generation which generates hydrogen using solar energy. New photocatalysts were synthesized, characterized and their photocatalytic properties were investigated for hydrogen generation using water and methanol mixture (Chapter 7 and 8). Here, in this chapter we summarize our objective, approach, major findings and scope for future work.

Our objective was to develop a suitable catalyst for sulfuric acid decomposition reaction i.e. a catalyst which is cheap, active and also stable under the hostile reaction environment (high temperature, steam, oxygen and oxides of sulfur). Attempts were also made to understand the probable mechanism of the catalytic action. Thus, emphasis was made on both fundamental and applied catalysis aspects of catalyst development for the said reaction. Sulfuric acid decomposition reaction is currently gaining enormous importance because the reaction is the thermal to chemical energy conversion step in the sulfur based thermochemical cycles which are promising hydrogen generation process for future employing either solar or nuclear energy. For efficient conversion, catalyst is required, hence development of catalyst is a major issue.

The objective of our study in photocatalytic hydrogen generation was to design a photocatalyst which can generate hydrogen efficiently under visible light. With this view we have investigated a novel ternary oxide In_2TiO_5, comprising of a d^0 metal ion Ti^{4+}, and a d^{10} metal ion In^{3+}, for photocatalytic properties for hydrogen generation.

The conventional catalyst mostly explored for sulfuric acid decomposition was Pt-based catalyst but it suffered deactivation under the harsh catalytic environments. So, our approach was to investigate oxide based catalysts for sulfuric acid decomposition which are considered to be a cheaper but catalytically active alternative to noble metal catalysts. The strategies adopted was - (i) Design and fabricate catalytic reactors for the evaluation of catalytic properties of different materials, (ii) preparation of various oxide catalysts based on iron, (iii) the evaluation of their catalytic properties for sulfuric acid decomposition in small scale and an enhanced scale as a function of temperature, time and flux of sulfuric acid and compare with a standard Pt-based catalyst (iv) characterize both the unused and the used catalysts for structure, morphology, redox and thermal properties to evaluate the catalyst and its stability using X-ray Diffraction, N_2-adsorption-desorption, Fourier Transform Infrared Spectroscopy, Temperature Programmed Reduction/Oxidation/Desorption, Pulsed Chemisorption Scanning Electron Microscopy, Transmission Electron Microscopy and Evolved Gas Analysis and (v) provide insights on the mechanistic aspects of the said reaction over the oxide catalysts.

To study the catalytic activities for sulfuric acid decomposition two small scale catalytic reactors were designed and fabricated to evaluate powder catalyst (0.2-2 g) and an enhanced scale reactor to evaluate catalyst in pellet form (20 g). Both the undoped and the chromium doped iron oxide $Fe_{2(1-x)}Cr_{2x}O_3$ $(0.0 \leq x \leq 0.2)$ catalysts facilitated the thermal decomposition of sulfuric acid in temperature range of 550-800 °C as compared to the uncatalysed reaction. 10% Cr substitution in Fe_2O_3 lattice resulted in enhanced reproducibility toward repeated reduction–oxidation cycles and also imparted phase stability to the oxide catalyst towards sulfuric acid decomposition reaction. Spinel ferrites which crystallize into different crystal structures but are ternary oxides of iron, viz; AFe_2O_4 (A = Cu^{2+}, Co^{3+} and Ni^{2}), were also investigated to explore their suitability under harsh reaction conditions. Single phasic spinel ferrites were successfully prepared by glycine-nitrate gel combustion method. Copper ferrite exhibited the highest SO_2 conversion at 800 °C among all the ferrites. Characterization of the fresh and the used catalyst enabled us to delineate the most probable mechanism of sulfuric acid decomposition over these ferrite catalysts which involved a surface metal sulfate formation and then decomposition followed with an oxygen evolution step, with the metal sulfate decomposition step playing the most crucial role in determining the reaction kinetics. The lower thermal stability of sulfate and better reducibility are responsible for the improved catalytic properties of copper ferrite among the three ferrospinels investigated for sulfuric acid decomposition. For practical applicability, the catalytic activities of iron oxide, 10 % chromium doped iron oxide and a commercial Pt (~0.5 wt.%)/Al_2O_3 in granular or pellet form (~4-6 mm spherical beads) were compared for sulfuric acid decomposition in an enhanced scale catalytic reactor (20 g catalyst) in absence of any diluents like nitrogen. In the temperature dependent catalytic runs, the SO_2 conversions for the Cr-doped sample and Pt/Al_2O_3 were comparable but that of iron oxide was less. No decrease in catalytic activity was observed during the long term (100 h) experiment for the two oxide catalysts but a slight decrease in catalytic activity was observed with Pt/Al_2O_3 catalyst pellets as a function of time for 100 h. All the three catalysts exhibited a loss in catalytic activity when subjected to very high flow of sulfuric acid of more than 2 ml/min. From the ex-situ analysis of the fresh and spent catalyst samples the most probable mechanism of the high temperature sulfuric acid decomposition reaction was proposed over the oxide catalysts. While for the Pt/Al_2O_3 catalyst the reason for the decrease in activity of Pt-catalyst was found to be mostly due to metal particle agglomeration. Besides we also observed bulk sulfation of alumina substrate, decrease in N_2-BET surface area, reduction of porosity of support.

The outcome from our investigations of both the oxide based catalysts and the conventional supported noble metal catalyst is that the $Fe_{1.8}Cr_{0.2}O_3$ composition stands best among all the catalysts investigated. On the basis of the overall results obtained from our studies we recommended the $Fe_{1.8}Cr_{0.2}O_3$ catalyst for use in the Sulfur-Iodine demonstration facility at Chemical Technology Division (ChTD), an engineering division in BARC, who has taken up the task of demonstration of the sulfur-iodine cycle at a laboratory scale in quartz. To state a typical result in the testing of the individual sections in the plant a SO_2 conversion of 84 % was achieved at WHSV of 0.05 h^{-1} (98 % H_2SO_4), at 900 °C with 715 g $Fe_{1.8}Cr_{0.2}O_3$ catalyst.

The crystal structure of Indium titanate - In_2TiO_5 was investigated using Rietveld analysis and was found to consist of TiO_6 and InO_6 octahedra with suitable co-ordination environment for having photocatalytic properties. In_2TiO_5 was found to have a band gap in the UV region and also exhibited high photocatalytic activity for hydrogen generation reaction under UV-visible irradiation (16% UV) which is attributed to its favourable electronic structure and crystal structure. In_2TiO_5 was prepared by various methods (solid state, polyol and solvothermal) and investigated for structure, crystallinity, morphology, light absorption properties and their effect on photocatalytic hydrogen generation from water-methanol mixture was investigated under UV-visible irradiation. Ni-doping in indium titanate lattice at A-site induced a lowering in band gap of these semiconductor oxides. All the Ni-doped samples were active for hydrogen generation by water splitting in presence of methanol as a sacrificial agent, under UV-visible irradiation. The photocatalytic activity increased with Ni-doping with the $In_{1.8}Ni_{0.2}TiO_{5-\delta}$ sample showing the highest rate of hydrogen evolution. This increase in photocatalytic activity can be attributed to the favorable crystal structure and better light absorption properties.

The experiments performed with our proposed oxide based catalysts gave us some light regarding the future scope of study to be taken up. One such study is the poisoning effect due to the presence of ppm levels of I_2/I^- in the sulfuric acid stream on the oxide catalyst. Although no HI/I_2 was detected in the sulfuric acid obtained after purification and concentration steps in the demonstration plant of hydrogen generation, but any inefficiency in the above processes can lead to a situation where the catalyst is susceptible to poisons like HI or I_2. So, we would like to take up the studies of poisoning effect of HI or I_2 in minor amounts on the catalytic efficiency of our oxide catalyst for sulfuric acid decomposition. Besides, regarding catalyst development we would also like to disperse the oxide catalyst on suitable supports and evaluate their efficiency.

Regarding photocatalytic water splitting it is an attractive and challenging theme in chemistry and the target for efficient water splitting into H_2 and O_2 (30% in terms of quantum yield at 600 nm) in this research field is yet to be achieved. Hence, the development of new and superior photocatalyst materials is still a major issue. The photocatalytic studies with indium titanate materials provide insights into the band structure and the photocatalytic performance of these materials. The present work can be extended by N-doping in the anionic sublattice of indium titanate. However, efforts have to continue to find newer materials with suitable crystal and band structure which can produce hydrogen with higher efficiencies.

List of publications

Journal Publications:

1. **A. M. Banerjee**, M. R. Pai, K. Bhattacharya, A. K. Tripathi, V. S. Kamble, S. R. Bharadwaj and S. K. Kulshreshtha Catalytic Decomposition of Sulfuric Acid on Mixed Cr/Fe Oxide Samples and its Application in Sulfur–Iodine Cycle for Hydrogen Production, *International Journal of Hydrogen Energy* 33 (2008) 319-326.

2. **A. M. Banerjee**, M. R. Pai, S. S. Meena , A. K. Tripathi and S. R. Bharadwaj, Catalytic Activities of Cobalt, Nickel and Copper Ferrospinels for Sulfuric Acid Decomposition: The High Temperature Step in Sulfur Based Thermochemical Water Splitting Cycles, *International Journal of Hydrogen Energy* 36 (2011) 4768.

3. **A. M. Banerjee**, M. R. Pai, S. R. Bharadwaj, Influence of Ni Substitution on Redox Properties of $In_{2(1-x)}Ni_{2x}TiO_{5-\delta}$, *Thermochimica Acta* 516 (2011) 40–45.

4. M. R. Pai**,** A. Singhal, **A. M. Banerjee**, R. Tiwari, G. K. Dey, A. K. Tyagi, S. R. Bharadwaj, Synthesis, Characterization and Photocatalytic H2 generation over Ternary Indium Titanate Nanoparticles, *Journal of Nanoscience and Nanotechnology* 11 (2012) 1-10.

5. Mrinal R. Pai, Jerina Majeed, **Atindra M. Banerjee**, Ashok Arya, Shovit Bhattacharya, Rekha Rao, and Shyamala R. Bharadwaj, Role of Nd^{3+} Ions in Modifying the Band Structure and Photocatalytic Properties of Substituted Indium Titanates, $In_{2(1-x)}Nd_{2x}TiO_5$ Oxides, *Journal of Physical Chemistry C* 116 (2012) 1458-1471.

6. M. R. Pai, **A. M. Banerjee**, S. R. Bharadwaj and S. K. Kulshreshtha, Synthesis, Characterization, Thermal Stability and Redox Behavior of $In^{3+}{}_2Ti^{4+}{}_{1-x}Tm^{3+}{}_xO_{5-\delta}$ (Tm = Fe^{3+} and Cr^{3+}, $0.0 \leq x \leq 0.2$) Mixed Metal Oxide Catalysts, J of Mater. Res., 22 (2007) 1787.

7. **A. M. Banerjee**, A. R. Shirole, M. R. Pai, A. K. Tripathi, S. R. Bharadwaj, D. Das, P. K. Sinha, Catalytic Activities of Fe_2O_3 and Chromium Doped Fe_2O_3 for Sulfuric Acid

Decomposition Reaction in an integrated boiler, preheater and catalytic decomposer, *Applied Catalysis B: Environmental,* 127 (2012) 36-46.

8. **A. M. Banerjee**, M. R. Pai, S. R. Bharadwaj, Role of Ni substitution on photocatalytic properties of In_2TiO_5, *Journal of Materials Research*, *to be communicated*
9. **A. M. Banerjee**, M. R. Pai, A. K. Tripathi, S. R. Bharadwaj and D. Das, Catalytic decomposition of sulfuric acid over Pt/Al_2O_3 catalysts in pellet form, *manuscript under preparation.*

Books:

1. Mrinal R. Pai, **Atindra M. Banerjee**, A. K. Tripathi and Shyamala R. Bharadwaj, authored Chapter 14 titled "Fundamentals and Appplications of the Photoctalytic Water Splitting Reaction", in book "*Functional Materials: Preparations, Processing and Applications*" edited by S. banerjee and A. K. Tyagi, published by Elsevier Insights, USA, 2012, pg. 579- 606.

Journal Publications (Other than thesis, in related field):

1. K. K. Kartha, M. R. Pai, **A. M. Banerjee**, R. V. Pai, S. S. Meena and S. R. Bharadwaj, Modified Surface and Bulk Properties of Fe-Substituted Lanthanum Titanates enhances Catalytic activity for $CO+N_2O$ reaction, J. Molec. Catal. A, 335 (2011) 158–168.
2. M. R. Pai, **A. M. Banerjee**, K. Karha, R. V. Pai, V. S. Kamble, S. R. Bharadwaj, Mechanism of $CO + N_2O$ Reaction via Transient CO_3^{2-} Species over Crystalline Fe-Substituted Lanthanum Titanates, J. Phys. Chem. B, 114 (2010), 6943–6953.

Symposium/Conferences/Research Scholars Meet/School:

1. **A. M. Banerjee**, A. R. Shirole, M. R. Pai, A. K. Tripathi, S. R. Bharadwaj and D. Das, Kinetics of sulfuric acid decomposition over iron oxide based catalysts, presented in Joint IAEA – ICTP Advanced School on "Development and characterization of materials for hydrogen-based energy systems: Role of nuclear technology" held at International Centre for Theoritical Physics (ICTP), Trieste, Italy on 13-18 June 2011.
2. **A. M. Banerjee** and S. R. Bharadwaj, "Studies on Catalysts for Sulfuric Acid Decomposition Reaction", presented orally at Research Scholars Meet - 2011 held during Feb-2011 organized by Indian Chemical Society.
3. **A. M. Banerjee**, A. R. Shirole, M. R. Pai, A. K. Tripathi and S. R. Bharadwaj, "Synthesis, characterization and Catalytic Activity of Mixed Metal Oxides for Energy and Environment Related Reactions" presented orally at CATSCHOL-2011 ICT, Mumbai Mar-2011.
4. **A. M. Banerjee**, A. R. Shirole, M. R. Pai, A. K. Tripathi, S. R. Bharadwaj and D. Das "Catalytic decomposition of sulfuric acid over Fe_2O_3 and Pt/Al_2O_3: A comparative study" poster presentation at 3rd DAE-BRNS ISMC-2010 held at BARC, Mumbai on 7-11th Dec 2010.
5. **A. M. Banerjee**, A. R. Shirole, M. R. Pai, A. K. Tripathi, V. S. Kamble, S. R. Bharadwaj, D. Das, P. K. Sinha "Catalytic decomposition of sulfuric acid: an important step in sulfur-iodine thermochemical cycle for hydrogen generation using nuclear heat from CHTR", Poster presentation at Peaceful Uses of Atomic Energy (PUAE-09) held in Delhi during 29th Sept to 1st Oct 2009. AR-8 pp. 250-251.
6. **A. M. Banerjee**, M. R. Pai, A. K. Tripathi and S. R. Bharadwaj on "Application of transition metal ferrites AFe_2O_4 (A= Co, Ni, Cu) for the catalytic decomposition of sulphuric acid involved in Sulphur-Iodine Thermochemical Cycle for Nuclear Hydrogen production"

was presented at Peaceful uses of atomic energy (PUAE-09) held in Delhi during 29th Sept to 1st Oct 2009.

7. **A. M. Banerjee**, A. R. Shirole, M. R. Pai, A. K. Tripathi, V. S. Kamble, S. R. Bharadwaj and D. Das "Studies on sulfuric acid decomposition over iron oxide catalyst" was presented at World Hydrogen Technologies Convention, (WHTC-09) held at New Delhi on 26-28 Aug' 2009.
8. M. R. Pai, **Atindra M. Banerjee**, Jerina Majeed, Shyamala. R. Bharadwaj on "Photocatalytic Water Splitting Reaction under actual Sun Light/Sunlight-type Irradiation using Substituted Indium Titanates, $In_{2(1-x)}A_{2x}Ti_{1-y}Tm_yO_5$ (A = Ni^{2+} and Nd^{3+}, Tm = Fe^{3+} and Cr^{3+}, x/y=0.0-0.2)" was presented at World Hydrogen Technologies Convention, (WHTC-09) held at New Delhi on 26-28 Aug' 2009.
9. **A. M. Banerjee**, A. R. Shirole, K. Bhattacharyya, M. R. Pai, S. Varma, A. K. Tripathi, V. S. Kamble, S. R. Bharadwaj, S. R. Nair, P. K. Sinha and D. Das, Results on long term catalytic activity of iron oxide for decomposition of sulfuric acid" poster presentation in ISMC-2008 held at BARC, Mumbai on 2-6th Dec 2008.
10. **A. M. Banerjee**, M. R. Pai, and S. R. Bharadwaj, Preparation and characterization of mixed oxides for environmental and energy related reactions; oral presentation in National Symposium for Materials Research Scholars- MR08, held at Indian Institute of Technology, Powai, Mumbai on 17th-18th May (2008) 42.
11. **A. M. Banerjee**, M. R. Pai, and S. R. Bharadwaj; Temperature programmed reduction of $In_{2(1-x)}$ $Ni_{2x}TiO_{5-\delta}$ oxides; oral presentation in Sixteenth national Symposium on Thermal Analysis (THERMANS-2008) at IGCAR, Kalpakkam, Feb 4-6, (2008), 293-295.
12. **A. M. Banerjee**, M. R. Pai, K. Bhattacharya, A. K. Tripathi, V. S. Kamble, S. R. Bharadwaj, S. K. Kulshreshtha, "Studies on sulfur-iodine thermochemical cycle for

hydrogen production" poster presentation in the 3rd DAE-BRNS ISMC-2010 held at BARC, Mumbai on 7-11th Dec 2010.

Awards:

1. One of the recipient of **DAE Group Achievement Award 2010**, titled “Development of Catalysts for Various Applications Related to DAE Programme”
2. **Best Paper Award (third) for poster presentation**: A. M. Banerjee et al for “Studies on Sulfur-Iodine Thermochemical cycle for Hydrogen Production” in ISMC-2006 held at BARC, Mumbai on Dec 2006.
3. **Best Paper Award (Second) for oral presentation**: A. M. Banerjee et al for "Preparation and characterization of mixed oxides for environmental and energy related reactions“ in National Symposium for Materials Research Scholars- MR08, held on 17th-18th May, 2008 at Indian Institute of Technology, Bombay.
4. **Best Paper Award (Second) for oral presentation**: A. M. Banerjee et al for "Temperature programmed reduction of $In_{2(1-x)}$ $Ni_{2x}TiO_{5-d}$ oxides” in Sixteenth national Symposium on Thermal Analysis (THERMANS-2008) at IGCAR, Kalpakkam, Feb 4-6, 2008.
5. **Best Paper Award (Second) for poster presentation**: A.M. Banerjee et al for “Catalytic decomposition of sulfuric acid over Fe_2O_3 and Pt/Al_2O_3: A comparative study” in ISMC-2010 held at BARC, Mumbai on 7-11th Dec 2010.